

Clemson University

**TigerPrints**

---

All Dissertations

Dissertations

---

December 2020

## Understanding Corrosion in Modular Acetabular Tapers: Retrieval Analysis, In Vitro Testing and Cell-Material Interactions

Aarti Shenoy

Clemson University, [aarti.shenoy17@gmail.com](mailto:aarti.shenoy17@gmail.com)

Follow this and additional works at: [https://tigerprints.clemson.edu/all\\_dissertations](https://tigerprints.clemson.edu/all_dissertations)

---

### Recommended Citation

Shenoy, Aarti, "Understanding Corrosion in Modular Acetabular Tapers: Retrieval Analysis, In Vitro Testing and Cell-Material Interactions" (2020). *All Dissertations*. 2725.

[https://tigerprints.clemson.edu/all\\_dissertations/2725](https://tigerprints.clemson.edu/all_dissertations/2725)

This Dissertation is brought to you for free and open access by the Dissertations at TigerPrints. It has been accepted for inclusion in All Dissertations by an authorized administrator of TigerPrints. For more information, please contact [kokeefe@clemson.edu](mailto:kokeefe@clemson.edu).

UNDERSTANDING CORROSION IN MODULAR ACETABULAR TAPERS:  
RETRIEVAL ANALYSIS, IN VITRO TESTING AND  
CELL-MATERIAL INTERACTIONS

---

A Dissertation  
Presented to  
the Graduate School of  
Clemson University

---

In Partial Fulfillment  
of the Requirements for the Degree  
Doctor of Philosophy  
Bioengineering

---

by  
Aarti Shenoy  
December 2020

---

Accepted by:  
Jeremy Gilbert, Ph.D., Committee Chair  
Martine LaBerge, Ph.D.  
John DesJardins, Ph.D.  
Melinda Harman, Ph.D.

## Abstract

Modular metal-on-metal acetabular tapers comprise two overarching design categories: a titanium shell and a metal/ceramic/polymer liner pair, or a dual-mobility articulation design with an added polymeric insert containing a freely rotating femoral head. Both designs often include a metal-on-metal (MoM) or modular dual-mobility (MDM) shell-liner interfaces, which is prone to corrosion and associated local effects. The goals of this dissertation were to document and distinguish between corrosion modes at this modular junction, to design in vitro test methods to characterize mechanical modes, and to examine their interactions with macrophages, which represent a critical part of the immune response.

Through retrieval analysis, we established that MoM acetabular tapers are less susceptible to mechanically-assisted corrosion (MAC). Retrieved CoCrMo liners revealed a prevalence of chemically driven corrosion damage modes (intergranular corrosion (IGC), pitting, phase boundary corrosion (PBC)) over mechanically-driven ones (fretting corrosion, large-scale wear, stress cracking). Importantly, corrosion was detected outside engagement regions, where no physical interfacial contact can occur, or tight crevice exists. Cellular remnants were also identified within these tight crevice-like taper surfaces, which fit a narrow size distribution similar to macrophages. In vitro testing revealed that contact areas between shell-liner pairs remained a fraction of the total taper surface area, which translated to low currents (under  $1\mu\text{A}$ ) generated over a short-term incremental cyclic loading test.

An electrochemical impedance spectroscopy (EIS)-based method was used to examine resulting impedance changes in retrieved CoCrMo liner surfaces associated with specific surface features, associated with IGC, oxide deposits and PBC. Indeed, surface impedance was correlated to the type of surface damage. Impedance analysis proved to be a valuable tool for identifying corrosion modes and adds a quantitative method to the retrieval analysis paradigm.

Finally, we developed assays to examine macrophage viability outcomes in response to different corrosion and fretting corrosion stimuli. Ongoing fretting corrosion, and the associated debris generation and negative potential shifts seemed to be the most influential factors on macrophage mortality. In a separate study, where CoCrMo alloy was corroded at high anodic potentials to generate ions and debris, we found macrophage mortality was affected in a dose-dependent manner, primarily by chromium ions in culture media, whereas solid cobalt oxide debris particles killed macrophages in a proximity-dependent manner. A sublethal dose (LD50) of metal ions was found to induce a weak proinflammatory response, measured by cytokine (TNF- $\alpha$ , interleukin (IL)-1 $\beta$ , IFN- $\gamma$  and IL-27) and chemokine expression, at 24 h. We also detected comparable levels of IL-13, which is a known mediator of the anti-inflammatory M2 phenotype in macrophages.

With the results described in this study, we can conclude that chemically driven corrosion modes dominate acetabular taper corrosion over mechanical modes. Corrosion byproducts might also initiate adverse local reactions by inducing cell death and activation of macrophages. Thus, MoM acetabular junctions represent a significant factor

in total hip arthroplasty outcomes. Since MDM device usage is on the rise owing to its excellent outcomes in high dislocation risk patients, understanding possible corrosion and associated phagocytic responses proves to be crucial in ensuring satisfactory patient outcomes and to make prudent decisions during surgical planning in terms of device and material choices.

## **Dedication**

To my family, Anil, Anjana, and Akshata, thank you for being a constant source of support, motivation, and endless cheerleading. This dissertation belongs to you as much as it does to me.

To the rest of my family, uncles, aunts, grandparents, and cousins, for always encouraging me and showing your love and support at every family gathering and on every phone call.

To my friends, Manjistha, Sachin, Neehar, Ryan, Shalaka, Rohan, Saloni, Ruchika, Aditi, Pooja, and Poonam, you celebrated my triumphs, big and small, and helped me see the light at the end of the tunnel during the lows. Thank you for bringing levity, laughter, and much-needed sanity to days when I did not know which way is up.

To Albus, for bringing structure and love into my daily life, and also for being a constant companion while I wrote this thesis.

Finally, I dedicate this thesis to all first-generation graduate students everywhere: your perspective and your presence in STEM is valuable. I hope you find mentors and colleagues who make the journey less difficult and more enjoyable. I also hope you find the resilience and strength within yourself to build the path ahead. You deserve to be here, and you deserve to be happy and healthy while accomplishing your professional goals.

## **Acknowledgements**

It has been an 8 year long journey to earn this degree. I started as a Biomedical Engineering MS student at Syracuse University, transitioned to the PhD program, then transferred to the Clemson-MUSC Bioengineering Program at Clemson University where my journey culminates in a PhD degree and the title of “Doctor”. I have been lucky to have found wonderful colleagues and mentors throughout.

First, I am thankful to have started my graduate school journey in Dr. Jeremy Gilbert’s group as a newly arrived student from India. I cherish our conversations and discussions, which were often a morale boost and sometimes left me overwhelmed with the directions my research could take. I always came away from our meetings with new ideas, renewed vigor, and often a textbook or two (Dr. Gilbert, I promise I will return each textbook back to you). I am grateful for his feedback and encouragement for helping me improve my writing, speaking and mentoring skills as well. I have learnt so much beyond science and engineering skills, and I am lucky to have him as a mentor going forward.

I also want to thank members of my PhD committee, Dr. Martine LaBerge, Dr. John DesJardins, and Dr. Melinda Harman at Clemson Bioengineering. Their thoughtful advice, interesting questions and feedback on my research endeavors helped hone my dissertation into its present shape. Dr. LaBerge also supported and guided me in securing an internship in technology transfer, for which I am very thankful.

I want to acknowledge Dr. Ann Foley and Dr. Robin Muise-Helmericks for teaching me cell culture techniques and analysis methods. They also allowed me to use their lab space

for those experiments and made time in their schedule to guide me through troubleshooting when I needed help. I must also thank Dr. Vincent Pellegrini who allowed me to observe orthopedic surgeries in his operating room. I will always remember how he discussed his surgical methods and device selection thought process with me and answered my questions with care.

My graduate school journey was made all the more fun and interesting because of the colleagues I got to work with. Dr. Sachin Mali, Dr. Yangping Liu, Dr. Shiril Sivan and Dr. Eric Ouellette were early mentors in the laboratory and taught me the basics of electrochemistry and corrosion testing. Drs. Mali and Ouellette helped me learn device testing methods and guided me as I ran my first few experiments. Dr. Sivan has, till date, made himself available to share his thoughts and his knowledge in corrosion, materials science, and post-PhD career paths. Dr. Liu first helped me learn pin-on-disk experimental techniques and continues to help with troubleshooting experiments. I also want to acknowledge Dr. Jua Kim, Dongkai Zhu and Can Aslan for their help with experimental techniques, and for being excellent colleagues and friends. I have enjoyed our casual midday chats around the lab which made my time in the Gilbert group all the more fun. I specifically want to thank Ryan Barrs, Dr. Piyush Khullar and Dr. Michael Wiegand, for doing all of the above and also being a true friend to me. Thank you for making MUSC feel less unfamiliar. I would also like to acknowledge Brianna Gamble, my high school mentee during the summer of 2019, who conducted some of the experiments and analysis for the work under aim 2c. I enjoyed working with her, and her enthusiasm and drive to learn laboratory skills are sure to carry her far in her career.



I want to thank Lynore de la Rosa and Karen Low at Syracuse University, and Tommy Gallien, Maria Torres, Cameron Hay and Trish Nigro at Clemson-MUSC, whose prompt handling of administrative matters helped me navigate those hurdles with relative ease. They helped me place orders, reminded me to fill out important forms and overall, made my time at each university that much easier. I also want to acknowledge the machinists, Dick Chave and Bill Dossert at Syracuse University and Jeff Holliday and the team at Clemson University, for their invaluable help in fabricating the fixtures that made some of my experiments possible.

I must acknowledge my team at the Clemson University Research Foundation (CURF), where I spent the last few months of my PhD journey learning about technology transfer and commercialization. Chris Gesswein and Andy Bluvas have been great supervisors and have been instrumental in broadening my understanding of academic research and its place in the larger context. I will carry this knowledge and experience with me for the rest of my career. Finally, I also want to thank DePuy Synthes Inc. for funding part of my graduate research and for providing test samples and materials.

## TABLE OF CONTENTS

	Page
Title page .....	i
Abstract .....	ii
Dedication .....	v
Acknowledgements .....	vi
List of tables .....	xiii
List of figures .....	xiv
<b>1 Introduction</b>	
1.1 Background .....	1
1.2 Modular Metal-on-Metal Acetabular Tapers .....	2
1.3 Clinical Causes for Acetabular Revision .....	3
1.4 Modular Dual-Mobility Acetabular Tapers .....	4
1.5 Corrosion Modes in Metal-on-Metal Acetabular Tapers .....	5
1.6 In Vivo Corrosion Mechanisms and Immune System Interactions .....	6
1.7 Motivation .....	13
<b>2 Goals and Hypotheses .....</b>	<b>14</b>
<b>3 Non-Tribological Corrosion Modes Dominate Wrought CoCrMo Acetabular Taper Corrosion: A Retrieval Study .....</b>	<b>22</b>
3.1 Abstract .....	23
3.2 Introduction .....	25
3.3 Materials & methods	
3.3.1 Sample description .....	27
3.3.2 Corrosion modes and their description .....	29
3.3.3 Imaging methodology .....	31
3.3.4 Sectioning of severely corroded liner .....	32
3.3.5 Calculation of cell-like features size distribution .....	33
3.4 Results .....	33
3.4.1 Intergranular corrosion (IGC) .....	36
3.4.2 Pitting attack .....	38
3.4.3 Phase boundary dissolution .....	39
3.4.4 Preferential etching/transgranular corrosion .....	40
3.4.5 Fretting and material transfer .....	41
3.4.6 Cell-like remnants and biological deposits .....	42

	3.4.7	Sectioned implant: IGC evaluation.....	44
	3.5	Discussion.....	45
	3.6	Conclusions.....	52
4		Near-field Electrochemical Impedance Spectroscopy of Retrieved Hip Implants	
	4.1	Abstract.....	53
	4.2	Introduction.....	56
	4.3	Materials & methods	
	4.3.1	Sample description.....	58
	4.3.2	Near-field EIS technique.....	60
	4.3.3	Symmetry-based EIS analysis method.....	61
	4.3.4	Statistical analysis.....	64
	4.4	Results.....	65
	4.5	Discussion.....	76
	4.6	Conclusions.....	87
5		In Vitro Test Methods for Seating and Fretting Corrosion Behavior of Modular Metal-on-Metal Acetabular Tapers.....	89
	5.1	Abstract.....	90
	5.2	Introduction.....	92
	5.3	Materials & methods	
	5.3.1	Sample description.....	95
	5.3.2	Sample preparation.....	97
	5.3.3	Stage I: Seating method and push-out.....	98
	5.3.4	Stage II: ICFC test and push-out.....	99
	5.3.5	Post-test characterization.....	102
	5.3.6	Statistical comparisons.....	102
	5.4	Results	
	5.4.1	Stage I: Seating and push-out.....	103
	5.4.2	Stage II: ICFC and push-out.....	106
	5.5	Discussion.....	109
	5.6	Conclusions.....	118
6		Measuring Acetabular Shell and Liner Taper Compliance	
	6.1	Abstract.....	120
	6.2	Introduction.....	121
	6.3	Materials & methods	
	6.3.1	Sample description.....	122
	6.3.2	Method.....	124
	6.4	Results.....	125
	6.5	Discussion.....	128

6.6	Conclusions.....	133
7	Tribocorrosion Debris and Cathodic Voltage Shifts in CoCrMo Affect Murine Macrophage Viability Outcomes in In Vitro Fretting Corrosion	
7.1	Abstract.....	135
7.2	Introduction.....	137
7.3	Materials & methods	
7.3.1	Sample description.....	139
7.3.2	Cell culture and testing matrix.....	140
7.3.3	Pin-on-disk fretting test.....	142
7.3.4	Cell viability assay.....	144
7.3.5	Cell count and size calculations.....	145
7.3.6	Cell morphology and debris characterization.....	146
7.3.7	Statistical analysis.....	147
7.4	Results	
7.4.1	Fretting corrosion.....	147
7.4.2	Fretting site: debris and cells.....	149
7.4.3	Macrophage viability.....	151
7.4.4	Cell size and morphology.....	154
7.5	Discussion.....	157
7.6	Conclusions.....	167
8	Metal Ions and Oxide Particles Generated from CoCrMo Anodic Polarization Affect Murine Macrophage Mortality and Activation	
8.1	Abstract.....	169
8.2	Introduction.....	171
8.3	Materials & methods	
8.3.1	Generation of corrosion byproducts.....	173
8.3.2	Corrosion fluid characterization.....	174
8.3.3	Solid debris characterization.....	175
8.3.4	Cell culture.....	176
8.3.5	MTT viability assay.....	177
8.3.6	Live-dead fluorescent imaging.....	178
8.3.7	Cytokine and chemokine expression profile.....	179
8.3.8	Statistical analysis.....	180
8.4	Results.....	180
8.4.1	Corrosion fluid ionic composition.....	181
8.4.2	Solid debris morphology, composition, and size distribution..	181
8.4.3	Macrophage viability effects.....	183
8.4.4	Proximity effects of solid debris (red particles) exposure.....	185

	8.4.5 Cytokine and chemokine expression in response to sublethal dose of metal ions.....	186
	8.5 Discussion.....	188
	8.6 Conclusions.....	194
9	Discussion.....	196
10	Conclusions.....	206
11	Future Work.....	211
	References.....	216
	Appendix	
	A1. Retrieved device sectioning & surface preparation for microstructural analysis.....	239
	A2. Preparation of microelectrode for near-field EIS measurements.....	241
	A3. Preparation of tribocorrosion chamber for fretting corrosion experiment with macrophages.....	242
	A4. Preparation of cells in tribocorrosion chamber (petri dish + metal disk) sample for SEM analysis.....	243
	Curriculum Vitae.....	245

## List of Tables

4.1: Summary of calculated equivalent circuit parameters for all samples across all groups.....	73
7.1: Test matrix applied for this study showing different electrochemical conditions and inclusion or exclusion of fretting motion.....	141
7.2: Summary of average viability for all groups and locations.....	152
8.1: ICP-MS results for cobalt, chromium, and molybdenum ion concentrations in corrosion fluid.....	181

## List of Figures

3.1: Schematic and photograph showing the engagement region formed between an acetabular shell-liner couple .....	28
3.2: Retrieved liner with a band of intergranular corrosion (IGC) in the lower taper engagement region .....	32
3.3: Scanning electron micrographs showing typical microstructure of the low carbon wrought CoCrMo alloy .....	34
3.4: Schematic showing different types of damage seen within the taper region of one sample .....	36
3.5: Examples of pitting attack in acetabular liner tapers .....	38
3.6: Examples of phase boundary dissolution in retrieved acetabular liner tapers .....	39
3.7: Transgranular corrosion lines in a single sample.....	40
3.8: Fretting scars seen in an examined sample .....	41
3.9: Cellular remnants and their size distribution .....	42
3.10: Sectioned liner showing macroscale IGC on the taper surface .....	44
4.1: Photographs showing test samples for IGC, oxide deposits and PBC test regions ....	59
4.2: Schematic and photograph of test setup for NEIS measurement.....	60
4.3: Equivalent circuit for CPE-Randle's and coated model along with the Bode plots showing $\log  Z $ and phase angle .....	61
4.4: Bode plots for control sample .....	65
4.5: Bode plots summarized, for IGC samples .....	67
4.6: Bode plots summarized, for oxide deposit sample .....	68
4.7: Bode plots summarized, for PBC samples.....	70
4.8: Calculated Bode plots for all tested samples .....	72
4.9: Average $\alpha$ , $Q$ and $R_p$ across three damage modes and control samples.....	74
4.10: Average $Q$ vs $\alpha$ , average $R_p$ vs $\alpha$ , average $R_p$ vs $Q$ across all test groups.....	75
4.11: Comparisons of electron micrographs and Bode plots for representative samples from each group, IGC, oxide deposits, PBC and control.....	78

4.12: Plot showing a linear log-log relationship between Q and Rp for PBC, oxides and control groups .....	83
5.1: Schematic showing the acetabular shell-liner junction with (inset) showing the actual geometry in the taper and the distinct areas of contact.....	95
5.2: Scanning electron micrographs showing (a) the liner taper surface and (b) the shell taper surface.....	97
5.3: Experimental setup for displacement measurement during assembly of the shell-liner construct.....	97
5.4: Experimental setup showing the three-electrode system for the short-term ICFC test with the construct held at physiological angle of 55.....	100
5.5: Representative plots of seating load (N) vs seating displacement ( $\mu\text{m}$ ); seating displacement ( $\mu\text{m}$ ) and seating load (N) vs time for DVRT1 data; seating stiffness ( $\text{N}/\mu\text{m}$ ), k, across all three groups.....	103
5.6: Average push-out load, for Stage I and II testing.....	105
5.7: Plots showing raw data for fretting currents .....	106
5.8: Average onset load (N) for each material group and average current at 3600 N across all three groups tested ( $n = 5$ ) .....	107
5.9: Pre- and post-test surface characterization of shell and liner taper surfaces .....	108
5.10: Seating stiffness ( $\text{N}/\mu\text{m}$ ) of head-neck taper vs acetabular taper .....	111
5.11: Low and high magnification electron micrographs of surface area in contact and material transfer on shell-liner tapers post-test.....	116
6.1: Acetabular shells and liners used in this study .....	122
6.2: Schematic showing the test method setup .....	124
6.3: Representative plots showing load-deflection curve and stiffness calculation using linear portion of the load-deflection curve.....	126
6.4: Summarized stiffness data for all tested liners across two sizes and three materials .....	126
6.5: Stiffness-deflection plot showing overall differences between liners of different sizes and materials .....	128
6.6: Average stiffness and change in diameter for all components across sizes and materials .....	131



7.1: Schematic and photograph of test setup showing pin-on-disk used for experiment and the sample setup of disk and adhered petri dish .....	142
7.2: Locations where live/dead fluorescent images were captured.....	145
7.3: Representative plots showing example electrochemical results of fretting currents and potential shifts due to fretting motion .....	148
7.4: Electron micrographs of groups 1 and 2 samples showing differences in post-test surface features .....	149
7.5: Summarized viability results for all test conditions and locations within the test chamber.....	151
7.6: Live/dead fluorescence images for -50 mV + fretting; OCP + fretting; OCP + no fretting; -500 mV + no fretting .....	153
7.7: Average cell size ( $\mu\text{m}^2$ ) calculated from live and dead cells across all four groups, representing projected cell area calculated from fluorescent images (n=5) .....	154
7.8: Secondary electron micrographs for -50 mV + fretting; OCP + fretting; OCP + no fretting; -500 mV + no fretting showing morphological differences between cells in each group .....	156
7.9: High magnification electron micrographs showing debris composition at fretting site .....	158
7.10: Electron micrograph and EDS analysis of fretting site.....	159
7.11: Current density for one trial -500 mV + no fretting .....	161
7.12: Electron micrograph and EDS analysis of debris and salt deposits in proximity to macrophages adjacent to the fretting site.....	163
8.1: Solid debris characterization results including digital optical and electron micrographs and EDS analysis .....	181
8.2: Viability (%) vs concentration plots for corrosion fluid and solid debris (red particles only) .....	183
8.3: Brightfield and fluorescent images showing proximity-dependent viability effects on macrophages in response to solid debris particles .....	185
8.4: Cytokine and chemokine protein array results .....	186

# Chapter 1

## Introduction

### 1.1 *Background*

Orthopedic implants, particularly hip replacement systems, have a long history, both in terms of design and the materials used. Early designs, prior to Sir John Charnley's introduction of low-friction polyethylene and stainless steel design in the 1960s, comprised of a monolithic femoral component replete with a femoral head inserted into the femur interfaced with a cup fitted into the acetabulum. Initially, materials like cobalt-chromium-based Vitallium were used with Teflon forming the articulating cup component. After Sir John Charnley pioneered the modern-day equivalent total hip arthroplasty procedure, overall device design and surgical procedures have remained more or less the same [1]. Charnley's work through the 1960s and 1970s led the path to the use of ultra-high molecular weight polyethylene (UHMWPE) as a bearing material instead of Teflon which was associated with high levels of toxicity due to the wear particles it released [2]. The monobloc designs and the materials used at the time were also associated with clinical concerns. Monobloc designs severely restricted the surgeon's ability to customize devices for patients, leading to leg length discrepancies, and the cemented fixation was associated with increased instance of bone loss and mechanical failure of the device [3], [4].

Joint replacement surgeries are indicated in end-stage osteoarthritis [5] as well as in cases of other inflammatory conditions of the joint or traumatic injury, with remarkable success

in restoring mobility and quality of life for patients over a wide range of age groups. Today, THAs are among the high volume surgical procedures being conducted and the annual number of joint replacement surgeries, including total knee arthroplasty (TKA), is predicted to grow exponentially over the next decade, with an increase of around 240% for primary THAs and 401% for primary TKAs by 2040 [6]. They are also among the most successful surgical procedures, with a revision rate of under 5% per year.

Modularity, or the use of multiple components that are assembled in situ during surgery, was introduced during the 1970s, and has been one of the most important design improvements in the total joint replacement world. It has allowed for more precise pre-operative planning, made inventory management in hospitals more efficient and has improved clinical outcomes by allowing greater flexibility in device component choice and by making revision surgeries less damaging to the bone stock by making selective component revision possible.

## 1.2 *Modular metal-on-metal acetabular tapers*

One such modular junction is formed at the acetabular junction, formed between a shell and a liner. A porous-coated titanium acetabular shell, usually Ti6Al4V alloy, is impacted into an under-reamed native acetabulum to allow stronger, cementless initial fixation and easier bone ingrowth, or osseointegration, into the acetabular shell coating. A liner or insert is then press-fit into the shell forming a tight connection at the taper regions of the shell and liner. Taper designs vary among manufacturers, but this principle remains uniform. Liners were introduced as a way to minimize bone loss in cases of

revision and to allow screw-fixation of the shell in patients with low amounts of viable bone stock [7]. Well-fixed acetabular shells could be saved, and the liner replaced easily due to modularity.

Early designs used the UHMWPE insert, which unfortunately generated wear particles due to delamination at the bearing surface [8]. These wear particles were known to cause severe osteolysis and aseptic loosening of the device, and hence, alternative bearing surfaces such as metals (mostly CoCrMo) and ceramic liners were brought back into use [8], [9]. However, the metal inserts forming a metal-on-metal junction with the titanium shell were also susceptible to corrosion and subsequent metal ion release [10]–[13], and in recent years, are not used as much.

### 1.3 *Clinical causes for acetabular revision*

The THA surgery is a very successful surgery in terms of failure rates, with revision occurring in only 1-3% cases of the total number of primary surgeries per year [14]. Credit for this success goes to continuous improvement of surgical techniques, device design advancement and improved patient risk assessment for mitigating risk factors [15], [16]. However, with a low but near-constant rate of revision and exponentially rising volume of surgeries, the number of patients affected and the healthcare cost burden associated with revision surgeries continues to rise [17]. The rate of revision remaining constant might be related to the decreasing age of primary THA recipients, who go on to lead more active lifestyles and enjoy a longer lifespan, often extending beyond the average lifespan of the implanted device.

The leading causes of revision in the otherwise successful THA surgery are dislocation and/or instability, infection and mechanical or aseptic loosening of the femoral or acetabular component [10], [18]–[20]. Gwam et al. indicate in their study that among 258,461 total revision surgeries between January 2009 to December 2013, dislocation (17.3%) prevailed as the main cause for revision followed by mechanical loosening (16.8%). Out of these, revision due to failure of the acetabular component occurred in 24.7% cases out of 53,508 cases, and all-component revision was the most common outcome, a total of 41% of the revision surgeries [18]. Gascoyne et al. also found a correlation between cup inclination angle and impingement wear, which is often associated with dislocation and loosening, with higher inclination angles tending to result in dislocation [10].

Other causes for acetabular revision include malpositioning of components and adverse local tissue reactions (ALTRs) [10], [11], [20]. ALTR is a blanket term used to denote localized tissue damage encompassing osteolysis (bone loss), pseudotumor or avascular necrosis and fluid retention, and is thought to be associated with wear debris and corrosion byproducts released from the implanted device [21]. However, direct links between wear and corrosion byproducts and ALTRs have not yet been demonstrated.

#### 1.4 *Modular dual-mobility acetabular tapers*

One of the strategies for mitigating dislocation risk is the use of dual-mobility tapers, which can either be a monobloc design with an acetabular shell and a polymer insert with a freely rotating femoral component, or an acetabular shell-liner pair with the same

polymer insert. The liner delivers the same advantage as in the MoM acetabular component. These devices have shown great promise in minimizing dislocation risk and thereby lowering possibility of revision [22]–[24]. Revision after dislocation surgery with MDM acetabular devices have shown excellent survivorship and reported patient satisfaction remains high with Harris Hip Scores above 95 [25]. Dual-mobility devices are seeing a drastic increase in use, especially in revision surgeries after initial primary implant dislocation. However, the modular junction formed at the shell-liner junction, where a metallic liner is often used, is still susceptible to corrosion.

#### 1.5 *Corrosion modes in metal-on-metal acetabular junctions*

Retrieval analysis reports of MoM acetabular tapers often report mechanically-assisted crevice corrosion (MACC) as the leading cause of corrosion [26]–[28]. Retrieval analysis is an excellent starting point for understanding taper corrosion mechanisms in vivo by directly documenting and studying the outcomes. Previously reported studies have placed an emphasis on the clinical causes for revision, wear-related damage and metal ions release [10], design factors [29], volumetric material loss measurements [30] and overall severity of visible damage [31]. These are important factors that have a significant impact on THA outcomes. However, a comprehensive discussion of the different corrosion and damage modes observed within the acetabular taper junctions is missing from the literature. The contribution of the biomaterial itself to the corrosion of the specific component also has not been discussed.

Close examination of MoM acetabular taper surfaces might bring to light in vivo processes that result in pivotal observations and pave the path for new research directions. Imaging techniques like scanning electron microscopy and x-ray based compositional analysis of retrieved device surfaces can yield important information that is not discerned by visual examination [32], [33]. Therefore, these techniques can be employed to the as-yet unexamined damage features of MoM acetabular tapers to uncover new observations.

#### 1.5.1 *Cobalt-chromium-molybdenum alloy*

Biomedical alloys for THAs are chosen based on their mechanical properties of strength and modulus, wear resistance and hardness and in more recent years, due to their corrosion resistance. The present form of the cobalt-chromium-molybdenum (CoCrMo) alloy has been used for load-bearing applications in THAs since 1990s, for the femoral head and the acetabular liner applications, due to its superior wear resistance and excellent mechanical properties.

CoCrMo alloys present a typical composition of “58.9–69.5% Co, 27.0–30% Cr, 5.0–7.0% Mo” [34], the rest composed of carbon, and other trace elements. The CoCrMo alloys used in biomedical applications can be wrought or cast, based on the heat processing the material goes through, but both forms exhibit a metastable fcc phase [34]. This thesis focuses primarily on the wrought CoCrMo alloy, due to its unique microstructure comprised of fine-grained alloy interspersed with heat treatment-derived carbides, thus forming high carbon (0.05-0.35%) and low carbon (<0.05%) variants. The

wrought alloy was developed to have superior wear properties and corrosion resistance compared to the cast alloy. However, the heat treatments used to create these carbides also lead to grain boundary sensitization [35] sensitizing the boundary regions to corrosion. Thus, the alloy microstructure plays a role in the alloy's resistance or susceptibility to corrosion and must be investigated. Corrosion resistance in biomedical alloys relies upon the presence of a stable passivating oxide film which form spontaneously and mitigate corrosion of the underlying metal [36]. The oxide film in CoCrMo alloys is comprised primarily of chromium oxides ( $\text{Cr}_2\text{O}_3$ ) and is largely stable.

#### 1.5.2 *Quantitative techniques for retrieval analysis*

Corrosion is an electrochemical process, largely driven by redox reactions occurring in aqueous conditions. The passivating oxide film combined with the underlying metal when in contact with an electrolyte can be modeled as an equivalent circuit composed of resistive and capacitive elements, based on its impedance [36]. The impedance of a surface determines its corrosion resistance, and recent studies have shown a correlation between extent of corrosion damage in retrievals and impedance values [37], [38].

In studies outside the medical devices field, EIS is widely used to study corrosion-protective films and coatings. Organic coatings can be modelled as a tortuosity pore model [39] where a coating is treated as a ternary system comprised of solid, liquid and gaseous states (implying porous structure analogous to discontinuous surfaces marked by material loss). Another study in 1990 demonstrated that inhomogeneities in the surface (defects, chemical contaminants, etc.) can be detected using EIS, and can be modeled as a



coated model equivalent circuit [40]. Finally, researchers also found that diffusion plays a prominent role in defining thin film impedance, when film thickness is exceedingly small compared to the distance between working and reference electrodes, and that hydration of the coating or thin film influences the final impedance readout [41].

Retrieval analysis methods often include quantification of surface material loss [30] or visual scoring of severity of damage [42]. These techniques do not account for impedance of the surface or how corrosion and wear related damage might alter this impedance.

Applying methods cited above in acetabular tapers, in conjunction with visual observations made through imaging, might present a more holistic picture of corrosion at these tapers. Therefore, a goal of this study was to develop a test method to perform electrochemical impedance spectroscopy (EIS) on small surface areas of a retrieved device, over a range of high to low frequencies, and to compare these impedance responses across different corrosion modes and visual damage modes identified on retrieved CoCrMo liner taper surfaces.

### 1.5.3 *Mechanically-assisted crevice corrosion (MACC) in MoM acetabular tapers*

Evidence of MACC has been reported extensively in head-neck tapers with a Ti6Al4V-CoCrMo material combination [42]–[46]. Retrieval studies of both MoM and MDM acetabular tapers often attribute corrosion related damage in these tapers to MACC as well [11], [26], [27], [29]. However, no systematic in vitro test method has been developed that can assess MACC at acetabular tapers. In vitro test methods for head-neck tapers provide a wealth of knowledge and understanding of how interfacial micromotion

[47] and design factors [45] influence fretting corrosion performance. Seating load has been found to be proportional to the disengagement load [48], and also, low initial seating loads were found to lead to higher subsidence between the head and the neck [47] implying that initial assembly determines subsequent fretting corrosion performance.

Similar test methods must be developed for acetabular test methods that can assess the taper junction's susceptibility to MACC. The acetabular taper junction has a geometry distinct from the head-neck taper junction, where the engagement region in acetabular junctions forms a thin ring with a much larger diameter. This test method development formed one of the goals of this thesis. We designed test methods to assess the seating event of the liner into the shell, and to investigate subsequent fretting corrosion at the shell-liner junction in response to incremental cyclic loading regimen applied to the construct.

#### 1.6 *In vivo corrosion mechanisms and immune system interactions*

Leading clinical causes for THA revision include dislocation, mechanical loosening and periprosthetic infection [18], among others such as mechanical failure, unexplained pain and so on. Out of these, infection is not associated with device performance but is a function of intraoperative human error or pathogens. Dislocation, mechanical loosening, and device failure, however, are clearly outcomes of device performance. The factors leading to dislocation or mechanical loosening can be improved upon by device designs and material selection changes and through understanding how biological interactions

with the implant can exacerbate failure mechanisms. Therefore, the possible mechanisms leading to some of these failures will be addressed in this work.

#### 1.6.1 *Foreign body reaction to CoCrMo implant tribocorrosion*

Introduction of any foreign material into the body elicits an immune reaction: this is a well-established medical fact. Much emphasis has been placed on the foreign body reaction to biomaterials as well, across material classes. Studies have shown substrate stiffness modulates macrophage activation [49] and that surface chemistry or hydrophobic/hydrophilic nature of the surface affects monocyte/macrophage/foreign body giant cell activation [50].

In metals and metallic implants, the interactions with the innate immune system might follow similar principles, but there are other factors at play, specifically whether the biological environment might also drive device failure. In recent years there is a push to understand how the foreign body reaction might affect implant degradation. The wound healing cascade follows a well-known series of steps: injury, platelet activation, platelet adhesion, acute inflammation, chronic inflammation, granulation tissue formation, foreign body reaction, fibrous encapsulation [51]. After injury or introduction of the foreign body and blood-material interactions which set in motion the ensuing inflammatory and foreign body response, neutrophils initiate the acute inflammatory response [51], which includes recruiting phagocytic cells (monocytes, macrophages, mast cells, etc.) to the site.

Macrophage reactions to implants and implant degradation byproducts continue to form a focal point in understanding innate immune system-mediated implant degradation.

Macrophage infiltration has been found in retrieved periprosthetic tissue from a TJR revision, and more significantly, has appeared alongside the presence of corrosion and wear byproducts [52]. Scharf et al. also report identifying wear debris inside macrophage vesicles from these tissue samples [52]. Macrophages are phagocytic cells and so, the presence of foreign body particles inside macrophages retrieved from an implant site is expected. However, we do not yet fully understand the mechanisms that occur between the debris generation, to phagocytosis and whether these processes have deleterious effects on the implant itself.

Ongoing implant degradation at MoM junctions, driven by wear or tribocorrosion or chemically-driven corrosion modes (crevice corrosion, intergranular corrosion), add a continuous stream of metal ions, metal particles, oxide debris and electrochemical shifts in the vicinity of these junctions. We know in in vitro assessments, these byproducts have been shown to induce cell death and macrophage activation. However, the further downstream effects of activation are not understood. Does macrophage activation lead to chronic inflammation, thereby creating an inflammatory environment around the implant replete with molecules like reactive oxygen species (ROS)? ROS are especially pertinent to this question, since they play a role in corrosion of CoCrMo and titanium alloys [53]–[56] and are also produced as a result of reduction-oxidation reactions at alloy surfaces.

Recent studies have shown that CoCrMo wear debris can modulate phenotypic changes and increased cell mortality in macrophages [57], [58]. Similar studies with metal ions

released from CoCrMo,  $\text{Cr}^{3+}$ ,  $\text{Co}^{2+}$  in particular, can induce cell death by apoptosis and by necrosis depending on duration of exposure [59].  $\text{Cr}^{3+}$ ,  $\text{Co}^{2+}$  at increasing concentrations also induce proinflammatory cytokine (TNF- $\alpha$ , interleukin (IL)-6, IL-1 $\beta$ ) production in macrophages [60]–[63]. We also know, necrosis is a product and a propagator of inflammation, since cell fragments formed from necrotic cells can induce a phagocytic response, which is mediated through ROS production by phagocytes [64]. ROS, in turn, along with other byproducts of inflammation like hypochlorous acid, are known to cause surface oxide changes [53] and anodic polarization of CoCrMo alloys [65], [66].

However, most if not all of these studies are in vitro interactions between macrophages exposed to metal ion generated from dissolved metal salts, or metal wear particles generated solely through wear processes, excluding corrosion. We know that in MoM junctions, wear and corrosion often go hand-in-hand and that fretting corrosion in particular generates cathodic excursions, currents, metal ions and oxide debris simultaneously. The dynamism of ongoing fretting corrosion would have a more complex outcome on macrophages in the vicinity, and this is what we propose to investigate as part of this thesis work. We have designed a test method that exposes macrophages on different substrates (CoCrMo disk and petri dish electrically isolated from the disk) to ongoing fretting corrosion. Our goal is to investigate macrophage viability in response to fretting corrosion of CoCrMo.

Similarly, when exposing macrophages to metal ions, we propose to generate these ions through anodic polarization rather than dissolved metal salts. The advantage of this

method is that along with a solution rich in metal ions, we also generate oxide-based solid debris particles which represent a unique agonist as yet uninvestigated. The goal is to analyze macrophage mortality in response to metal ions-rich solution and oxide debris particles in a dose-dependent manner, and to investigate macrophage activation through cytokine and chemokine expression in response to a sublethal dose of ions.

### 1.7 *Motivation:*

Overall, the mechanisms of corrosion at modular acetabular taper junctions encompass a vast range of catalysts and propagators, some of which, like the role of corrosion byproducts and ROS, are applicable to other modular junctions and other metallic implants in general. This thesis aims to design test methods to study specific parts of this overarching theme: mechanically-assisted crevice corrosion at modular acetabular tapers, in vivo corrosion mechanisms and quantitative retrieval analysis techniques for assessing them, and finally, interactions of corrosion processes and their byproducts with macrophage mortality and activation. Our motivation is to present the larger scientific field with techniques to conduct independent analyses into the various factors that drive total hip arthroplasty degradation. Ultimately, understanding implant degradation leads to improvements in design and material selection, promoting device longevity and improving patient outcomes.

## Chapter 2

### Goals & Hypotheses

Acetabular modular tapers are seeing significant growth in their use as more and more surgeons are using dual mobility articulating surfaces in order to prevent dislocation of the device. Retrieval studies often characterize damage seen in acetabular components as the result of MACC or wear, but these studies tend to overlook the role of surrounding biology. While it is well known that implant corrosion and wear are associated with ALTRs (pseudotumor, osteolysis), little is understood about the effect of the immune system and inflammation on corrosion and tribocorrosion processes. That there may exist a positive feedback between corrosion and inflammation is a new paradigm with which to investigate implant-body interactions. Our *primary goal* was to develop and validate test methods to investigate modular acetabular taper corrosion and characterize its mechanical and electrochemical causes and investigate immune system interactions. Our *primary hypothesis* was that corrosion at acetabular tapers is dominated by biological interactions and local chemistry rather than by MACC processes and that there exists a feedback between the implant and the biological environment.

Taper mechanics, fretting corrosion and taper engagement were studied using in vitro fretting corrosion and seating tests. Retrieved acetabular components were examined using electron microscopy and x-ray surface characterization techniques to document and describe damage that might have led to failure. New techniques were developed to quantitatively compare damage modes on retrieved device surfaces. The macrophage-

implant corrosion paradigm was studied, with a focus on effects of corrosion processes and byproducts on macrophage viability and activation cues.

**Aim 1: Examine and document the mechanical, chemical, and biological modes of corrosion in retrieved acetabular liners and develop a quantitative tool to differentiate between them**

Retrieved devices can yield a lot of information on the kind of damage and associated mechanisms that might have occurred in vivo. We *hypothesized* that corrosion at the acetabular taper is driven mainly by biological/chemical processes rather than MACC. We examined the shell and liner surfaces and documented damage visible on the surface and the underlying bulk alloy (through implant sections, where possible). For the second part of this aim, we *hypothesized* that different forms of corrosion will alter the surface impedance in unique ways. Hence, near-field electrochemical impedance spectroscopy (EIS) techniques were developed and used as a quantitative tool to distinguish between damage modes objectively.

*Aim 1a: Document corrosion modes and surface damage in retrieved acetabular liners*

Scanning electron microscopy (SEM) imaging is a versatile tool that allows observation of surface damage over a wide range of magnification and image modes. In the secondary electron mode at high kV accelerating voltage, SEM imaging shows the surface topography as is, at high resolution. Within the secondary mode, varying the acceleration voltage to lower kV allows the capture of additional information based on differential emission characteristics of metals, biological material, and corrosion debris.



Low voltage imaging shows differential contrast of superficial features such as protein deposits and biological remnants coating the surface. High voltage imaging shows more of the underlying alloy topography and limits contrast associated with protein deposits and induces charging of larger biological features (e.g., cells) [67]. Differences in composition between metals, oxides, particles, biological materials, and, in case of a highly polished surface, the microstructure can be discerned using the backscattered electron imaging mode. Different compositions were more discernable due to the contrast differences where brighter regions correspond to higher atomic number elements like metallic materials, intermediate contrast (gray) regions correspond to oxides and secondary phase carbides, and dark regions belong to cells, salts and organic material (i.e., carbon-rich biological remnants and proteins). Energy dispersive x-ray spectroscopy (EDS) was used to identify the different elements present on a surface using x-rays generated by the materials when acted upon by an electron beam. These SEM and EDS imaging and analysis tools, when properly used, can provide significant information on the nature of the materials present.

*Aim 1b: Develop methods for electrochemical impedance spectroscopy (EIS) of retrieved surfaces to distinguish between corrosion forms*

The current method for categorizing and assessing severity of corrosion on retrieved components is to examine the surface visually, score the component as a whole based on a scoring method developed by Goldberg et al in 2002 [42]. This scoring method is widely used while others have investigated volumetric or stereoscopic surface analysis to determine amount of material loss. Corrosion is fundamentally a process driven by

electrochemistry and local reduction-oxidation reaction pairs, that can alter the alloy surface in predictable ways. Surface impedance is one such electrochemical metric that can be modelled as electrical circuits, which can then be determined through impedance spectroscopy. Using EIS techniques, we can quantitatively measure differences in surface impedance as a result of different corrosion modes and determine if impedance represents a distinguishing factor among different corrosion modes occurring *in vivo*.

Thus, surface corrosion damage was *hypothesized* to influence the impedance behavior of the surface in a localized manner, with a characteristic impedance behavior, which can be captured using EIS [68], [69]. Local measurement of impedance provides distinct and quantitative measures of the nature and severity of the corrosion damage present at each location testing and this approach offers a quantitative approach to scoring corrosion damage.

## **Aim 2: Develop and perform seating and fretting corrosion tests of MoM acetabular shell-liner couples**

The acetabular shell-liner interface differs from the head-neck taper junction due to differences in geometry and taper mechanical features. *We hypothesized* that MACC occurs at the acetabular shell-liner interface due to micromotion between the shell and liner in a component stiffness-dependent manner, and seating mechanics and applied cyclic load influence this behavior. We developed an *in vitro* test method to study taper seating mechanics and a separate test method to study fretting corrosion behavior at the acetabular junction. Component stiffness was measured for shells and liners of two

different sizes to determine if increase in diameter leads to change in stiffness, which might influence seating mechanics and subsequent fretting mechanisms.

*Aim 2a: Develop in vitro seating and disengagement test methods for acetabular tapers*

Modular hip implants are assembled in situ during surgery by the surgeon, usually by impaction. The proposed test method allowed the study of shell-liner couple assembly using a quasistatic ramp load. The second part of the test method measured disengagement force required, which is an indicator of taper engagement strength. Three different material combinations were tested to assess if any difference in assembly or disengagement can occur due to materials used.

*Aim 2b: Develop an incremental cyclic fretting corrosion (ICFC) test method for acetabular tapers*

Here, we applied the short-term incremental cyclic fretting corrosion (ICFC) test method developed for head-neck taper testing by Mali et al [47] to measure fretting currents generated at the shell-liner taper interface. The same samples were used as in 1A, since the nature of taper contact is stochastic and elastic, which means that the taper surfaces can be re-tested without interfering with subsequent results

*Aim 2c: Develop component compliance in vitro test method for shell and liners of different sizes and materials*

Taper compliance (inverse stiffness) is considered to be an important factor in determining taper engagement and micromotion behavior at the taper interface. We

*hypothesized* that a change in diameter of these radially symmetric components i.e. shells and liners, would lead to a change in the ring compliance.

**Aim 3: Develop methods to study effects of CoCrMo corrosion byproducts on murine macrophage cell viability and activation**

Corrosion and redox reactions on the implant surface are associated with generation of metal ions, oxide debris and the release of submicron particles from the alloy surface and bulk. Studies have also shown that tribocorrosion and resulting debris can induce viability changes and activation of macrophages, evidenced by proinflammatory cytokine and chemokine expression. Once activated, macrophages and other phagocytes are known to release chemical species such as reactive oxygen species (ROS) which can have deleterious effects on metal surfaces. Therefore, the link between corrosion processes and byproducts and immune cell behavior also needs to be understood. We *hypothesized* that ongoing tribocorrosion and other corrosion byproducts can lead to severe cellular damage and/or activation of macrophages in a concentration and/or proximity-dependent manner. We designed test methods for systematic exposure of cultured macrophages to ongoing fretting corrosion and different corrosion byproducts generated during CoCrMo corrosion (different concentrations of Co and Cr ion-rich fluid, and solid, particulate debris) and measuring viability changes, followed by analyzing cytokine expression.

*Aim 3a: Develop a test method to study macrophage viability and morphology changes resulting from exposure to ongoing fretting corrosion on CoCrMo surfaces*

A previous study has shown a link between fretting corrosion on Ti6Al4V and preosteoblasts viability in its proximity where viability was lower due to fretting corrosion and due to cathodic bias. We designed a test method to expose macrophages, which play a significant role in the innate immune response and in continuing chronic inflammation, to fretting corrosion. This is likely to occur in vivo, where interfaces within modular junctions undergo intermittent fretting corrosion and therefore, propagate environment of released metal and oxide debris, potential excursion precipitated by oxide abrasion and resulting electrochemical changes in the vicinity. We hypothesize that exposure to fretting corrosion constitutes a specific threat to macrophages, where the onslaught of debris particles, currents and cathodic excursions of surface potential can have a combined lethal effect that only cathodic excursions cannot reproduce.

*Aim 3b: Study macrophage viability and activation in response to byproducts of anodic polarization*

Inflammatory conditions often feature reactive oxygen species (ROS) prominently; as an example, ROS are known to be produced in the course of phagocytosis, which is known to occur as a result of foreign body reaction. ROS are also known to anodically polarize electrode surfaces, and anodic polarization that exceeds the passivating potential range of an electrode also leads to progressive oxide breakdown and promotes alloy surface oxidation, releasing ions and oxide debris. In the presence of these byproducts, it is likely that macrophages undergo significant stress. We hypothesize that metal ions and solid debris would be generated from a CoCrMo surface in response to long-term anodic polarization conditions, and that these byproducts would have a lethal effect on

macrophages in their vicinity in a concentration-dependent and proximity-dependent manner. We also hypothesize that sublethal doses will not cause significant loss in viability, but will induce proinflammatory behavior in the macrophages, which can be detected through cytokine and chemokine expression profiles.

## Chapter 3

### **Non-Tribological Corrosion Modes Dominate Wrought CoCrMo Acetabular Taper**

#### **Corrosion: A Retrieval Study**

(under review)

Shenoy, Aarti A., M.S.<sup>[1], [2]</sup>; Kurtz, Steven M., Ph.D.<sup>[3], [4]</sup>; Gilbert, Jeremy L., Ph.D.<sup>[1], [2]</sup>

[1] Department of Bioengineering, College of Engineering, Computing & Applied Science, Clemson University, Clemson SC 29634 USA

[2] Clemson-MUSC Bioengineering Program, Medical University of South Carolina, Charleston SC 29425 USA

[3] School of Biomedical Engineering, Science & Health Systems, Drexel University, Philadelphia PA 19104 USA

[4] Exponent, Inc., Philadelphia PA 19104 USA

### 3.1 ABSTRACT:

Corrosion of modular metal-on-metal acetabular tapers in total hip arthroplasty (THA) systems is often attributed to mechanically driven processes. Recent findings suggest that mechanically-assisted crevice corrosion (MACC) might not be the dominant cause of corrosion in shell-liner tapers. This study aims to document and present the corrosion modes observed in metal-metal acetabular liners.

Twenty-one retrieved wrought CoCrMo liners were examined using digital optical microscopy (DOM), scanning electron microscopy (SEM) and energy dispersive x-ray spectroscopy (EDS). Corrosion-related damage was documented in non-engagement taper regions, outside of direct taper contact. Within engagement regions, non-mechanically driven corrosion features (pitting, intergranular corrosion) were observed adjacent to fretting and material transfer, which rely on mechanical contact; corrosion independent of MACC was observed even in contact regions. Corrosion types observed included intergranular corrosion (IGC), pitting attack, phase boundary dissolution outside and inside of taper junctions, and mechanically-assisted crevice corrosion (MACC) within contact regions of the taper. Typical fretting scars associated with MACC were mostly absent and were not always associated with corrosion damage where present. Finally, hard phase particles (Mo-Si-O) released from the wrought CoCrMo microstructure had redeposited within regions with material loss.

Acetabular taper corrosion modes differ significantly from those in head-neck tapers and are dominated by electrochemically-driven processes, not mechanical processes, as



indicated by corrosion in non-contact regions. With greater prevalence of dual mobility hip implants, acetabular taper corrosion processes must be understood in order to limit their impact on device performance.

*Keywords: wrought CoCrMo alloy, retrieval analysis, corrosion, hip arthroplasty, modular acetabular tapers*

### 3.2 INTRODUCTION:

Total hip arthroplasty (THA) surgeries and device systems have undergone significant changes over the decades since their inception in the 1900s. One of the most successful changes is the introduction of modularity. Modularity allows for improved customization to fit individual needs and easier revision of individual components. In particular, modular acetabular components, comprised of a shell and a liner, improve implant positioning and integration in cases of bone tissue loss, or where the hip anatomy requires it [29]. Cobalt-chromium-molybdenum (CoCrMo) alloys have been typically used for the metal insert, or liner. Examples of a metal-on-metal (MOM) acetabular junction include the Ultamet inserts (PINNACLE acetabular system, DePuy Orthopedics Inc., Warsaw IN) and the R3 inserts (R3 acetabular system, Smith & Nephew, Memphis TN) [27].

Additionally, modular dual-mobility (MDM) designs, which employ CoCr liners with a polymer insert, were introduced to mitigate the risk of dislocation, especially in high risk patients, or in case of revision surgery after primary failure due to dislocation [19], [22], [70]. According to the 2013 Nationwide Inpatient Sample (NIS) database, dislocation was the leading cause for revision (17.3% cases out of 308,723 total revision surgeries) between 2009 to 2013. Thus, the MDM design is here to stay, and is seeing widespread usage. However, revision of acetabular components and isolated head/liner components each comprise 14.5% of the total revision surgeries performed, according to a study published in 2017 [18]. Adding the shell-liner taper junction into the modular THA system further introduces an additional potential location for corrosion and wear related damage.

One of the widely reported, leading causes of severe corrosion damage in metal-metal tapers is mechanically-assisted crevice corrosion (MACC), specifically in head-neck tapers [44], [71], [72]. Retrieval analysis studies of acetabular components have reported similar findings [11], [26], [27], [29], [30]. However, a recently published in vitro study has found that MACC may not be a significant driver of taper corrosion in titanium shell-CoCrMo liner acetabular tapers [73], especially when compared with head-neck tapers with the same material combination. Apart from taper geometry and loading environment, the in vivo conditions experienced by the acetabular taper differ significantly from head-neck tapers, considering the former's proximity to the pelvic bone and surrounding soft tissue. Causes for revision are also attributed to the shell-liner junction [18], [26], [27], [29], [74], and so, the question arises, what processes lead to these failures? We sought to answer this question through close examination of revised acetabular liners, in order to understand the tribocorrosion and non-tribocorrosion damage modes that occur at these taper junctions.

Employing imaging and surface characterization techniques, we can deconvolute corrosion-only and tribocorrosion-based mechanisms underlying the damage. Thus, the goal of this study is to examine the taper surface of retrieved CoCrMo liners from metal-metal acetabular couples using scanning electron microscopy (SEM) and energy dispersive x-ray spectroscopy (EDS) techniques, and to describe the damage features seen therein. Our hypothesis is that corrosion in metal-metal acetabular tapers is not solely, or even primarily mechanically driven, and might be more influenced by local

chemistry. The wrought CoCrMo alloy microstructure will also be discussed, with a focus on how its unique features might influence subsequent biological interactions.

### 3.3 MATERIALS AND METHODS:

#### 3.3.1 *Sample description*

Twenty-one retrieved CoCrMo acetabular liners were obtained from a multi-institutional orthopedic implant retrieval center. This cohort was previously used in a study by Agne et al. [30] to develop a method for estimating volumetric material loss from the taper surfaces of these liners. All implants were metal-on-metal articulating bearing devices with a CoCrMo acetabular liner affixed to a Ti-6Al-4V acetabular shell by way of the modular taper junction being studied. All liners studied here were made of wrought CoCrMo alloy by the same manufacturer. Liners were of the same design, but different sizes. They were all obtained during revision surgery from 21 patients between 2003 – 2014, and all implants of this design obtained from this center were used in this study. Included in the cohort were 13 male and 8 female patients, with average body mass index (BMI) of  $31.8 \pm 8 \text{ kg/m}^2$ . Mean implantation time calculated for 18 out of the 21 liners (data not available for 3 liners) was  $3.22 \pm 2.24$  years. Causes for revision surgery were loosening (n = 11), instability (n = 2), pain (n = 2), infection (n = 2), dislocation (n = 1), malpositioned cup (n = 1) and other reasons (n = 2). Detailed clinical data can be found in the previously published work [75].

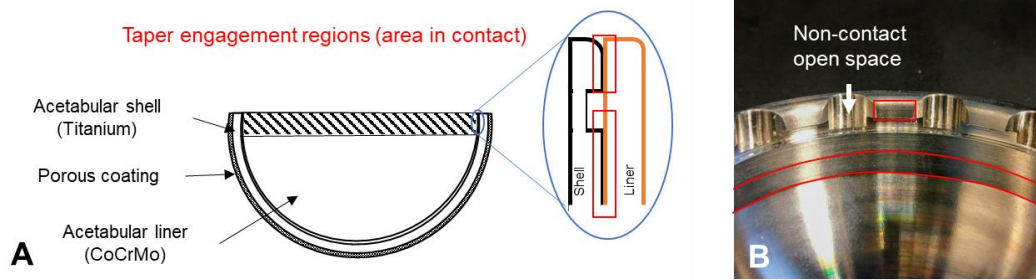


Figure 1: (a) Schematic showing the engagement region formed between an acetabular shell-liner couple (b) Picture showing an acetabular shell taper that could interface with the liners examined here. Note the antirotation tabs and the lower engagement region (marked in red) and the non-contact region between the tabs (white arrow). Figure adapted from Shenoy et al. [13]

The liner taper region in this design is divided into two distinct parts: an engagement region in which the liner surface is nominally in contact with the interfacing shell taper, and a non-engagement region which is not in contact with the shell taper surface. The typical opposing shell design features a unique geometry, and creates an engagement region comprised of a lower cylindrical taper contact region and regularly spaced antirotation tabs closer to the rim of the shell where, between tabs, there is open space on the surface and no direct contact across the junction (Figure 1). The taper surface outside this engagement region forms the non-contact, non-engagement region, which should be independent of any mechanical abrasion or related damage barring any intervention from third body debris. This forms a crucial basis for distinguishing damage features that may originate as a direct result of mechanical contact and abrasion (i.e., tribocorrosion, within engagement region) and damage features which have occurred independent of mechanical contact (outside engagement regions).

The taper surfaces of the liners were visually examined for signs of corrosion and wear-related damage using digital optical microscopy (DOM). Areas of interest were selected for further analysis using scanning electron microscopy (SEM, Model S-3700N, Hitachi High- Technologies, Schaumburg IL) and energy dispersive x-ray spectroscopy (EDS, X-Max<sup>N</sup> detector, Oxford Instruments, Concord, MA) techniques. All devices underwent SEM and EDS analysis.

### 3.3.2 *Corrosion modes and their description*

Known modes of corrosion such as intergranular corrosion (IGC), pitting attack, phase boundary dissolution, fretting and tribological material transfer were specifically identified in taper regions during examination, while also allowing for new forms of damage to be identified. These known corrosion modes are described below:

Intergranular corrosion: This form of corrosion is characterized by material loss along grain boundaries of the alloy microstructure, and features loss of entire grains from the microstructure. It is a penetrating form of corrosion where dissolution occurs to multiple grain depths into the surface but progresses along grain boundaries.

Pitting attack: This form of corrosion is characterized by small defects (~1-2  $\mu\text{m}$ , or smaller) that are visible on the alloy surface under high magnification, with the possibility of propagation under the surface. The pits can grow in size under the surface due to accumulation of fluid in restrictive geometries.

Phase boundary dissolution: The wrought CoCrMo microstructure consists of at least two phases: the primary alloy phase with fine grains of cobalt, chromium and molybdenum,

and the secondary (hard) phases with either chromium-rich carbides or molybdenum-silicon-oxygen (Mo-Si-O) particles. The Mo-Si-O particles are submicron sized and are distributed or clustered linearly along the primary grain boundaries. This form of corrosion selectively propagates along the phase boundaries between the carbides and/or Mo-Si-O particles and the alloy. The primary difference between IGC and phase boundary dissolution is that in IGC corrosion attack progresses along alloy grain boundaries whereas in phase boundary dissolution, the boundaries along secondary phase particles (carbides and Mo-Si-O particles) are selectively corroded, while the alloy grain boundaries remain more or less intact.

Fretting and material transfer: Fretting corrosion is caused due to the mechanical abrasion of the passive oxide film by an opposing hard surface, initiating corrosion of underlying metal. The fretting scars are typically parallel and under 100  $\mu\text{m}$  long. Fretting in these hard-on-hard contact tapers typically leads to corrosion reactions (repassivation and ionic dissolution) in the presence of solution. Therefore, fretting damage is characterized by the presence of multiple parallel fretting scars usually associated with corrosion damage.

Material transfer occurs due to localized adhesion at asperities, followed by material fracture caused by dissociation of those asperity contacts. It can also occur from fretting corrosion debris being subsequently pressed into the surface as third body particles and result in tribochemical mixing of the outer layers [76]. Material transfer can be identified by chemical characterization of the adhered material, which would differ from the substrate.

### 3.3.3 *Imaging methodology*

Both backscatter (BEC) and secondary (SEI) modes of SEM imaging were used to gain different types of information about the retrieval surfaces. The SEM imaging methods also included both high accelerating voltages (high kV, 12-15 kV) and low acceleration voltages (low kV, 2-4 kV). High kV SEI imaging is used mainly to visualize the surface and identify corrosion and other damage features, while high kV BEC imaging produces image contrast based primarily on compositional differences (and will show some morphology). Carbon-based deposits and features appear as dark regions since these low atomic weight materials do not generate significant backscattered electron signal. Oxides and carbides (secondary phase particles in alloy microstructures) appear as intermediate contrast (gray) regions in the backscattered image. The metal alloy appears as the brightest regions in a backscattered image, since these generate the most backscattered electrons. Thus, we can distinguish between different surface features compositionally using SEM imaging. High kV secondary electrons can easily penetrate through cell membranes and superficial biological features rendering these features transparent. Low kV secondary imaging, however, returns signal from such low density and low atomic number materials, and was thus used to preferentially visualize superficial biological features. We differentiate between protein layers and other biological features (e.g., cells) by their differential secondary electron emission characteristics [67]. EDS analysis was used to identify elemental compositions of specific areas and/or features of interest. This method depends on the generation of characteristic x-rays by the incident electron beam, usually at 15-20 kV.



### 3.3.4 Sectioning of severely corroded liner

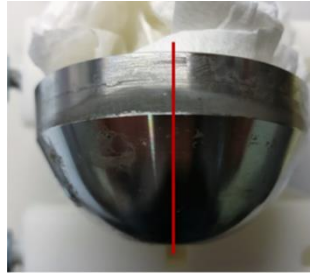


Figure 2: Retrieved liner with a band of intergranular corrosion (IGC) in the lower taper engagement region. Red line denotes where the device was sectioned to examine subsurface corrosion damage

Since IGC is a form of penetrating corrosion, we sectioned one of the devices exhibiting IGC damage along the middle of the band of IGC to examine any subsurface features (Fig. 2). A high-speed cut-off wheel (Metcut-10, Metlab Corporation, Niagara Falls NY) was used to section the liner. An ethylene glycol-based coolant was continuously cycled over the implant surface to minimize any heat damage. The high-speed sectioning prevented discernable mechanical damage except immediately adjacent to the section. Once sectioned, both pieces of the liner were polished systematically, first using wet emery paper from 240 to 600 grit, then up to a mirror finish with 0.3  $\mu\text{m}$  alumina suspension (Buehler Corp., Lake Bluff IL). The polishing serves two purposes: one, to remove the locally damaged material immediately adjacent to the section. The second purpose was to create a smooth mirror finish on the surface critical for visualizing the subsurface penetration of IGC and alloy microstructural features. Once polished, the sections were individually sonicated for 15 min to remove any debris, and air-dried. The sectioned face was then examined using SEM and EDS in conjunction with the taper

surface to determine IGC penetration depth and to detect biological material and/or oxides.

### 3.3.5 *Calculation of cell-like feature size distribution*

In a study by Gilbert et al., particular morphologically-similar biological remnants were seen across acetabular liners [32]. These had a characteristic angular edge and a fluttered edge morphology and were thought to be cellular remnants. We identified ten liners with the highest number of similar morphological features. We first confirmed these features to be of biological origin using SEM and EDS analysis. We then measured the longest diameter of individual features and determined the size distribution across samples. The number of these remnants analyzed varied across the samples (between one to five), with overall twenty-one individual features included from the ten samples. Measurements were made using ImageJ software, and a size distribution histogram was generated using Minitab™ statistical analysis software.

## 3.4 RESULTS:

Of the twenty-one liners examined, all showed visible signs of corrosion, for example, grey burnished regions, rainbow-colored discoloration, or deposits (black or cloudy in appearance), or combinations thereof. Visual damage scores for 15/21 liners have been previously reported [46].

Most importantly, corrosion damage was discovered adjacent to, but outside of, the taper engagement region in 14/21 devices (67%). In 4 devices, visual signs of damage were mostly absent except for a rainbow-colored film or mild discoloration. Upon closer

examination, we discovered either intergranular or phase boundary type corrosion with intermittent pitting. More interestingly, in 3 devices, there was little to no visible damage, but SEM analysis revealed extensive pitting and PBC. In all these devices, the corrosion damage had also occurred in surfaces outside of the taper contact regions. We documented the following known damage modes in the liner taper regions: intergranular corrosion (ICG), pitting attack, phase boundary dissolution, fretting and tribological material transfer, all described in the previous section. In addition to these, we found evidence of a new form of damage, which appeared as selectively dissolved parallel lines across multiple grains, which will be described later. Other notable features observed in the taper surfaces include cell-like remnants, protein or fiber network remnants, and presence of carbon-rich biological origin deposits in corroded regions as well as on undamaged surfaces. Observations of each of these forms of corrosion are described below and examples are presented.

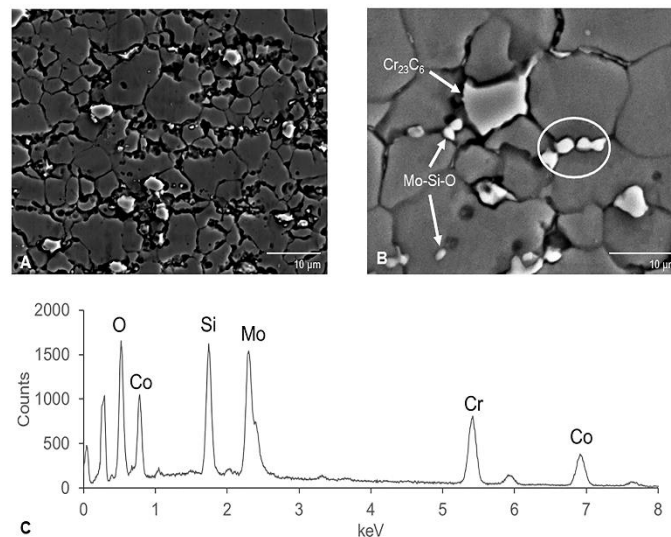


Figure 3: Scanning electron micrographs showing typical microstructure of the wrought CoCrMo alloy. (a) Lower magnification image shows distribution of the secondary phase

particles ( $\text{Cr}_{23}\text{C}_6$  carbides and Mo-Si-O nanoparticles) along with the cobalt-chromium-molybdenum grains. (b) Higher magnification image shows morphology of the particles. (c) EDS spectrum for region in (b) marked in white circle shows the smaller, hard phase particles are rich in Mo, Si and O.

The wrought CoCrMo alloy has a fine-grained microstructure (grain size  $\sim 2\text{-}10\ \mu\text{m}$ , Fig. 3), with abundant carbides and Mo-Si-O particles within the grain boundaries of the alloy that may be clustered in linear assemblies (see Figs. 3a and 3b). These particles are released from the alloy matrix during corrosion and are collected within corroded regions and were even seen encapsulated within biological materials present in the intergranular regions. The presence of molybdenum, oxygen, and silicon peaks on EDS spectra (Fig. 3c) confirm the composition of the particles. Along with the redeposited particles, carbon-rich deposits (most likely to be biological in origin) were also seen filling up the space left behind by material loss.

We documented the previously described known damage modes in the liner taper regions: intergranular corrosion (ICG), pitting attack, phase boundary dissolution, fretting and tribological material transfer. Additionally, we found evidence of a new form of damage, which appeared as selectively dissolved parallel lines across multiple grains. Other notable features observed in the taper surfaces include cell-like remnants, protein or fibrous network remnants, and carbon-rich biological origin deposits in corroded regions as well as on undamaged surfaces. Observations of each of these forms of corrosion are described below and examples are presented.

### 3.4.1 Intergranular corrosion (IGC)

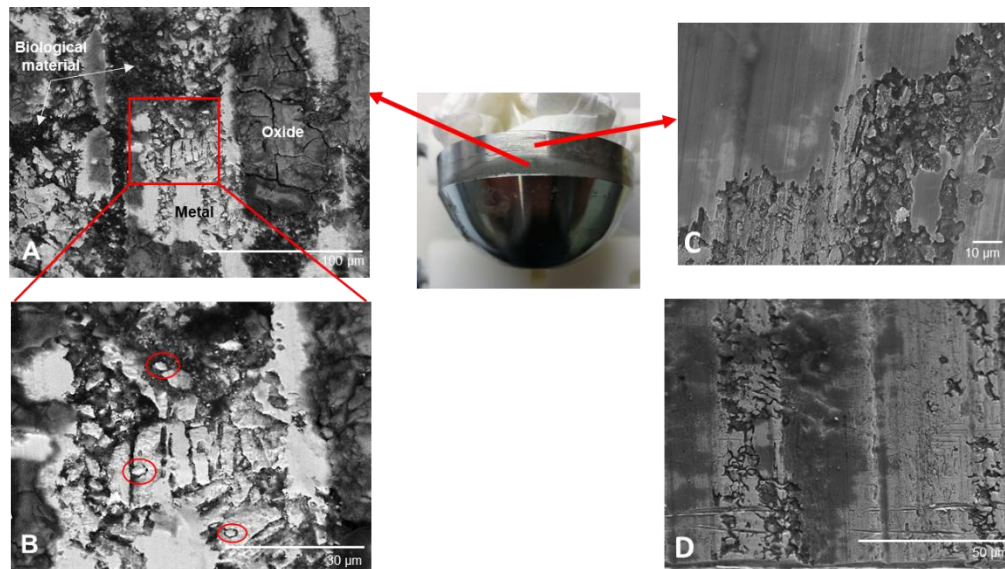


Figure 4: Schematic showing different types of damage seen within the taper region of one sample. Evidence of intergranular corrosion (IGC) clearly visible on the taper surface (a) Backscattered electron image of corrosion damage seen within the engagement region, with biological material (carbon-rich, dark regions), oxide deposits (grey regions) and metal alloy (light grey region) seen side-by-side (b) High magnification image of the area within the red square from (a). Linear etched lines ( $> 10 \mu\text{m}$  length, red arrow) of material loss across multiple grains (red circles,  $\sim 2\text{-}5 \mu\text{m}$  size) can be seen surrounded by nanoscale Mo-Si-O particles. (c) Secondary electron image of IGC observed in the non-engagement region directly above the lower engagement region. Bands of similar IGC were seen moving further upwards from the lower engagement region (d) Evidence of bands of IGC seen in non-engagement region. Scratches seen here are due to disengagement during revision.

6/21 liners (27%) showed evidence of IGC, and in three devices, the damage was severe enough to be directly visible to the eye on the taper surface. An example (photograph in center of Fig. 4) showed severe corrosion within the engagement region (gray area in the lower engagement region in photograph and Figs. 4a, 4b), with moderate intergranular

corrosion and material loss occurring outside the engagement region (Fig. 4c, 4d). In Figs. 4a and 4b, we see an accumulation of oxide debris (gray regions), and biological materials (dark regions), as well as linear parallel corrosion lines spanning across multiple grains (i.e., transgranular corrosion, red arrow Fig. 4b) and interphase corrosion or IGC showing individual alloy grains (red circles, Fig. 4b). Many hard phase particles (Mo-Si-O) can be seen to have been released from the microstructure and appear to be embedded in the organic materials within the region (see Fig. 4b).

Corrosion damage was also documented occurring completely outside of the engagement region (high kV secondary images of Figs. 4c and 4d) with no tribological processes possible in these areas. Clear evidence of IGC, transgranular corrosion and pitting is seen. Importantly, no fretting corrosion was observed, and the adjacent space was large and non-crevice-like in its geometry. This external-site corrosion developed, in part, within bands along the machining lines and was seen in the non-engagement region (Fig. 4d). Here, the corrosion attack has become severe enough to cause some material loss, as well as development of IGC and surfaces with corrosion attack lines running across several grains (i.e., transgranular corrosion). These corrosion bands appear as undamaged surfaces to the naked eye and only appear as severely corroded under the SEM.

### 3.4.2 Pitting attack

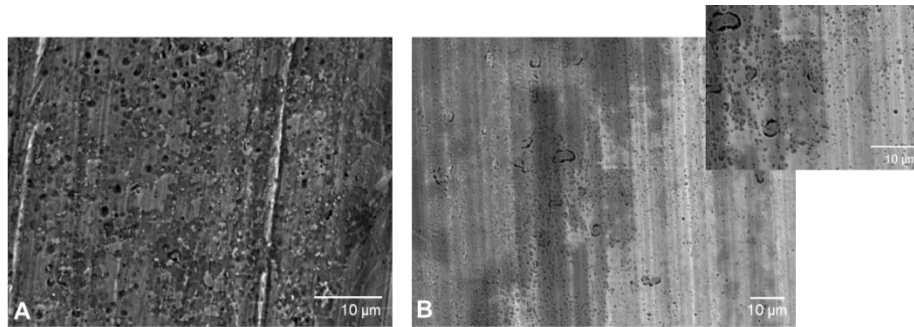


Figure 5: (a) Severe pitting attack, seen in non-engagement region of a sample (secondary mode) (b) Pitting attack in a different sample, overlapping with phase boundary dissolution (notice larger carbides and smaller Mo-Si particles with material loss around their boundaries). Pits are on the same size scale as the Mo-Si-O particles ( $< 2$  microns). Inset shows a higher magnification micrograph.

While pitting was seen to some extent in all examined devices, in 15/21 devices (68%) it was more extensive (Fig. 5). Pits observed were on the order of  $1 \mu\text{m}$  or smaller. The pitting attack was not evident with direct visual observation, especially in 3 devices which showed no visible signs of damage other than a film-like deposit (Fig. 5a). Notably, the shape of the deposit indicates a fluid flow condition coming from the lower engagement region and hemispherical region. This would have been marked as moderate corrosion in a visual scoring system. However, using SEM, we determined these deposits to be severe pitting attack on the alloy (Fig. 5b). In another sample, the pitting attack was present all over the taper surface, in both engagement and non-engagement regions, and was present alongside phase boundary dissolution (Fig. 5c). Since the Mo-Si-O particles are approximately the same size as corrosion pits ( $< 2 \mu\text{m}$ ), it can be difficult to

distinguish between pitting and phase boundary dissolution in the wrought CoCrMo microstructure. Numerous Mo-Si-O particles can be seen occupying pits (Fig. 5b). Again, this corrosion damage is outside of a crevice and not directly associated with any mechanically assisted corrosion process.

### 3.4.3 Phase boundary dissolution

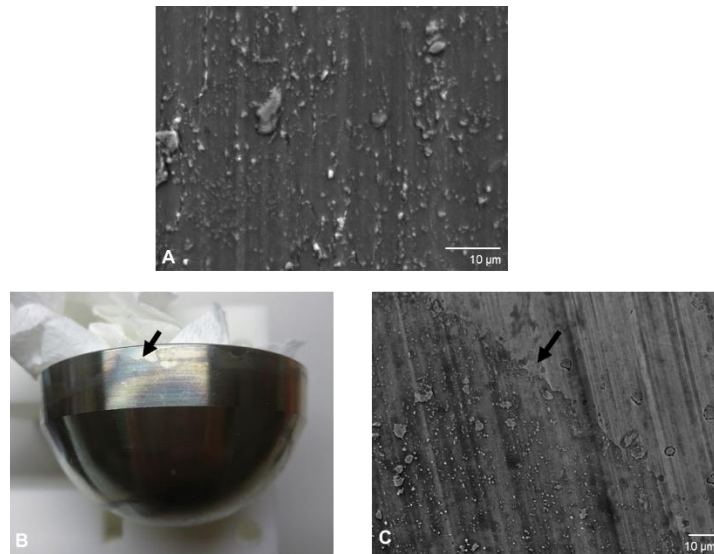


Figure 6: (a) Mo-Si particles and carbides (hard phases) are arranged along the grain boundaries in a linear orientation and have been exposed by material loss from the surface (b) Retrieved liner with discolored region extending outside the engagement region (black arrow) (c) Secondary mode SEM image of the area marked by the black arrow showing phase boundary dissolution in the discolored area, and a less severe form outside the discolored area.

Figure 6a shows PBC, which selectively propagated along the phase boundaries between the carbides and/or Mo-Si-O particles and the alloy, and was found in 16/21 devices (73%, Figure 6b). The visual discoloration (shown by the black arrow in Fig. 6b), which is, in fact, corrosion attack, clearly extends beyond the annular engagement region and is



adjacent to the antirotation tab (seen outlined adjacent to the black arrow, Fig. 6b). Close examination of this region shows a clear demarcation between the corroded region (discolored) and the relatively less corroded region (Fig. 6c, black arrow). Some preliminary PBC can be seen (Fig. 6c) outside of the line of demarcation (upper right), while carbide and Mo-Si-O particles are clearly visible (lower-left) while still being embedded in the microstructure associated with the discolored and more corroded region.

#### 3.4.4 Preferential Etching/Transgranular Corrosion

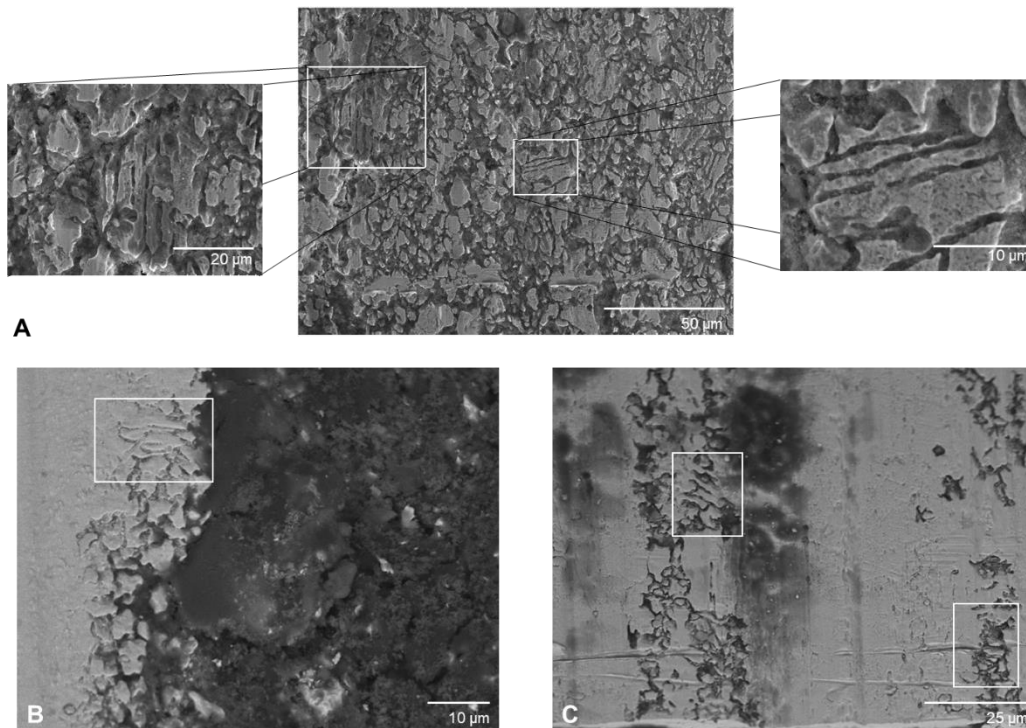


Figure 7: (a) Transgranular corrosion lines in a single sample, within a region of intergranular corrosion. Higher magnification insets show specific regions in close-up, displaying the parallel lines traversing multiple grains (~2-10 microns in size). Note the differences in orientation between the two etch-corrosion regions shown here, which eliminates the possibility of these lines being mechanically caused. (b) & (c) Backscattered electron micrographs of a sample showing early stages of intergranular

corrosion (IGC). Note the regions marked in white, where it appears that Mo-Si-O particles were removed from grain boundaries and show possible evidence of early stages of the preferential etching corrosion damage discussed in this study.

An interesting new form of damage observed in this cohort was the presence of what appear to be multiple sets of preferential parallel etched lines across several grains. These transgranular parallel tracks extended around 20 microns in some cases, which would traverse around 3-5 grains, as seen in Fig. 7a. This form of damage was only seen in four devices, observed in conjunction with IGC. Some of the remaining grains within the corroded region marked by severe material loss exhibited the preferential etched lines. Multiple regions of parallel preferential etching occurred within the same IGC region in one sample, oriented along different directions. In addition, Figs. 7b and c show some evidence of what might be early stages of this preferential etching corrosion (marked in white boxes). The appearance of these lines may be associated with removal of second phase Mo-Si-O particles from their position along grain boundaries.

#### 3.4.5 *Fretting and material transfer*

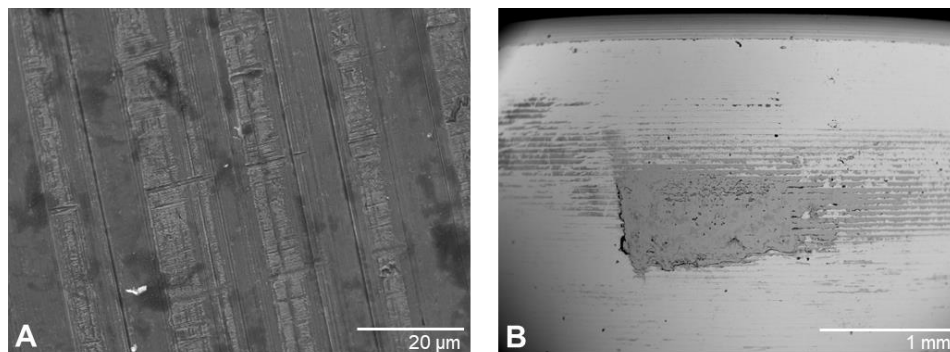


Figure 8: (a) Fretting scars seen in an examined sample. Actual contact area is minimal, and the abrasion did not lead to severe corrosion. (b) A backscatter electron micrograph

showing material transfer (titanium oxide, visible as an intermediate contrast region) on the liner taper region interfacing with the antirotation tab on the shell taper.

15/21 devices (68%) showed evidence of fretting, characterized by repetitive unidirectional scratches, usually less than 100  $\mu\text{m}$  in length (Fig. 8a and 8b). This evidence was sparse when compared to fretting corrosion seen in head-neck tapers [20–23], and the actual contact area remained small. 18/21 devices had Ti-alloy material transfer onto the CoCrMo surface, which originated from the interfacing titanium shell (Fig. 8b), confirmed by EDS analysis (data not shown).

### 3.4.6 Cell-like remnants and biological deposits

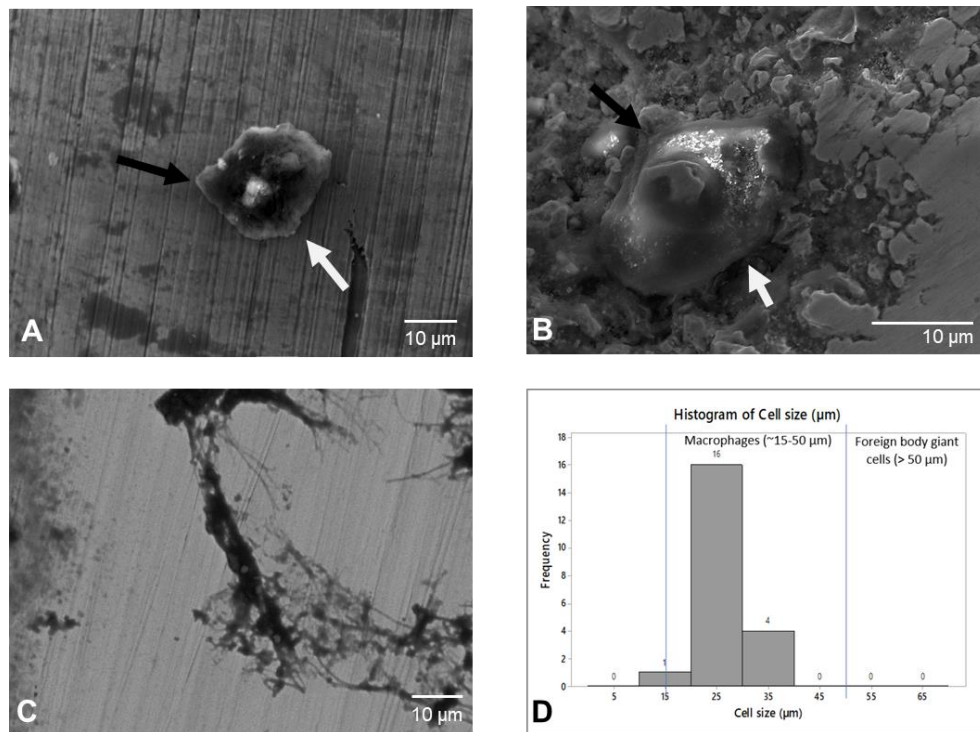


Figure 9: (a) Secondary electron image of a single cell-like feature with characteristic morphology, with an angular edge (black arrow), and a fluttered edge (white arrow) seen in similar features across all samples (b) Secondary electron image of another such biological feature with similar morphology seen within a severely corroded part of the

engagement region (different sample than (a)) (c) Backscattered electron image of fibrous network, which appear dark implying a low atomic weight element, and confirmed on EDS as carbon (data not shown) (d) Histogram showing size distribution of the cell-like features. This was calculated from 10 different samples, with different numbers of cell-like features.

All the devices examined showed presence of morphologically consistent, biological origin remnants on the taper surface. Figure 9a shows an example of a typical biological feature seen in the retrieved liners, which had a characteristic morphology with an angular edge (marked by black arrow) and a fluttered edge (marked by white arrow). These often occurred outside the engagement region where they seemed to be spread out on the taper surface. In 7 samples (Fig. 9b), the cell-like features were observed in engagement regions, within a severely corroded area. These cell-like regions appear to have significant clusters of particles present. Another form of biological remnant observed is shown in Figure 9c, carbon-rich deposits which appear to be fiber-like networks. Biological deposits (confirmed by EDS as carbon-rich matter) were also seen embedded amongst the loosened grains in heavily corroded regions of the taper contact region, as shown in Figure 4a. Figure 9d shows the size distribution of cell-like features across ten samples, derived from a total of twenty one individual features. The size distribution falls narrowly within the typical size range for macrophage cells [24].

### 3.4.7 Sectioned implant: IGC evaluation

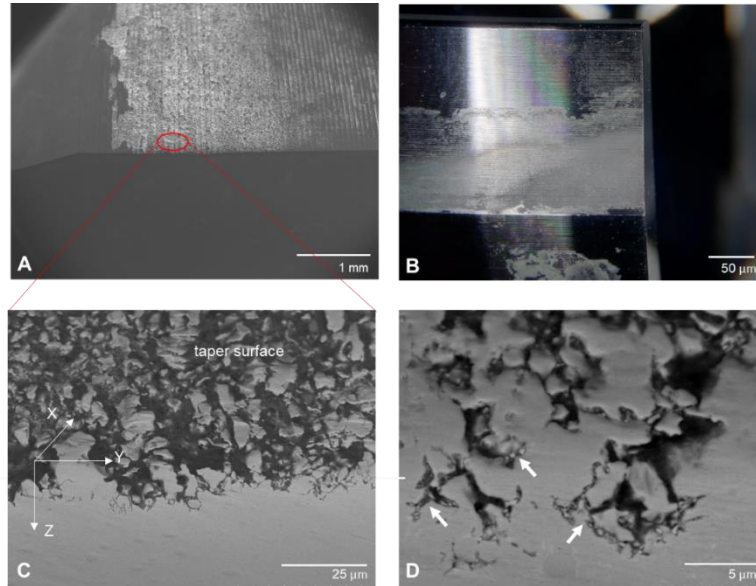


Figure 10: (a) Low magnification secondary electron image of the sectioned liner showing macroscale IGC on the taper surface. (b) Photograph of the sectioned liner showing grey burnished area (rotated 90 degrees anticlockwise from (a)) (c) High magnification backscattered electron image of the area marked in red from 10a. White line denotes the section edge. Note the biological material (dark regions) embedded within the IGC damage on the taper surface and penetrating into the bulk. (d) High magnification backscattered image showing the sectioned surface. The channels are formed by penetrating corrosion damage, and contain biological matter as well as Mo-Si-O particles (white arrows)

To examine subsurface penetration of IGC, one of the severely corroded samples was sectioned (see Figure 10a and 10b). From this sectioned surface, we see the non-uniform IGC penetration into the bulk (Figure 10c). There is clear evidence of material loss along the grain boundaries, along with Mo-Si-O particle release which appear to be embedded in the channels formed (Figure 10d, white arrows). The subsurface channels were filled with biological matter, visualized using backscatter SEM imaging (dark contrast regions,

carbon-rich on EDS, Figure 10d). The depth of penetration was non-uniform with the maximum measured depth being approximately 20  $\mu\text{m}$  below the top edge of the section.

### 3.5 DISCUSSION:

Taper corrosion in modular orthopedic devices, considered a significant clinical challenge that may affect patient outcomes, can lead to material loss and adverse local tissue reactions (ALTRs) at the modular acetabular tapers formed between the shell and liner, as reported in multiple retrieval studies [1,2,10,11,25]. These studies also report ALTR, acetabular cup loosening, dislocation, and unexplained pain as causes for revision. The causes of corrosion damage reported in these studies range from galvanic corrosion and pitting to crevice corrosion and fretting corrosion, but the overarching finding in metal-metal devices is that corrosion was limited to the engagement region of the liner-shell interface. We have found that corrosion in acetabular tapers occurs outside taper contact, in non-engagement regions, and is primarily driven by electrochemical and/or chemical processes.

Corrosion outside of the taper contact region was observed in multiple samples, indicating that this may be a prevalent process in these devices. Corrosion types observed outside contact regions were mainly phase boundary corrosion (PBC), intergranular corrosion (IGC) and pitting, in some samples. All three forms of corrosion are typically not initiated by mechanical abrasion. These forms of corrosion are also exacerbated by severe local solution chemistry, leading to localized degradation and material loss.

However, retrieval analyses of shell-liner tapers typically limit the causes of corrosion to MACC and mechanical contact processes.

In recent retrieval studies [1,2,26], we see that some visible damage extends into the non-engagement region that was not specifically identified or discussed. Closer examination of the visible damage was warranted and might have revealed findings similar to those in this study. For example, in 3 samples from our cohort, we observed a similar extension of corrosion damage beyond the defined boundaries of taper contact, which appeared to be either a discolored film or a rainbow-colored layer. In each case, these were determined to be regions of either PBC or IGC, with intermittent pitting, all of which are chemically or electrochemically driven forms of corrosion.

Similarly, mechanical abrasion and associated fretting scars or corrosion were largely absent in these tapers. In engagement regions, there is some evidence of material transfer from the interfacing titanium shells, visible as light contrast regions in backscatter SEM mode, and confirmed by EDS analysis. A recent study by Shenoy et al. [27] shows the actual area in contact is minimal compared to the entire shell-liner taper interface available for contact, which explains the low fretting currents (under 1  $\mu\text{A}$ ) recorded in the short-term in vitro fretting corrosion tests. This was corroborated in this study, where we found dispersed regions of fretting, indicating minimal direct contact within the engagement region. More importantly, there was little to no associated corrosion damage (see Figure 8). Fretting scars were also limited to the tops of machining lines on the liner surface, and did not cover large surface areas, indicating that throughout implantation, the

actual contact area in the liners examined here was only a fraction of the total potential engagement surface area.

It is possible that fretting corrosion initiated crevice corrosion [28,29] like behavior to cause the more severe corrosion damage seen in these retrievals, but the fact that corrosion damage was seen remote from the taper contact region disproves it in this case. However, chemistry changes in the local solution from processes within the contact regions may result in these non-tribological forms of corrosion and such fluid may egress from the crevice and induce similar corrosion processes in the adjacent alloy surfaces resulting in the discoloration and local pitting. Figure 5a represents a possible example of such a situation.

The liners examined in this study were made of wrought CoCrMo alloy (ASTM-F1537) which has a fine-grained (2-10  $\mu\text{m}$  in size) microstructure interspersed with secondary hard phase carbides and submicron Mo-Si-O particles. A 2017 study by Pourzal et al. [30] found that microstructural features such as hard phase particles, and their location within the microstructure as well as alloy segregation can exacerbate PBC, pitting and etching. In this study, we see the hard phases exposed through a selective dissolution of surrounding alloy material shown (see Figure 6a). The hard phase particles are distributed along grain boundaries and could be associated with IGC occurrence in this alloy.

CoCrMo alloys are excellent biomaterials for orthopedic load-bearing applications, due to the corrosion and wear resistant protective chromium oxide film that spontaneously forms on the alloy surface [31]. However, the alloy grain boundaries become depleted in



chromium due to heat treatments, during carbide and hard phase precipitate formation, potentially leading to grain boundary sensitization and rendering them vulnerable to selective corrosion attack. A study by Hoffman et al. in 2016 describes these concepts and demonstrates how hard phase precipitation associates with surface corrosion in CoCrMo alloy [31]. Thus, the unique fine-grained microstructure of the wrought high carbon CoCrMo alloy interspersed with hard phase carbides and secondary particles might increase corrosion vulnerability.

A consequence of IGC and PBC is the material loss, potentially releasing micro and nano-scale secondary phase particles from the microstructure. These particles can also be released into the surrounding tissues during implantation, and combined with metal ion release from metallic tapers, may trigger adverse local tissue reactions (ALTRs) [32–36]. The interactions of fine particles and the immune system have been widely reported [7,22,37–41], and particles have been shown to induce a proinflammatory response from phagocytic cells. Thus, the advantages offered by the fine-grained high carbon wrought CoCrMo alloy microstructure [42] must be weighed against undesirable consequences of second phase particle release. We estimate about 108 particles per mm<sup>3</sup> of carbides and hard secondary phases are present in this alloy. The concept of microstructural biocompatibility needs to be considered where the alloy microstructure may, if corroded away, contribute to accelerated corrosion, particulate release, and potentially adverse local tissue reactions.

Similar release of second phase particles was seen in the vicinity of the transgranular corrosion type features seen in 4 devices. Evidently, Mo-Si-O particle release from the

grain boundaries along multiple adjacent grains might lead to the formation of these “etch lines”. As seen in Figures 7b and 7c, Mo-Si-O particle loss might be a starting point for the preferential material loss to initiate, leading to this particular feature. These etch lines span multiple grains thus are not likely related to twinning within individual grains; they consist of a set of parallel corroded regions interspersed with remnant alloy; biological debris can permeate the etched regions, and they are randomly oriented eliminating fretting as probable cause. This is the first time this kind of damage has been reported in the literature and further study is recommended.

The presence of cell-like entities is another aspect that warrants further study. Sivan et al. suggested that these features might be cellular remnants in their retrieval study [18].

Although morphologically consistent, we have not definitively shown that these ubiquitous carbon-rich features are, in fact, cells. The consistent repeatable size, morphology, and carbon-rich nature of these remnants demonstrated here indicates that these are not random adsorbed proteins. Bijukumar et al. in a recent study also indicate the presence of similar features with a similar size distribution within head-neck tapers on retrieved devices [43]. In future work, retrieved devices with well-preserved biological material can be analyzed through sputter-coated SEM analysis [44] or Fourier transform infra-red spectroscopy (FTIR) [45]. Scharf et al. published findings from periprosthetic retrieved tissue histology that show corrosion debris phagocytosed by a macrophage cell [46]. This is indicative of macrophage interactions with implants, which needs to be investigated further.

In addition, we documented carbon-rich fibrous networks or continuous film-like deposits (Fig. 9c). These could be protein remnants, cellular attachment filaments or extracellular matrix (ECM) remnants, however, this analysis was not pursued due to the small quantities of protein per sample available and the resulting difficulty in characterizing these materials.

The foreign body reaction is a well-known and established phenomenon [47], especially in the presence of a surgically placed device surrounded by soft tissue and vasculature. During inflammatory responses, phagocytic cells are also known to generate short-lived reactive oxygen and nitrogen species (amongst others) [48,49], which exacerbate corrosion processes and hasten oxide film breakdown [50]. Thus, the interactions of cells, particularly phagocytic cells, with the implanted devices is a crucial area of study.

Restrictive geometries formed within tapers not only create crevice-like environments but also allow close interaction of cells with the implant surfaces.

What is clear from this work is that in vivo corrosion damage to CoCrMo alloy surfaces can occur outside of the taper crevice region and can occur independent of direct fretting-initiated crevice corrosion. The electrochemical (solution, potential) conditions under which such corrosion occurs have not been replicated in vitro in any lab-based test. This represents a significant gap in our understanding of the crevice aspects of the mechanically assisted crevice corrosion process.

This study presents strong evidence for the unique corrosion processes occurring at acetabular shell-liner tapers, but it is not without caveats. The sample size for this study is

small, with devices from a single manufacturer, and most of the analysis carried out by a single observer. We also did not include clinical data analysis and patient demographics. This study aims to describe the nature of corrosion-related damage that can occur on CoCrMo acetabular liner surfaces and it was not likely that any strong correlations with demographic data would be discerned with twenty one samples of a single design.

Only select regions of each implant identified as containing observable corrosion damage were imaged and analyzed. Decisions to study specific regions were made by visual assessment of the entire taper surface. We also did not conduct any material loss measurements, beyond those already performed by Agne et al. [12], since the novel microstructural features examined herein are minute and the resolution required to properly measure volumetric loss of these features is at or below the micron-scale. Finally, these observations were made in liners of a single material type (wrought CoCrMo) from a single manufacturer. While significant for distinguishing acetabular taper corrosion from other tapers, these observations cannot be treated as generally applicable to other metallic alloys, like the cast CoCrMo alloy. It is likewise unclear whether these observations apply to dual mobility CoCrMo liners, that articulate against a polyethylene mobile bearing, unlike in MOM total hip arthroplasty. Because the CoCrMo alloy selection and liner-shell taper tolerances are manufacturer and design specific, additional investigation into a broader range of CoCrMo liner designs would prove useful.

Overall, retrieval analysis remains an effective tool in understanding orthopedic device revision. It can be further improved by introducing more quantitative, non-destructive

techniques such as electrochemical impedance spectroscopy (EIS), since surface impedance can be indicative of different forms of corrosion damage [51].

### 3.6 CONCLUSIONS:

We used SEM and EDS surface analysis methods to conduct detailed characterization of in vivo damage in CoCrMo acetabular taper regions of modular acetabular total hip prosthesis constructs. Most importantly, we documented corrosion attack outside of the taper contact region and etch-line corrosion processes that are not strictly intergranular corrosion processes. Corrosion in MoM acetabular tapers is not driven primarily by mechanically-assisted crevice corrosion but are more affected by electrochemical or biologically driven processes that leads to corrosion attack even in the absence of mechanical contact. Significant quantities of micron and submicron secondary phase particles (carbides, molybdenum-silicates) are released from the wrought CoCrMo microstructure by corrosion, which can be released into surrounding tissues in vivo. These particles can induce local immune reactions and subsequent inflammatory cascades, thus introducing the concept of microstructural biocompatibility. In conclusion, corrosion of acetabular taper junctions is less driven by mechanically assisted corrosion processes than other (e.g., head-neck) taper junctions as evidenced by the limited evidence of fretting corrosion damage and the preponderance of other corrosion dominated processes. Finally, these kinds of in vivo corrosion damage have not been recreated in laboratory settings, and thus presents a major gap in our understanding of biological interactions with implanted devices.

## Chapter 4

### **Near-field Electrochemical Impedance Spectroscopy of Retrieved Hip Implants**

#### 4.1 ABSTRACT:

Retrieved hip implant components present with different kinds of corrosion damage often on small surface areas of the taper region. Retrieval analysis, using visualization techniques, offers a qualitative assessment of different types of corrosion. However, quantification is usually limited to damage scoring based on visual assessments and volumetric material loss measurements, neither of which take into consideration corrosion-related changes to the device surface. Impedance, measured by electrochemical impedance spectroscopy, is an important tool for determining corrosion resistance as well as electrochemical properties of a surface. Recent studies have shown promise in using this technique on a localized, or near-field, basis as well as globally over the entire taper surface to draw conclusions about the extent of corrosion damage and susceptibility. The goal of this study was to systematically assess different types of corrosion modes found on retrieved wrought CoCrMo liners in terms of near-field impedance measurements and to find distinguishing features. We developed a technique featuring an easy-to-manufacture microelectrode, that assesses near-field impedance and enables direct comparison of impedance findings with visual observations. We found that impedance measurements are a good indicator of different forms of corrosion-related damage. Near-field impedance measurements were able to capture nuances of the corrosion damage and we were able to describe the surfaces in terms of unique electrical circuit models and

resistive and capacitive elements. Intergranular corrosion (IGC) and oxide deposits were found to match a coated model behavior, with a characteristic double-hump phase angle response and phase boundary corrosion (PBC) and control (polished CoCrMo disk) were found to match a constant-phase-element Randle's circuit model with a mostly intact surface with minimal to no material loss. We also found that oxide deposits and IGC exhibit higher corrosion susceptibility compared to PBC. Our findings demonstrate the versatility of using this technique in analyzing different types of retrieved device surfaces to make objective determinations in terms of their continued corrosion susceptibility. Further developing this technique and testing it on a variety of tribocorrosion features and different biomedical alloys will help ascertain its applications in retrieval analysis and in determining device damage extent during revision surgery.

## 4.2 INTRODUCTION:

Retrieval analysis provides a paradigm for evaluating failed implants both quantitatively and qualitatively. In the previous chapter, qualitative retrieval analysis was presented, describing failure modes and associated surface damage features in retrieved wrought CoCrMo acetabular liners. Visual assessment of damage modes, expanding upon earlier retrieval study methods [26], [27], [29], were conducted to find that multiple damage modes and resulting damage features occurred adjacent to one another within the same region. These analyses were qualitative in nature, and as such, did not include quantifiable metrics for assessing corrosion and tribological processes occurring *in vivo*.

In this chapter, we focus on quantitative methods for retrieval analysis. Visual scoring [31], [42], [46] and volumetric material loss measurements [75], [77] are examples of quantification included in retrieval analysis. While visual scoring remains a convenient, validated, and quick method for categorizing implants based on damage severity, drawbacks include a lack of objectivity and the reliance on human observation and discretion. Often, visual scoring precludes close examination of the devices under high magnification, leading to a lack of nuance in distinguishing between different sources of damage (electrochemical corrosion mode versus mechanical wear) seen over the entire taper surface. Volumetric material loss measurements using surface coordinate mapping offers a more objective approach, quantifying the material lost from the taper surface in a given retrieved device. However, these material loss measurements do not provide a complete picture of how much material was lost *in vivo* and how much was lost subsequently during revision and device extraction, or during cleaning and post-surgical



processing and storage. Surface coordinate mapping for material loss measurements also do not distinguish between different causes of material loss and cannot distinguish specific mechanisms of damage.

Corrosion of metallic surfaces is a result of complex electrochemical interactions at the solution-metal interface. The nanometers-thick, strongly adhered, dynamic oxide thin films, which form spontaneously on biomedical alloy surfaces, protect the underlying metal from some of these corrosion processes by kinetically limiting them [78]. These oxides also change chemically and are capable of growing in thickness or developing defects depending on the electrochemical conditions present. Thus, an electrochemical approach to studying retrieved device surfaces is an alternative approach to characterizing and quantifying the surfaces in terms of the properties of its oxide and the effect of damage on changes in its oxide due to corrosion or tribological processes or combinations of the two.

Thus, in this study, we propose a method to introduce objective electrochemistry-based surface analysis of retrieved devices, based on a well-established measurement technique: electrochemical impedance spectroscopy (EIS). Frequency-based EIS is typically employed on devices and alloys (full immersion conditions) to determine the average impedance response of the entire surface area [68], [79], [80]. Beyond medical devices, EIS is also used to determine corrosion resistance of coatings and paints [81], [82]. The EIS technique measures the steady state current response to an applied cyclic voltage input to the surface under analysis. The surface impedance is, thus, the surface's resistance or opposition to the current flow and its capacitance, or its ability to store

charge. The applied voltage sweeps through a range of pre-determined frequencies, from high to low, in order to measure all of the characteristics of the solution-oxide-metal interface as an electric circuit.

Normally, the EIS technique relies on both high and low frequency responses to generate the phased angle,  $\theta$ , and impedance magnitude,  $|Z|$  plots as functions of the Log of the frequency (so-called Bode Plots). The low frequency measurements can take up to several hours, prolonging the test duration, and potentially introducing surface changes due to increased hydration of the oxide, as an example. A recent study proposed a new method to minimize this time duration using a novel analysis technique based on symmetry of the impedance functions across Log of the frequency [83].

Utilizing this method, we can capture full spectrum impedance responses from a range of metallic surfaces, including retrieved devices exhibiting different forms of damage and corrosion in a very short time period (a few seconds to under 30 minutes). Retrieved devices present a range of damage features within a small region on the device surface, often exhibiting overlapping corrosion modes. If the EIS method were scaled down to a near-field approach, similar to that employed by Wiegand et al [84], to model a small region of retrieved device taper surface as an equivalent idealized electric circuit, we could capture nuances of different corrosion modes and the resulting changes in impedance response. We could also distinguish between adjacent areas in terms of corrosion type and surface damage.

Therefore, the goal of this study was to develop and utilize a near-field symmetry-based electrochemical impedance spectroscopy method to distinguish between three surface corrosion modes: intergranular corrosion (IGC), phase boundary corrosion (PB) and oxide deposits from fretting corrosion and to compare them to control, uncorroded surfaces. Hypothesizing that each corrosion type would alter the surface in unique ways, we expect the distinguishable surface features can be modeled as specific circuit types. Each different circuit model would then yield a set of calculated resistive and capacitive elements.

### 4.3 MATERIALS & METHODS:

#### 4.3.1 *Sample description*

Wrought CoCrMo retrieved liners from the cohort described in the previous chapter were used for this study. Devices were selected based on visual damage features, identified using SEM and EDS analysis. The following categories of surface features were studied: 1. intergranular corrosion (IGC), 2. phase boundary corrosion (PBC) and 3. oxide deposits. Intergranular corrosion (IGC) is identified by corrosion propagating along grain boundaries and resulting in material loss in some cases. Phase boundary corrosion (PBC) is characterized by corrosion propagating along the secondary phase particle boundaries, that is, corrosion that causes material loss and exposes the hard phases. In the wrought CoCrMo alloys, these are carbides and Mo-Si-O particles embedded within the primary phase alloy. The oxide deposits are typically the result of the generation and deposition of metal oxides arising from fretting corrosion mechanisms. Here, regions of the metal are

abraded by fretting and subsequent corrosion reactions result in oxide formation where these oxides can adhere to the underlying damaged metal. The control sample was a freshly polished CoCrMo disk. Devices were selected only if the available surface area of the damage feature was extensive enough to enable reliable contact with the microelectrode tip used to conduct impedance measurements. Thus, we had three devices each for IGC and PBC and only one device with oxide deposits with sufficient surface area for use in this study (Figure 1).

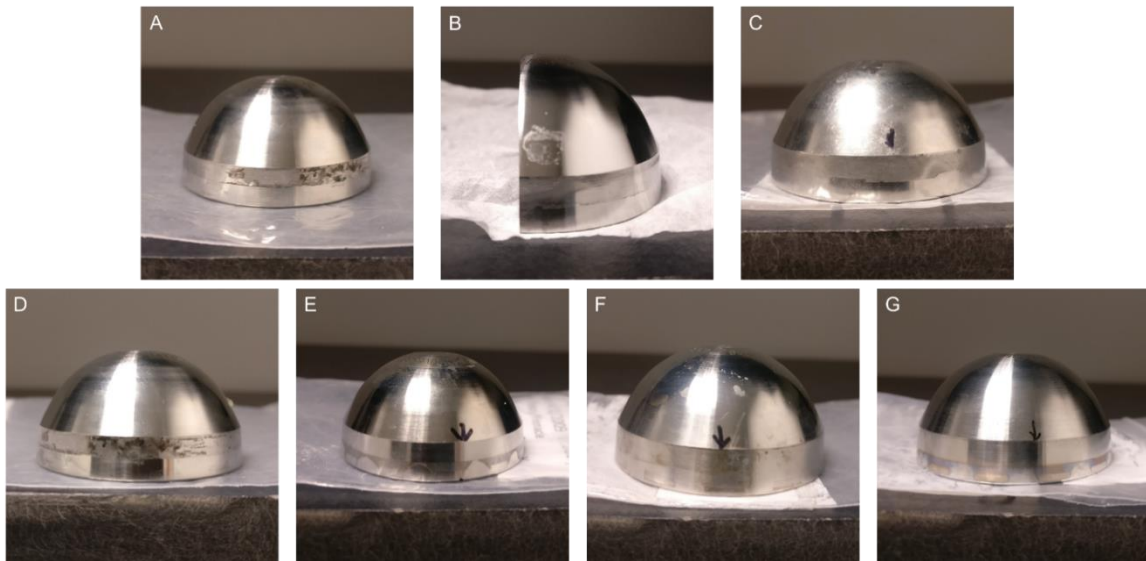


Figure 1: Test samples for: (A) IGC1 (grey burnished region visible in lower taper engagement region) (B) IGC2 (grey burnished area close to the edge of the sectioning plane in the lower taper engagement region) (C) IGC3 (grey burnished region visible in lower taper engagement region) (D) Oxides (dark deposits visible in the lower taper engagement region) (E) PBC1 (curved edge of the discolored region in the upper taper region) (F) PBC2 (brownish deposits in the lower taper engagement region) (G) PBC3 (curved edge of the discolored region in the upper taper region)

### 4.3.2 Near-field EIS technique

A microelectrode was designed using a 1000  $\mu\text{L}$  pipette tip (diameter = 780  $\mu\text{m}$ ; cross-section area =  $4.78 \times 10^5 \mu\text{m}^2$ ) with an ionic bridge at the tip using 2% agar in 0.154 M PBS. Reference (chlorided Ag wire) and counter (platinum wire) electrodes were placed inside the pipette through the top. The pipette was brought into firm contact with the area of interest on the liner surface (Fig. 2a).

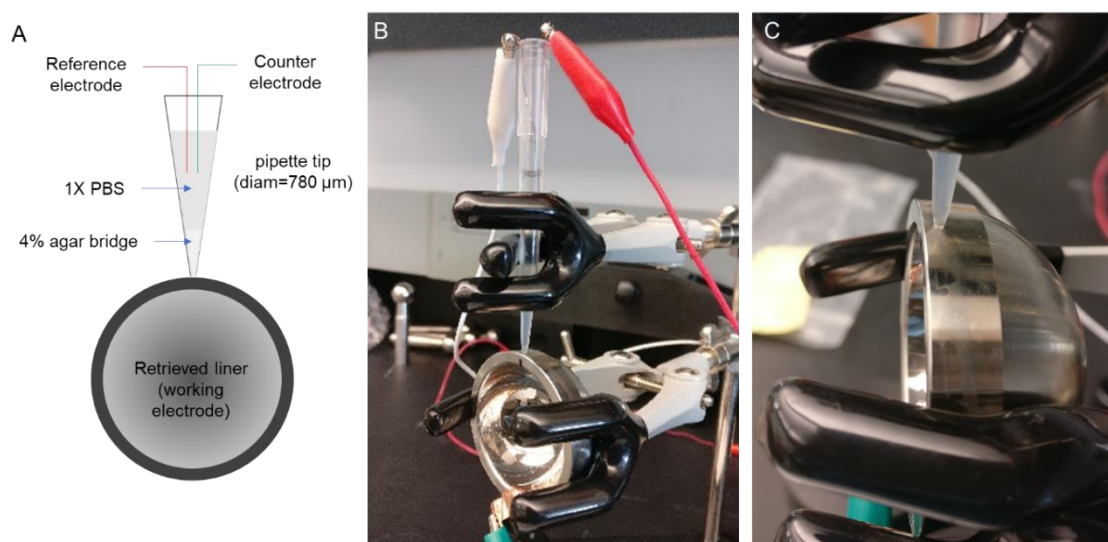


Figure 2: (A) Schematic for test setup featuring the microelectrode for the NEIS measurement, with 4% agar bridge (B) Photograph of the actual setup with a sample (C) Close-up of the device surface-tip interface showing that the surrounding area remained dry, and the only region acting as working electrode is the region directly corresponding to the tip area.

The opening was then covered with parafilm to form a partial-vacuum condition to further control any leakage of PBS from the tip. Copper tape was used to form an electrical connection with the liner, the working electrode (Fig. 2b). A potentiostat (Versastat 4, Princeton Applied Research, Oak Ridge TN,) was used to monitor open

circuit potential (OCP) for 1 hour. Then, impedance measurements were performed across frequencies ranging from 10 kHz to 10 mHz, with a sinusoidal voltage of amplitude 10 mV about OCP. The impedance response was recorded as a pair of Bode plots, one of which was a phase angle ( $\theta$ ) plot, representing the phase shift between the input voltage and the output current, and the other was the magnitude of the impedance ( $|Z|$ ), both plotted against frequency. Typically, this impedance response can then be modelled as an electric circuit [14], with the solution (electrolyte)-oxide-metal interfaces represented by combinations of resistive, capacitive and/or inductive elements. VersaStudio software (Princeton Applied Research, Oak Ridge TN) was used to measure the sinusoidal current response and to determine the  $|Z|$  and the  $\theta$ . Measurements were performed three times for each region tested.

#### 4.3.3 Symmetry-based EIS analysis method

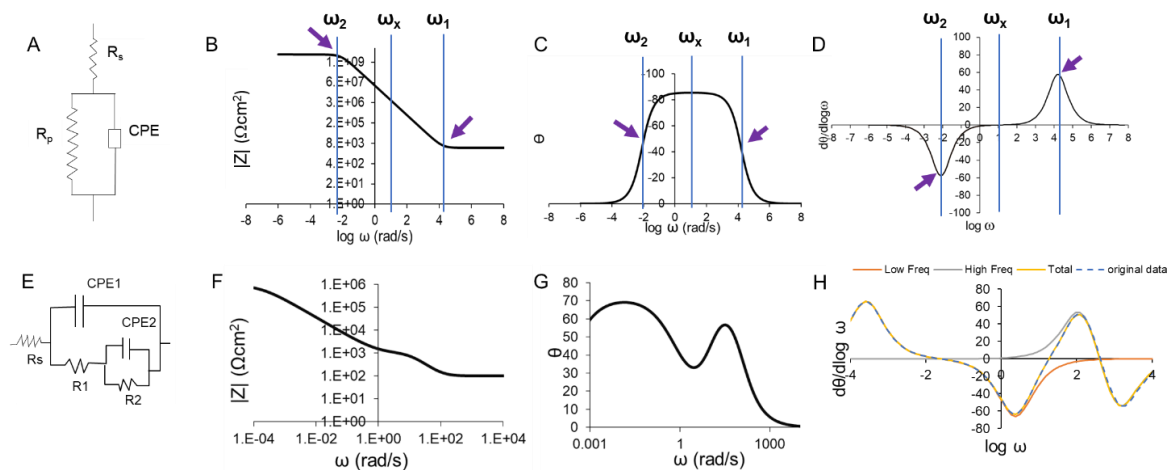


Figure 3: (A) Randle's circuit with constant phase element (CPE) in place of capacitor (Bode plot for a Randle's circuit response for  $\log |Z|$ , indicative of characteristic frequencies three characteristic frequencies marked on the figure ( $\omega_1$ ,  $\omega_x$ ,  $\omega_2$ )).  $\omega_1$  and  $\omega_2$

correspond to the elbow regions (purple arrows), signifying time constants based on  $R_sQ$  (high frequency) and  $R_{aps}$  (low frequency) (C) Bode plot of  $\theta$  vs log of frequency. The arrows point out the elbow regions in (B) (D) Derivative of  $\theta$  vs log frequency, creating the characteristic frequency peaks (arrows), and showcasing the symmetry of the phase angle with respect to frequency (E) A coated model equivalent circuit showing additional R and CPE elements, which alter the Bode plots accordingly (F) Bode plot for  $\text{Log } |Z|$  for the coated model circuit shown in (E). Note the change in slope (red arrow) between the elbow regions (purple arrows) which are similar to the Randle's circuit response in (B). (G) Bode plot of phase angle ( $\theta$ ) vs log of frequency.

The capacitor in these equivalent circuit models is replaced by a constant phase element (CPE), a capacitive element with properties closer to the real-world metallic biomaterial surfaces, reflecting inhomogeneities, microscale topographies and so on. The impedance of a CPE is shown in the equation below:

$$Z_{CPE} = \frac{1}{(i\omega)^{\alpha Q}} \quad \text{Eqn. 1}$$

where,  $\omega$  is the frequency,  $\alpha$  is the exponent (values range from 0 to 1), and  $Q$  is the parameter denoting magnitude of CPE. When  $\alpha$  is equal to 1, the CPE acts as a capacitor, and  $\alpha$  values below 1 indicate a progressively resistive nature for the CPE. Thus, the CPE denotes an imperfect capacitive element.

In a standard CPE Randle's circuit (Fig. 3a), the  $\text{Log } |Z|$  vs  $\text{Log}$  frequency response has two elbow regions (Fig. 3b) and the  $\theta$  response (Fig. 3c) is symmetric about a frequency, termed the crossover frequency,  $\omega_x$ . This symmetry is clearly demonstrated through the derivative of the phase angle with log of frequency ( $d\theta/d\log \omega$ ), shown in Figure 3d. Similarly, the coated model is shown in Figure 3e. The  $|Z|$  Bode plot (Fig. 3f) shows an

additional elbow region mid-slope, indicating an overlap and additional time constants, which is reflected in the dip in the phase angle Bode plot (Fig. 3g). The corresponding  $d\theta/d\log \omega$  plot clearly demonstrates the overlapping high and low frequency plots, which adds up to the final plot (Fig. 3h).

To minimize the scan time, which can extend up to several hours, and to capture low frequency (under 10 mHz) behavior of the surface, a numerical analysis technique developed by Khullar & Gilbert was used [83]. Briefly, this method leverages the symmetry of the phase angle ( $\theta$ ) response (Fig. 3c) when plotted against log frequency to predict low frequency response using only the high frequency response captured within a few minutes. This method will be referred to as the symmetry-based EIS method (sbEIS).

The sbEIS method relies on three frequency values typical in a classic Randle's or constant phase element Randle's (CPE-Randle's) circuit. These are: first characteristic frequency ( $\omega_1$ ), the crossover frequency ( $\omega_x$ ) and the second characteristic frequency ( $\omega_2$ ). We generated the  $\omega_1$  and  $\omega_x$  values through experimental means and used the symmetrical response of  $d\theta/d\log \omega$  to calculate the  $\omega_2$  value. Subsequently the entire low frequency response is mapped. In a simple R-C circuit, the time constant is represented by  $\tau=RC$ . In the coated model, it is assumed that a coating or an adhered layer, an oxide layer, for example, creates a more complex surface containing multiple overlapping time constants comprised of additional R-C circuits in series or parallel. When using CPE-Randle's circuit elements, the time constants are of the form  $\tau^\alpha = RQ$  where tau is the



time constant,  $\alpha$  is the CPE exponent and  $Q$  is the CPE magnitude. The constant  $R$  reflects the solution, oxide, or other resistive element in the circuit.

#### 4.3.4 *Parameter calculation and statistical analysis*

We conducted three measurements at the same location in each sample tested. The shape of the Bode plots served as a starting point to determine the model to be used for each damage type. The surface itself was also considered, since retrieval surfaces do not always present large, uniform swathes of the same surface features (IGC, oxide deposits, etc.). Using sbEIS, we used the high frequency data to model the lower frequency response.  $R_s$  is obtained from the high frequency plateau. From the overall modeled response, we then calculated the polarization resistance ( $R_p$ ),  $Q$  and  $\alpha$  for the CPE-Randle's circuit, and other  $R$  and CPE elements from the coated model circuit. The  $\alpha$  reported for coated model was the low frequency value, since that reflects the slope closest to the low frequency end of the Bode plot corresponding to the innermost interface. In the case of the coated model used here (Fig. 3e), the  $R_1$  and CPE1 elements represent the outermost interface, that is, the coating-electrolyte, whereas the  $R_2$  and CPE2 and low frequency  $\alpha$  represent the inner interface between the metal-coating. Hence, when comparing the  $R_p$  and  $Q$  values for CPE-Randle's across PBC and control, the corresponding values from the IGC and oxide deposit samples are the  $R_2$  and  $Q_2$  parameters, since both these sets of elements represent the oxide/metal surface in the particular sample. Details of the calculation are explained in Gilbert et al. [83]. All these parameters and  $|Z|$  calculated and experimental values were normalized by the cross-sectional pipette tip area, to reflect intrinsic values. The statistical significance of these

intrinsic values was determined using one-way ANOVA with post-hoc Tukey's analysis of means across three measurements made at a particular location. For example, the three Q values calculated for IGC sample 1 were compared to each other, and so on. The same statistical analyses were used to compare all measurements grouped according to damage type for differences.  $P < 0.05$  was set as the level of significance.

#### 4.4 RESULTS:

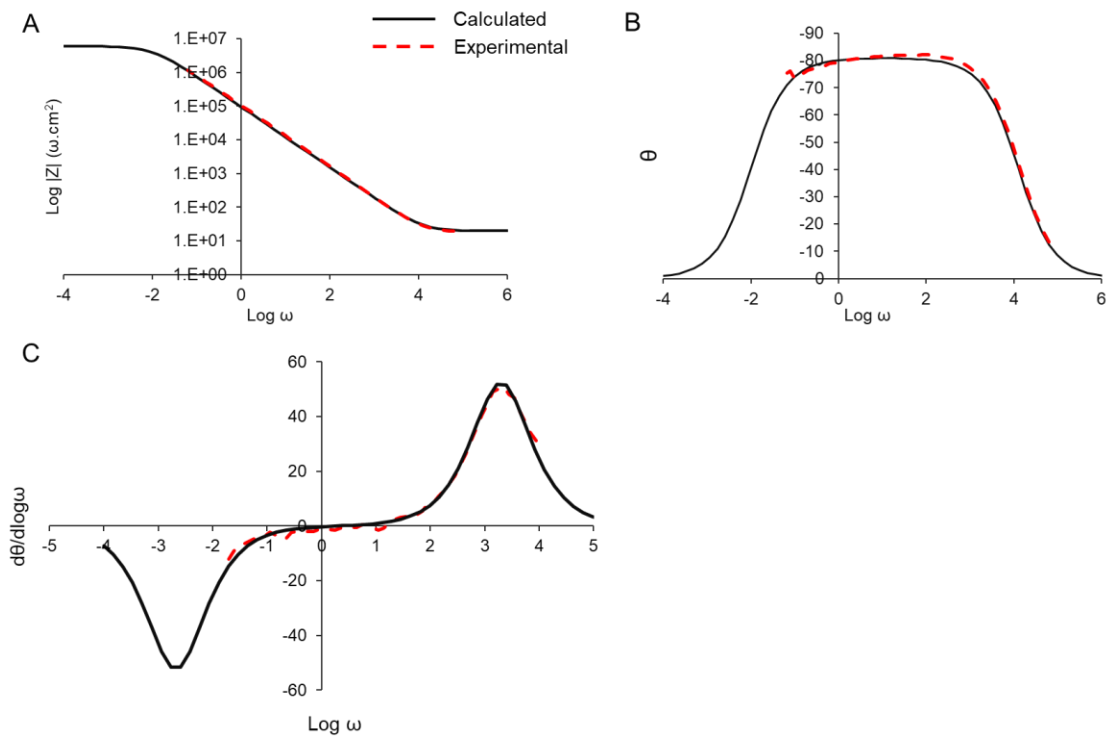


Figure 4: (A) Bode plot showing  $|Z|$  vs log frequency for a polished CoCrMo disk surface (B) Bode plot showing phase angle,  $\theta$ , plotted against log frequency (C) Derivative of phase angle,  $\theta$ , against log frequency ( $d\theta/d\log \omega$ ), showing the symmetry of the phase angle response with respect to the crossover frequency ( $\omega_x$ ), which in this case equals to 0.3 approximately on the X axis (D) Calculated values for Q,  $R_p$ ,  $R_s$  and  $\alpha$  for this experiment

We used the microelectrode setup shown in Figure 2 to perform near-field electrochemical impedance spectroscopy (NEIS) measurements on retrieved acetabular liners showing evidence of corrosion damage. A polished CoCrMo disk was used as control, and the method and analysis were applied to the impedance results thereof. The resulting Bode plots are shown in Figure 4, superimposed by the modelled data. The experimental Log  $|Z|$  Bode plot (Figure 4a) shows an initial high frequency plateau corresponding to  $R_s$  (around  $19.545 \Omega\text{cm}^2$ ), followed by an inflection point corresponding to the time constant representing  $(R_sQ)^{1/\alpha}$ . The subsequent slope (and the peak of the phase derivative) is proportional to the exponent  $\alpha$ . The second inflection point corresponding to  $(R_pQ)^{1/\alpha}$  and the final plateau, which is  $R_p$ , is not seen in the experimental data. This lower frequency data is obtained from the model. Similarly, the phase angle ( $\theta$ ) has a symmetrical shape with a flat top, indicating a CPE Randle's circuit (Fig. 4b). The  $d\theta/d\log \omega$  response is also obtained using the model, and shows a symmetrical response about the crossover frequency,  $\log \omega_x = 0.3$  (Fig. 4c).

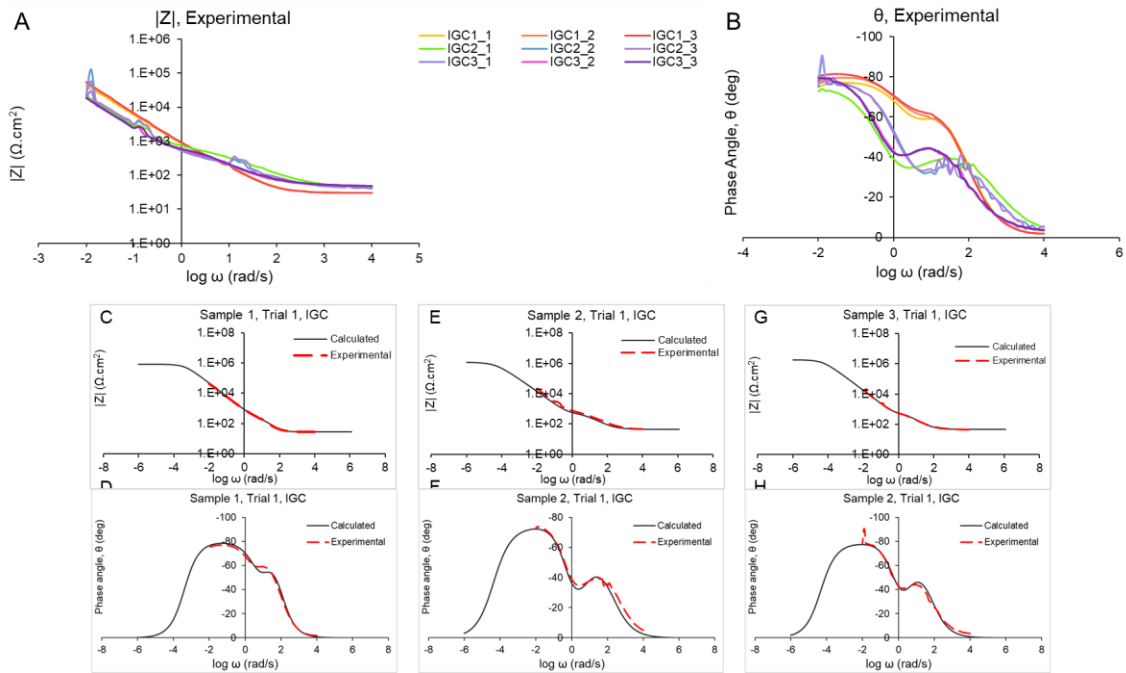


Figure 5: (A) Experimental  $|Z|$  Bode plots for all IGC samples, three trials each. Note the subtle differences in shape, IGC1 plots with a slight plateau mid-slope; IGC2 rising above IGC1 with the plateau mid-slope; IGC3 with a lower slope and prolonged high frequency elbow region (B) Experimental phase angle Bode plots showing pronounced differences among IGC samples: IGC1 with higher initial plateau; IGC2 with the lowest initial plateau and slightly wider phase angle plots; IGC3 with intermediate behavior between IGC1 and IGC3 (c-h) Individual Bode plots of calculated and experimental  $|Z|$  and  $\theta$  for one trial for each IGC sample displaying accuracy of the model used

Similarly, the Bode plots for IGC samples are shown in Figure 5. The sbEIS impedance responses from all samples with IGC damage fit the coated model. The shape of the Log  $|Z|$  and phase angle plots are shown in Figure 5a and 5b, demonstrating a range of similar behavior. The characteristic double hump shape of the phase angle plot was seen in each sample's response, over three trials. The overall shape, however, varied between the three samples, along with the slope and the elbow region in the Log  $|Z|$  plot. We compared the

calculated  $|Z|$  and phase angle plots against the experimental plots for a single trial from each sample, and found consistent agreement between the two, barring some fluctuations in experimental data due to noise (Figs. 5c-5h). The average values for each sample  $\alpha$ , R1, R2, Q1 and Q2 are shown in Table I.

One-way ANOVA comparison across the three IGC samples showed that all three calculated parameters, Rs, alpha, R2 and Q2 were significantly different from one another ( $p < 0.05$ ). Tukey's post-hoc analysis shows that sample 3 differed from 1 & 2 in terms of alpha; sample 2 was intermediate between samples 1 and 3 in terms of R2, whereas the calculated Q2 value for sample 1 was significantly different than 2 & 3. Distinctive surface features in each of the three IGC regions tested could be the cause behind these differences.

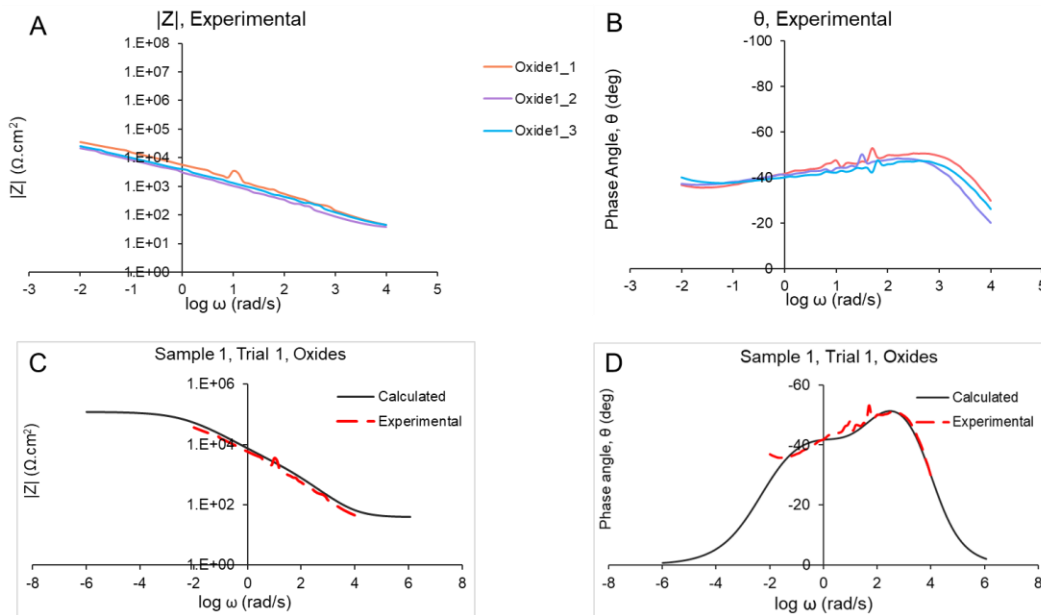


Figure 6: (A) Experimental  $|Z|$  Bode plots for oxide deposits sample. Note the almost absent initial plateau at high frequency and the curved shape of the plots (B) Experimental  $\theta$ , phase angle Bode plots showing the double plateau shape, which differs

significantly from the IGC samples. Note the low phase angle values and the widened shape (c-d) Bode plots showing accurate modeling of the experimental  $|Z|$  and  $\theta$  data using sbEIS

Since most samples lacked large enough areas of continuous oxide deposit, we analyzed a single sample for this damage type. Hence, no statistical analysis was conducted. Three sets of measurements were obtained from the same area, as per protocol. The shape of the Bode plots (Figs. 6a & 6b) is markedly different from that observed in IGC samples (Figs. 5a & 5b), even though the phase angle response matches a coated model, albeit with an  $\alpha$  value much lower than that seen in IGC samples [83]. The modelled  $\text{Log } |Z|$  vs frequency plot (Fig. 6c) shows a more gradual change in slope, which is equal to  $-\alpha$ , in the high and low frequency elbow regions, which correspond with the modelled phase angle vs frequency plot having a shorter peak compared to the IGC samples. The average values for  $R_2$ ,  $\alpha$  and  $Q_2$  are shown in Table I.

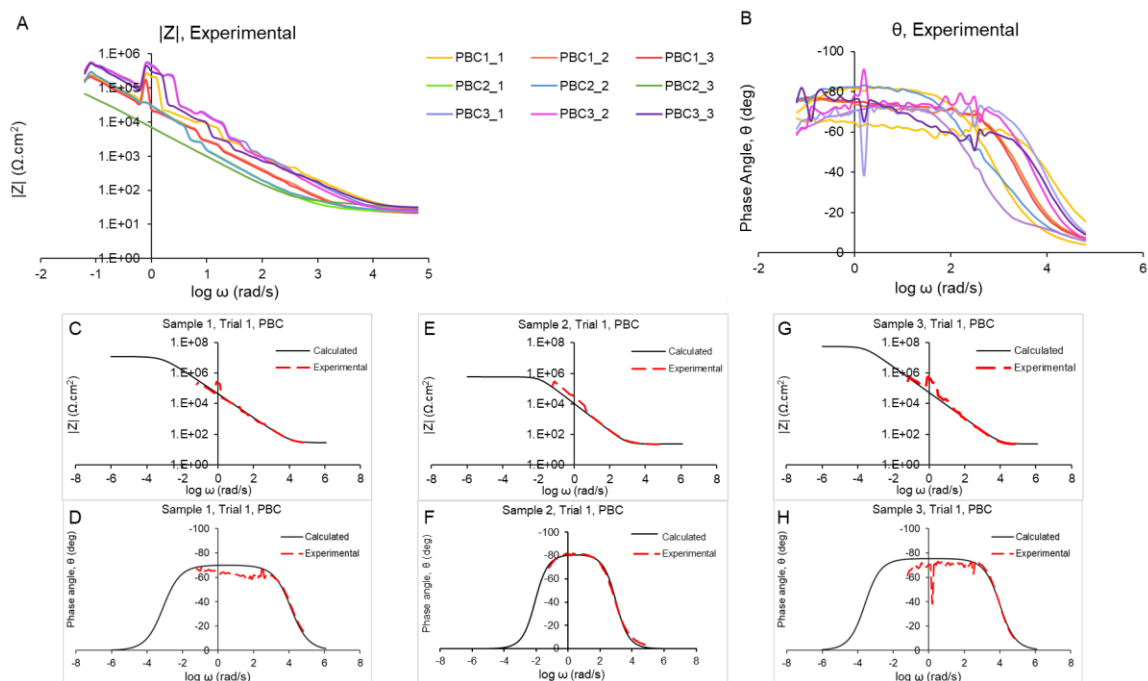


Figure 7: (A) Experimental Log  $|Z|$  Bode plots for all PBC samples, three trials each. Note the shift in the high frequency elbow region while the slopes remain more or less equal (B) Experimental phase angle Bode plots with a generally single plateau shape with differences in width and height (c-h) Individual Bode plots of calculated and experimental Log  $|Z|$  and  $\theta$  for one trial for each PBC sample displaying accuracy of the CPE-Randle's circuit model used.

With the PBC samples, all three surfaces could be fitted to the CPE Randle's circuit model. Minor differences in phase angle and  $|Z|$  response did arise (Figs. 7a & 7b), but the general single plateau shape in the phase angle vs frequency and the distinct high frequency elbow of Log  $|Z|$  vs frequency plot with a lack of mid-slope plateau (seen in IGC samples (Fig. 5)) remained consistent across all impedance measurements. These tests did show a specific artifact, appearing as a ledge in the Log  $|Z|$  vs frequency plot at lower frequencies where the  $|Z|$  value exceeds  $10^7$  ohms.cm<sup>2</sup>. The artifact does not modify subsequent measurements and is a noise source, which the modelled  $|Z|$  response

bypasses effectively while accurately modeling the rest of the  $|Z|$  and phase angle response (Figs. 7c-7h). The average values for each sample  $R_p$ ,  $\alpha$  and  $Q$  are shown in Table I.

Interestingly, among the PB samples, while  $\alpha$  calculated was not statistically different across the three samples, the  $Q$  and  $R_p$  calculated were significantly different among the three samples (data not shown). The Bode plots themselves appear different, particularly the ones for sample 2. The lowered  $R_p$  compared to samples 1 and 3 indicates greater corrosion susceptibility and a more damaged or discontinuous oxide film. The corresponding phase angle plot is narrower, with the height of the plateau remaining consistent. This corroborates the similar alpha values among the three samples. The shortened interval between the high and low frequency elbow regions, corresponding to  $R_sQ$  and  $R_pQ$  time constants for a given surface, distinguish sample 2 from 1 & 3. We also see in Figure 7a, the slope of the line (proportional to  $\alpha$ ) in the  $|Z|$  vs frequency plot is consistent across samples, but the elbows at both the high and low frequency range shifts horizontally, indicating changes in the  $R_sQ$  (mostly  $Q$  varying) and  $R_pQ$  time constants. The differences arise from the non-uniform nature of the surfaces themselves, when comparing all three samples tested for PBC EIS. These differences will be discussed in detail in the discussion section below.



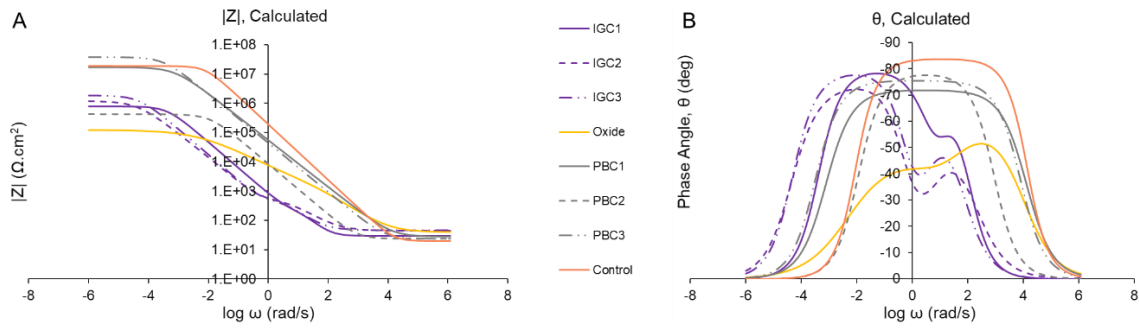


Figure 8: Calculated (A)  $|Z|$  and (B)  $\theta$  Bode plots, one trial from each sample of IGC, oxides and PBC, respectively. Note the differences in shape with each corrosion type having consistent and distinct impedance responses, with PBC exhibiting behavior close to a pristine CoCrMo surface but with lower slope in  $|Z|$  and phase angle maximum, IGC and oxides showing the double plateau coated model behavior, while remaining distinct from one another.

We compare example plots from each of the corrosion damage types in Figure 8. The differences between each of them are distinctive and uniquely identifying: the coated model type surfaces, IGC and oxide deposits, present a change in slope in the  $\text{Log } |Z|$  plot (Fig. 8a), with the oxides plot having a more gradual transition at the elbow regions for the  $\text{Log } |Z|$  plot. These differences also correspond with the double plateau phase angle (Fig. 8b) indicating multiple time constants at intermediate frequencies. The PBC phase angle plots are similar in shape to the control and fit the CPE Randle's circuit model. The corresponding  $\text{Log } |Z|$  plots are also similar in shape to the control, have  $R_p$  values comparable to the control, but have lower peak phase angles and lower  $\alpha$ , i.e., slopes of the  $|\text{Log } Z|$  vs frequency plots. The  $R^2$  values in the IGC and oxides groups are much lower than the control or PBC samples.

Sample	Rs	$\alpha$	Rp	Q	R1	R2	Q1	Q2
IGC1	29.5 ±	0.858 ±	-	-	3.75E2 ±	8.46E5 ±	6.62E-4 ±	1.11E-3 ±
	0.19	0.010			1.27E2	4.10E5	1.48E-4	5.16E-4
IGC2	43.0 ±	0.877 ±	-	-	4.42E2 ±	1.48E6 ±	4.75E-4 ±	2.32E-3 ±
	2.43	0.006			1.43E2	4.08E5	1.32E-4	4.58E-4
IGC3	46.6 ±	0.927 ±	-	-	6.57E2 ±	1.82 E6	8.39E-4 ±	2.81E-3 ±
	1.31	0.006			8.25E1	± 7.86E4	7E-5	2.36E-4
Oxides	38.1 ±	0.487 ±	-	-	2.56E3 ±	9.55E4 ±	6.34E-5 ±	1.3E-4 ±
	0.59	0.009			4.21E2	2.2E4	1.42E-5	2.36E-5
PBC1	23.7 ±	0.817 ±	8.52E6 ±	4.82E-5	-	-	-	-
	3.61	0.032	2.62E6	± 2.2E-5				
PBC2	26.0 ±	0.863 ±	2.62E5 ±	1.68E-4	-	-	-	-
	3.77	0.012	1.58E5	± 4.6E-5				
PBC3	27.3 ±	0.85 ±	5.79E7 ±	1.76E-5	-	-	-	-
	4.41	0.017	1.83E7	± 3.4E-6				
Control	17.5 ±	0.907 ±	4.09E6 ±	1.87E-5	-	-	-	-
	2.00	0.006	1.70E+6	± 8.6E-6				

\* Units for all Q: (S.cm<sup>-2</sup>s) <sup>$\alpha$</sup>  and all R:  $\Omega$ cm<sup>2</sup>

Table I: Calculated equivalent circuit parameters for all samples for the IGC, oxide deposits, PBC and control samples tested. R2 and Q2 for IGC and oxide are comparable to Rp and Q for PBC and control since both represent the metal/oxide interface. N=3 for IGC and PBC, and N=1 for oxides and control (average ± standard deviation)

Table I summarizes all calculated parameters for each surface type tested: IGC, oxide deposits, PBC and control. IGC and oxide samples exhibited coated model behavior and therefore we present R1, R2, Q1 and Q2 element parameters along with low frequency  $\alpha$ , whereas PBC and control samples exhibited CPE-Randle's circuit behavior and have only Q, Rp and  $\alpha$  parameters associated. Rs values fell between 10-50  $\Omega$ cm<sup>2</sup> (overall

average:  $31.477 \Omega\text{cm}^2$ ; std. deviation:  $9.896 \Omega\text{cm}^2$ ). Statistical analysis results corresponding to these calculated values are shown in Figure 9.

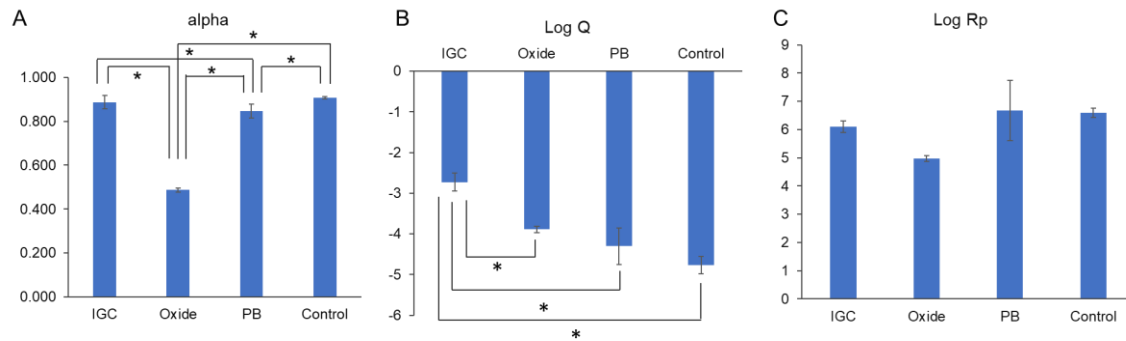


Figure 9: (A) Average  $\alpha$  across the three damage modes, with IGC and PBC displaying comparable values (confirmed by Tukey's post-hoc analysis) and oxides showing lower value ( $p < 0.05$ ) (B) Average Q across the three damage modes, with PBC exhibiting highest value, and IGC the lowest ( $p < 0.05$ ) (C) Average R across three damage modes, with PBC exhibiting the highest R and oxides showing the lowest ( $p > 0.05$ ). Asterisk represents statistically significant difference between indicated groups

Next, we compared the  $\alpha$ , R, Q across all three damage modes and control using one-way ANOVA with post-hoc Tukey's analysis of means. Q and  $\alpha$  were statistically different (Figs. 9a-9b,  $p < 0.05$ ); R was not statistically different among the four groups. Tukey's analysis of means indicated in terms of alpha, all three modes, IGC, oxides and PBC, were significantly different. For Q, the IGC mean was the largest followed by oxides and then PBC. Rs values were statistically different across the three damage modes ( $p < 0.05$ , data not shown) even though the same electrolyte and same microelectrode design were used for all experiments. Tukey's analysis showed that IGC and oxides had similar Rs values, and PBC and control had similar Rs values. Overall, the results point to alpha being a better predictor for differentiating between different damage and corrosion types,

compared to Q or R, which are typically considered as an indicators for corrosion resistance (typically higher R and lower Q are associated with greater corrosion resistance).

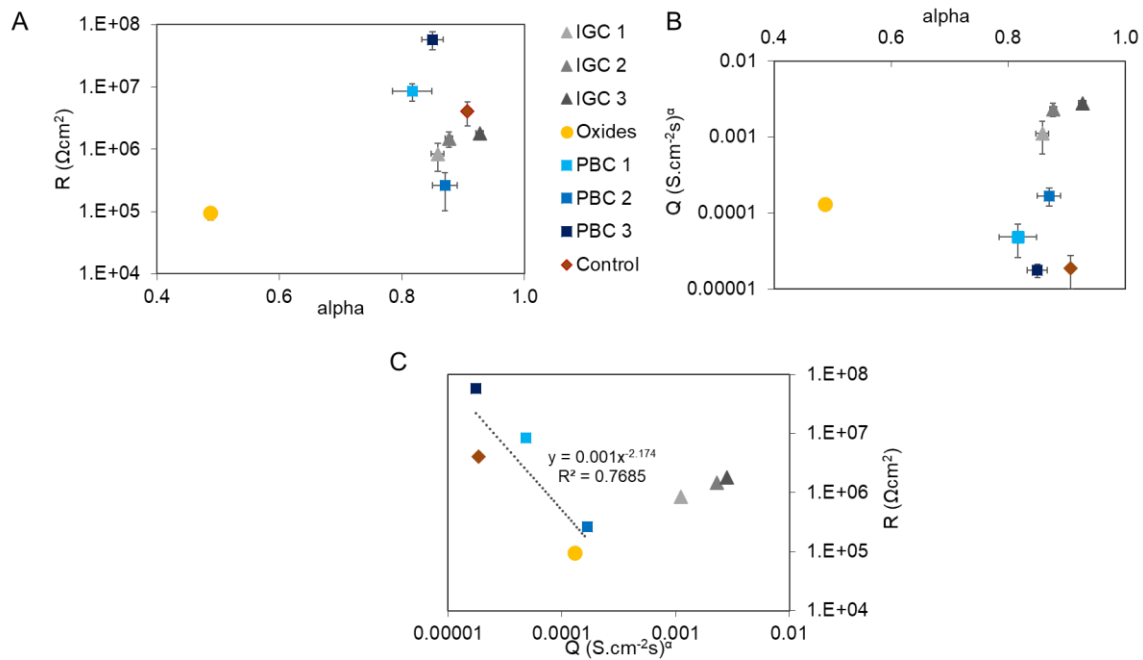


Figure 10: (A) Average R vs  $\alpha$  where oxides exhibit lowest R and  $\alpha$  values. PBC has the highest R values, with PBC2 lower than IGC samples (B) Average Q vs  $\alpha$  showing that the different types of surface damage separate themselves according to the surface features. Note that PBC2 is intermediate between IGC and other PBC samples, which are clustered with the control sample (C) Average R vs Q showing oxides have the lowest R and Q compared to PBC and IGC samples. Axes have been adjusted to illustrate differences among individual samples and error bars indicate standard deviation (n=3 for IGC and PBC and n=1 for oxide and control)

In order to draw further distinctions among the three damage modes, we compared R vs alpha (Fig. 10a), Q vs alpha (Fig. 10b) and R vs Q (Fig. 10c). We generated scatter plots using the average Q, R, and alpha values of the three trials per sample in each damage

mode, except oxides and control, which only had one sample. The error bars indicate standard deviation. We found that visualizing the data this way clarifies patterns among the seven samples tested overall; first, that the oxide deposit surface tested here was distinct in terms of the overall impedance response; second, when comparing Q and R<sub>p</sub> values across IGC and PBC, the Q values neatly separate according to damage type, IGC surfaces showing higher capacitive characteristics compared to PBC (Fig. 10a), and PBC surfaces showing a higher resistive characteristic, with the exception of sample 2 from the PBC group, which was closer to IGC in the R<sub>p</sub> vs alpha plot (Fig. 10b) PBC1 and 3, in fact, exhibit a higher R value than the control sample too, although this difference was not statistically significant. Alpha values were fairly similar among IGC and PBC samples, however it must be noted that Q and R<sub>p</sub> are plotted on a log scale, which minimizes differences between individual data points.

In Figure 10b, the log-log linear relationship between R<sub>p</sub> and Q becomes clear among the control, PBC and oxide deposit surface. Fitting a power law trendline to the data points pertaining to these surface types, we find the exponent of the power law relationship between R<sub>p</sub> and Q is -2.174. R<sup>2</sup>=0.768 indicates that R<sub>p</sub> and Q are linked and knowing one parameter may help predict the other.

#### 4.5 DISCUSSION:

We set out to design a quantitative method based on impedance spectroscopy to analyze small regions on retrieved device surfaces and distinguish between corrosion types and resulting surface features based on impedance characteristics. Using sbEIS analysis and a

near-field microelectrode design, we have demonstrated the unique and characteristic responses of the surface that depends on the type and extent of the corrosion present in retrieved CoCrMo alloy acetabular liner components. Clear and characteristic impedance response differences were seen for intergranular corrosion, phase boundary corrosion, oxide film accumulation due to fretting corrosion as compared to the uncorroded control surface. The small area investigated and the advanced symmetry-based EIS method combined were able to isolate each distinct region and evaluate its response non-destructively as a result of the test. We also were able to reduce measurement or scan times from several hours to under 30 minutes.

Impedance data describes the surface's ability to withstand corrosion, through the R value associated with the metal/oxide surface. A higher R value is associated with greater corrosion resistance, which in the CPE-Randle's model is indicated by  $R_p$  and in the CPE coated model is indicated by  $R_2$ . Whereas the Q and  $\alpha$  describe the dielectric nature of the surface, and the charge transfer mechanism across the oxide-metal interface into the electrolyte layer immediately adjacent to the working electrode surface. The combination of a near field (small area) impedance test coupled with the symmetry-based EIS method, which extends the frequency range able to be captured, creates a powerful test method to discern the nuances of the local corrosion damage in retrieved surfaces.

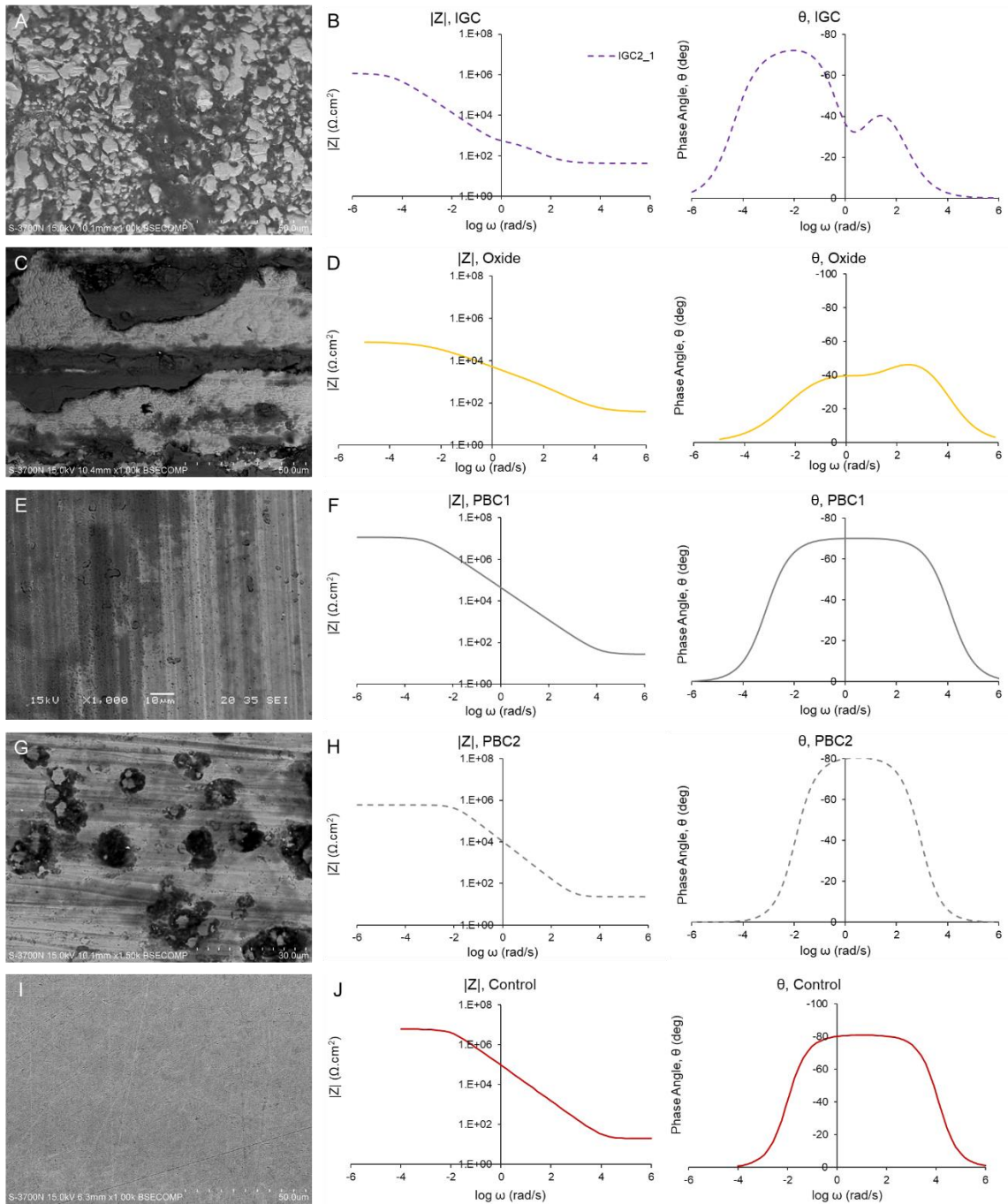


Figure 11: (A) Backscattered electron micrograph of IGC test surface. Note the extensive material loss and presence of biological material (dark contrast region) (B) Bode plots for  $\log |Z|$  and theta vs log frequency for IGC region shown in (A). The double hump in theta corresponds to the change in slope in  $|Z|$ , which denote a compromised surface with

overlapping time constants (C) Secondary electron micrograph of PBC1 test surface. The test area is mostly continuous with several minute pits, and minor material loss along carbide boundaries (D) Bode plots for  $\log |Z|$  and theta vs  $\log$  frequency showing single hump phase response corresponding to a single slope  $|Z|$  plot, clearly indicating low degree of material loss and a more homogenous surface (E) Backscattered electron micrograph of PBC2 test surface displaying a greater degree of material loss and pitting along carbide boundaries and intact grains (F) Bode plots for  $\log |Z|$  and theta vs  $\log$  frequency showing a narrower slope between the two inflection points in  $|Z|$  and a narrower phase angle plot, but still with a single hump indicating a more homogenous surface than IGC but greater degree of material loss illustrated by the lowered  $R_p$  (second plateau in  $|Z|$ ) (G) Backscattered electron micrograph for oxide deposits surface showing a clear coating of oxides (darker contrast) adhered atop a corroded region (bright contrast) (H) Bode plots for  $\log |Z|$  and theta vs  $\log$  frequency showing a coated model response with a double hump phase, markedly different than the IGC response shown in (B). Lower  $R_p$  and phase angle response indicate a more corrosion susceptible surface with a diffusion-like element present

Figure 11 illustrates the crux of this study: impedance response of a surface accurately represents the nature of the surface and clearly portrays salient damage characteristics. Each of the conditions (IGC, PBC, oxide deposit, control) resulted in very different EIS responses that can be used to distinguish each based on the impedance properties alone. For example, both IGC (Fig. 11a & 11b) and oxide coated surface (Fig. 11c & 11d) show impedance characteristics similar to the defective coating models sometimes used to describe electrode responses [36], [40], [83]. Such “double hump” phase angles responses are due to multiple layers being present at the electrode surface. However, the response was very different for the IGC and oxide cases with a much lower  $R_p$  and  $\alpha$ , and higher  $Q$  for the oxide surfaces compared to the IGC samples. Thus, while the coated model



response was seen for both cases, large differences were observed between these two types of corrosion damage such that they could be easily distinguished.

The coating or oxide layer (Fig. 11c) is most likely to be a mixed oxide tribochemical deposit with the interfacing surface also transferring some of its oxide through cold welding or material transfer [85]–[87]. EDS analysis (data not shown here) confirms these oxide deposits to be a mixed oxide of molybdenum, titanium, and chromium. Seeing the gradual change in slope in  $|Z|$  and the comparatively flattened phase angle plot, we can confirm that oxide deposits, while presenting as a coated model circuit, definitely exhibit characteristics distinct from an IGC surface. Here we introduce the idea of these oxide deposits acting as a coated model with a Warburg element. The Warburg element is a CPE-type element that models diffusion of ionic species within a dielectric. It is characterized by a charge-transfer resistance and is typically associated with a  $\log |Z|$  vs  $\log \omega$  plot with a slope of  $-1/2$ . *Impedance Spectroscopy*, edited by J. Ross Macdonald [88] outlines the Warburg element in considerable detail. This is also reflected in the statistical similarity between  $R_s$  values for IGC and oxide samples, which were different than PBC and control samples, which did not correspond to a coated model. There might be an increase in solution resistance due to the presence of a coating acting as a diffusion layer, or due to the increase in working electrode area and/or path length seen in IGC samples. Further experimentation and development of new models to incorporate Warburg and other elements into the equivalent circuits is therefore warranted.

More importantly, the low  $R$ , high  $Q$  and low  $\alpha$  for the tribochemical mixed oxide deposits are indicative of a compromised metal surface that leaves these regions much more susceptible to continued corrosion than the well passivated control or more lightly corroded regions. That is, accumulated corrosion damage on a surface renders the surface increasingly susceptible to corrosion attack by compromising the properties of the oxide film due to the damage present. Previous studies indicate that tribochemical layers formed of metal ions and protein-metallic complexes might impart a protective characteristic to the surface, if the layer is formed on a pristine undamaged alloy surface [89], [90]. However, little effort has been made, to date, to assess the role of prior damage on the ongoing corrosion susceptibility of the alloy surface. Such tests could be important to better understand the nature of the ongoing degradation processes in these alloys.

The phase boundary corrosion (Fig. 11e-h) exhibited a single hump (CPE-Randle's) response, similar to the control (uncorroded) surfaces (Fig. 11i & 11j), however, while they typically had similar  $R_p$  and  $Q$ , the CPE exponent was smaller for PBC compared to the control, forming a crucial distinction between a corroded surface and a polished, undamaged surface. In Figure 11e, we see that the PBC surface is more continuous with little to no material loss or continuous deposits, analogous to the control surface. The same nominal surface area in IGC, and in PBC2 (Fig. 11g), includes a larger actual surface area due to the topographical changes introduced by material loss, and the nature of the interface is altered due to the addition of oxide deposits. Thus, a different impedance response is generated.

The major differences between IGC (Fig. 11a), PBC1 (Fig. 11e) and PBC2 (Fig. 11g) are the extent of material loss from the surface, the type of deposit present in those regions of material loss, and the spatial distribution of these features across the test surface. A direct consequence of material loss is an increase in working electrode surface area, caused by the tortuous path created by missing grains. Resistance is a function of the length of the path followed by the current,  $l$ , and the surface area of the electrode,  $A$ , given by

$$R = \frac{\rho l}{A} \quad \text{Eqn. 1}$$

where,  $\rho$  is the resistivity of the surface, and is a property of the material itself. Thus, a larger surface area can lead to lower resistance. Thus, the impedance response for PBC2 (Fig. 11h) lies intermediate between the IGC sample (Fig. 11a) and PBC1 (Fig. 11e). PBC2 shows more material loss in conjunction with pitting (Fig. 11g), yielding a discontinuous surface compared with PBC1 (Fig. 11e) & PBC3 (data not shown), manifesting as lower  $R_p$  for PBC2 compared with PBC1 (Figs. 11f and 11h). Samples 1 and 3 both exhibited lesser material loss compared to 2, and the surface is continuous except at phase boundaries, with little to no oxide or biological material present, tying in to the higher  $R_p$  value. Additionally, biological deposits tend to behave like non-conducting materials, due to their carbon-rich chemical composition. Under NEIS conditions, biological materials as seen in the IGC samples, could function as a capacitive element, storing electric charge, and causing shifts in  $\alpha$  towards a more capacitive nature for the CPE elements.

Similar to resistance being a function of  $l$  and  $A$ , capacitance is also a function of both these parameters, and is expressed as

$$C = \frac{\epsilon_0 \epsilon_r A}{l} \quad \text{Eqn. 2}$$

where  $\epsilon_0$  is a constant called the permittivity of free space and  $\epsilon_r$  is the relative permittivity of the dielectric material between the plates of the capacitor of area  $A$  at a distance  $l$  from one another. The time constant,  $\tau$ , denoted by  $(R_s Q)^{1/\alpha}$  or  $(R_p Q)^{1/\alpha}$  or  $(R_2 Q_2)^{1/\alpha}$  or similar combinations of  $R$  and  $Q$  pairs forming the coated model surface, where  $Q$  is the capacitive magnitude of the CPE elements. can be designated as follows, based on Equations 1 & 2:

$$\tau = \epsilon_0 \epsilon_r \rho \quad \text{Eqn. 3}$$

implying that the relationship between  $R_p$  and  $Q$  is an intrinsic property in itself, independent of surface topography and roughness.

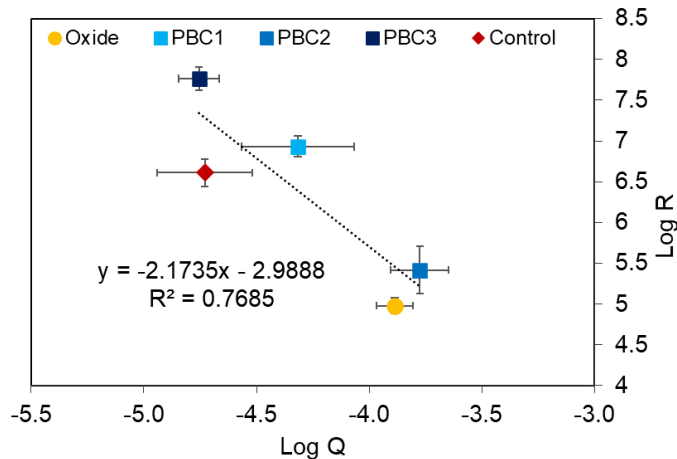


Figure 12: Log  $R_p$  vs Log  $Q$  plot showing linear correlation between the  $R_p$  and  $Q$  values for PBC, oxide deposits and control surfaces

Importantly, Figure 12 shows a linear correlation between log R and log Q values for PBC, control and oxide deposits samples, with a slope of -2.174. These three surface types, despite their distinct visual presentation and impedance results, seem to follow a linear correlation between the R and Q values, indicating that the R-Q combination might represent an intrinsic property of the material itself, instead of being a function of corrosion processes or external conditions. Notably, IGC surfaces do not fit this linear trend, suggesting that the depth penetration property unique to IGC and the introduction of secondary and tertiary materials into gaps left behind due to material loss introduces additional variables to surface impedance. Systematic study of how R-C type element pairs might describe fundamental material properties, and how materials might differ from one another in terms of R-C pairs and/or impedance characteristics could lead to a deeper understanding of biomedical alloys.

EIS as a quantitative retrieval analysis method is still a novel concept. Others have previously utilized impedance in conjunction with visual scoring to show that impedance parameters ( $|Z|$ ,  $\alpha$ , Q) can be correlated to damage scores, with high damage scores being associated with lower  $|Z|$  [37], [84], or  $\alpha$  bears a strong correlation with damage scores [91]. These observations corroborate many of the findings in this study and provide further context for the impedance behavior of individual test areas.

Using the NEIS technique, we are able to isolate small areas for evaluation, while the sbEIS technique allows us to capture the entire spectrum of impedance response with a few minutes of actual scan time. Using a two-step approach of visual assessment followed by an impedance assessment provides an expanded framework to convey the

granularity of the retrieved device surfaces. This study demonstrates the value of this system to assess metallic device surfaces, especially complex ones such as a retrieved implant taper. The design of the microelectrode makes it accessible and easy to fabricate, while being small enough to be used with unique taper geometries.

Despite the advantages of this system, it is not without limitations. The study was restricted in the number of samples available, and therefore, could only analyze a limited range of retrieval surfaces. We also recognize that three samples per damage type are not sufficient to make a general observation. Indeed, a general observation would not apply even to the same kind of damage features across multiple devices, as we proved with the PBC samples. Retrieval device surfaces are complex, and often exhibit several damage modes within the same region. The NEIS system with the symmetry-based EIS modelling method has the potential to discern the nuances of a given surface. We foresee using this technique in conjunction with neural networks and deep learning algorithms, wherein several thousands of inputs from several thousand retrieval surfaces can be used to create a predictive model. Potentially, such a system, given the Bode plots from an unknown surface, could create a map of the damage features, and predict the kind of surface damage that has occurred.

Additionally, impedance measurements are highly dependent on the system itself; oxide hydration, related to the amount of time since the electrolyte is brought in contact with the surface, and positioning of the electrodes relative to the working electrode (length of path, from Eqn. 2) can influence outcomes. We were able to obtain repeatable and accurate results from the setup described in the methods section, however, with the 1

hour long OCP measurement being key for optimal oxide hydration in our experiments. Importantly, the scale of measurements was limited by the microelectrode tip itself. Damage features on a scale smaller than 780  $\mu\text{m}$ , which is the working electrode area dictated by the pipette tip used here, were not resolved. The choice of working electrode area is a crucial one, because a smaller exposed area (using a smaller volume pipette tip, for example) is not necessarily better. The solution resistance,  $R_s$ , depends upon the area exposed, with smaller areas developing larger resistance (Eqn. 2), with smaller areas resulting in larger resistance drops across the electrolyte-device interface. Finally, the sbEIS method used here is not comprehensive, and the models are not applicable to every type of retrieval surface. More complex models can be created, bringing into consideration other electrical elements such as Warburg elements, to more closely represent surfaces which do not fully fit the CPE-Randle's circuit, or the coated model described here.

Overall, we were able to demonstrate the benefits of using a near-field EIS measurement system in conjunction with the sbEIS technique to bring objectivity and a much-needed quantitative metric to retrieval analysis. With further refinement of the analysis models, and improved microelectrode design, this system can find application in areas of study beyond retrieval analysis, including in situ surgical assessment of implant surfaces to gauge their electrochemical properties.

#### 4.6 CONCLUSIONS:

This study developed, utilized, and demonstrated that symmetry-based near field EIS can effectively measure and quantify the impedance properties of corroded CoCrMo alloy surfaces with varying corrosion damage modes. The results showed distinct, characteristic, and quantitative measures of the corrosion damage in small areas of retrieved implant devices that depended on the type of corrosion damage present. It was found that oxide debris covered surfaces demonstrated low R values compared to other forms of corrosion or the control surface, that IGC showed characteristic defective coating model response and that phase boundary corrosion had an impedance response more similar to the control surface, but with a lower CPE exponent value. The different characteristics for each mode, along with small-area impedance measurements provided a non-destructive means to quantitatively assess the corrosion damage present. Importantly, corrosion-damaged surface result in degraded impedance properties of the surface rendering these damaged regions even more susceptible to continued corrosion attack.

New methods of impedance analysis – using both small microelectrodes for a near-field analysis – and symmetry-based EIS techniques provided new abilities to evaluate metal implant surface corrosion conditions non-destructively.

In doing so, we shortened scan times from several hours to under 30 minutes and extended the frequency range capable of analysis. We found close agreement between experimental and calculated  $|Z|$  and  $\theta$  values, and that IGC and oxides deposit surfaces match a coated model response, whereas a PBC surface matches a CPE Randle's



response. PBC circuits with lesser material loss were found to be approaching a freshly polished CoCrMo disk in impedance characteristics, while IGC and PBC surfaces with greater degree of material loss were associated with lowered  $R_p$ . Finally, the differences in the retrieval surfaces were reflected in subtle changes in the Bode plots from individual devices, even when the broad categorization for the type of damage seen on those devices was the same, establishing the potential for this method to discern the granularities of retrieved device surface electrochemistry.

## Chapter 5

### **In Vitro Test Methods for Seating and Fretting Corrosion Behavior of Modular Metal-on-Metal Acetabular Tapers**

A. A. Shenoy and J. L. Gilbert, “In vitro test methods for seating and fretting corrosion behavior of modular metal-on-metal acetabular tapers,” *J. Orthop. Res.*, p. jor.24554, Dec. 2019.

Aarti A. Shenoy <sup>a, b</sup>; Jeremy L. Gilbert <sup>a, b \*</sup>

- a. Department of Biomedical & Chemical Engineering, Syracuse University,  
Syracuse, NY, USA 13244
- b. Syracuse Biomaterials Institute, Syracuse, NY USA 13244

## 5.1 ABSTRACT:

Retrieval studies show metal-on-metal acetabular shell-liner tapers are susceptible to corrosion, which is hypothesized to arise from mechanically-assisted crevice corrosion (MACC). The role of materials on MACC of acetabular tapers has not been previously studied. In vitro tests of seating, pushout and fretting corrosion performance of acetabular tapers are presented to assess the role of material combinations (Ti-6Al-4V shells, and HC CoCrMo, LC CoCrMo and 316L SS liners). Acetabular tapers were wet-assembled to a seating load of 1000 N. Liner load-displacement seating mechanics were measured. Fretting corrosion currents were evaluated using a uniaxial incremental cyclic compression test up to 4000 N, with the load applied at 55° angle to the taper interface. Fretting currents, fretting onset loads, taper disengagement strength, load-displacement plots were measured. Push-out tests were also performed pre- and post-fretting corrosion. Average liner seating displacements varied from 134-226 µm across groups. Fretting currents at 3600 N cyclic load were low and ranged between 0.05 and 0.27 µA and were independent of material combination ( $p>0.05$ ), reflecting small amounts of fretting. Fretting corrosion onset loads were between 1800 N to 2100 N and did not differ across groups ( $p>0.05$ ). Push-out loads were 27–43 % of the maximum load applied. Fretting corrosion levels were very low for all material combinations and not different from one another. Seating and push-out responses were also not material dependent. The low fretting currents measured imply that MACC may not be a major cause for acetabular taper corrosion.

*Keywords:* total hip arthroplasty; acetabular taper junction; taper mechanics; modular orthopedic implant; acetabular taper testing

## 5.2 INTRODUCTION:

Modular acetabular components have been in use since the Charnley design in total hip arthroplasty (THA) was introduced in the 1960s, with a polyethylene liner inserted into a metal acetabular shell (or cup) to mitigate friction at the acetabular interface [2]. Benefits of using an acetabular liner within a shell include ease of revision by changing the liner without removing a well-integrated acetabular cup. In addition, shell fixation with screws is required in cases of bone tissue loss, and a modular acetabular component allows for this possibility without interfering with the bearing surface of the femoral component [26]. Early designs comprised of non-cross-linked ultra-high molecular weight polyethylene (UHMWPE). This material exhibited high wear rates, and, in some cases, was associated with adverse local tissue reactions leading to aseptic loosening and osteolysis [92]. Metallic liners were introduced in the early 2000s as an alternative to using UHMWPE [93]. While experimental evidence showed metal-on-metal (MoM) bearing surfaces had lower wear rates compared with metal-on-polyethylene bearing surfaces [94], significant concerns arose related to adverse tissue reactions to the tribocorrosion processes.

Dislocation of the head component following THA is one of the prevalent causes for implant failure [18], [70]. Gwam et al. conducted an epidemiological survey using the National Inpatient Samples (NIS) database and found that dislocation-related acetabular revision occurs in 24.7% of cases out of 53,508 cases requiring revision surgery [18]. One of the strategies employed to reduce the risk of dislocation in high-risk patients is to

incorporate a dual-mobility articulation for both primary and revision surgeries [13], [23], [24], [95]. As the number of THAs has risen each year, the risk of dislocation has also remained more or less constant. Hence, the number of patients that require a dual mobility construct is likely to increase. This design features an acetabular shell, usually made of porous-coated titanium, with a metallic liner, usually CoCrMo, with a polyethylene insert and a freely-rotating femoral head. Thus, a metal-on-metal taper is formed at the acetabular shell-liner interface (Figure 1). The unique geometry of the taper junction leads to unique mechanics and might distinguish the seating mechanics, subsequent engagement as well as micromotion behavior during cyclic loading.

Recent retrieval studies have shown that modular acetabular components, primarily associated with MoM designs, sustain damage in their taper junctions, usually attributed to mechanically-assisted crevice corrosion (MACC) and wear [11], [26], [27], [29]. However, the nature of the damage observed in these tapers is distinctly different than that seen in, for example, head-neck junctions. It is often not directly based on fretting/mechanical damage, but rather appears to be intergranular [11] in nature and arises from non-mechanically-based crevice corrosion or other corrosion-based mechanisms.

In order to understand the corrosion mechanisms at the acetabular taper junction, it is important to examine the taper locking mechanics and subsequent corrosion performance, particularly MACC, which is reported as the leading cause of failure. So far, no study has systematically studied the seating mechanics or MACC performance; thus, there is a need for in vitro test methods that describe the fundamental mechanics and corrosion processes

at acetabular tapers. Taper seating mechanics in head-neck taper was shown to depend upon the taper design, and engagement strength was shown to depend on maximum seating load in a study by Ouellette et al. [48]. Mali et al. [47] published an incremental cyclic fretting corrosion (ICFC) test method to study fretting corrosion behavior in head-neck tapers, correlating mechanical motion and corrosion behavior. Using similar methods, it is possible to assess the acute fretting corrosion behavior of acetabular tapers.

Additionally, there are questions related to the material combination between shell (normally made from Ti-6Al-4V) and liner, where the liner may be comprised of high carbon CoCrMo (HC CoCrMo), low carbon CoCrMo (LC CoCrMo) or 316L stainless steel (SS), (which may be considered for use in some countries). Hence, the goal of this study was to develop an in vitro method to assess both the seating mechanics and engagement (push-out) strength of the acetabular liner into a porous-coated shell, and the subsequent fretting corrosion behavior in a short-term incremental cyclic fretting corrosion test. We compared the above three different material combinations with the same component design to investigate the effects of varying liner material on overall fretting corrosion behavior.

### 5.3 MATERIALS & METHODS:

#### 5.3.1 *Sample description:*

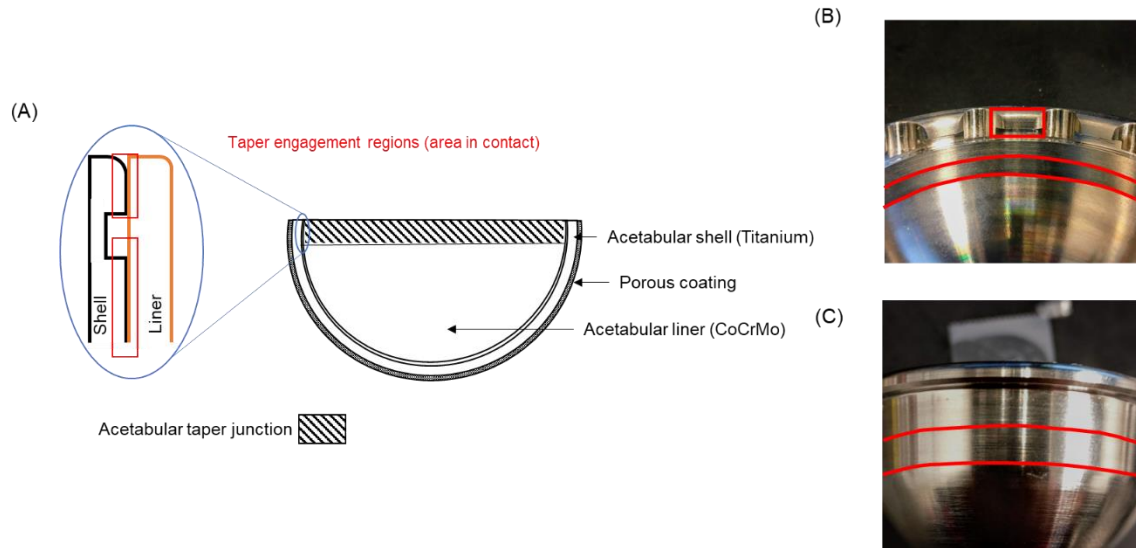


Figure 1: (A) Schematic showing the acetabular shell-liner junction with (inset) showing the actual geometry in the taper and the distinct areas of contact. (B) Titanium shell taper junction with the tabs and cylindrical engagement region in red (C) CoCrMo liner taper with the lower engagement region in red.

Each construct consisted of two components: an acetabular shell and a full-lipped metal liner (Figure 1a). These shells and liners (provided by DePuy Synthes) are not in current commercial use but are experimental in nature. The lipped nature of the design was developed as a possible alternative design geometry. This lip is not involved in the locking mechanism of the taper but does provide a flat top for attachment of sensor targets for displacement measurements. However, they have been manufactured as they would be for distribution. Shells were porous-coated Ti6Al4V with a 50 mm diameter. Liners (size 38/50) were made of three different materials, and these formed the three groups that were tested for this study: group 1- high-carbon CoCrMo (HC CoCrMo),



group 2- low-carbon CoCrMo (LC CoCrMo), group 3- 316L stainless steel (SS). Apart from the material combinations, the three groups did not vary in geometry, design, or test protocol. Five samples were tested for each group.

The taper engagement between shell and liner components is similar to the taper locking design of the DePuy Pinnacle acetabular taper which was measured to have a nominal conical half angle of 4 degrees. The shell taper is broken into two parts with the upper engagement region made of rectangular tabs (nominally 5 mm x 2 mm) spaced equally around the perimeter and a full cylindrical taper engagement lower region around the shell that is about 5 mm in width (Figure 1b). The full cylindrical engagement region and the rectangular engagement sections are separated by a full perimeter channel that is about 1.5 mm wide and about 2 mm deep; the depth of the channel reduces to approximately 0.5 mm directly below the tabs. The liner taper length (Figure 1b) is about 8 mm wide and the engagement region is formed at the bottom half (approximately 4 mm in width) as well as the parts in the upper half which interface with the rectangular tabs in the shell taper. The surface finish of the liner consisted of a spiral machined surface with under 5  $\mu\text{m}$  ridge heights separated by about 40  $\mu\text{m}$ , while the shell had an as-ground surface finish with no ridges or grooves (see Fig. 2a and 2b).

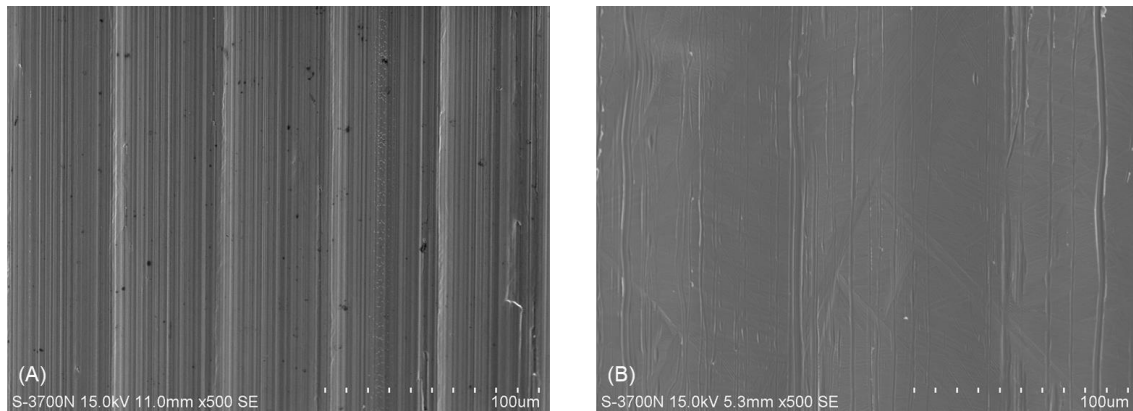


Figure 2: Scanning electron micrographs showing (a) the liner taper surface and (b) the shell taper surface. Note the ridges seen in the liner taper, spaced about 40  $\mu\text{m}$  apart. The height of these ridges was under 5  $\mu\text{m}$  (not shown), showing a low roughness surface. The shell taper has a ground surface finish, which appears as a mostly flat topography.

### 5.3.2 Sample preparation:

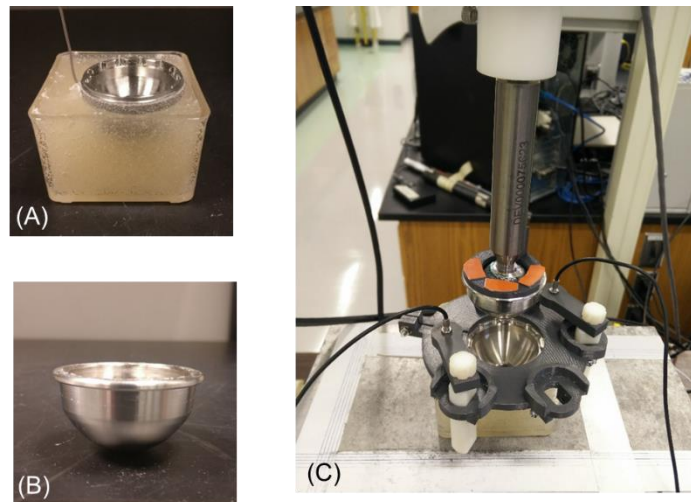


Figure 3: (a) Potted titanium shell with a titanium wire for electrical connectivity (b) Metal liner (full-lipped design) (c) Experimental setup for displacement measurement during assembly of the shell-liner construct. The orange parts correspond to the aluminum targets for the non-contact DVRTs which are threaded into the grey arms on the ring.

The shells were fixed using dental acrylic in a clear acrylic container (Figure 3a). A titanium wire was electrically coupled to the shell for subsequent electrical connections. The liner is shown in Figure 3b. After allowing the shell potting mixture to harden, a custom-designed circular holder was affixed to the rim of the shell. The holder held two non-contact differential variable reluctance transducers (DVRTs, Lion Precision Inc.) at an angle of 120° to each other. The DVRTs allow accurate measurement of vertical relative motion between the shell and the liner with a resolution of  $\pm 1 \mu\text{m}$ . An aluminum target ring was attached to the rim of the liner (Figure 3c) that interfaced with the DVRTs and was used to measure the displacement of the liner into the shell during seating.

### 5.3.3 *Stage I: Seating and Pushout:*

The seating and push-out study was performed in two stages: in Stage I, the construct was assembled using the setup seen in Figure 3c. The taper surfaces were wetted with phosphate buffered saline (PBS) prior to seating to simulate a wet interface during assembly. An incremental ramp load was applied using a servo-hydraulic test frame (Instron 1530) up to a maximum of 1000 N at 100 N/s. This load was selected to represent a lower end of the impaction loads typically used to assemble tapers and represented a more worst-case scenario for fretting corrosion to occur. Once assembled, a push-out test was performed using the same test frame. A ramp load was applied to the liner using a conical-tipped loading nose which pushed on the center of the backside of the liner through an opening in the center of the shell to separate the liner and shell while the shell-holder construct was held fixed. The load required for disengagement was

recorded as the push-out load. A minimum of five samples per group were tested for push-out strength immediately after seating.

Seating mechanics were analyzed by capturing the seating load and seating displacement over time during seating using a custom-designed data acquisition program in LabVIEW™ (National Instruments). These data were used to generate the load versus displacement plots for each sample. Several parameters of the seating mechanics were calculated, including the seating stiffness which is defined in this study as the slope of the load-displacement plots near 1000 N, and the work of seating (or seating energy) which is the hysteresis energy in the load-displacement curve over a complete load and unload during seating [47], [48]. These parameters were used to compare the seating mechanics for each sample tested.

#### 5.3.4 *Stage II: ICFC test and Pushout:*

The same shell-liner couples were re-assembled using the same protocol as before. Samples were reused for testing in this manner since the taper asperity contact points are stochastic in nature. The components as well as the materials behave in an overall elastic manner except at the asperity contact points which plastically deform and are not likely to be the same for each test. It should be noted that prior testing of repeated seating and push-out showed no effect on the push-out strength of the interface.

### ICFC Test Method

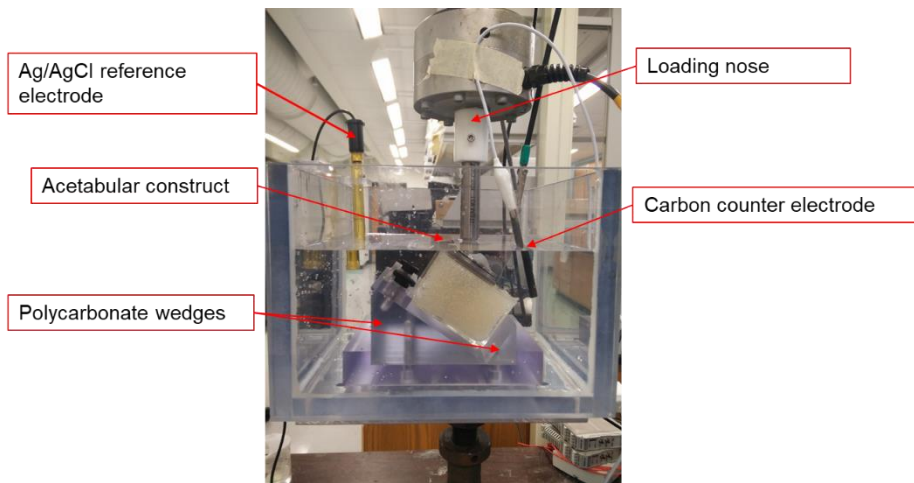


Figure 4: Experimental setup showing the three-electrode system for the short-term ICFC test with the construct held at a joint-force-cup-orientation angle of  $55^\circ$ . This reflects at  $45^\circ$  physiological inclination angle and a joint force orientation of  $10^\circ$ . The loading nose was electrically isolated from the acetabular components and it applied the cyclic load according to the program executed by Instron WaveMatrix software.

Post-assembly, a short-term ICFC test was performed using the setup shown in Figure 4. The construct was held at a  $35^\circ$  angle versus the horizontal. This angle reflects an anatomical inclination angle for the acetabular component of 45 degrees with a hip joint force oriented at about 10 degrees from the vertical in single-leg stance. The loading head on the test frame (Instron 1530) was electrically isolated from the acetabular component using acrylic to prevent any stray electrochemical currents arising from head-cup contact. Phosphate buffered saline (PBS) at room temperature was used as the solution for electrochemical measurements. A three-electrode setup with a silver-silver chloride (Ag/AgCl) reference electrode, carbon counter electrode and the construct as the working electrode was used. The samples were held potentiostatically at  $-50$  mV vs

Ag/AgCl during testing after an initial resting period of 15 minutes to allow the open circuit potential of the construct to settle. This potential is close to and representative of the resting (non-loaded) open circuit potential of the construct and provided a low baseline current from which to measure fretting currents. It also fixes the conditions (potential) for oxide repassivation so that comparisons between designs can be made. Cyclic compression loads were applied for 3 minutes each, at a rate of 3 Hz ( $R = 0.1$ ), starting at 100 N maximum cyclic compressive load, incremented up to 1000 N in increments of 100 N, and then up to 4000 N in increments of 200 N. This loading protocol was applied using the Instron WaveMatrix<sup>TM</sup> program, which also recorded the servohydraulic test frame displacements and fretting currents generated throughout the test. DVRT-based micromotion of the tapers was not possible in this test set up due to space limitations in the test fixture within the environmental chamber.

Importantly, between each increment in cyclic load there was a short (10 s) pause where no cyclic loading was applied prior to moving to the next cyclic load magnitude. This pause allowed for a short period where the currents resulting from the fretting corrosion processes could recover prior to the next increment in load being applied. Current, load and displacements were also captured 6 times at each cyclic load level using 1 second of data capture at 200 pts per second. This allowed for detailed cyclic load-displacement-current versus time data to be observed and analyzed. Average fretting currents at each cyclic load were determined by calculating average currents at that cyclic load, and then subtracting the baseline current measured just prior to the start of that loading cycle. This calculated current value reflects only the currents arising due to the fretting motion,

which is indicative of fretting corrosion at that load level. From these data the cyclic load at onset of fretting corrosion was determined as the cyclic load where fretting currents began to rise above the baseline corrosion currents. In addition, the average fretting corrosion currents at 3600 N were used as a comparative measure of fretting corrosion between groups.

Following the ICFC test, another push-out test was performed to measure the minimum force required to separate the shell and liner after cyclic loading up to 4000 N.

#### *5.3.5 Post-test characterization:*

Taper surfaces were observed in a digital optical microscope (DOM) (Hirox Co. Ltd., Hackensack NJ) after disengagement, after Stage I and II. Shell and liner taper surfaces were also observed in a scanning electron microscope (SEM) (Hitachi S-3700N) to closely examine evidence of fretting post-ICFC. Energy Dispersive X-ray Spectrometry (EDS) (Oxford Instruments, AZTech) was carried out as required to confirm the elemental composition of the surface features. Data collected included the displacement and load applied during seating, the displacement throughout the test as well as currents generated during the ICFC tests, and the push-out force required to separate the shell and liner.

#### *5.3.6 Statistical comparisons:*

Statistical analysis of the resulting data was performed parametrically, using one-way ANOVA to test for statistical significance between groups with post-hoc Tukey's analysis of means. Student's t-tests were used to determine differences in means within

groups between measurements made at the two DVRTs (displacement, seating energy, push-out load). The level of significance was set at  $p < 0.05$  for all statistical determinations.

## 5.4 RESULTS:

### 5.4.1 Stage I: Seating and Pushout:

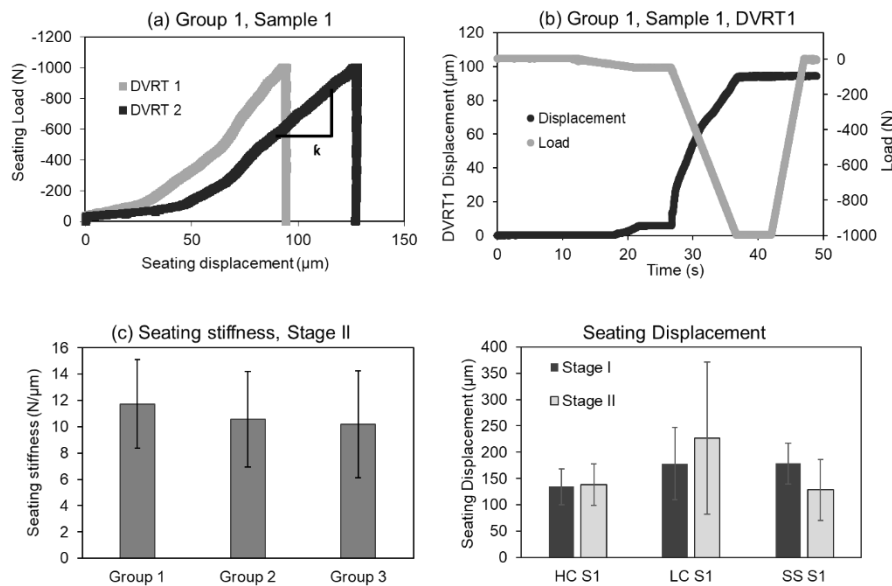


Figure 5: Representative plots of (a) seating load (N) vs seating displacement ( $\mu\text{m}$ ) (b) seating displacement ( $\mu\text{m}$ ) and seating load (N) vs time for DVRT1 data. Note the correlation between applied load and measured displacement. (c) Seating stiffness ( $\text{N}/\mu\text{m}$ ),  $k$ , across all three groups shows no significant difference with material combination ( $p > 0.05$ ,  $n = 5$ ). (d) Summary of the average seating displacement for each group.

Figure 5a shows representative plots of the seating load-displacement data of a single construct, at the first seating recorded from two separate DVRT's. From these graphs, we can calculate seating displacement at each DVRT location. The same plot can be used to calculate taper seating stiffness (slope of the loading curve,  $k$ , at the upper load level) and



the seating energy (area under the curve, SE). Figure 5b is a raw data graph of seating load and seating displacement plotted against time. It shows that applied seating load results in liner-shell relative displacement which can be measured at each DVRT independently.

The seating stiffness,  $k$ , is calculated as the slope of the load-displacement plot at the 1000 N level, as shown in Figure 5a. Taper seating stiffness was compared across all three groups with average seating stiffness in the range of 10 to 12 N/ $\mu\text{m}$ . No statistically significant difference was found ( $p>0.05$ ) (Figure 5c).

Seating displacement is also measured during the seating test as the maximum displacement recorded by each DVRT at the end of unloading. Average seating displacement ranged between 134-178.5  $\mu\text{m}$  for Stage I seating, and between 138-226  $\mu\text{m}$  for Stage II seating. Seating displacement did not differ significantly across groups within Stage I or Stage II seating ( $p>0.05$ ), nor did the Stage I and II seating displacement measurements differ from each other ( $p>0.05$ ) (Figure 5d).

Seating energies were calculated as the area under the seating load vs displacement curve, or the area integral of the load-displacement plot. Seating energies across groups both in Stage I and II seating were in the range of 0.024 J to 0.187 J and were not significantly different across groups (data not shown).

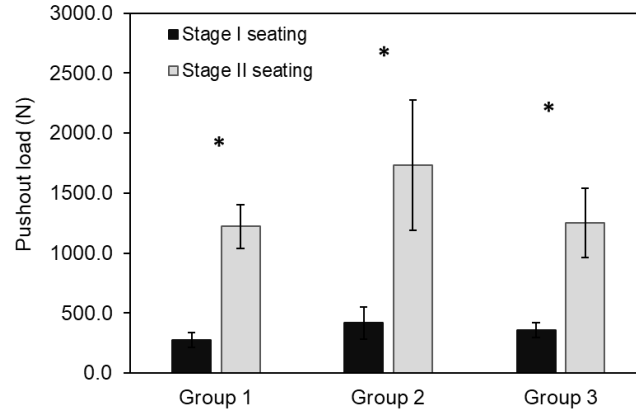


Figure 6: Average push-out load, for Stage I and II testing. No significant difference across groups ( $p > 0.05$ ,  $n = 5$ ). The asterisk denotes statistically significant difference between Stage I & II push-out loads ( $p < 0.05$ ).

Push-out loads (Figure 6) across all three material combinations in both Stage I and Stage II testing were not significantly different across the materials tested. There were significantly increased loads to push-out after ICFC testing compared to the 1000 N immediate push-out test. This implies that cyclic testing of the interface continued to seat the taper constructs, raising the locking strength. Push-out loads were calculated to be between 27-41% of the maximum seating load (1000 N) for Stage I, and between 30-43% of the maximum compressive load applied (4000 N) for Stage II.

### 5.4.2 Stage II: ICFC and Push-out:

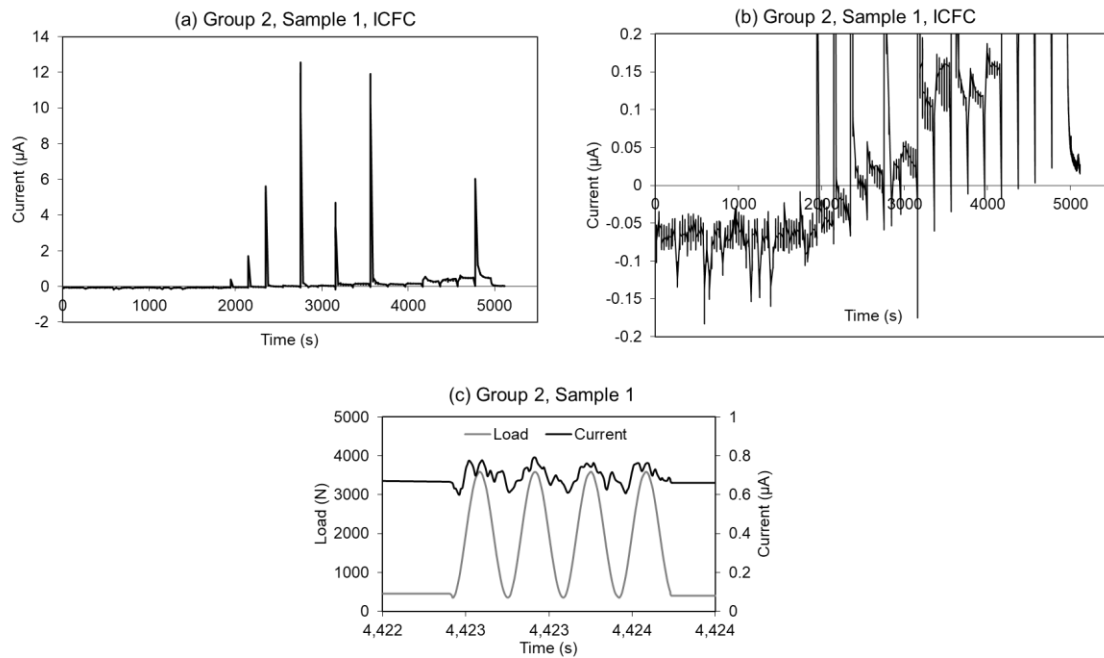


Figure 7: Plots showing raw data for (a) raw fretting current data in its entirety showing high current transients (b) fretting current ( $\mu\text{A}$ ) over the entire test duration with the vertical axis expanded to show the fretting current response, and (c) fretting current ( $\mu\text{A}$ ) and load applied (N) over 1 second, for Group 1, Sample 1, Stage I seating. Each upward spike in (a) denotes the start of a fretting cycle with a large current transient and quick recovery soon after. The more steady-state current measurements can be seen in (b). Note the correlation of current over time with the loading and unloading cycles, indicating a biphasic relationship between current and load applied.

Figures 7a & b show representative plots of the raw current data versus time captured during one entire ICFC test. Figure 7a shows the entirety of the captured current data with high transients at the beginning of some load cycles. These peak transient currents could rise to as high as  $73 \mu\text{A}$ , but they also rapidly decreased to lower cyclic currents.

Figure 7b shows the same data without the transients to show the nuances of the current

behavior. The baseline current remained approximately constant (around  $-0.06 \mu\text{A}$ ) until about 1900 s where current spikes and a rise in the average current were observed. This is the point of onset of the fretting corrosion response. Additional spikes off the top of the plot were periodically observed corresponding to the start-up of the next increment in cyclic loading. The fretting current oscillated and was synchronized to the applied cyclic load (Figure 7c). The current baseline (initial current prior to start of the ICFC test) seemed to rise over the course of the ICFC test, in some cases. Average fretting corrosion currents vs peak cyclic load for each sample tested shows that currents did not always rise with increasing cyclic loading implying that little to no fretting corrosion was taking place in some samples.

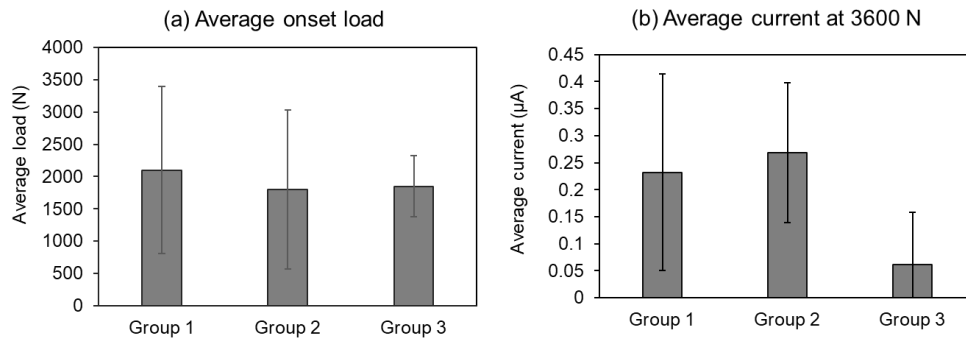


Figure 8: (a) Average onset load (N) for each material group. (b) Average current at 3600 N across all three groups tested ( $n = 5$ ). There were no statistically significant differences between groups seen.

Onset load is defined as the load at which fretting corrosion behavior is initiated, where a clear and continuous rise is seen in the recorded current. The three groups tested did not show significantly different onset loads (Figure 8a). Overall, onset loads were in the range of 1000 to 2000 N, indicating a resistance to fretting corrosion. In some cases,

fretting corrosion did not initiate at all resulting in an onset load of 4000 N. Average fretting currents measured at 3600 N were relatively low in the range of 0.05  $\mu\text{A}$  to 0.28  $\mu\text{A}$ , excluding the high initial transients sometimes observed in the start-up. There were no significant differences in fretting currents across all three groups ( $p = 0.082$ ) (Figure 8b). The average currents showed variation within each group indicating that some were not fretting while others had some, albeit low, fretting currents.

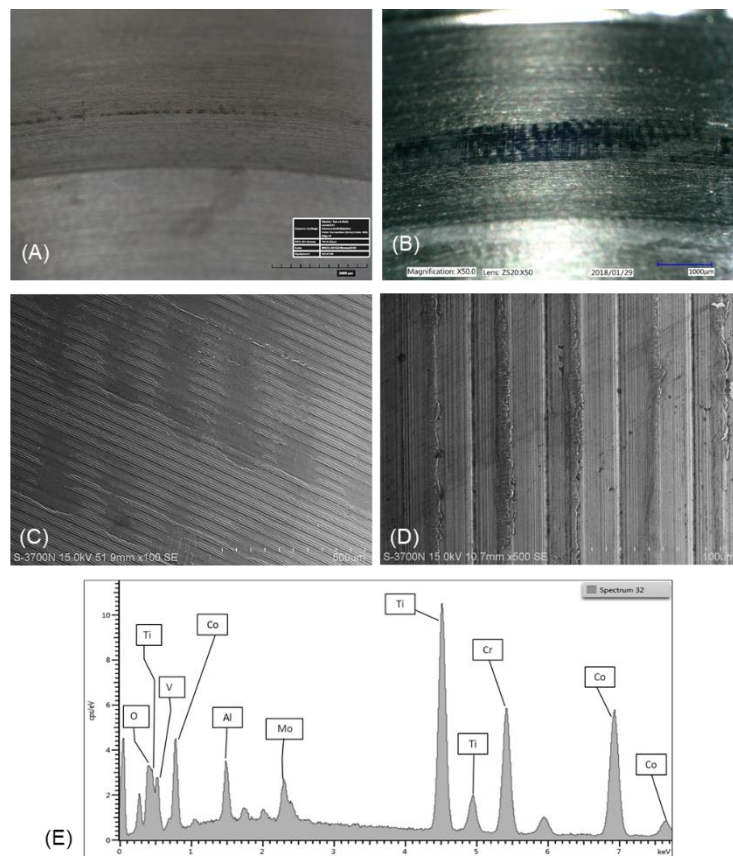


Figure 9: Digital optical microscopy (DOM) images of Ti shell taper for Group 2 (LC-CoCrMo) (a) pre-ICFC, (b) post-ICFC showing further scarring after ICFC testing. Scanning electron microscopy (SEM) images of the same sample (c) shell and (d) liner after ICFC testing showing deformation of the machining lines but limited corrosion damage (e) EDS spectrum for the region marked in white on 9d. Notice the titanium peaks on the CoCrMo surface.

Figures 9a & b are digital optical micrographs of the shell taper surfaces showing that simply seating and disengaging the modular acetabular taper can cause some mechanical damage (Figure 9a), which is then exacerbated by the cyclic loading during ICFC (Figure 9b). The scarring on the shell was more extensive than the liner, although both components, across all tested samples did not exhibit severe damage due to fretting corrosion. This was confirmed by observing select samples under the SEM after cyclic testing (Figures 9c & d) which shows intact machining lines, and minimal plastic deformation. In cases where there was plastic deformation and/or material transfer, it was restricted to the machining ridges on the liner surface. EDS was used to confirm the presence of titanium, aluminum, and vanadium, perhaps in the form of oxides, on the CoCrMo and 316LSS liners (Figure 9e).

## 5.5 DISCUSSION:

This study describes test methods designed to evaluate metal-on-metal acetabular shell-liner taper junctions during seating, and the acute fretting corrosion behavior of the same taper during incremental cyclic compressive loading. The acetabular MoM junction between the shell and liner has not been previously studied in this quantitative manner, and there is no description of the seating mechanics of the liner within the shell.

This work shows that the method described can capture the onset conditions for fretting corrosion of acetabular tapers and measure the magnitude of the fretting currents observed, which can serve as a comparative measure of fretting corrosion performance. In addition, the seating mechanics tests describe the load-displacement behavior during

quasistatic seating of these taper locking systems, which can also be used for comparative quantitative assessment of different materials and designs.

Using these new test methods, the role, if any, of the different materials used for the acetabular liners was assessed in terms of the fretting corrosion performance. No significant differences were seen between low and high carbon CoCrMo alloys or 316L stainless steel. Fretting currents at specific loads, and the onset loads for fretting corrosion were not significantly different implying these alloy differences are not significant in response to fretting corrosion.

Seating mechanics and push-out testing in conjunction with incremental cyclic fretting corrosion methods helps to assess the interplay between the seating conditions, fretting corrosion response and the forces needed to disengage components. This work showed, for example, that the push out loads significantly increased as a result of the incremental cyclic fretting corrosion testing which increased the seating/locking of the liner in the shell. It is unlikely that material transfer contributed to this increase since the number of cycles of loading was relatively low and the extent of damage observed was minimal.

The seating mechanics test measured seating displacement, seating stiffness and seating energy calculated using the load-displacement plots. There was no significant difference in the seating displacement measured across the three material combinations studied here, which can be explained by the similarity in modulus of 316L stainless steel to CoCrMo alloy [96], [97], which were the liner materials, as well as the coefficient of friction between Ti-6Al-4V and these alloys [98], [99]. The displacement measured at each

DVRT in a single test was found to be non-uniform, which was the case with most of the constructs, with both Stage I & II seating tests. This can be attributed to the non-uniform nature of the initial taper contact or due to misalignment of the liner with respect to the shell at the start of seating, in certain cases. The high variance within groups is indicative of the individual nature of taper asperity contact, which led to differences in subsidence.

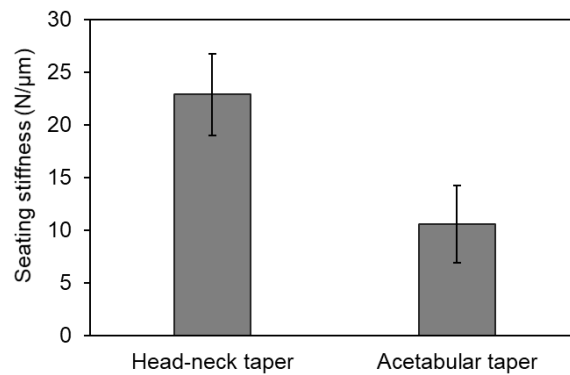


Figure 10: Seating stiffness ( $\text{N}/\mu\text{m}$ ) of head-neck taper (head-neck data from Ouellette et al, 2017, [15]) vs acetabular taper, with material combination and seating protocol remaining the same ( $n = 5$ )

Seating stiffness,  $k$ , which is the slope of the loading curve in the load-displacement plot, is a useful metric to show that the acetabular MoM junction varies quantifiably from the head-neck MoM taper junction with the same material combination. Comparing the  $k$  value of all acetabular tapers from this study with the  $k$  values of 9-10 head-neck tapers from the seating mechanics study by Ouellette et al [48], shows that the head-neck taper ( $22.85 \pm 3.88 \text{ N}/\mu\text{m}$ ) is twice as stiff as the acetabular taper ( $10.57 \pm 3.64 \text{ N}/\mu\text{m}$ ), material combination remaining uniform (Figure 10).



Two major differences are present between these two tapers. First, there is the taper angle, which for the head-neck taper is approximately 5 degrees 40 minutes and for the acetabular taper is around 8 degrees. The taper angle for the acetabular taper is nearly twice as large as the head-neck taper angle and might influence the overall seating mechanics of the acetabular taper. Second, the overall diameter and geometry of the two tapers differ. While there is a significant difference in the total nominal area of contact between head-neck and acetabular tapers, with acetabular tapers having a much larger area (e.g., 450 mm<sup>2</sup> for head-neck tapers and about 2100 mm<sup>2</sup> for acetabular tapers), this has no effect on the true area of contact or the fretted area of contact. This latter value is not dictated by the nominal geometry, but rather by the hardness of the alloys and the forces used to assemble the taper and is only a fraction (about 1%) of the nominal area. This is true because of the asperity nature of the surface and the fact that it is only at the highest asperities where true contact occurs.

The geometric effects on compliance can arise from the macroscopic geometry and/or the local surface topography. High stiffness is anticipated to occur with the smaller-radius 9/10 or 12/14 tapers compared to the acetabular tapers based on factors like the radius of the taper (smaller is stiffer), and the geometry of the constructs (ring-like for acetabular tapers versus conical for head-neck tapers). It is possible that lower stiffness can lead to better engagement and might be a way to mitigate micromotion at the taper interface. Lower seating stiffness results in larger seating displacements for the same seating load. If small subsidence motions occur, the more compliant interface will see a smaller drop in locking pressure than high stiffness interfaces. This effect introduces better tolerance

for interfacial micromotion, and therefore possibly limits oxide abrasion, mitigating fretting corrosion.

The push-out load measured at both stages, once just after seating and once after seating and ICFC test, denote the engagement strength between the shell and liner. Push-out loads were found to be between 27-41 % of the seating load for seating followed by push-out. After ICFC testing, the push-out load was found to be between 30-43% of the maximum load applied i.e. 4000 N, significantly higher than the immediately post-seated pushout results. The three material combinations did not experience significantly different push-out loads ( $p > 0.05$ ) implying that the material combination did not influence engagement strength at the acetabular taper, which can again be attributed to the similar moduli [96], [97] and friction [98], [99] of the liner materials.

Fretting currents were generated under potentiostatic conditions (-50 mV vs Ag/AgCl) by the application of cyclic compression during the short-term ICFC test. Currents remained low after initial transients at the start of arbitrary loading cycles in some samples.

However, these high transients subsided rapidly (within a few cycles of load), and subsequent currents remained low. The average fretting currents measured in these tests were well below those typically seen in head-neck taper junctions under similar solution and potential conditions [47], [48] implying that these tapers are more resistant to fretting corrosion processes than head-neck tapers.

The fretting corrosion behavior did not remain deleteriously high across all three groups, as seen from the average fretting currents measured for each sample. The interspersed

transients can be explained by intermittent shell-liner subsidence at the beginning of a new loading cycle, where overall subsidence of the liner in the shell causes relative motion at the interface and brings new regions into contact. It is important to remember that movement at the shell-liner taper is not limited to vertical subsidence but might include canting to one side or even twisting of the liner within the shell. However, once the abrasion and repassivation from this contact is complete, fretting damage does not propagate further, as seen in the post-test imaging for shells and liners both. Further study of the associated micromotions at the shell-liner interface is needed, which can then be analyzed in relation to the fretting corrosion behavior.

The baseline current which is the current measured prior to any load application, was not completely stable during the test but may have drifted either positively or negatively with time. The fretting currents reported here are measured relative to this baseline and therefore removes the net anodic or cathodic reactions ongoing that are not associated with the fretting corrosion process. In addition, the repassivation currents are known to be potential dependent and by fixing the potential at -50 mV vs Ag/AgCl results in a consistent potentiostatic condition to make quantitative comparisons between designs and materials. No significant differences were found in average fretting current between the three groups.

The onset load was more clearly defined as the point where the currents increased above this baseline. In some samples, onset did not occur at all, which means the baseline current remained more or less consistent and the current response was not cyclic nor in sync with the loading. Onset loads were also not significantly different across three

groups, with high variance within groups, which implies a greater dependence on individual asperity contact occurring in each sample rather than on the material itself. This behavior was not particular to any material combination.

MACC in modular tapers is a function of the oxide abrasion and repassivation events occurring at various contact points in the entire taper surface. Seating mechanics, engagement strength as well as the fretting current generation can be described as a function of this contact. Similar dependence is seen in head-neck tapers, wherein the fretting corrosion behavior depends upon the micromotion at the taper interface, as shown by Mali et al [47]. However, there are differences between the head-neck taper fretting corrosion behavior and that of the acetabular shell-liner taper. The test methods applied are similar, with quasi-static seating method used for assembly followed by a short-term incremental cyclic compression force applied to measure fretting currents. The difference arises in how severe and sustained the fretting currents are in acetabular tapers compared to the head-neck taper, the material combination remaining consistent.

Acetabular tapers tended to experience lower currents, and smaller shifts in the overall baseline current. There was no evidence in these tests of any sustained crevice corrosion processes propagating when cyclic loading ceased, implying that little to no crevice corrosion occurred.

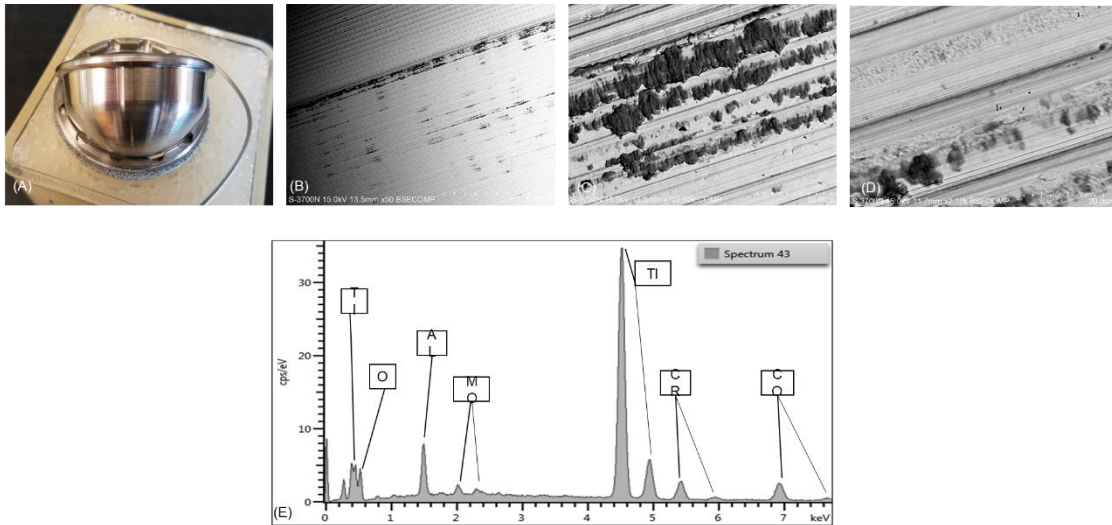


Figure 11: (a) Image showing the taper surface from sample 4, group 2 (low carbon CoCrMo) liner examined for surface damage. Note the lack of visible damage here. (b) Backscatter scanning electron micrograph of taper surface shown in 10a. Note the relatively sparse dark regions indicative of contact and resulting material transfer, compared to the non-contact regions. (c) Higher magnification image of surface from 10b. (d) Fretting scars seen in the same taper engagement region. Note the small amplitude of fretting (2-5  $\mu\text{m}$ ) (e) EDS spectra of the dark material in (c) indicating the material transferred is predominantly titanium oxide.

Closer examination of the acetabular liner surface post-ICFC testing yielded some interesting observations. The surface discussed here is the taper engagement region of sample 4 from group 2, a low carbon CoCrMo liner shown in Figure 11a, which appears undamaged visually. However, as seen in Figure 11b & c, we see evidence of sparse contact over the entire engagement region. These darker contrast areas in Figure 11b are confirmed to be titanium-fretting corrosion deposits transferred from the interfacing shell, using EDS analysis (Figure 11e). Fretting scars around 2-5  $\mu\text{m}$  in length are seen in contact bands in Figure 11d, confirming that fretting in acetabular tapers is minimal. The

low abrasion rates associated with smaller fretting scars corroborate the low fretting currents recorded during the short-term ICFC test, since fretting currents generated can be directly dependent on volume of oxide abraded [98]. Importantly, the short-term test reflects an acute test condition, spanning 13,500 cycles of loading approximately. Long-term testing, perhaps a million cycles of cyclic loading, will potentially bring more areas into contact, and cause more surface damage. Currents generated over long-term tests might be more indicative of how fretting can influence taper corrosion in implanted devices.

The test methods described have several limitations. The cyclic loading regime applied to the assembled shell-liner couple does not reflect physiological conditions in terms of moments generated from frictional motion of the head within the cup, even though the setup emulated the loading profile of the physiological hip joint angle. During normal gait cycle, the hip joint undergoes rotation and torsion, generating moments and loading patterns which were not faithfully recreated in our test setup. Additionally, the electrolyte used in our electrochemical setup, PBS, does not approach the complex nature of the synovial fluid and other biological fluids that would be present *in vivo*. The role of biological conditions and local inflammatory conditions on the MACC or fretting corrosion behavior of the acetabular taper junction was not studied here.

The specific couples tested did not have their taper angular mismatch measured as this has been raised as a potential source of variability in fretting corrosion response or push out behavior. However, prior work in our group has shown that angular mismatch for

head-neck tapers has no effect on fretting corrosion or pushout behavior of head-neck tapers [45], and it is unlikely to be significant here.

These tests do not attempt to reproduce the long-term damage modes seen in retrieved acetabular tapers, but rather focus on the initial (acute) fretting corrosion response to increasing cyclic loads applied to the tapers. However, these types of acute tests are capable of distinguishing between the initial response of tapers which is an indication of the progression of fretting corrosion beyond this initial time period. Finally, the pre-seating damage to the taper surfaces may impact the fretting corrosion response in subsequently tested taper junctions. However, this damage would only have served to increase the potential for fretting corrosion in these tapers which contradicts the low fretting currents observed in these tests.

## 5.6 CONCLUSIONS:

The acetabular modular taper seating and fretting corrosion test methods presented here are a reliable way to study the seating behavior of the acetabular metal-on-metal modular junction and the acute fretting corrosion behavior. The seating mechanics of the shell-liner construct assembly can be used to understand the stochastic nature of taper contact mechanics and the fretting corrosion response measured is an excellent means of comparing differences in assembly, materials, and designs.

The results of this study showed that the fretting corrosion response of acetabular tapers did not depend on material type used for the liner. It also showed that the fretting currents

were small to non-existent in some cases except for when sudden transient current spikes arose at the start of the next higher cyclic load.

The seating mechanics of these tapers were different than head-neck tapers in that the seating stiffness was less in the acetabular tapers. These differences in seating mechanics may influence the subsequent fretting corrosion response and could be used as a tool for designing improved taper engagements.



## Chapter 6

### Measuring Acetabular Shell and Liner Taper Compliance

#### 6.1 ABSTRACT:

From the previous chapter we see that cyclic loading at the acetabular taper junction does not lead to significant fretting corrosion currents. Fretting corrosion at modular tapers is caused by interfacial micromotion which abrades the oxide film. Thus, mitigating interfacial micromotion is a vital strategy in reducing fretting corrosion. Matching the compliance of the modular components is a strategy for ensuring lower micromotion. Therefore, the goal of this study was to investigate stiffness of the ring-like taper formed at the shell and liner engagement regions of different materials and sizes. Two different sizes of shells (62 mm and 50 mm) and liners (62/50 and 50/38) were studied. The liners were of three different material types: high-carbon CoCrMo, low-carbon CoCrMo and 316L stainless steel, whereas the shells were porous-coated titanium. Compliance was tested by application of an incremental compression load at two diametrically opposite ends of the device, held between two flat, rigid plates. Results show that for HC and LC CoCrMo, the compliance of liners does not change with size, and is matched with respective size shells. 316L SS liners were compliance matched across sizes but seemed to be statistically different than the titanium shell of the same size. These findings may explain the high degree of variation in fretting currents measured in the previous study in 316L SS-paired shell-liner couples.

## 6.2 INTRODUCTION:

From the previous chapter we see that the relative micromotion at taper interfaces plays an important role in determining area of actual contact and has a bearing on tribocorrosion and wear behavior at modular tapers. Overall fretting motion and resulting corrosion is known to be influenced by the mechanics of the taper [100] and micromotion at the taper junction [47]. Previously, the idea of sticky-compliant interfaces was introduced as a means to control fretting corrosion through frictional interactions enabled micromotion control [71]. Recent work has shown that indeed, compliant interfaces can mitigate fretting currents by limiting interfacial micromotion and minimizing oxide abrasion [101]. Acetabular shell-liner couples, particularly titanium shells and metallic liners, have been shown to generate lower average fretting currents than head-neck tapers of the same design. From the previous chapter we also see that acetabular shell-liner tapers have a lower seating stiffness compared to the head-neck taper, with the same material combination. The shell-liner taper interface is geometrically a ring, whereas the head-neck taper is a cylindrical geometry. These differences influence the overall taper compliance, leading to lower micromotion. Investigating the individual compliance of each device will shed some light on why acetabular tapers are not as susceptible to fretting corrosion as head-neck tapers.

The goal of this study was to develop a test setup and method to investigate the individual component compliance. The main hypothesis is that in the acetabular shell-liner couple, the individual components have stiffness values that allow for one device to deform around the other, and thus form a strong interfacial connection, leading to improved

compliance matching. In addition, we will investigate the changes in compliance brought about by changes in size of the component. We hypothesize that changes in the diameter of individual components will not bring about significant changes in the stiffness, provided the thickness of the device or other design parameters are changed accordingly. Custom designed fixtures will be fabricated and used for measuring the change in radial displacement brought about application of a compressive load to diametrically-opposite ends of each component held vertically. The change in displacement corresponding to load application will be used to calculate component stiffness in the same way that seating stiffness was calculated in the previous chapter.

### 6.3 MATERIALS & METHODS:

#### 6.3.1 *Sample description:*

We measured the compliance of two different sizes of titanium shells (50 mm and 62 mm) and full-lipped metal liner inserts (size 50/38 and 62/50).



Figure 1: (a) Acetabular shells, 62 mm and 50 mm respectively (b) Acetabular shells, size 62/50 and 50/38 respectively. These are the CoCrMo HC liners, but the LC and SS liners were identical in design

Figure 1 shows examples of the tested components. The shells were porous-coated with sintered titanium. Barring the difference in size, the shells were identical in design. The liners were made of three different materials, 1. high-carbon CoCrMo (HC), 2. low carbon CoCrMo (LC) and 3. 316L stainless steel (SS). The larger diameter liners appeared to be thicker than the smaller components at the taper region, however it was challenging to measure the actual thickness of the component because of the full-lipped design. We compared the compliance of the liners to the shells, between the two different sizes of liners and shells, and between the three materials for the liners. We tested three devices in each group.

The taper region of the shell comprised of equidistant antirotation tabs (nominally 5 mm x 2 mm for 50 mm and 8 mm x 2 mm for 62 mm) close to the rim, with a cylindrical channel (1.5 mm wide, 2 mm deep for both shell sizes) going around the circumference directly below them, followed by a cylindrical engagement region (approximately 5 mm wide for 50 mm shell and 7 mm for 62 mm shell). The shell also has a 1 mm lip at the rim, which is formed by the porous coating sintered atop the base titanium shell. The liner taper region is comprised of a uniform cylindrical surface (nominally 8 mm wide for 50 mm shell and 10 mm for 62 mm shell), with the lower half forming the engagement region where it is in nominal contact with the shell. Both taper regions have an as-machined surface with small ridges (under 100  $\mu\text{m}$  height) present.

### 6.3.2 Method:

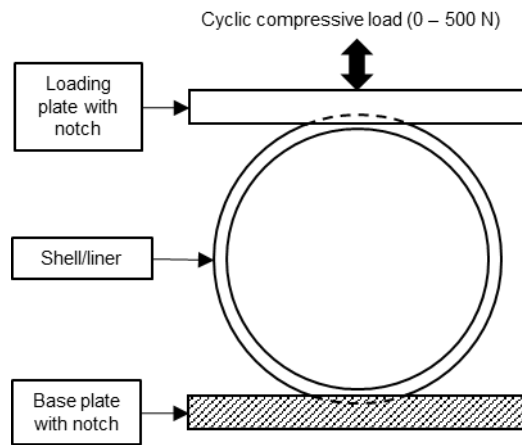


Figure 2: (a) Schematic showing the test method setup, with the dotted arcs representing the grooves cut into the plates to hold each device in place (b) Test setup with a device held in place by the plates

Custom aluminum fixtures were designed for this study, to act as flat plates between which each component could be securely held, as shown in Figure 2. The plates designed for the shells had a 1 cm wide groove machined into the inner surfaces, contoured to fit the acetabular shell circumference closely. Similarly, a notch was machined into the liner plates which was the same dimension as the lip on the liner. This allowed for the components to be held securely in the absence of a horizontal enclosure, to prevent the component from being horizontally displaced during application of compressive loads. The machined groove/notch also enabled closer contact between the plates and the actual taper surface, in the case of the liner, and closer contact with the corresponding outer region of the shell taper. Since the shell body itself is rigid, there would be direct translation of compressive forces from the test frame actuator to the inner taper region or on the corresponding outer shell surface. The upper plates were designed to have a

threaded rod that can be securely screwed into the grips of the servohydraulic test frame whereas the lower plate was simply placed on the platform of the test frame.

After assembling each component in the MTS Bionix Servohydraulic Test Frame (Model 370.02, MTS Systems, Eden Prairie MN) as shown in Figure 2, the MTS Test Suite software was used to apply the load regimen and to measure the resulting change in diameter. A preload of 100 N was applied initially to ensure a rigid system, followed by a hold of 5 seconds. Then a ramp load of up to 1000 N was applied at 10 N/s. After holding the load at maximum for 5 seconds to allow steady displacement measurement, the load was ramped down to 50 N in 10 seconds. Change in diameter was calculated as the difference between the position of the actuator at maximum load (~1000 N) and the initial position at the start of the test. The stiffness ( $k$ , N/mm) was calculated as slope of the line formed by plotting load vs displacement for each component, considering the portion between 500 N to 1000 N. Three samples were tested per group. To compare the results across all the tested groups, 2-sample t-tests were used for: shells of two different sizes, liners of two different sizes but the same material and between shell and liner pairs of the same size. One-way ANOVA with Tukey's analysis of means was used to compare stiffness and change in diameter results among the three liner materials within each size.

#### 6.4 RESULTS:

Each component was tested as per the above method. The resulting data was plotted as a load-deflection plot. Figure 3 shows a representative plot from a 62/50 HC liner.

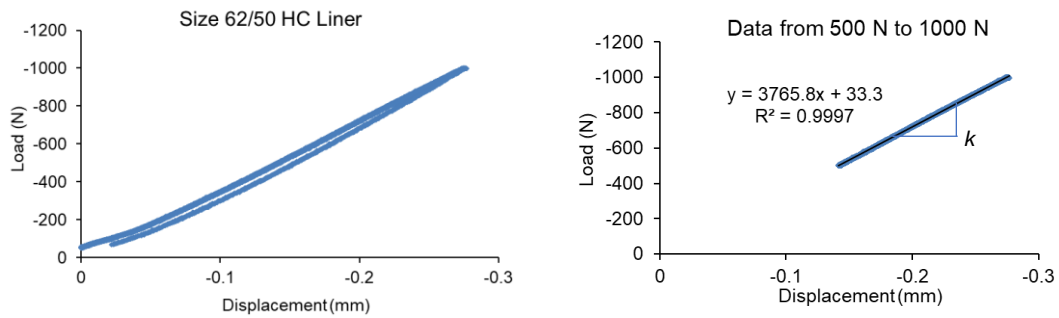


Figure 3: Representative plot showing (a) load-deflection data obtained from a single compression test on a size 62/50 HC liner. Note the short initial toe region and the constant slope beyond the toe region. (b) Data for the same test, condensed to include only those data points between 500 N to 1000 N to capture the true linear portion of the loading curve. A linear data fit provides the  $k$  value, which is the slope of the line (3765.8 N/mm in this case)

Since the compression and decompression were conducted within the elastic region, the plot does not show any hysteresis, indicating no plastic deformation. The slope of the line calculated between 500 N to 1000 N represents the stiffness of the individual taper region.

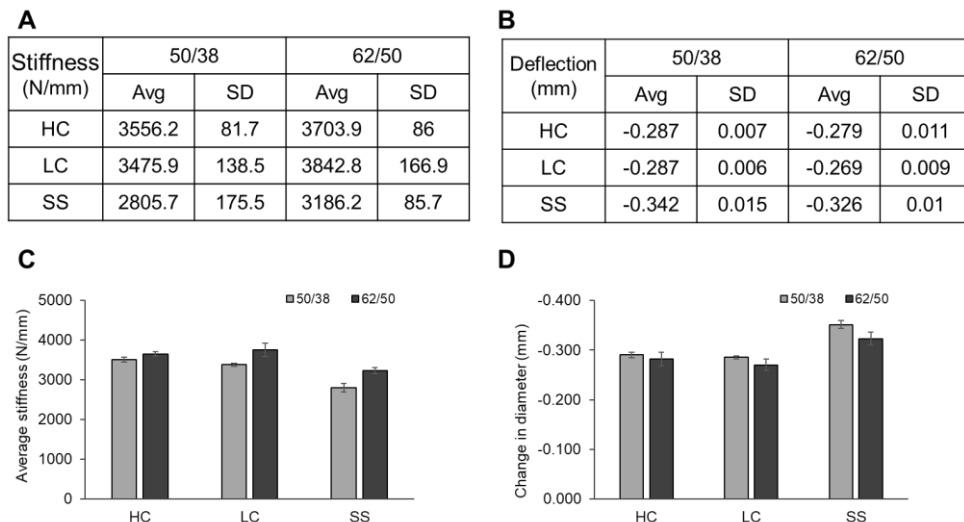


Figure 4: Summarized data for all tested liners across materials and sizes. (a) Average stiffness calculated values for all tested liners (b) Average deflection values measured for

all liners (c) Comparison of stiffness values shows significantly higher stiffness in HC and LC liners compared to SS in both sizes, and higher stiffness in larger sized liners. (d) Comparison of measured deflection shows that SS liners experienced higher elastic deformation compared to HC and LC liners. Between the two sizes, deflection was significantly different only in LC liners.

Figure 4 shows the average stiffness and change in diameter values calculated for all the liners compared across materials and size. Figure 4a shows the calculated average stiffness and standard deviation across all groups. Figure 4b shows calculated average deflection of shells and liners between materials and between sizes. Among the materials, the SS liners in each size were significantly less stiff than the HC and LC liners ( $p=0.000$ ) of the same size. When comparing the two sizes of liners, the stiffness values were not significantly different, except for the SS liners ( $p<0.05$ ). Figure 4c shows calculated change in diameter and standard deviation across all groups. Change in diameter measured in SS liners were significantly higher than that measured in the HC and LC liners, size remaining the same ( $p=0.000$ ). Among pairs of liners with same material, the change in diameter followed the stiffness statistics, where HC and LC liners did not show significant differences in the change in diameter, but the SS liners were significantly different.

Acetabular shells followed the same behavior as the liners; between the two sizes, stiffness and change in diameter were not significantly different from each other. We also compared stiffness and change in diameter of shell-liner pairs, and found that HC, LC, and SS liners were not statistically different from the shells of the same size group. The



compliance of devices seems to be matched between the shell-liner pairs, and even between different sizes except for in SS liners.

We plotted the calculated stiffness values for all groups, across three materials and two sizes, against the corresponding measured deflection. The resulting plot shows that the deflection measurements have a strong linear correlation with the stiffness calculations (Figure 6).

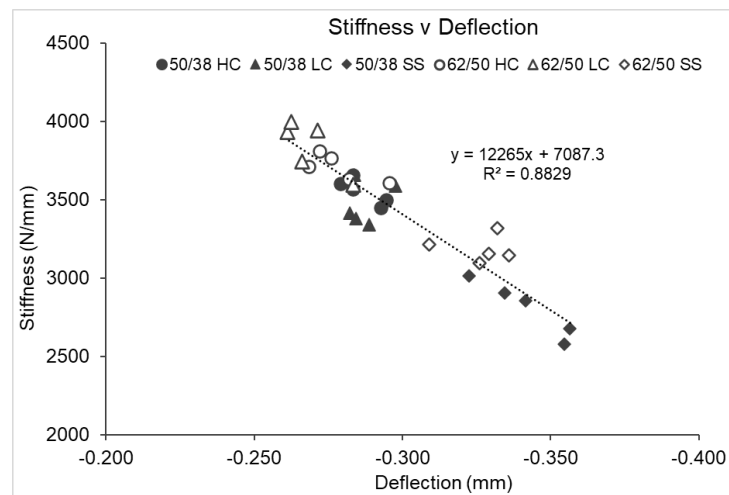


Figure 5: Stiffness-deflection plot showing the overall differences between the liners of different sizes and materials. The HC and LC CoCrMo liners are clustered towards the higher stiffness, higher deflection end of the linear fit, and SS liners are clustered towards the lower end

## 6.5 DISCUSSION:

In the 1988 study, Vingsbo and Soderberg [102] described the three regimes of tribocorrosion: stick (no interfacial motion), mixed stick-slip (partial sticking of surfaces and partial interfacial motion) and gross slip (leading to sliding wear and plastic deformation). Under the stick regime, we see minimal fretting, reduced oxide wear and therefore mitigated fretting corrosion. This is the goal, to design modular taper junctions

that have minimized interfacial motion, and therefore, minimized fretting corrosion.

Compliance plays a huge role in lowering interfacial motion, and as such, is a critical design feature for all modular devices.

Previously reported assembly and subsequent ICFC data for acetabular shell-liner junctions raised the possibility that taper geometry and stiffness influence the overall taper mechanics at the shell-liner taper junction. In order to assess differences in the taper compliance a test method was designed to determine how taper stiffness might vary with changes in size and material for individual shells and liners. The load range selected was to ensure that the stresses placed on each device did not plastically deform the device, and only compressed it in a repeatable and elastic manner.

The calculated stiffness for liners was found to vary with the material, in this case, 316L stainless steel liners were less stiff compared to both high carbon and low carbon CoCrMo liners of the same size. The modulus of 316L SS is 10% lower than that of CoCrMo, for both HC and LC CoCrMo materials, since the amount of carbides present does not have an effect on modulus of the material. Within the same materials, the larger liners (size 62/50) were not found to be stiffer or less so than the smaller (size 50/38) liners. If we think about the thin-walled ring-like taper being compressed in isolation, the hoop stress it experiences is described by

$$\sigma = \frac{Pr}{t}$$

where,  $\sigma$  is the radial stress,  $P$  is the internal pressure in response to external compressive force  $r$  is the mean radius and  $t$  is the thickness of the ring. This equation indicates that the stress experienced by the ring relies on radius and the thickness of the shell/liner taper and that these two parameters act inversely proportional to one another to balance the eventual stress experienced by the taper ring.

Nominal measurements of the taper region thickness of the liners show that the larger liners were thicker than the smaller size components. This increase in thickness could lead to a stiffer taper region and therefore, the overall stiffness of the larger diameter device matched that of the smaller one. The same results were found among the shells, and the same reasoning follows.

The resulting change in diameter was measured as another metric to compare the devices. The deflection measured within each size showed SS liners compressed to a larger degree than both the HC & LC liners, which corroborated the lower stiffness calculated for the SS liners. It was found that the similar stiffness of the larger devices translated into similar change in diameter measurements across HC, LC liners and shells. The results of 2-sample t-tests on the comparisons between shells, and HC and LC liners showed no significant differences based on the diameter of the device, which follows from the stiffness results discussed previously: equivalent stiffness leads to equivalent change in diameter in response to a compressive force.

However, this was not true for the SS liners. Comparing the size 50/38 liner with the size 48/38 liner of stainless steel material, both the stiffness and change in diameter were

statistically different, with the larger device exhibiting a higher stiffness and lower change in diameter. The dimensions of the liners and the design remained consistent with the HC and LC liners, and yet we see a statistically significant difference in response to the application of the same force regimen. We can attribute this difference to the slightly lower modulus of stainless steel compared to CoCrMo. Interestingly, there was no statistical difference in the calculated stiffness or change in diameter comparisons between the small and large shell and the SS liners of each size, respectively. This indicates a compliance matching between the shell and liners of each material. An overarching comparison (Fig. 6) shows that the shell stiffness and change in diameter values are intermediate between the HC and LC liners, and the SS liners.

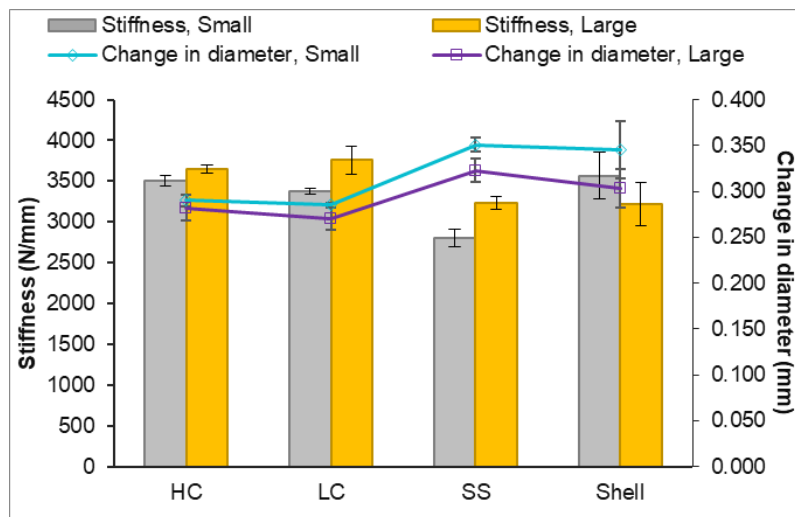


Figure 6: Average stiffness (bars) for each tested group: HC, LC, SS liners and titanium shells of small (50 mm) and large (62 mm) diameter, in combination with average change in diameter (lines) for each of the aforementioned groups

Overall, this study presents some supporting evidence for the results from the previous chapter: SS liners in combination with the titanium shells had more variance in the

fretting currents generated during short-term incremental fretting corrosion (ICFC) testing. Although the currents measured did not differ statistically among HC, LC and SS liner coupled with titanium shells, the increased variance in the SS group can be attributed to differences in compliance between the HC, LC and SS liners found in this study. Compliance mismatch is a critical predictor of eventual interfacial micromotion, and a compliance-matched interface can lead to improved taper connection strength and lesser micromotion, leading to lowered fretting corrosion due to oxide abrasion. Our hypothesis that one of either the shell or liner will be less stiff or more compliant than the other is disproved by this data, implying that the taper connection mechanics rely on more than simply interfacial pressure induced at the taper due to impaction of the liner into the shell, as has been hypothesized to be the case in head-neck tapers [48], [71].

This study, however, is not without limitations. The compression load applied to the devices was restricted to two diametrically opposite points on the taper circumference, as opposed to a circumferential compression which would be more representative of the actual pressure applied on the device during assembly and subsequent locking and loading. However, as a proof of concept, this method shows us the primary differences in compliance arising out of material selection and device dimensions including thickness and size. The shell cohort had a sintered porous coating which potentially acted as a cushion, absorbing some of the applied load before it could be translated to the underlying solid shell. This was corrected for in the design of the fixture plates, by including the groove which closely matched the porous coating and translated the load to the outer rim of the shell. In actual use, the compression on the shell would act outwards

from the inner taper surface and would mostly be concentrated on the nominal engagement region comprised of the tabs and the lower cylindrical taper. Thus, the load application in this method does not directly reflect the in vivo compressive forces that enable a secure lock between the shell and the liner. Also, due to the anisotropic nature of the cancellous bone in the acetabular region, the stress distribution is non-uniform even along the circumference of the impacted shell [103], [104]. With non-uniform stress distributions along the circumference of the shell, the compression and deformation of the shell itself is not uniform, which in turn leads to non-uniform compression of the liner being seated within the shell. Hence, our method is a simplified version of measuring compliance, whereas the in vivo conditions are far more complex. Further study of shells and liners undergoing non-uniform deformation, and a measure of interfacial compliance of assembled shell-liner couples are recommended.

## 6.6 CONCLUSIONS:

With this study, we aimed to develop a straightforward method to measure and compare radial stiffness of acetabular shell and liner devices, of two different sizes. We also compared three different liner materials (high carbon, low carbon CoCrMo and 316L stainless steel). Additionally, we wanted to ask whether application of the same compressive load on the tapers of each device generates the same change in diameter. The method we developed required minimal instrumentation, and generated repeatable tests, which were completed in under 10 minutes each. We found that stiffness for both shells, HC and LC liners did not change with size; larger devices were as stiff or as compliant as smaller ones. This was not true for SS liners, where the larger device was

stiffer (approximately 500 N/mm more) than the smaller one. The shell stiffness values were not significantly different from any of the liners, regardless of size or material. This difference between the HC and LC liners, and SS liners was reflected in the one-way ANOVA results comparing stiffness and change in diameter within each size cohort: SS liners differed significantly from HC and LC liners in both metrics. Overall, taper compliance might be a strong predictor of eventual interfacial micromotion at modular tapers, with less compliant tapers being more prone to fretting corrosion. Further investigation into taper compliance, and development of compliant tapers might present a way forward towards mitigating mechanically-assisted crevice corrosion (MACC) in modular tapers.

## Chapter 7

### **Tribocorrosion Debris and Cathodic Voltage Shifts in CoCrMo Affect Murine Macrophage Viability Outcomes in In Vitro Fretting Corrosion**

#### 7.1 ABSTRACT:

Tribocorrosion in vivo can result in similar byproducts as has been reported in in vitro tests: oxide debris, repassivating currents, cathodic potential excursions, and metal ion release. Studies have shown, independently, how each of these agonists can affect macrophage viability: debris and metal ions have a dose-dependent lethal effect, and cathodic potentials up to -1 V do not have a 100% killing effect on macrophages cultured on CoCrMo surfaces. However, no study yet has studied the consequences of ongoing fretting corrosion on macrophage viability. Thus, the goal of this study was to design a test method to systematically analyze macrophage viability changes over 24 h, both directly on the CoCrMo surface and on adjacent tissue culture plastic, resulting from fretting corrosion, both potentiostatically controlled and uncontrolled, and to compare it to external cathodic bias only. Results show that macrophages experienced the most fatality in response to potentiostatically controlled at -50 mV fretting corrosion, followed by non-potentiostatically controlled fretting corrosion where an average of -500 mV cathodic bias was induced without external application of potential. The major difference between these two conditions appeared to be the amount of debris generated over the course of the 24h fretting. In comparison, macrophages remained around 80% viable in the presence of an externally applied cathodic bias of -500 mV, implying that cell



mortality is a function of oxide debris and accumulated current density over time as opposed to just cathodic bias application.

## 7.2 INTRODUCTION:

Chapter 2 showed that implanted CoCrMo acetabular liners can experience corrosion-related damage independent of mechanically-assisted corrosion processes, including fretting corrosion. Chapter 4 of this thesis demonstrated that in the absence of proteins or inflammatory species in the solution in in vitro conditions, fretting corrosion by itself does not lead to significant damage in CoCrMo-Ti6Al4V acetabular couples, and resulting fretting currents in these tapers remained under 1  $\mu$ A. In this chapter, we investigate fretting corrosion of the CoCrMo alloy in the presence of proteins and effects on macrophage viability.

Mechanically-associated crevice corrosion (MACC), including fretting corrosion, has been widely investigated as a cause for corrosion related damage and device failure in orthopedic implants. Fretting corrosion in particular results from repetitive interfacial micromotion between at least a metallic surface and an opposing hard surface, which can also be metallic, with a sliding magnitude under 100  $\mu$ m. This repetitive fretting motion can cause oxide fracture due to abrasion, leading to release of oxide particles and metal particles, especially if wear occurs simultaneously. Passivating oxide film removal then leads to an instantaneous rise in repassivation oxidation reactions at the metal surface, which create excess electrons within the metal, initiating a cathodic excursion in surface potential [105]. Viswanathan & Gilbert [106] showed that this potential drop in CoCrMo-CoCrMo pairs can reach -0.8 V, in vitro. This instantaneous process is also associated with a repassivating current, which can lead to release of metal ions into solution. These processes can, and do, occur in in vivo environments. The byproducts of fretting

corrosion can thus interact with the biological environment, including macrophages, and have been found to be associated with adverse effects.

Oxide debris, metal ions and metal particles being released from the metal surface act as instigators that modulate phenotypic changes and proinflammatory behavior in macrophages and osteoclasts in vitro [107]–[110]. Previous studies have amply demonstrated the adverse reactions associated with fretting corrosion byproducts from metallic implants in particular, the clinical manifestations of which include osteolysis, pseudotumor, necrosis and ALVAL [21], [62], [111], [112].

Hui et al. have shown that preosteoblasts experience increased cell mortality in the presence of ongoing fretting corrosion of Ti6Al4V [113]. However, no such study has been conducted with CoCrMo alloy, especially with macrophages, which are a critical component of the innate immune system and a well-established part of the wound healing cascade. Cathodic biases applied externally have also been shown to have a fatal effect on preosteoblasts and macrophage cell lines before [114]–[116] on both titanium and CoCrMo surfaces. Wiegand and Gilbert recently showed that U937 cells (a macrophage-like immortalized cell line), cultured on polarized CoCrMo alloy surfaces exhibited cell killing under cathodic potentials, this effect was significantly diminished relative to MC3T3 preosteoblast-like cells such that U937 cells could withstand more severe cathodic potentials with less killing and that these cells were almost fully viable at 24 h to potentials as low as -500 mV [14]. However, a direct link between cathodic bias generated by fretting corrosion of CoCrMo and macrophage mortality has not been

demonstrated especially when the potentials resulting from tribocorrosion do not fall below -500 mV.

Thus, the goal of this study is to design a test method that exposes macrophage cells to ongoing fretting corrosion in vitro. We hypothesize that macrophages will experience loss in viability due to fretting corrosion byproducts, primarily. Exposure to cathodic bias applied externally will not affect cell viability dramatically, since macrophages exhibit protective mechanisms for minimizing oxidative stress, such as expressing glutathione that acts as an antioxidant and quenches ROS generated through corrosion of CoCrMo [116].

### 7.3 MATERIALS & METHODS:

#### 7.3.1 *Sample description:*

Wrought CoCrMo alloy disks (25 mm diameter) were used as the substrate in this study, coupled with CoCrMo conical pins with 1.8 mm<sup>2</sup> nominal contact surface area, although the true contact area depends on the normal load applied and the asperity-asperity contact depending on surface topography and hardness. Each disk and pin contact surface was systematically wet-polished using 240-600 grit emery paper, and up to a mirror finish using 1 μm alumina suspension. The disks and pins were individually sonicated in an ultrasonic water bath at room temperature in a 50% EtOH solution in DI water for 10 minutes. After air drying, a modified petri dish was adhered to the polished disk surface using a peelable, waterproof, silicone based sealant, while the pin body, from the edge of the contact surface to the conical surface and up to 1 cm beyond that, was coated in nail

polish to electrically isolate the tip. The petri dish (35 mm diameter, CellTreat product line) was equipped with a circular opening by drilling a 0.18 cm<sup>2</sup> hole in the base. This would allow for cells to be cultured within the same petri dish container, but on two separate substrates: the metal disk and the petri dish. The silicone sealant was carefully applied to ensure a water-tight seal along the circular edge and allowed to air dry for up to 24 hours. An electric wire was adhered to the base of the disk to facilitate electrical connectivity. The disk-petri dish couple and the pin were then UV sterilized for 24-48 hours prior to use in the experiments.

### 7.3.2 *Cell culture and testing matrix:*

RAW 264.7 murine macrophage cells obtained from ATCC (TIB-71) were used for this study. Cultures were maintained in Dulbecco's Modified Eagle's Medium (DMEM, D5671, Sigma Aldrich, St. Louis MO) with 4mM l-glutamine, 1mM sodium pyruvate, 4500 g/mol glucose, 10% heat-inactivated fetal bovine serum (FBS, Gibco) and 1% penicillin-streptomycin-glutamine (PSG, Corning, Manassas VA) in T-75 flasks (Corning, Manassas VA). Cells were passaged up to 10 times; this cell line shows phenotypic and functional stability up to 30 passages [117]. For the experiment, 2 million cells were plated onto the disk-petri dish couple, taking care to ensure confluence on the metal surface. Cells were incubated for 24 hours, in 2 mL complete culture media, before the disk-petri dish couple was integrated into a custom-designed pin-on-disk fretting test assembly for experiments. 1 mL media was added prior to starting experiments to

ensure even coverage of all electrodes in the petri dish.

Group	Potentiostatic Control or OCP	Fretting?
Group 1, “-50 mV + fretting”	-50 mV vs Ag/AgCl reference	Yes
Group 2, “OCP + fretting”	OCP, no potentiostatic control	Yes
Group 3, “OCP + no fretting”	OCP, no potentiostatic control	No
Group 4, “-500 mV + no fretting”	-500 mV vs Ag/AgCl reference	No

Table I: Test matrix applied for this study showing different electrochemical conditions and inclusion or exclusion of fretting motion

All experiments were conducted over 24 hours, and cell viability and morphology were investigated at the end of the 24 hour period. We devised the following test matrix to study 4 different conditions, each group tested in triplicate: 1. under -50 mV potentiostatic hold and 1 Hz fretting, 2. under no applied potential (freely changing OCP) and 1 Hz fretting, 3. no applied potential (OCP) and no fretting, and 4. an applied potential equal to the minimum recorded potential from condition 2 and no fretting. These conditions were chosen to distinguish between cell viability outcomes due to fretting corrosion processes and byproducts versus those caused by cathodic excursions, both externally applied and induced by fretting corrosion. Groups 3 and 4 are included as controls to establish viability baselines in the absence of fretting corrosion.

### 7.3.3 Pin-on-disk fretting test

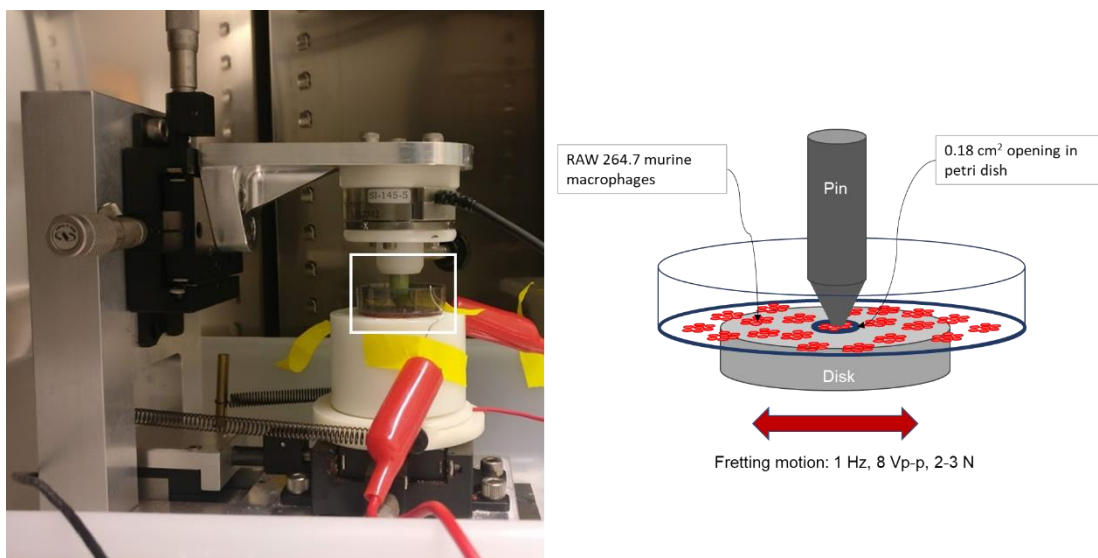


Figure 1: Photograph showing the custom-designed pin-on-disk system. A 6-axis load cell is used to apply a normal load of 2-3 N between the pin and the disk, and also measure loads along X, Y and Z axes. A piezo-actuator modulated stage applies the sliding motion to the sample holder into which the disk-petri dish construct is set. Schematic illustrates the pin-disk-petri dish set up with cells. Fretting motion was applied to the disk at 1 Hz, with sliding distance up to 100  $\mu\text{m}$ , while the pin remains stationary. Detailed description can be found in Liu et al. [118].

A custom-designed pin-on-disk test system was used for this experiment (Fig. 1). Detailed description of this system is included in a recent publication [118]. A three-electrode electrochemical cell was used for the fretting corrosion experiment; the exposed area on the disk-pin couple formed the working electrode, a platinum wire was used as counter and a chloride silver wire was used as a reference. The reference electrode was checked against a pristine Ag/AgCl (in 4 M sat. KCl) electrode to ensure stability and consistency. A potentiostat (Versastat 4, Princeton Applied Research, Oak Ridge TN) in conjunction with the VersaStudio software was used to apply and measure any potentials

or currents within the electrochemical cell. The entire pin-on-disk system was placed inside a CO<sub>2</sub> incubator under 37°C, 5% CO<sub>2</sub> and high humidity to simulate physiological conditions and to maintain the cells cultured on the working electrode surface.

The fretting motion was created using a 1 Hz waveform output from a function generator, resulting in a back-and-forth 100 μm magnitude sliding motion per second. This was passed through an amplifier to a piezoelectric actuator and delivered to an X-Y stage that held the sample holder. Thus, the disk was moved back and forth, creating the fretting motion at the pin-disk interface. The maximum normal load applied at the pin-disk junction was 3 N, through a 6-axis load cell (ATI Industrial Automation, Apex NC) fitted with a micrometer gauge for vertical translation of the pin. The 1 Hz frequency, 100 μm sliding motion and 3 N normal load was selected to ensure a full slip regime (based on the Vingsbo-Soderberg fretting regimes [102]) at the pin-disk interface.

In test groups 1 and 2, where fretting motion was applied, the pin and disk were both held under immersion, but without any physical contact at open circuit potential (OCP) for 600 s to allow equilibration of the resting potential and currents on the surface. The pin and disk were brought into contact, to a maximum load of 3 N. At 600 s, for test group 1, a potentiostatic hold of -50 mV was applied for another 600 s before the fretting motion commenced. For group 2, no external potential was applied, and fretting motion was started at 600 s. For group 3, no potential was applied, nor was fretting motion induced, and for group 4, a potentiostatic hold of -500 mV was applied at 600 s without any fretting motion. In groups 1 and 2, fretting currents were recorded for the duration of the test. Fretting currents were calculated as the average current generated during fretting,



minus the average baseline current recorded just prior to start of fretting [98]. Using LabVIEW (National Instruments) we monitored the mechanical parameters of normal load and forces along X, Y and Z axes using the load cell, to track the progression of pin-disk contact. The mechanics of pin-disk contact and its association with interfacial friction and fretting currents is fairly well described in literature [98], [101], [106], [118], so those analyses were not included in this study. After 24 hours of fretting, the system was allowed to recover, characterized by the raised currents dropping to baseline, first at the potentiostatic hold of -50 mV, and then at OCP. In groups 3 & 4, currents and surface potentials were monitored throughout the experimental runtime and no external mechanical input was added. Average current density was calculated by normalizing each average measured current value by normalizing for the twice the fretting contact area to account for pin and disk surfaces, or the 0.18 cm<sup>2</sup> exposed area for non-fretting conditions.

#### 7.3.4 *Cell viability assay*

Cell viability was determined using a live/dead cytotoxicity kit for mammalian cells (L-3224, Invitrogen, Oregon) containing calcein AM and ethidium homodimer-1 (EthD-1). In every group, at the end of 24 hours of experimentation, the test media was extracted, and the surface was rinsed with 1X phosphate-buffered saline (PBS) at room temperature. 3 mL of PBS containing 4 μM EthD-1 and 3.33 μM of calcein AM was added to the petri dish. Concentrations were chosen based off a previous study conducted within our group using a similar cell type [116]. The cells were allowed to incubate for 30 minutes at room temperature, under aluminum foil inside a dark biosafety cabinet to prevent

photobleaching. At the end of 30 minutes, enough PBS to fill the dish to the brim was added and the lid was closed. The disk-petri dish construct was then inverted onto the stage of an inverted fluorescence microscope (Leica DFC 340 FX, Leica, Germany). A CCD mono 12-bit camera (Q-imaging, Canada) and an X-cite 120 light source (EXFO America, TX) was used to capture images. Using LAS-X software (Leica, Germany), minimum of five images per region were recorded at 10x-20x magnification, using fluorescein bandpass filter (FITC) and Texas red dye filters for live and dead cells, respectively. Live cells were labeled with the green-flourescing calcein AM due to acetoxymethyl ester bond hydrolysis, whereas the dead cells are stained red from the EthD-1 which binds to fragmented DNA within the cells. Images were captured at three separate regions: disk, petri dish adjacent to the disk, petri dish periphery (Fig. 2). This demarcation was used to assess any changes in cell viability arising from proximity to the fretting site.

### 7.3.5 Cell count and size calculations

Using the images obtained from live/dead fluorescent imaging, the average cell size of both live and dead cells was determined using ImageJ (NIH). Each image, live and dead,

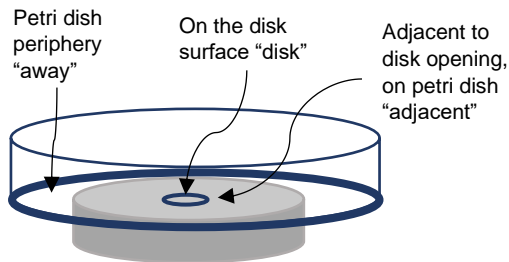


Figure 2: Locations where live/dead fluorescent images were captured

was loaded onto ImageJ. The image was converted to 8-bit, if it was not already 8-bit type, then inverted to flip the background and foreground colors. After thresholding, the image to clearly demarcate cellular bodies from debris and background fluorescence,

the image was converted to binary, then the ‘fill holes’ and ‘watershed’ utilities within ImageJ were applied to further isolate individual cells from clusters. The scale was set (1.22 pixels/ $\mu\text{m}$  for 20x images; 0.57 pixels/ $\mu\text{m}$  for 10x images) and the analyze particles utility was used to measure individual projected cell areas and to count the number of cells within the field. The parameters were set to include only those features which show circularity between 0.3 to 1.00. The average cell count and size with standard deviation was calculated from the results obtained.

#### 7.3.6 *Cell morphology and debris characterization*

After live/dead staining and imaging, the cells were fixed using 2 mL of 4% paraformaldehyde solution at  $-4^{\circ}\text{C}$  for 2 hours. Then the cells were dehydrated at room temperature in graded EtOH (50%, 75%, 90%, 100%) for 15 minutes each, followed by overnight freeze-drying at  $-20^{\circ}\text{C}$ . The surface was then sputter coated with gold for 60 seconds under 50 mTorr vacuum (Model Desk II, Denton Vacuum, NJ). Each sample was imaged in a scanning electron microscope (SEM, Model S-3700N, Hitachi High-Technologies, Schaumburg IL). Images were taken at 4-10 keV accelerating voltage at 500x up to 1500x magnification, using both backscattered and secondary electron modes to visualize fretting corrosion debris and cells. The micrographs were used to calculate fretting contact area and area covered by debris immediately surrounding the fretting contact area. ImageJ was used to measure both areas, using the ‘measure’ function after setting the scale to match the magnification of the particular image. Elemental analysis using energy dispersive x-ray spectroscopy (EDS) was used to identify debris composition at the fretting site.

### 7.3.7 *Statistical analysis*

All cell size and viability analyses across five groups were compared using one-way ANOVA with post-hoc Tukey's analysis of means to determine if cell viability differed between groups or within a group depending on the location (disk, opening adjacent or petri dish periphery). Cell size comparisons between live and dead cells within a test condition and the same location were compared with a paired t-test.  $P=0.05$  was considered to be significant for all analyses.

## 7.4 RESULTS:

### 7.4.1 *Fretting corrosion*

Fretting motion applied at the pin-disk interface led to a distinct onset of fretting currents, as shown in Figure 3a. Correlation of sliding motion and fretting currents generated have a biphasic relationship as described by Viswanathan & Gilbert [98] (data not shown). The -50 mV potentiostatic hold allowed initial currents to remain close to zero in the absence of fretting. At the start of fretting, we recorded a gradual increase in currents, rising to a global average of  $1.623 \mu\text{A}$  across three trials. As long as fretting continued, with the pin remaining in contact with the disk and in full slip condition, the currents remained stable.

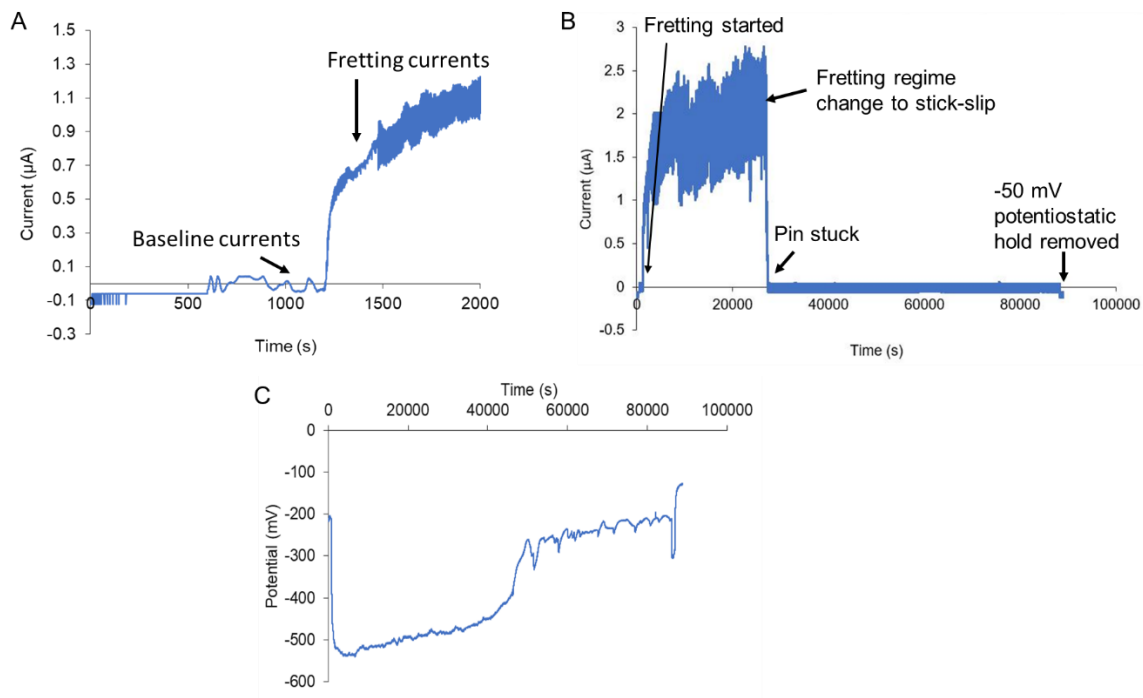


Figure 3: (a) Representative plot showing fretting corrosion onset and distinction from baseline currents prior to fretting (b) Example of a full 24-hour fretting test raw currents. Note that the full slip regime changed to stick-slip or full stick around 25000 s, leading to a drop in fretting currents (c) Variation in potential over a 24 h test for an OCP test. Transition to a sticking condition occurred around 40000 s. Reported values represent average current density and error bars refer to standard deviation across three trials per group

As shown in Figure 3b, full-slip fretting occurred in this particular test from the start of fretting (around 1200 s) to approximately 25000s, where the fretting motion stopped, leading to a drop in currents. In all three trials in group 1, fretting motion shifted from full slip to stick-slip and finally to full stick during the first 12 hours and currents returned to baseline. In the second group, where no potential was applied, we observed no significant external fretting currents arising from fretting motion, instead cathodic excursions in potential were observed (Fig. 3c). The average minimum recorded potential

over 3 trials was  $-518.9 \pm 20.89$  mV. Thus, we applied a -500 mV potentiostatic hold in group 3 to measure loss in viability resulting isolated external cathodic bias opposed to fretting corrosion-driven cathodic potential drop and its byproducts. During the no-fretting experiments under groups 3 and 4, no observable currents arose under OCP in group 3 whereas in group 4, overall current dropped from almost 0 at the start of -500 mV potentiostatic hold to before recovering back to almost 0 once the potentiostatic hold was removed. Fretting under potentiostatic hold at -50 mV led to the highest average currents, whereas in the absence of fretting and any applied potential, currents remained close to zero.

#### 7.4.2 Fretting site: debris and cells

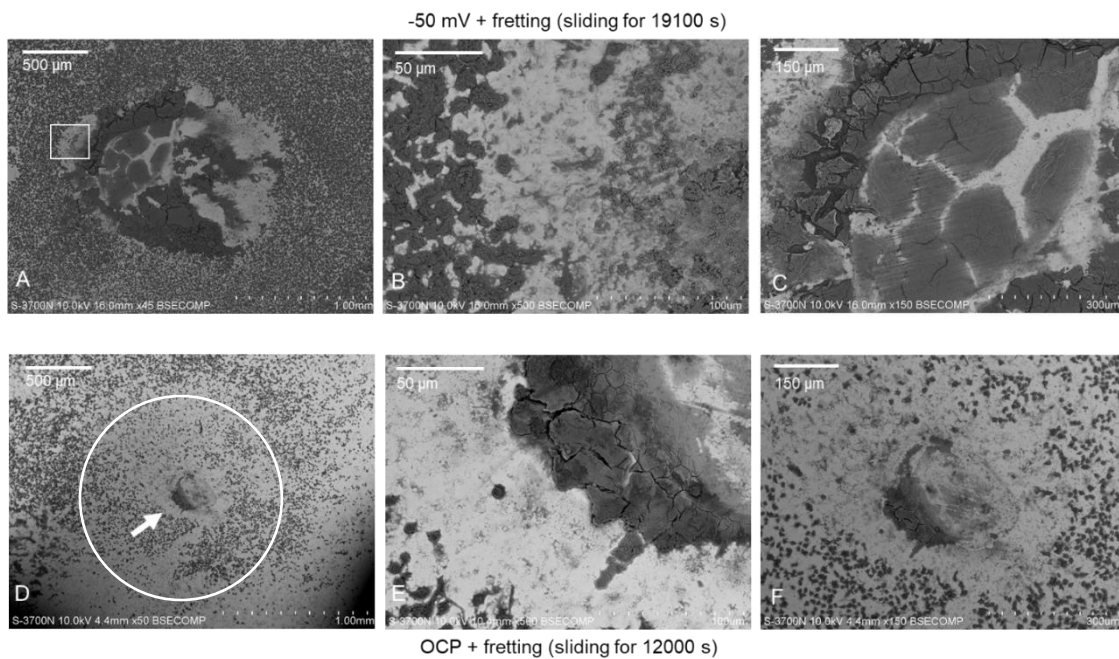


Figure 4: (a) Backscattered electron micrograph showing fretting contact area surrounded by oxide debris (dark contrast region, confirmed by EDS, data not shown) from group 1, -50 mV + fretting (b) A relatively cells-free ‘dead zone’ formed at the edge of the accumulated debris (inset in (a)). The actual cells are covered in proteins on the left,

which is a darker contrast than the oxide debris on the right. (c) Actual fretting contact region with parallel, repetitive fretting scars roughly horizontal. (d) Backscattered electron micrograph showing fretting contact area surrounded by oxide debris (white arrow, dark contrast region, confirmed by EDS, data not shown) from group 2, OCP + fretting. Note the smaller quantity of debris generated in this experiment. White circle represents approximate area of the pin surface area projected onto the disk (e) Similar cells-free 'dead zone' formed adjacent to debris as seen in (b). The amount of debris is less and the surface appears cleaner (f) Higher magnification of the pin surface area projection showing that cells from all around the fretting contact area have either been mechanically abraded away or have detached from the surface

Scanning electron micrographs of the fretting site and debris for representative experiments from groups 1 & 2 are shown in Figure 4 above. The first row of micrographs represents group 1, held at -50 mV with fretting and the second row represents group 2, with no potentiostatic hold (OCP monitored) and fretting corrosion. We observed a difference in the amount of debris generated between group 1 and 2 (Figs. 4a & 4d). The amount of debris generated under potentiostatic hold covered approximately  $0.798 \text{ mm}^2$  surface area (Fig. 4a) compared to approximately  $0.020 \text{ mm}^2$  under open circuit potential (Fig. 4d). One critical difference appears to be the actual contact area in each case is significantly different visually. In Figure 4d, we also see a large number of cells still adhered to the disk substrate at the end of the 24-hour test. These cells were mostly dead, but remained adherent, nonetheless. Figure 4b and 4e show a 'dead zone' between the projected area of the pin, representing the nominal contact area of the entire pin surface, and the remaining cells on the disk. The boundary between the adhered debris and the rest of the cells is demarcated clearly. Figure 4c shows the fretting

contact area identified by the parallel fretting scars. Note the complete absence of any cellular remnants here, since these would have been mechanically damaged and removed, but a layer of adhered protein remains behind. Figure 4f shows that the ‘dead zone’ seems to extend all around the pin contact area in the OCP + fretting condition, but in the -50 mV + fretting condition (Fig. 4a), the ‘dead zone’ extends only on the opposite end of where debris seems to have accumulated.

### 7.4.3 Macrophage viability

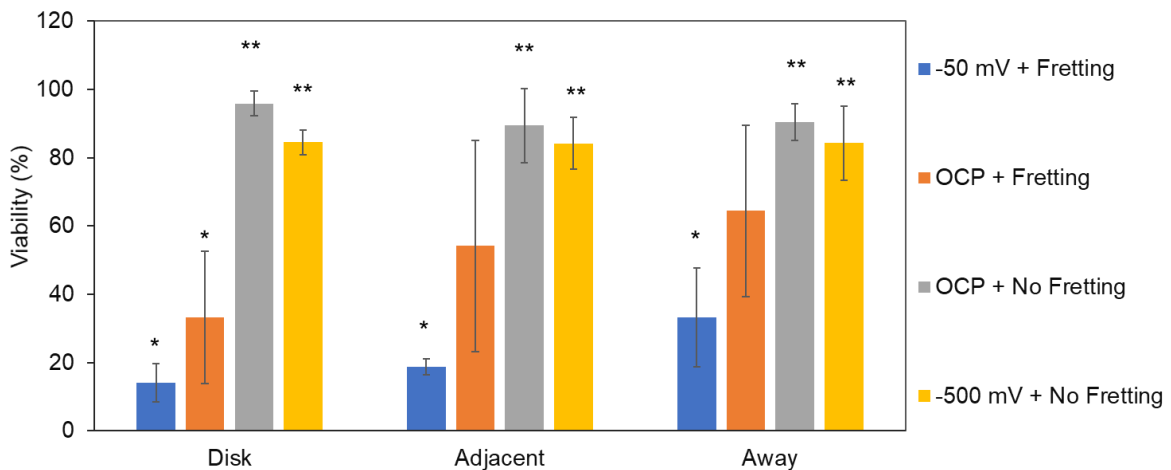


Figure 5: Summarized viability results for all test conditions and locations within the test chamber. Columns represent average viability calculated as percentage of live cells among total number of cells counted per image field. Error bars represent standard deviation across three trials. Single asterisk is statistically similar and statistically different from double asterisk columns. Average viability for OCP + fretting at adjacent and away locations lay intermediate between -50 mV + fretting and the other two groups



Group		Average	SD
Group 1	Disk	14.12	5.55
	Adjacent	18.74	2.41
	Away	33.19	14.49
Group 2	Disk	33.2	19.3
	Adjacent	54.2	30.9
	Away	64.5	25.1
Group 3	Disk	95.86	3.64
	Adjacent	89.38	10.88
	Away	90.38	5.4
Group 4	Disk	84.53	3.67
	Adjacent	84.21	7.59
	Away	84.33	10.86

Table II: Summary of average viability for all groups and locations

We found that cell viability was significantly different among the four groups tested. Viability was highest among the control group 3, followed by group 4, and was lowest for group 1, as shown in Figure 5 above. Tukey's analysis of means across all four groups showed that for cells cultured directly on the disk, average viability for groups 1 & 2 were similar and 3 & 4 were similar, whereas for cells immediately adjacent to and cells at the petri dish

periphery, average viability for group 1 was significantly lower than in groups 3 & 4, and average viability in group 2 was intermediate between the lower group 1 viability and higher group 3 & 4 viability. We also found that within individual test chambers, viability did not significantly change based on the location where images were taken. Cells cultured directly on the disk did not suffer greater loss in viability than those cultured on the attached petri dish, either immediately adjacent to the disk opening or towards the dish periphery ( $p > 0.05$ ) for each group. Table II summarizes the average viability and standard deviation for each group and location.

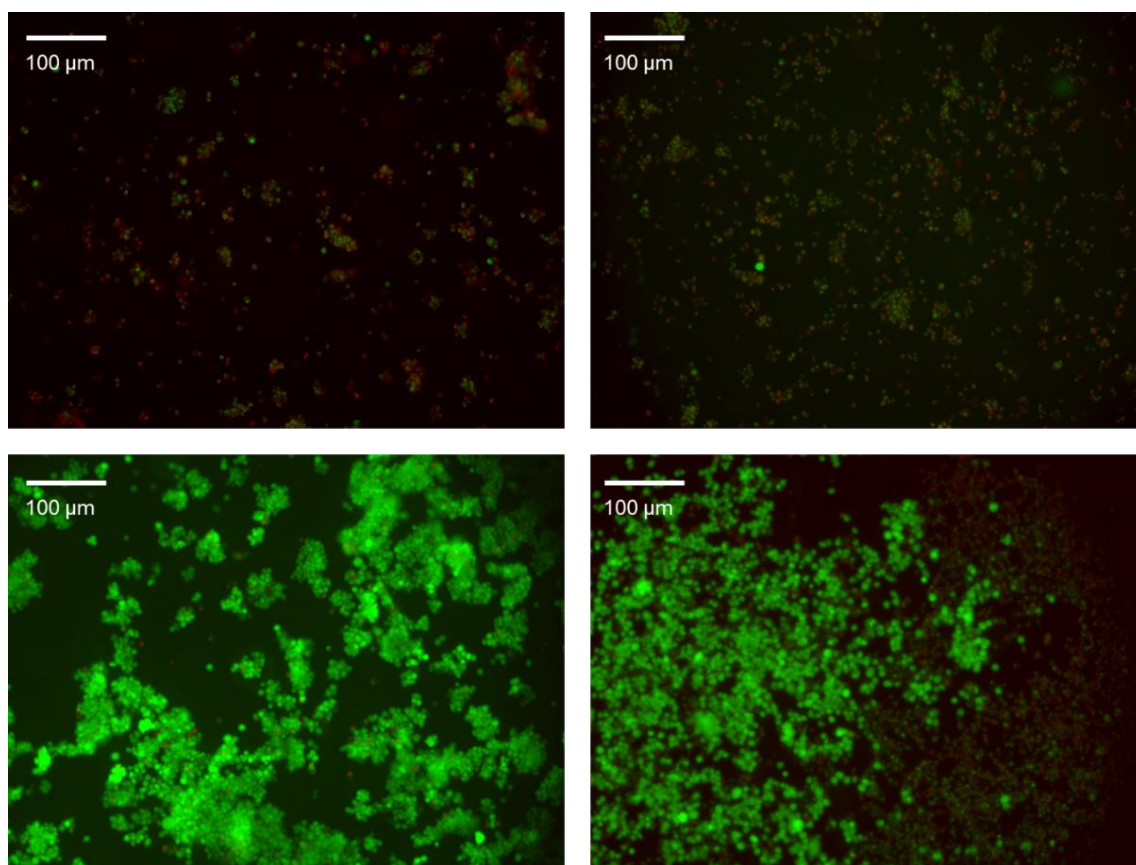


Figure 6: Live/dead fluorescence images for (a) -50 mV + fretting (b) OCP + fretting (c) OCP + no fretting (d) -500 mV + no fretting. All images are acquired from the metal disk substrate. Note the overlap in red stained dead cells and green stained live cells in (b)

Cells stained with calcein AM (live, green stain) and ethidium homodimer-1 (dead, red stain) for each test condition are shown in Figure 6 above. Following from the viability results, we see that the -50 mV + fretting group shows the least number of live cells (Fig. 6a), followed by the OCP + fretting group. Notably, in group 2, the same cells appear stained with both the live and the dead dye, as seen from the overlap between green and red cells in Figure 6b. Figures 6c and 6d correspond to OCP + no fretting (group 3) and -500 mV + no fretting (group 4) respectively, with the most number of live cells,

confirmed with the Tukey's analysis of means: the mean viability for groups 3 & 4 were similar to one another.

#### 7.4.4 Cell size and morphology

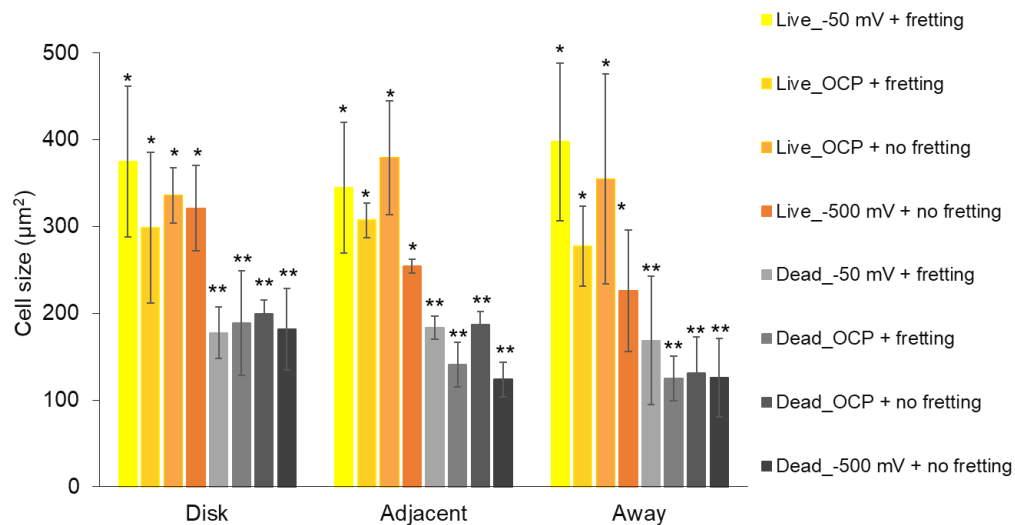


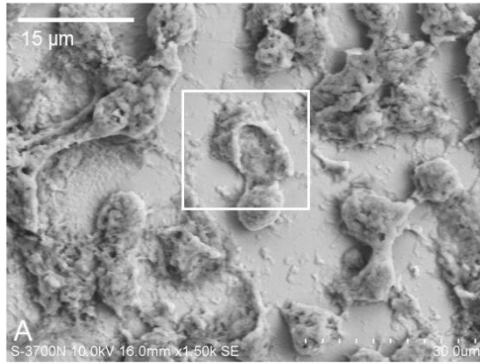
Figure 7: Average cell size ( $\mu\text{m}^2$ ) calculated from live and dead cells across all four groups, representing projected cell area calculated from fluorescent images ( $n=5$ ). Live cells within individual categories were significantly larger than dead cells, and cell sizes did not vary with differences in testing conditions. Single asterisk columns are similar to one another and statistically different than double asterisk columns.

We compared cell sizes, based on projected cell areas calculated from the fluorescent images, across the four conditions tested, and found that all live cells across the groups were similar in size, as were the dead cells ( $p>0.05$ ). Cells either remained alive and the same size or underwent cell death with a reduction in size. Live cells within individual test conditions and location were significantly larger than the dead cells within the same group ( $p<0.05$ ).

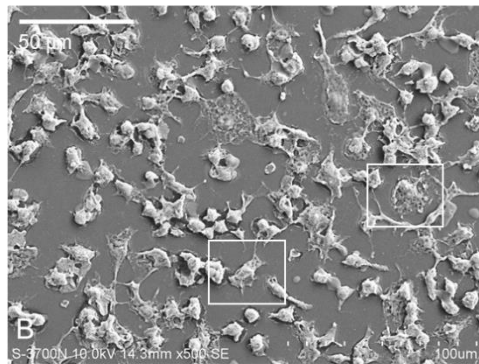
Figure 8 below shows disk and petri dish micrographs visualizing morphological changes in response to varying electrochemical conditions the RAW 264.7 cells were subject to during the 24 h experiments. Figures 8a and 8b show the cells on the disk and petri dish respectively for group 1. Cells on the disk (Fig. 8a) appear attached to the substrate, with a more rounded appearance than spread out. Some cells appear to have a ruptured membrane (marked with inset in Fig. 8a & 8b). Similarly, on the petri dish, the cells appear attached to the substrate, but in some spots, appear to have cell membranes ruptured and intracellular components spread out around them. Figures 8c and 8d show cells on the disk and petri dish respectively for group 2, where cells appear to have a defined, balled up appearance with seemingly intact cell membranes. Some cells appear to have spiky protrusions emanating from the cell body along their membrane. Figures 8e and 8f are the control group 3 images showing well spread, adhered cells on both substrates. Cells appear to be crowded and those that have formed clumps seem to have a more balled up appearance, however, cells close to the substrate are still spread out and well attached. Figures 8g and 8h show cells from group 4 on disk and petri dish, respectively. In Figure 8g, we can see three distinct morphologies: 1. cells either appear mostly spread out and adhered to the substrate (white inset), 2. cells still seem to have focal adhesion points intact, but are beginning to show a rounded appearance with protruding filaments (red inset) or 3. cells have a distinct balled up appearance. Similar observations can be seen in Figure 8h. Across the groups, we also see differences in ‘fluttered’ appearance of the cell membrane. Group 3 (control with no electrochemical inputs) appeared to have the least perturbed cell membrane, with most spread out looking

cells, and group 1 (Fig. 8a and 8b), groups 4 and 2 (Figs. 8c and 8d, and Figs. 8g and 8h) appeared to have progressively more fluttered, rougher looking membranes.

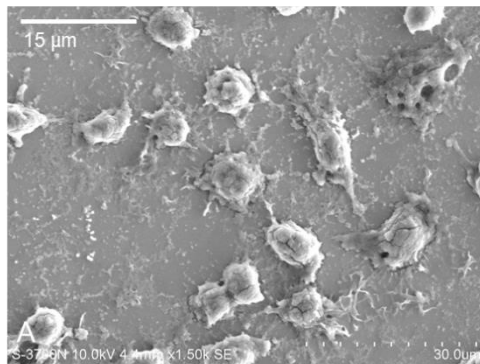
Cells on disk (-50 mV + fretting)



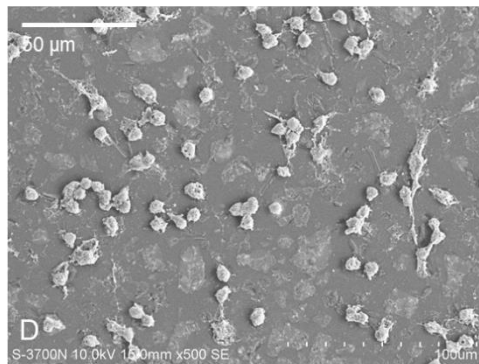
Cells on petri dish (-50 mV + fretting)



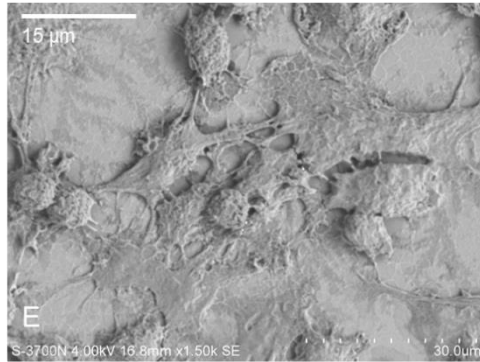
Cells on disk (OCP + fretting)



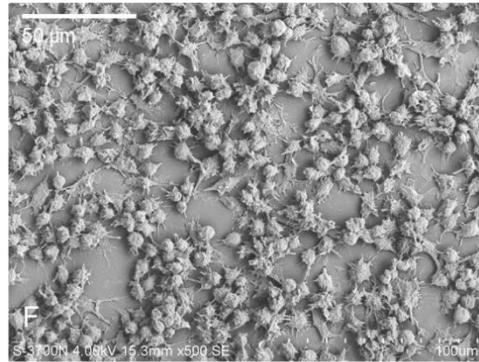
Cells on petri dish (OCP + fretting)



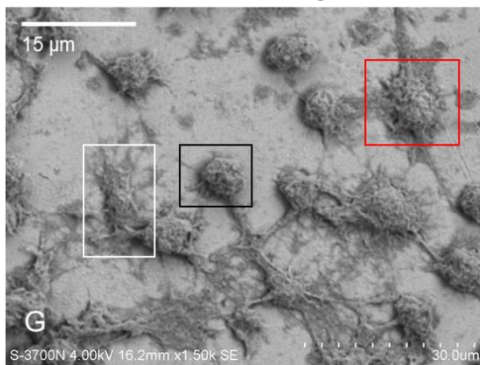
OCP + no fretting, disk



OCP + no fretting, petri dish



-500 mV + no fretting, disk



-500 mV + no fretting, petri dish

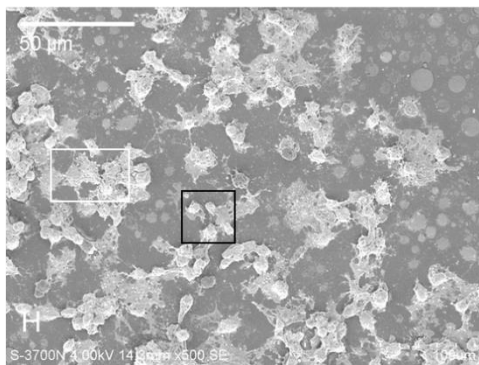


Figure 8: Secondary electron micrographs for (a) -50 mV + fretting, disk (b) -50 mV + fretting, petri dish. White insets show ruptured cells, with intercellular contents spilled around them. Other cells appear more rounded basally attached to the substrate (c) OCP + fretting, disk (d) OCP + fretting, petri dish. Note the balled-up appearance of the cells, with fewer focal adhesion points compared to 8a and 8b, with protrusions and general debris in their vicinity (e) OCP + no fretting, disk (f) OCP + no fretting, petri dish. Note the well spread out and attached cells in 8e. Comparatively, in 8f, cells appear to be more rounded, likely because of crowding (g) -500 mV + no fretting, disk (h) -500 mV + no fretting, petri dish. Cells are either spread out (white inset), cell membranes are beginning to contract (red inset) or cells are rounded and balled up (black inset)

## 7.5 DISCUSSION:

The goal of this study was to design an in vitro system where macrophages cultured on a conjoined CoCrMo disk-petri dish substrate could be exposed to ongoing fretting corrosion, enabling investigation of viability and morphology changes resulting from the interaction of macrophages with fretting corrosion byproducts. We have successfully designed this system and found that exposure to different electrochemical and corrosion conditions influences macrophage mortality in a repeatable manner.

Fretting currents and the amount of debris generated at the fretting site are correlated: the amount of debris generated in a potentiostatic control experiment was approximately 40 times greater than under an open circuit potential condition. The corresponding average fretting current recorded was 48 times greater in the potentiostatic control experiment compared with the open circuit potential experiment, where fretting motion occurred for 19100 s for the former and approximately 12000 s for the latter. It is important to note,

the amount of debris calculation is limited by the fact that the measurement was conducted through image analysis of electron micrographs to measure the surface area covered by the adhered debris, and is not a volumetric measurement. However, the correlation between quantity of debris generated with the fretting current measured is remarkable.

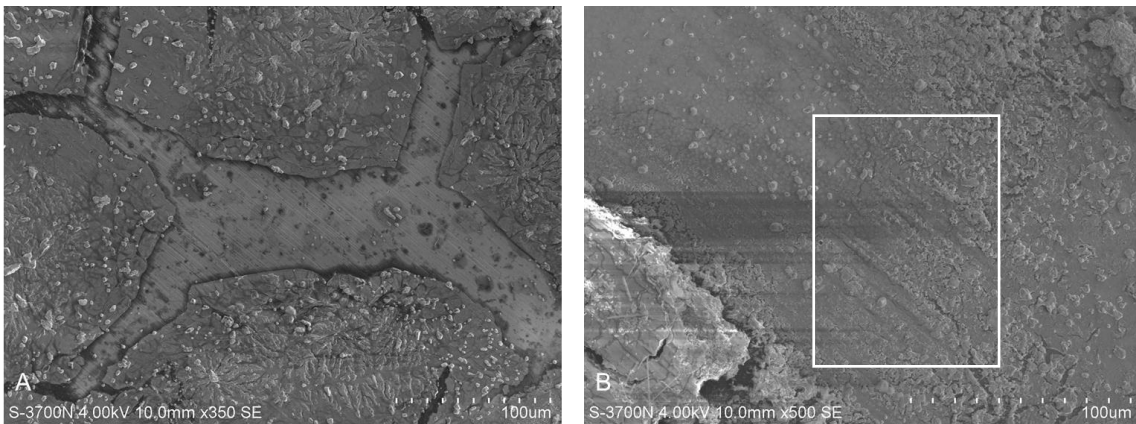


Figure 9: (a) Secondary electron micrograph showing a tribochemical layer rich in carbon, oxygen, chromium and phosphorus (EDS data not shown) formed atop the disk surface which shows the fretting scars (b) Secondary electron image showing the smeared accumulated debris which has protected the underlying disk surface and prevented oxide abrasion.

The transition to full stick, where it occurred, in this system was caused either due to accumulation of debris or due to the pin and disk losing contact since this was a fixed load test and material loss at the interface could have led to loss of contact. Through high magnification SEM imaging, we can see that the accumulated debris appears to have formed a layer atop the fretting scars (Fig. 10a), which probably explains why the fretting currents eventually dropped off and still fretting motion continued. Accumulated debris at the edges of the nominal contact region also appears to be carrying the contact area as



seen by the smearing of the debris seen in Figure 10b, and acting almost as a lubricant by facilitating motion while preventing oxide abrasion and resulting fretting corrosion. At what time during the 24-hour period this occurred is difficult to say.

Zhu et al. [119] recently published a study that describes the debris generation and distribution resulting from fretting corrosion of CoCrMo alloys in a 2D fretting system. Our results corroborate those findings since we also detected the adhered debris to be rich in chromium phosphates. The chromium phosphates have a characteristic green color to them, which can be seen in optical micrograph (Fig. 10a), which was confirmed to be chromium, oxygen and phosphorus rich with EDS analysis.

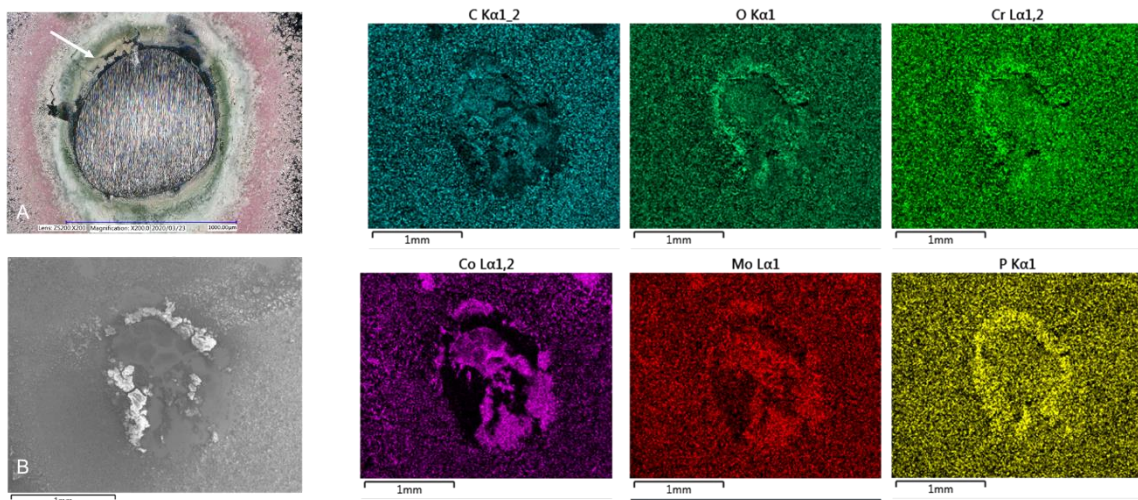


Figure 10: (a) Optical micrograph from a test condition without cells, showing the green deposits (white arrow) found to be rich in chromium, oxygen and phosphorus (b) Electron micrograph image of the fretting site from the -50 mV + fretting condition (with cells). Note the absence of cells seen through the carbon-nil regions in the first color plot. Debris detected here is mostly rich in chromium, oxygen, and phosphorus according to EDS analysis (color maps showing oxygen, chromium, phosphorus, molybdenum, and cobalt presence in clockwise direction)

Scharf et al. [52] published histological analysis of periprosthetic tissue, which showed significant macrophage infiltration, evidence of phagocytosed debris particles within a macrophage as well as presence of reddish and pale green crystalline debris in histological slides. Since cellular remnants have been found in retrieval studies [32], there might be a link between debris generated during in vivo fretting corrosion processes in modular metallic junctions and recruitment of immune cells, including macrophages, to the fretting site. Further investigation of macrophage migration in the presence of fretting corrosion could lead to a deeper understanding of in vivo phagocytosis and potential frustrated phagocytosis. The 'dead zone' reported in Figure 4 also warrants further investigation. Cells present just outside the pin surface area were selectively removed from the substrate, and this could be the result of overwhelming amount of debris causing these cells to be damaged enough to detach from the surface. Or it could be due to the formation of a crevice-like environment immediately under the pin and just adjacent to it, thus creating a hostile environment for the cells to survive in.

Macrophage mortality was affected by the electrochemical conditions they experienced during the 24 h exposure. The lowest recorded average viability was under -50 mV + fretting conditions, followed by OCP + fretting, then -500 mV + no fretting and finally, the control group, OCP + no fretting. The primary difference between these groups is in the average current density recorded and the surface potential, whether applied externally or induced through continuous oxide abrasion. Group 1 conditions were associated with an average current density of  $6.14 \mu\text{A}/\text{mm}^2$ . Among groups 2 and 4 no currents were generated since both groups were under OCP. However, the surface potential at the disk

surface under group 2 (OCP + fretting) and group 4 (-500 mV + no fretting) differed over time.

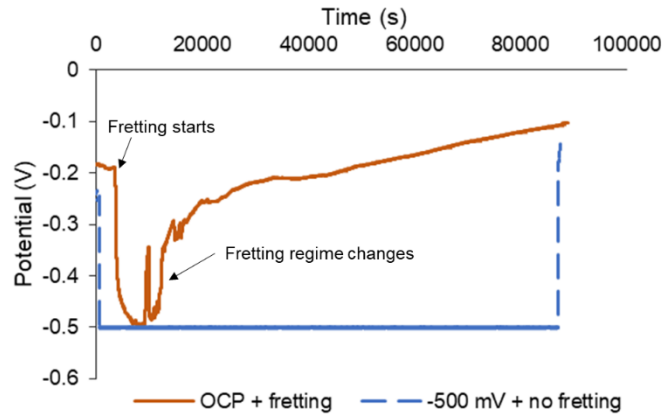


Figure 11: Graph showing differences in surface potential over time in groups 2 and 4. Note the anodic shift in recorded potential for group 2, OCP + fretting, over time, compared with the constant, externally applied potentiostatic hold in group 4

Figure 11 shows the differences in surface potential over time between groups 2 and 4. In the group 2 example, the potential changed over time, dropping to around -500 mV at the onset of fretting motion, and then, presumably due to creation of a tribochemical layer or a change in fretting regime to stick-slip, rising anodically back towards pre-fretting levels. In the group 4 exemplar, the potential remained uniform at -500mV throughout the 24-hour period. Thus, the major difference between groups 2 & 4, apart from the debris generated in group 2 due to fretting corrosion, seems to be a difference in charge transfer and/or accumulation over time. Sivan et al. hypothesized that duration of exposure to cathodic potentials has an effect on preosteoblast viability, with longer exposure times leading to higher cell death [115]. Our findings here indicate that the way the cathodic shift is achieved is also of significance, with fretting induced cathodic shifts corresponding with greater macrophage mortality. The effects of debris volume versus

the effects of cathodic potential needs to be studied in greater detail, especially in light of the study by Wiegand et al [116] indicating that macrophages have a greater tolerance for cathodic potentials, even up to -1 V compared to preosteoblasts. Of interest is the finding that cell viability did not differ significantly with change in substrate, that is, there was no significant difference in extent of cell death between cells on the CoCrMo disk and on the petri dish. The number of live cells counted in some instances varied significantly, leading to high standard deviations in the live cell count. This can be seen in Figure 5, especially with group 2 results. The average viability values for each location within group 1 and 2 seem to be different, but due to the high standard deviations, are not statistically significant.

Wiegand et al. found that macrophages remain viable to some extent up to -1000 mV on CoCrMo surfaces, but anodic potentials above +500 mV have a 100% killing effect [116]. Physiologically, and as seen in this study, cathodic excursions are derived from fretting corrosion like processes, that is, implants can experience cathodic shifts in potential from normal daily activities like walking which can cause micromotion at implant junctions. Anodic excursions are more likely due to changes in solution chemistry, such as inflammation associated with reactive species such as hypochlorous acid, hydrogen peroxide and reactive oxygen species (ROS). Each of these substances are known to accelerate the reduction reaction at the metal surface, and therefore, exacerbate corrosion [53], [65], [66].

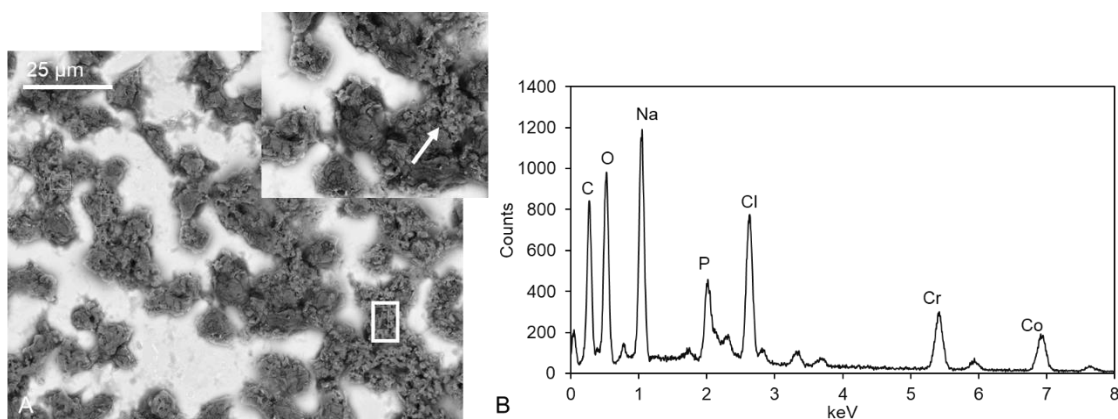


Figure 12: (a) Backscattered electron micrograph (at 15kV voltage) showing cells (dark structures) and oxide debris in close proximity adjacent to the fretting site. Inset shows a high magnification image of the cells with fluffy-looking debris marked by white arrow (b) EDS analysis of inset shows high amount of oxygen, chromium and cobalt peaks, showing a mixed oxide along with sodium, chlorine and phosphorus peaks indicating salts from the culture medium

Apart from cathodic excursions, the presence of debris might also contribute to macrophage mortality. Debris quantity and macrophage viability seem to have a correlation, as increasing quantities of debris led to greater mortality. Evidence of close interactions between oxide debris and cells can be seen in Figure 12a, where oxide and salt deposits are seen intermingling with macrophages (dark regions). EDS analysis (Fig 12b) shows the composition of the debris is a mixture of salts and mixed oxides of chromium and cobalt captured at 15 kV accelerating voltage. Other studies have shown that macrophage viability is modulated by CoCrMo wear particles [107]–[109], [120] and Ti6Al4V corrosion debris [55], [113]. We did not systematically investigate mortality effects by varying debris quantities, but the combination of ongoing fretting corrosion

processes and debris generation appears to be the most lethal for macrophages in this study.

Another key byproduct of fretting corrosion is metal ions.  $\text{Co}^{2+}$  and  $\text{Cr}^{3+}$  ions are the most ubiquitous forms of cobalt and chromium ions found in aqueous solutions. Studies have found that  $\text{Co}^{2+}$  is capable of activating cell death in macrophages by causing oxidative stress in a dose dependent manner [63], that both  $\text{Co}^{2+}$  and  $\text{Cr}^{3+}$  in combination can modulate cell death pathways in macrophages based on duration of exposure [59] and that at sublethal doses, metal ions can induce  $\text{TNF-}\alpha$  secretion [61] or activate different cell death pathways in macrophages [62].

The results of this study point to differences in how cell death occurred as a result of different test conditions, based on macrophage morphology captured using SEM. Ruptured cell membranes could be indicative of a necrotic cell death (Fig. 8a & 8b); physiologically, necrosis occurs as a result of inflammation or hypoxia [64], both of which are likely to occur in a fretting corrosion vicinity [56], [121]. Necrosis can also further propagate inflammation through spilling of intracellular contents onto surrounding tissue and therefore, consequences of cell rupture as seen in Figures 8a & 8b can be dire for implant corrosion in vivo. Histological analysis of retrieved periprosthetic tissue have revealed presence of necrotic tissue [122], [123], and necrosis is a well-established form of adverse local tissue reaction (ALTR) which is associated with implant corrosion.

Cells exposed to cathodic excursions around -500 mV by fretting corrosion or external applied potential also differed in their appearance depending on the origin of the excursion. In the former case, cells appear rounded and balled up with spiky protrusions (Fig. 8c & 8d) which are characteristic of different stages of apoptotic cell death [124]. In the latter case, three distinct appearances of cells (Figs. 8g & 8h), progressively: spread out with flattened nuclei, slightly rounded nuclei with spread out membrane and finally, balled up, could be illustrative of different stages of apoptotic cell death as well.

Prolonged exposure to cathodic bias beyond 24 h might lead pre-apoptotic cells to late stages of apoptosis. The differences in cell membrane appearance is prominently seen when comparing the control group cells (Fig 8e and 8f) to all the other conditions, showing that in the absence of any electrochemical or tribocorrosion stimuli, cells can remain on a metal substrate in a spread out, well-attached condition. An Annexin V/propidium iodide (PI) assay using flow cytometry can sort cells based on live, dead and early stages of apoptosis [125], which could be important next step in continuing this investigation.

Another marker of cell membrane integrity can be seen in the live/dead fluorescence images (Fig. 6). The dead cells stained red in Figure 6a appear brighter than those in Figure 6b, even though the dye concentration, incubation time, sample preparation and imaging parameters remained uniform. Ethidium homodimer-1, which is used as the dead stain here, has a mode of action reliant on penetrating compromised cell membranes and staining nucleic acid molecules within the dead cell [126]. If the cell membranes in Figure 6b, which we hypothesize are intact due to apoptotic cell death, are not permeable

to the dye, it would explain the lower brightness of the dead cells. Interestingly, there is a strong overlap between live and dead cells in Figure 6b, which is not the case in any of the other images. Calcein AM is converted to green-flourescing calcein by enzymatic activity within live cells, and an overlap in staining could point to cells that are about to be dead, with potentially damaged membranes.

Finally, metal ions and debris particles, when added to macrophage culture media in in vitro settings, have been known to induce phenotypic changes [58], [127] and modulate proinflammatory cytokine expression [60]. Similar mortality results on both the disk and the petri dish substrate point to additional mechanisms within the chamber propagating cell death that did not result from being directly exposed to currents or cathodic excursions, which would be limited to the disk surface. Future work to investigate fretting corrosion-macrophage interactions should address these phenomena, by detecting surface markers on macrophages that indicate pro- or anti-inflammatory phenotypes induced by exposure to ongoing fretting corrosion.

A limitation of this work that the tests were performed over a single time point (24h). Temporal effects of exposure to ongoing fretting corrosion can elucidate macrophage response evolution over time to fretting corrosion byproducts generation as well as sporadic potential excursions. In addition to phenotypic characterization and cell death pathway detection, future work could also include an investigation of macrophage chemotaxis in response to fretting corrosion. Retrieval studies often show the presence of



cell-like remnants within modular junctions, which are highly restricted geometries. For cellular ingress to occur, chemotactic cues have to have initiated such migration.

Overall, the system designed in this study presents many possibilities for further investigation. Further work can also incorporate inflammatory species in the culture medium or pre-activated macrophages to investigate the macrophage response to corrosion in an inflamed environment.

## 7.6 CONCLUSIONS:

The method proposed in this study successfully simulates a fretting corrosion environment for cell-based functional analysis. Fretting corrosion debris generated with potentiostatic control was an order of magnitude higher in quantity than when no potentiostatic control was applied. We found that macrophage viability was lowest in the presence of ongoing fretting corrosion with external potentiostatic control at -50 mV. Viability was lower when the cathodic excursions were induced by local redox reactions between the fretting site (anode) and the rest of the surface (cathode) and remained comparable to the control group when the cathodic bias was externally applied. There was no significant difference in macrophage viability based on the substrate, that is, cells cultured on the disk and cells cultured on the adjoining petri dish suffered the same degree of cell death within different test conditions. We also presented live/dead fluorescence images of the different conditions which indicates an overlap between live and dead cells when they were exposed to fretting corrosion without potentiostatic control, which was not necessarily the case for other conditions. Scanning electron

micrographs of cells remaining on the disk and petri dish substrates for all four conditions showed distinct morphological differences: cells under -50 mV + fretting presented ruptured membranes or somewhat balled up, cells under OCP + fretting appeared rounded with a distinct shape, cells under OCP + no fretting were well spread, attached to the substrate and mostly alive, and cells under -500 mV + no fretting appeared to be at different stages typical of apoptotic cell death, indicating that macrophage mortality might be a result of duration of exposure as well as current density and/or debris accumulation. Macrophages seem to be resilient to cathodic excursions up to -500 mV, which is diminished in the presence of ongoing fretting corrosion. Further investigation of phenotypic changes, cytokine expression and temporal effects of fretting corrosion is recommended.

## Chapter 8

### **Metal Ions and Oxide Particles Generated from CoCrMo Anodic Polarization**

#### **Affect Murine Macrophage Mortality and Activation**

##### 8.1 ABSTRACT:

The extent of corrosion-related damage observed in explants has not yet been recreated in laboratory conditions. A feedback loop between corrosion processes and byproducts, and the immune system cells has been hypothesized. Reactive oxygen species (ROS) like hydrogen peroxide, hypochlorous acid, and superoxide anion, amongst others are thought to be mediators of this feedback loop wherein they anodically polarize CoCrMo surfaces, leading to oxide film breakdown and unmitigated corrosion. Immune system cells including macrophages secrete ROS as part of the foreign body reaction, or in response to byproducts generated during corrosion and wear processes. The goal of this study was to investigate the effects of metal ion-rich fluid and solid oxide particles formed by CoCrMo anodic polarization on murine macrophage viability and activation. Our hypothesis was that both the fluid and solid debris will affect macrophage viability in a dose-dependent manner, and that a proinflammatory response will be elicited through sublethal dose exposure. We found that indeed, the ion-rich fluid, containing a high concentration of chromium ions, and significantly lower concentrations of cobalt and molybdenum ions, killed macrophages at 1% concentration, with a 50% lethal dose being 0.75% of the total culture medium volume. At 0.75%, a weak proinflammatory response was identified from the macrophages, by detection of low levels of proinflammatory

cytokines (IFN- $\gamma$ , TNF- $\alpha$ , interleukin (IL)-1 $\beta$ ) and chemokines (CXCL12, CXCL4, CCL2). Corrosion associated with inflammatory conditions mediated by ROS can play a role in perpetuating further corrosion damage and therefore, form a part of the corrosion-biology feedback loop.

## 8.2 INTRODUCTION:

Orthopedic implants, often comprised of modular components assembled in situ, are susceptible to corrosion and micromotion in vivo, while also being exposed to inflammatory conditions. Recent studies have explored the effects of simulated inflammatory conditions using hydrogen peroxide and hypochlorous acid (HOCl). Kubacki et al. demonstrated that inclusion of 30 mM HOCl in the surrounding electrolyte was sufficient to drive surface potentials of CoCrMo alloy higher into the transpassive range, where the passivating oxide film that protects the alloy surface from degradation begins to break down [66]. In vivo, HOCl is one of the reactive oxygen species (ROS) molecules released by phagocytes to eliminate pathogens [128]. Similarly, the effects of hydrogen peroxide ( $H_2O_2$ ), another form of ROS, were studied by Liu et al., and shown to drive corrosion currents higher on the CoCrMo alloy surface [65]. This form of corrosion induced by local chemistry and inflammatory conditions differs from tribocorrosion, which is characterized by drop in surface potential due to abrasion and repassivation of the oxide film. We can thus visualize a feedback loop consisting of extant inflammatory conditions driving implant corrosion, which in turn produces stimulatory byproducts which further exacerbate inflammatory and immune conditions. Anodic polarization can also result from simulated inflammatory conditions, similar to those persisting in the joint space, via generation of reactive oxygen species (ROS). Hydrogen peroxide and hypochlorous acid are some examples of ROS generated by activated immune cells either due to inflammatory conditions or in the course of phagocytosis, a process that is well established occurs in response to foreign body

introduction and release of wear and oxide debris in the periprosthetic space [51]. Studies have also shown that exposure to Co and Cr ions in solution can cause cell viability changes, as well as inducing proinflammatory behavior in macrophages [59], [107]. Macrophages challenged with Co and Cr ions or particulates tend to undergo apoptosis, or necrosis based on exposure times (48h instead of 24h), even at low doses [59]. In addition to inducing cell death, Co and Cr ions caused increased production of proinflammatory cytokines and chemokines in macrophages [109], [129]. In each of these studies, the ions were generated through metal salt dissolution and not through CoCrMo corrosion in aqueous medium.

Retrieval studies have also described extensive corrosion damage featuring intergranular corrosion and pitting of CoCrMo within tight modular junctions [44], which we also demonstrated in Chapter 3 of this dissertation, which have not yet been recreated under in vitro conditions. A study wherein intergranular corrosion and pitting was induced in CoCrMo in vitro could only achieve this with application of 1.8 V vs reference (saturated calomel electrode) [130]. There is no evidence yet that physiologically these voltages can be achieved, but the role of crevice conditions with restrictive geometries and saturated solutions as well as chronic inflammation remains to be investigated.

Our goal with this study is to examine the effects of corrosion byproducts on murine macrophage viability and activation in an in vitro setup. We hypothesize that corrosion byproducts generated as a result of transpassive electrochemical damage of CoCrMo can lead to loss of viability and/or activation of macrophages in a concentration – dependent

manner. We will investigate the viability changes and macrophage activation through systematic exposure of murine macrophages to different corrosion byproducts generated during CoCrMo corrosion by applying a transpassive voltage. These products are different than those generated by tribocorrosion processes and will be characterized in this study as well. Different concentrations of Co and Cr ion-rich fluid, and solid, particulate debris will be used to challenge the cells and changes in viability and cytokine expression will be measured.

### 8.3 MATERIALS & METHODS:

#### 8.3.1 *Generation of corrosion byproducts*

A CoCrMo disk was prepared for the corrosion process by systematically wet polishing the surface using emery paper ranging from 240 grit to 600 grit, followed by mirror polishing using a 1  $\mu\text{m}$  alumina suspension. The area exposed was restricted to 0.3  $\text{cm}^2$  using tape. Next, we set up a standard three-electrode electrochemical cell with the disk as the working electrode, a platinum wire as counter electrode and an Ag/AgCl epoxy matrix reference electrode in 1X phosphate-buffered saline (PBS). After monitoring OCP for 1 hour, we applied a 10  $\text{mA}/\text{cm}^2$  galvanostatic hold over 15 hours to the disk in order to polarize the electrode anodically and to generate corrosion byproducts (metal ions containing solution and solid debris particles), simulating inflammation within the biological environment. It is important to note, the high current density employed here has not been shown to occur physiologically. The goal was to cause extensive corrosion damage to the CoCrMo disk and generate a significant quantity of ions and debris.

At the end of 15 hours, the fluid, which had turned green in color, was extracted, and centrifuged at 3000g for 10 minutes to separate any solid debris that had formed. The supernatant was extracted, and the debris particles were repeatedly rinsed in PBS. Finally, the debris particles were separated and dried using 0.22  $\mu\text{m}$  filter paper (Catalog #GSWG047S6, Millipore Sigma, St. Louis MO). The fluid and debris particles were stored in conical tubes and Eppendorf tubes respectively, at room temperature, until they were used in the experiment.

### 8.3.2 *Corrosion fluid characterization*

The supernatant was analyzed by inductively coupled plasma mass spectroscopy (ICP-MS, Model ICAP RQ, ThermoFisher Scientific, Waltham, MA) following standard protocols. Briefly, 1:10:100:1000 serial dilutions of the supernatant were prepared in 3% nitric acid ( $\text{HNO}_3$ ) base to match the nitric acid concentration of the specific standard solutions used for calibration. Similar serial dilutions in 3% nitric acid were prepared for the standard solutions containing known concentrations of ions of interest ('external standard'). In this study, we were interested in cobalt (Co), chromium (Cr) and molybdenum (Mo) ions, so two separate external standards were run: one for cobalt and chromium and the other for molybdenum. An yttrium-based internal standard solution was used for rinsing the tubing and removing any ion remnants between samples. All standard solutions were obtained from ThermoFisher. Initially, the internal standard was run through the system while start-up procedures were completed. Then a standard performance report was run to ensure measurement accuracy and sensitivity. Once an error-free report was obtained, the serial dilutions of the external standards were used to



generate a standard calibration plot for Co, Cr and Mo each. Each dilution of the sample generated a concentration value at that dilution factor, which was then plotted on the standard curve to obtain final concentration values in the sample solution. Three measurements were made from every dilution and the average  $\pm$  standard deviation concentration for each ion was reported.

### 8.3.3 *Solid debris characterization*

The solid debris, upon centrifugation, appeared to be two different kinds. One was a fine, powdery greyish substance and the other consisted of red particles much larger and more regular in appearance than the grey debris. After drying, the debris was spread onto carbon tape and observed in a digital optical microscope (DOM, Model VK-8700, Keyence, Itasca, IL) and in a scanning electron microscope (SEM, S-3700N, Hitachi Technologies Inc., Tokyo, Japan). We also used energy dispersive x-ray spectroscopy (EDS, Oxford Instruments X-Max<sup>N</sup>, United Kingdom) to determine the elemental composition of each form of solid debris. After imaging, the red debris particle size distribution was determined from a series of 5 images taken at random locations on the tape and measuring the size of individual particles in ImageJ (NIH). The original greyscale, 8-bit image was thresholded and converted to binary to isolate individual particles. After setting the scale bar to match that on the image, the 'measure' utility was used to measure the projected surface area of individual particles. Assuming these particles are more or less spherical, the diameter values were used to create a size distribution. EDS analysis results were also reported alongside.

#### 8.3.4 *Cell culture*

RAW 264.7 murine macrophage cells obtained from ATCC (TIB-71) were used for this study. Cultures were maintained in Dulbecco's Modified Eagle's Medium (DMEM, D5671, Sigma Aldrich, St. Louis MO) with 4mM l-glutamine, 1mM sodium pyruvate, 4500 g/mol glucose, 10% heat-inactivated fetal bovine serum (FBS, Gibco) and 1% penicillin-streptomycin-glutamine (PSG, Corning, Manassas VA) in T-75 flasks (Corning, Manassas VA). Cells were passaged up to 10 times; this cell line shows phenotypic and functional stability up to 30 passages [117]. Around 200,000 cells per well were plated into 18 wells in a 24 well plate at 50000 cells/cm<sup>2</sup> density in 1 mL complete culture media and allowed to adhere for 24 hours. Separate experiments were conducted for the corrosion solution viability effects and the solid debris viability effects. At the end of 24 h, the media was replaced with 1 mL of fresh culture medium with increasing concentrations of the corrosion fluid ranging from 0.25%, 0.5%, 0.75% and 1%. As positive control, we added a 0.1% Triton-X solution to ensure 100% mortality and as negative control, fresh media was added without any additives. Each condition was tested in triplicate. Similarly, for the solid debris exposure, a known quantity of solid debris by weight was first added to complete culture media to create a stock solution (starting concentration: 132 mg/mL). The stock solution was diluted to four levels to obtain four test conditions: 1000 µg/mL, 750 µg/mL, 500 µg/mL, and 250 µg/mL. 1 mL of these freshly prepared solutions were added to respective wells, taking care to frequently perturb the solution through pipetting to ensure the debris particles were in suspension. Positive and negative controls remained the same as in the previous case. All

conditions were tested in triplicate. Exposure to corrosion fluid and the solid debris was conducted for 24 hours, then viability was determined using the MTT assay.

#### 8.3.5 *MTT viability assay*

To measure viability in the corrosion fluid exposure and solid debris exposure experiments, the MTT assay was used. The assay relies upon the conversion of water soluble MTT (3-(4,5-dimethylthiazol-2-yl)-2,5-diphenyltetrazolium bromide) to insoluble, purple-colored formazan crystals, proportional to the number of live cells. The formazan crystals are then solubilized using SDS sodium dodecyl sulfate solution to obtain solutions of varying levels of purple-blue solutions with different optical densities at 570 nm. Based on the absorbance of a specific solution in a well, the concentration of formazan is calculated, which then indicates the proportion of cell death within that well compared with a live condition well. The reagents and instructions for the assay were utilized as received in an MTT assay kit (V-13154, Molecular Probes Inc., Eugene OR). Briefly, at the end of the 24-hour exposure period, the media was discarded, and 0.5 mL of fresh media was added to each well. We then added 50  $\mu$ L of 12 mM MTT solution into each well. Three blank wells were also included to measure background absorbance. The well plate was incubated for 2-4 hours, or until visible blue crystals formed. Then we added 0.5 mL 10% SDS solution in 0.01 N HCl; this was thoroughly mixed by repetitive pipetting to solubilize the crystals. HCl was used to acidify any remaining phenol red in the media to avoid any wavelength overlap between phenol red and formazan at 540 nm. At the end of another 4-hour long incubation, the plate was read in a plate reader (Synergy HTX MultiMode Reader, Biotek, Winooski, VT) at 540 nm and at 690 nm for

background measurement. The ratio of normalized absorbance values for each well was calculated, and results obtained from the assay for corrosion solution and the solid debris were then reported as viability (%) vs concentration plots.

### 8.3.6 *Live-dead fluorescence imaging*

To investigate proximity solid debris effects on macrophage viability, we employed the live-dead imaging protocol from the previous chapter and captured fluorescent images of the 750  $\mu\text{g}/\text{mL}$  conditions to include maximum amount of debris without significant global viability effects. We used a live/dead cytotoxicity kit for mammalian cells (L-3224, Invitrogen, Oregon) containing calcein AM and ethidium homodimer-1 (EthD-1). After 24-hour exposure to 750  $\mu\text{g}/\text{mL}$  red particles in culture media, supernatant was extracted, and the surface was rinsed with 1X phosphate-buffered saline (PBS) at room temperature. 200  $\mu\text{L}$  of PBS containing 4  $\mu\text{M}$  EthD-1 and 3.33  $\mu\text{M}$  of calcein AM was added to each well. Concentrations were chosen based off a previous study conducted within our group using a similar cell type [116]. The cells were allowed to incubate for 30 minutes at room temperature, under aluminum foil inside a dark biosafety cabinet to prevent photobleaching. At the end of 30 minutes, the wells were imaged using an inverted fluorescence microscope (Leica DFC 340 FX, Leica, Germany). A CCD mono-12-bit camera (Q-imaging, Canada) and an X-cite 120 light source (EXFO America, TX) was used to capture images. Using LAS-X software (Leica, Germany), images were recorded at 10x-20x magnification in the vicinity of debris particles and at a distance from them, using fluorescein bandpass filter (FITC) and Texas red dye filters for live and

dead cells respectively. Fluorescent images were reported along with corresponding brightfield images, showing change in viability with proximity to red debris particles.

### 8.3.7 *Cytokine and chemokine expression profile*

In order to assess the effect of sublethal dose of metal ion exposure on macrophages, we used a protein array kit, the Proteome Profiler Array for mouse macrophages (Cytokine Array Panel A, Cat. # ARY006, R&D Systems, Minneapolis MN) to detect specific proinflammatory and anti-inflammatory proteins expressed by the RAW 264.7 cells. We chose a concentration of metal ions that would lead to 50% mortality, which was at 0.75% from the MTT assay results. Briefly, 50000/cm<sup>2</sup> RAW 264.7 cells were cultured in 0.5 mL media for 24 hours, followed by 24-hour exposure to 0.75% corrosion fluid in culture media. Control samples were included as well, a positive control condition where macrophages were activated with 100ng/mL lipopolysaccharide (LPS) and a negative control where macrophages were untreated. All conditions were tested in triplicate. After 24 h exposure, the cell culture supernatant was extracted and tested using the Bradford assay to ensure adequate protein had been expressed by the cells in each condition. 0.5 mL of each supernatant was then prepared for analysis and the kit was used as per manufacturer's instructions. The kit contained 4 nitrocellulose membranes with 20 proteins represented as highly specific dots of selective capture antibodies in duplicate, for a series of cytokines and chemokines that play a role in extracellular signaling. Using a solution of biotinylated antibodies for each of these proteins that can bind specific complexes within the sample solution, specific cytokines and chemokines can be detected based on the intensity of the corresponding dot on the membrane. This assay is semi-

quantitative, where the optical density of each dot can be calculated using densitometric analysis to obtain relative concentrations of each protein.

At the end of the assay, the membrane was set between two transparent plastic sheets and imaged using a ChemiDoc MP Imaging System (Bio-Rad, Hercules CA) to generate an array image of all the detected proteins. We analyzed cell culture supernatants from the 0.75% test condition, LPS-activated positive control and untreated negative control, thus obtaining three separate membranes. Using the Image Lab software (Bio-Rad, Hercules CA), we then performed densitometric analysis on individual dots to obtain an absolute intensity value, after subtracting the background. The intensity value facilitated quantitative comparison between the three treatments in terms of the level of each cytokine or chemokine expressed.

#### 8.3.8 *Statistical analysis*

We compared viability results from the MTT assay for both corrosion fluid and solid debris exposure using one-way ANOVA with post-hoc analysis of means using Tukey's method.  $P=0.05$  was considered significant.

#### 8.4 RESULTS:

Through application of the  $10 \text{ mA/cm}^2$  galvanostatic hold for 15 hours, the potential rose up to 0.85 V, before recovering over time.

### 8.4.1 Corrosion fluid ionic composition

Element	Concentration ( $\mu\text{g/mL}$ )
52Cr	$152.34 \pm 1.22$
53Cr	$155.30 \pm 6.21$
59Co	$0.5357 \pm 0.014$
95Mo	$32.649 \pm 0.457$
97Mo	$34.214 \pm 0.513$

Table I: ICP-MS results for cobalt, chromium, and molybdenum ion concentrations in corrosion fluid

Ionic concentrations for Co, Cr and Mo ions were obtained by ICP-MS analysis of the corrosion fluid, which had turned green in color over the course of the 15-hour galvanostatic experiment with the CoCrMo disk. We see that the fluid was rich in chromium ions and contained a much smaller concentration of cobalt ions.

### 8.4.2 Solid debris morphology, composition, and size distribution

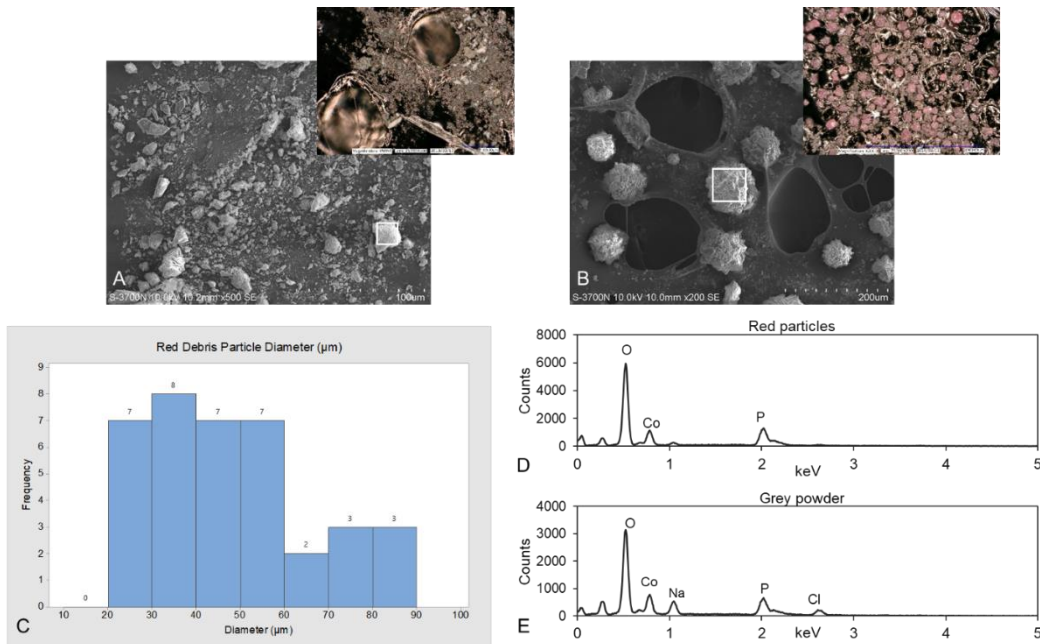


Figure 1: (a) Secondary electron micrograph of grey debris powder with (inset) digital optical micrograph showing the same. Note the lack of any specific shape or structure to

the powder (b) Secondary electron micrograph of red debris particles with (inset) digital optical micrograph showing the color. Note the jagged surface and the mostly spherical or elliptical shape of the particles (c) Size distribution of the red debris particles showing the diameter is on the tens of microns scale and has a relatively narrow distribution. EDS spectrum for (d) grey debris (region within white square in (a)) and (e) red debris particles (region within white square in (b)), showing both forms of solid debris were similar in composition, and appear to be cobalt oxide (peaks at oxygen and cobalt)

The solid debris was found to be of two types: a greyish, powdery substance (Fig. 1a) and red particles with a more spherical shape and jagged surface (Fig. 1b). The size distribution histogram shown in Figure 1c demonstrates a narrow size distribution on the micron scale. The grey debris did not have any form or structure, which made it difficult to characterize its morphology. The powder was also lighter and less dense, since during centrifugation and solid debris separation, the grey powder formed a distinct layer above the red particles layer, which sunk to the bottom of the tube. The elemental composition of both forms of solid debris is alike, both are cobalt and oxygen rich, as seen in Figures 1d and 1e.



### 8.4.3 Macrophage viability effects

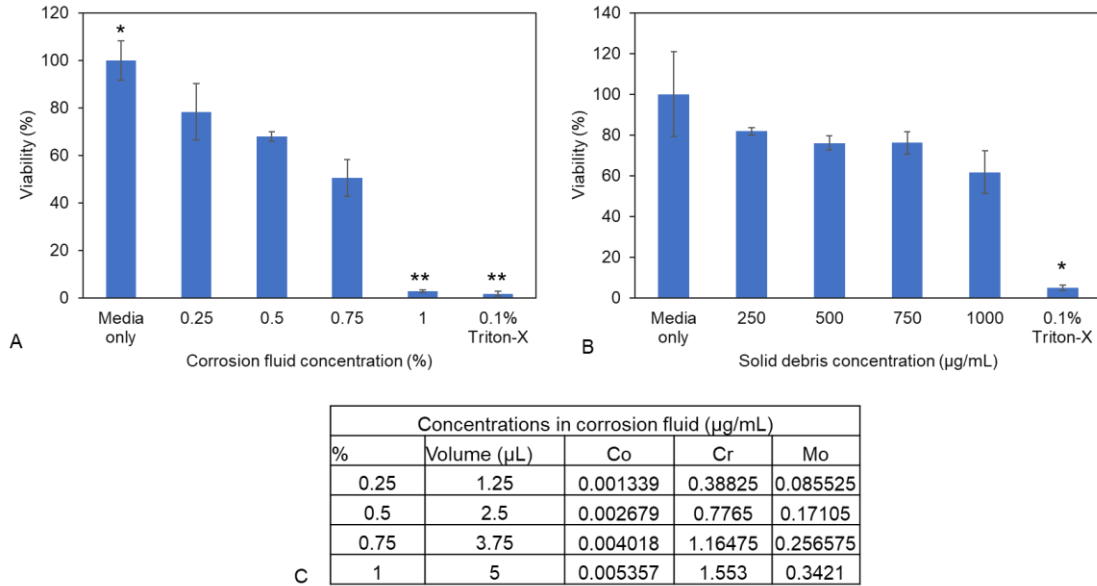


Figure 2: Viability (%) vs concentration plots for (a) corrosion fluid (b) solid debris (red particles only). Macrophage viability at 1% corrosion fluid condition was comparable to the positive control, killing 97.2% cells. Whereas increasing concentrations of solid debris up to 1000 µg/mL did not significantly reduce viability. All values represent average % viability with error bars representing standard deviation. N=3 in each case, asterisk and double asterisk indicate statistical similarity between groups (c) Table showing final concentrations of each ion introduced to each test condition based on initial concentrations of Co, Cr and Mo ions in the corrosion fluid and quantity of corrosion fluid per well added for each test condition

RAW 264.7 cells were significantly affected by exposure to metal ion-rich corrosion fluid (Fig. 2a). With increasing concentration, viability reduced, until it reached 2.8% at 1% corrosion fluid concentration. The % live cells in the 1% condition was comparable to the positive control, with nearly 100% cell death. Cell viability at 0.25%, 0.5% and 0.75% were statistically similar to one another, and significantly different when

compared with both media only (negative control) and 0.1% Triton-X (positive control) conditions, based on Tukey's analysis of means results.  $P=0.000$  for this experiment. This was not replicated in the solid debris exposure experiment, where increasing concentrations of red particles ranging from 250  $\mu\text{g/mL}$  to 1000  $\mu\text{g/mL}$  did not proportionally escalate cell mortality (Fig. 2b). Cell viability at 0.1% Triton-X (positive control) was the only condition significantly different than the other groups, where some overlap occurred between media only (negative control), 250  $\mu\text{g/mL}$ , 500  $\mu\text{g/mL}$  and 750  $\mu\text{g/mL}$  as well as between 500  $\mu\text{g/mL}$ , 750  $\mu\text{g/mL}$  and 1000  $\mu\text{g/mL}$ .  $P=0.000$  for this experiment as well, however, Tukey's analysis confirmed overlap between average cell viability as reported. Actual concentrations ( $\mu\text{g/mL}$ ) of Co, Cr and Mo ions added per test condition based on the initial concentrations in the corrosion fluid and the volume % added per condition is shown in Figure 2c.

#### 8.4.4 Proximity effects of solid debris (red particles) exposure

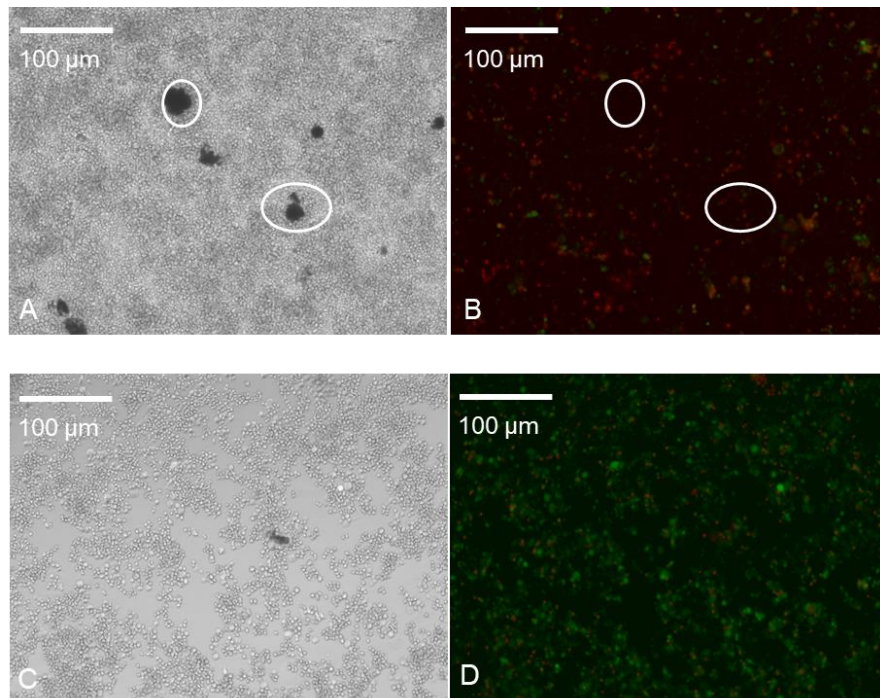


Figure 3: (a) Brightfield image of 750  $\mu\text{g}/\text{mL}$  red particles exposure condition showing debris particles dispersed around field of view (encircled in white) (b) Corresponding fluorescent images showing dead cells (red stained) and few live cells (green) with the approximate location of the debris particles indicated with white ellipses. (c) Brightfield image of 750  $\mu\text{g}/\text{mL}$  red particles exposure condition showing no debris particles within field of view (d) Corresponding fluorescent images showing dead cells (red stained) and greater number of live cells (green) compared with (b)

Figure 3 clearly demonstrates the proximity effect of red particles exposure to RAW 264.7 cells. Figures 3a and 3b show a region with some particles interspersed, with a greater number of red-stained cells, compared with Figure 3d, which shows a region without any visible debris particles (Fig. 3c). Here, the concentration of 750  $\mu\text{g}/\text{mL}$  debris particles in the culture media were used to ensure cells were exposed to a substantial number of particles without altering overall viability.

#### 8.4.5 Cytokine and chemokine expression in response to sublethal dose of metal ions

The cytokine and chemokine array kit used to detect signaling molecules secreted by macrophages after 24 h exposure to 0.75% corrosion fluid allowed for straightforward comparison of proinflammatory and anti-inflammatory cytokines as well as specific chemokines, relative to the LPS-activated group and the media only group. The results are sorted by type of protein and are summarized in Figure 4 below.

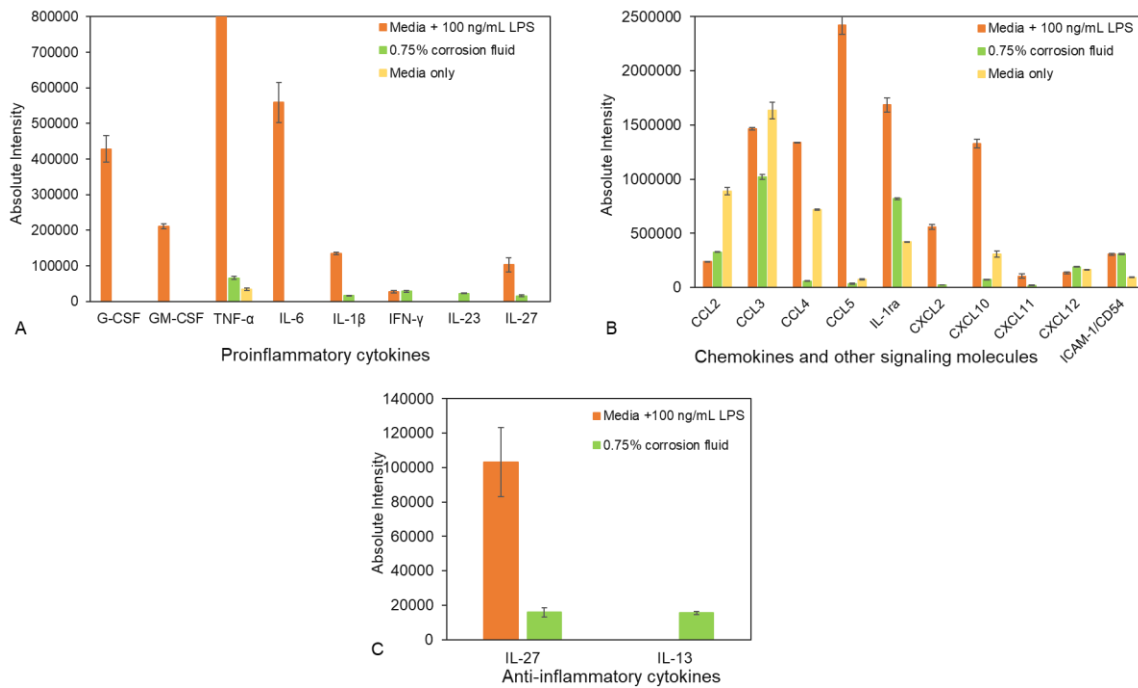


Figure 4: (a) Pro-inflammatory cytokines detected among all three groups, with a focus on all proinflammatory cytokines expressed by the test condition, as well as some classical markers of inflammation (G-CSF, GM-CSF, IL-6, IL-10) which were not detected in the test condition (b) Chemokines expressed by the test condition compared to the same chemokine expression in control groups (c) Anti-inflammatory cytokines expressed by the test condition compared to the LPS-activated group only, since these proteins were not detected in the media only group. Note that IL-27 is included in both

pro- and anti-inflammatory groups, since there is evidence it participates in self-regulatory feedback with IL-10

We found that exposure to 0.75% corrosion fluid for 24 h did not induce a high degree of proinflammatory cytokine expression, in comparison to the LPS-activated cells (Fig. 4a). Specific markers of inflammatory response, cytokines such as IL-6, GM-CSF, G-CSF, and IL-10 were not expressed at a detectable level, and TNF- $\alpha$  was expressed, but was significantly below that induced by LPS. The bar for LPS-induced TNF- $\alpha$  actually extends beyond the level shown here (actual intensity value:  $1972386 \pm 15185.82$ ), but the Y-axis scale has been adjusted to properly illustrate the much lower levels of other cytokines detected. IFN- $\gamma$  was expressed at a comparable level in the test group as in the LPS-activated control. Other than TNF- $\alpha$ , the media only group did not express any pro-inflammatory cytokines in a detectable quantity.

Chemokines detected in the test group are shown in Figure 4b. Most of these chemokines were also expressed to varying relative levels in the control groups. IL-27 is included in the anti- and proinflammatory graphs since it plays a role in both inducing and mitigating inflammatory processes physiologically. Seen in Figure 4c, the test group expressed IL-13 and IL-27 which are known markers of anti-inflammatory behavior. The media only control group did not express either of these proteins, and the LPS-activated group only expressed IL-27. Statistical analysis was not conducted on the protein quantification since multiple measurements were not performed.

## 8.5 DISCUSSION:

With this study, we wanted to investigate influence of anodic polarization byproducts, metal ions and solid debris, generated from a CoCrMo alloy in the transpassive region, on macrophage viability and implications on macrophage activation and phenotype. We were able to show that metal ions, even at small concentrations, led to a significant loss in viability whereas the solid debris, primarily cobalt oxide, did not affect viability significantly at the concentrations tested. The implications of this study are critical to the physiological feedback that might exist between corrosion processes in implants and immune system cells.

Corrosion at modular tapers happens over the entire duration of implantation of the device. This is usually a long period of time, where ample quantities of corrosion byproducts can be released into the surrounding biology. In some cases this taper corrosion has been associated with adverse local tissue reactions (ALTR) including a lymphocytic and macrophage infiltration into periprosthetic tissue [52]. In the case of the acetabular taper, the proximity to the pelvic bone and the surrounding soft tissues increases the possibility that a deleterious interaction between corrosion byproducts from the taper and macrophages in the vicinity can lead to adverse consequences. Transpassive anodic voltage excursions, precipitated through inflammatory solution chemistry containing ROS within the crevice environment formed at modular junctions, might further accelerate corrosion, and perpetuate inflammatory conditions, forming a feedback loop.

We have shown that high anodic voltages lead to generation of Co, Cr and Mo ions as well as cobalt oxide solid debris. ICP-MS analysis showed a four orders of magnitude higher concentration of Cr ions than Co, which is not reflective of clinical serum ion level analyses published [13], [131]. However, in the context of this study, since the debris particles were primarily composed of cobalt and oxygen, the fluid containing greater amount of chromium indicates differences between in vivo metal ion release and that occurring in this study. That these concentrations do not match clinical findings is an avenue for further investigation. Metal ions and solid debris, including oxide debris and metal particles, released from implanted orthopedic devices are associated with adverse local tissue reactions and device revision due to avascular necrosis, osteolysis and other causes [60], [132].

Metal ions, particularly Co and Cr, can induce proinflammatory behavior in macrophages and can cause cell mortality [59], [62], [107], [110]. Our study confirms this and shows that at even with concentrations as low as those shown in Figure 2c, cell viability was significantly affected upon incubation with metal ions. Other studies cited here have utilized a vast range of Co(II) and Cr(III) ion concentrations extending orders of magnitude higher and lower than that we employed for our study, and have reported extensive cell mortality and macrophage activation as well. The difference lies in the method of ion generation: our study generated the ions through corrosion process, whereas previous studies dissolved metal salts in solution to create different concentrations of metal ions. There is a likelihood in our study that chromium was oxidized to Cr(VI), which is a highly soluble form of Cr in saline solutions but is known

to be a relatively short-lived valence state in cellular systems. In the absence of any external sources of electron transfer, it is most likely Cr(VI) remains in solution, and this is why the corrosion fluid has adverse effects on macrophage viability at low concentrations. Cr(VI) is a well-known environmental toxin and a potent carcinogen. It is known to induce intracellular ROS generation through its reduction by glutathione, heightening oxidative stress, and damaging cellular DNA, lipids and proteins [133], [134]. We can extrapolate from the cell viability results in our study that Cr(VI) might be present in the corrosion fluid, but the valence states of the metal ions present in the fluid were not identified explicitly.

We also showed that at 24 hours of 0.75% corrosion fluid exposure, which amounts to 0.00401775  $\mu\text{g/mL}$  Co ions, 1.16475  $\mu\text{g/mL}$  Cr ions and 0.256575  $\mu\text{g/mL}$  Mo ions in solution, the RAW 264.7 cells did not strongly express proinflammatory cytokines, in comparison to LPS-activated cells. Studies investigating the interaction of murine macrophages with Co and Cr ions found that a higher dosage than that used for our study induced an appreciable amount of both TNF- $\alpha$  and IL-6, which are classic inflammation markers [61], [62], so potentially, future studies will need to evaluate a wider concentration range. However, cells did express IFN- $\gamma$  to a similar level as the LPS-activated cells in this study. IFN- $\gamma$  is a vital proinflammatory marker, mediating CD14<sup>+</sup> macrophages activation and the production of HLA-DR, and orchestrating immune cell migration to the inflammation site [135]. Downstream effects of proinflammatory activation of macrophages can lead to activation of caspase-1 cell death pathways and apoptotic cell death. Prolonged exposure to metal ions, 48 h according to this study [59]



rather than 24 h, also led to necrotic cell death in macrophages. Cell death by necrosis have profound downstream effects: necrosis leads to cell fragmentation and these cellular remnants and debris can attract phagocytes to the necrotic tissue site. Phagocytosis, in turn, secretes ROS as part of the mechanism to remove cell debris and remnants post-necrosis [64].

RAW 264.7 cells also expressed detectable levels of an anti-inflammatory cytokine, IL-13, albeit to a lower concentration. IL-13 has been shown to activate macrophages to an M2, anti-inflammatory phenotype [136]. Another cytokine of interest is IL-27, which was also secreted by the test condition cells. IL-27 is largely understood to be a pro-inflammatory marker, often secreted in sepsis and is implicated in increased susceptibility to a form of rheumatoid arthritis [137], [138]. However, there is also indication that IL-27 can induce IL-10 production, which is a well-established anti-inflammatory marker that mediates M2 phenotype in macrophages and also in turn limits IL-27 production [137]. The expression of IL-27 is an interesting result, especially in the absence of any detectable levels of IL-10 in the test condition, implying that exposure to metal ions might impair certain inhibitory pathways in the proinflammatory and anti-inflammatory feedback system. LPS-activated cells in this study did express a moderate level of IL-10, unlike the metal ions-activated group. There are mixed messages here, but the overall finding is that metal ions at the concentration used in this study partly induced a weak pro-inflammatory and an even weaker anti-inflammatory response. A recent study [58] exposing macrophages to wear debris from CoCrMo found that macrophages undergo a

phenotypic change to a state that is intermediate between M1 and M2 in response to wear debris, and our results point in the same direction.

Metal ions also induced chemokine expression in RAW 264.7 cells. Chemokines of the form CCL or CXCL are signaling molecules expressed by cells to induce chemotaxis, or cell migration, in target cells. Our study shows that metal ions exposure induced expression of macrophage inflammatory protein, MIP-1 $\alpha$  (CCL3) and MIP-1 $\beta$  (CCL4), as well as RANTES (CCL5) and monocyte chemoattractant protein, MCP-1 (CCL2) to varying degrees, all of which act as chemoattractant for different subsets of activated or unactivated T cells and macrophages/monocytes [135], [139]. CXCL12, expressed in each of the three conditions to a comparable amount, is responsible for inducing osteoclastogenesis, which in turn affects bone remodeling and resorption [140], [141]. The fact that it was expressed to equal degrees in all three groups indicates that metal ions may not selectively activate bone resorption via this mechanism. The relative amounts of different chemokines expressed by test condition cells could be indicative of specific pathways by which macrophages recruit specialized cells for specific functions. For example, MIP-1 $\beta$  regulates chemotaxis of natural killer cells, among others, whereas MIP-1 $\alpha$  has a more general mode of action towards neutrophils, polymorphonuclear cells (PMNs) and monocytes/macrophages. Further investigation of the specific chemoattractant pathways activated by metal ion exposure is critical to understanding the role of ongoing corrosion and phagocyte activation in chronic inflammation. This is especially crucial when retrieval analysis of revised devices show cellular remnants on taper surfaces, which usually form tight junctions and are not easily accessible to cells in

vivo [32]. Thus, the cells could be responding to specific cues from within the modular junction, including ongoing corrosion or chemotactic cues from other cells.

Similarly, the proximity effects of cobalt oxide particles exposure on macrophage viability is an important phenomenon to be investigated further. Previous studies have found a correlation between particle size and morphology on cell viability and activity, but not specifically on proximity [107]. The recent study by Bijukumar et al. [58] showing wear debris-induced phenotypic changes in macrophages also demonstrates a significant difference in terms of the concentration of particles used, compared with our study. The highest concentration they used was 1  $\mu\text{g/mL}$  and the average particle size was  $119 \pm 138$  nm [57]. The concentration used is significantly lower than that used in this study, and the average size of the particles is somewhat smaller, with the average size of debris particles used here being  $47.64 \pm 18.57$   $\mu\text{m}$ . There might also be some morphological differences between the wear particles and the corrosion debris particles. However, the critical difference between the wear debris and the corrosion debris particles used in this study is the composition: the wear debris was composed of chromium and cobalt metals, whereas the corrosion debris in our study is mostly oxides (Fig. 1a). There is a possibility that introducing metal particles into an aqueous medium causes them to oxidize and potentially induce local corrosion effects or even release of metal ions into the solution, which an already oxidized particle would not cause.

This study presents many important findings and opens avenues for further investigation into corrosion byproduct-macrophage interactions. One of the limitations of the study is

that temporal effects were not investigated. We only studied viability and protein expression at a single time point, 24 h, whereas shorter- or longer-term exposure might produce different results. Length of exposure was an important factor in modulating preosteoblast viability in a previous study involving cathodic bias applied to CoCrMo surfaces [115]. Cytokine and chemokine release kinetics over time is another aspect that was not investigated in this study. There is a strong possibility that the low levels of proinflammatory cytokines and the varying levels of chemokines expressed in the test condition could be emblematic of an acute proinflammatory response that dissipates over 24 h. A more quantitative approach, using western blotting or ELISAs, at earlier time points might address the knowledge gaps in cytokine expression kinetics. Another key factor affecting outcomes could be the test condition itself. At 0.75% corrosion fluid volume, 50% loss in viability was recorded. Therefore, some of the protein expression might be a direct result of the cell mortality, rather than reflective of immune system interactions. Finally, further investigation must include an analysis of phenotypic changes induced in response to the metal ions and corrosion debris particles.

## 8.6 CONCLUSIONS:

We investigated the effects of corrosion byproducts generated from anodic polarization of a CoCrMo disk surface on murine macrophage viability and subsequent cytokine expression. We found that metal ions released as a result of transpassive polarization of CoCrMo caused a dose-dependent loss in viability at concentrations as low as 0.005  $\mu\text{g/mL}$  of cobalt ions in combination with 1.3  $\mu\text{g/mL}$  of chromium ions. A possibility

here is that anodic polarization of CoCrMo generated Cr(VI) ionic specie which is a known cytotoxin and carcinogen. Solid debris, which were found to be an average of  $47.64 \pm 18.59 \mu\text{m}$  in diameter with a jagged surface and spherical shape, were composed mostly of cobalt and oxygen, and caused cell death in proximal cells while not affecting global viability significantly. Metal ions at LD50 also led to a mixed anti- and proinflammatory cytokine expression and a concurrent proinflammatory chemokine expression. This study presents a starting point for further investigation into macrophage-corrosion processes interactions to explain in vivo cell-material interactions that are associated with adverse outcomes and orthopedic implant revision.

## **Chapter 9**

### **Discussion**

Metal-on-metal modular acetabular tapers can be categorized into two designs: a shell-liner pair directly articulating with the femoral head (referred to as MoM), or a dual-mobility (MDM) type acetabular construct that also includes a polymeric insert with a freely rotating femoral head component. While MoM acetabular tapers are no longer commonly used, dual-mobility tapers use is rising mostly owing to their success in mitigating the risk of dislocation [20], [22]. Dislocation remains one of the leading causes of revision surgery in total hip replacement surgeries, which overall have a high success rate and good patient outcomes.

Dual-mobility tapers, however, in the relatively short time they have been employed in general orthopedic surgical practice, still undergo in vitro corrosion and related damage [27], [28]. While no direct association of acetabular taper corrosion and need for revision have been established as yet, investigating corrosion mechanisms within metal-metal acetabular junctions is crucial, especially in conjunction with the CoCrMo alloy which is routinely used in load bearing applications in TJR devices due to its wear and corrosion resistance as well as desirable mechanical properties. In this body of work, we have designed test methods to facilitate these investigations, covering various aspects of metal-metal acetabular taper corrosion. The goals of this thesis were to investigate the many causes and drivers of acetabular taper corrosion, and to explore macrophage-corrosion

interactions in two basic yet critical aspects: tribocorrosion processes and corrosion byproducts resulting from anodic polarization.

In our retrieval analysis study, we documented multiple modes of corrosion occurring on the CoCrMo acetabular liners which were used as part of MoM acetabular tapers of a specific design. Our findings showed that these liners seemed to suffer extensive damage independent of mechanical stimuli, evidenced by corrosion damage observed outside engagement regions where no mechanical contact can occur. Corrosion on the taper surface seemed to be driven more by local solution chemistry and crevice conditions, based on the recorded intergranular corrosion, pitting and phase boundary corrosion. While these damage features were not found to spread over large surface areas in all but four out of twenty one devices, the local damage within minute areas of the device warranted further investigation, especially to understand how extant damage might influence future performance.

Even small surface areas being damaged by corrosion, in the wrought CoCrMo alloy, presents a hazard in the form of large volumes of submicron, hard phase Mo-Si-O particles ubiquitous within the wrought alloy microstructure. These particles were seen to have been released and redeposited within regions of material loss. Volumetric material loss measurements conducted on this same cohort of devices estimated that up to 1.2 mm<sup>3</sup>/year material could be lost from the liner taper region due to wear processes [30]. Considering that the hard phase particles are present pretty close to the surface, and that wear depth measurements reached up to 51.2 μm in these liners [30], we can estimate a large volume of these particles could be released over the lifetime of the device. In our

observations, we found that the Mo-Si-O particles could be released seemingly independent of mechanical abrasion, through pitting attack and phase boundary dissolution. This large volume of particle release from small surface area volumes on the CoCrMo alloy broaches the concept of ‘microstructural biocompatibility’ when considered in conjunction with the adverse local effects precipitated by the immune system’s interaction with particulates in vivo.

We also presented evidence of a potentially new form of corrosion damage heretofore unreported in the literature. It appeared as sets of parallel grooves spanning multiple alloys grains, and oriented along different directions within the same engagement region. We hypothesize that this mode of corrosion might result from a selective etching process, similar to those termed as column damage in head-neck tapers. Further investigation of this damage mode is required, beginning with assessment of more devices to determine if it occurs in a significant percentage of revised devices, since in our study, this type of damage was found in only 4 out of twenty one devices, and in each of these devices, it was found to a very limited extent.

Leading from the occurrence of multiple damage types resulting from unique corrosion modes adjacent to one another or even coexisting within the same region, we presented a method to utilize surface impedance concepts to distinguish between different forms of corrosion damage including intergranular corrosion, oxide deposits and phase boundary corrosion from a freshly polished CoCrMo alloy surface. We demonstrated that impedance measurements taken over micron scale surface areas to distinctly capture highly localized surface and oxide characteristics can successfully depict the granularity



of different co-occurring corrosion modes within that region. We also showed a practical application of a newly published numerical analysis technique that leverages the symmetrical nature of the phase angle response in impedance measurements to minimize scan times for an impedance experiment. It does so by employing the high frequency data only and modeling not only the low frequency data which otherwise requires several hours to be generated, but also determining the quintessential circuit parameters (resistors, capacitors, constant phase elements) that form any charge-conducting surface. Thus, we were able to prove that different corrosion mechanisms alter the alloy surface and its oxide in uniquely identifiable ways. This method can pave the way for more nuanced assessment of implanted devices during revision surgery: we can envision a device built using a microelectrode probe that can, within minutes, measure surface impedance and produce an output that helps the surgeon make an informed decision of whether to revise a particular component or not.

Our investigation of isolated mechanical-assisted crevice corrosion (MACC) processes, specifically fretting corrosion, at these tapers was undertaken to further illustrate the low susceptibility of the metal-metal acetabular taper junction to this form of corrosion. We found that not only is the actual contact area between the shell and liner a very small fraction of the entire taper surface area, but also that the overall fretting currents generated by this area in contact did not rise to a significant level, relative to head-neck tapers of similar material combination. This further strengthens the theory that corrosion in MoM acetabular tapers does not occur solely or even primarily through mechanically-assisted mechanisms. We also showed that the compliance of individual components does

not change significantly with the size of CoCrMo shells and liners but was found to be the case in 316L stainless steel. Since the 316L stainless steel liner group was also found to have the highest variance in fretting currents resulting from incremental cyclic loading at the shell-liner taper, the compliance between shells and liners might play a role in determining corrosion susceptibility and the extent of resulting damage.

Tribocorrosion, through a combination of fretting, wear, and corrosion-related electrochemical changes, can lead to generation and release of metal ions, local redox reactions, repassivation and related cathodic potential excursions as well as generation of oxide and metal debris. In the biological environment, these debris are distributed into periprosthetic tissue, where they interact with systemic immune cells, especially phagocytes like macrophages. In our study with murine macrophages exposed to ongoing fretting corrosion, we found that cell mortality is significantly higher while fretting corrosion occurs than when macrophages are exposed to cathodic bias at the same level. The amount of debris generated also regulated cell viability, since the debris generated in the potentiostatic hold condition was much higher than that in free-floating potential conditions. Macrophages have been shown to be more resilient to cathodic bias than other cell types in previous studies, however the combined attack of debris, ongoing metal ion release and cathodic bias seems to heighten cell mortality.

Importantly, not only did cells experience fatal effects as a result of different combinations of agonists, but the mode of cell death also seemed to vary, depending on the electrochemical conditions. Although it wasn't in the scope of the study to systematically investigate these modes, morphological differences observed in post-

experiment electron micrographs indicate that fretting corrosion with potentiostatic control lead to membrane rupture whereas fretting corrosion in the absence of potentiostatic control lead to an apoptotic cell death pathway, since the cells appeared more rounded and balled up. Under cathodic bias with no fretting corrosion cells appeared to be in various stages of apoptotic cell death, with some appearing well spread out, others appearing to be in early stages of balling up and some appeared to be completely rounded and dead. The differences in cell morphology in this condition corroborates the overall higher cell viability observed relative to the fretting corrosion conditions, implying a cumulative nature to cell death instigators. The current density measured over the duration of the experiment differed between the cathodic bias only condition and that where the same surface potential was achieved purely through fretting corrosion. There was also no visible debris generated in the cathodic bias only condition, which might have also enhanced killing in the fretting corrosion case.

Transcribing these results to clinical findings, studies have shown that retrieved periprosthetic tissue contains debris particles, often surrounded by a severe macrophage and/or lymphocyte infiltration [52], [111]. We also know that the presence of foreign bodies or necrotic cell debris is a strong driver of local inflammation which can persist as long as the agonists persist in the environment [64], [142]. Simulated inflammatory conditions featuring reactive oxygen species (ROS), which are also a key factor in phagocytosis of foreign bodies, have been shown to exacerbate corrosion of CoCrMo alloy surfaces [65], [143], [144], often by modifying the oxide or facilitating non-passivating conditions through anodic polarization. Without a robust passivating oxide

film on the alloy surface, continued corrosion is a given, resulting in electrochemical shifts in local oxygen concentration at the surface and metal ion release in high volumes.

Anodic polarization also actively breaks down the passivating oxide film, leading to generation of oxide debris and metal ions released as a result of active metal corrosion. Metal ions and solid debris particles released as byproducts of anodic polarization of CoCrMo alloy were thus tested for their influence on macrophage viability and activation. We found that small concentrations of a solution rich in chromium ions and containing a small amount of cobalt and molybdenum ions have a drastic killing effect on macrophages. Since anodic polarization of CoCrMo is known to generate the cytotoxic and carcinogenic Cr(VI) valence state of the Chromium ion, we can attribute the high killing effect of small concentrations ( $\leq 1\%$  by volume) of the corrosion fluid. Sublethal doses were shown induce a weak proinflammatory activation, which were presented through the secreted cytokines and chemokines. We concluded that the proinflammatory response wasn't as strong as that seen in LPS-activated cells, but this could be a result of cytokine secretion kinetics leading to a more immediate, heightened response which was dampened by the 24 h time point investigated in our study. It is also likely that the metal ions do not activate the same pathways of cell death and activation that LPS activates in macrophages, which is mediated by classical activation pathways involving nuclear factor-kappa light-chain-enhancer of activated-B cells (NF- $\kappa$ B), signal transducer and activator of transcription 1 (STAT1), as well as interferon regulatory factor 5 (IRF 5), all of which lead to recruitment of TH-1 helper cells [145]. Cr(VI), on the other hand, is known to induce high levels of oxidative stress in cultured macrophages and cause DNA

damage [146], ultimately leading to apoptosis-related cell death [134]. It is likely that exposure to Cr(VI) and other ionic species at a sublethal dose created a compound effect of activation and cell death, and therefore, the cytokine levels were lower compared to LPS-activated cells.

Crucially, the solid debris rich in cobalt oxides did not elicit a high killing effect in macrophages with the concentration used in our study. This contrasts with another recent study that utilized three orders of magnitude fewer particles of a slightly smaller size, and reported a higher rate of killing [57]. We attribute this difference mainly to the composition of the particles used in each study: in our study, we used corrosion byproduct debris, which were oxide rich and relatively stable electrochemically. Whereas the study cited here used wear debris, which are primarily metal particles which are likely to oxidize in aqueous conditions. Nanoparticles are also known to be more lethal to cells than larger-sized particles [107].

When considering that a total hip arthroplasty device in a biological environment might be under attack from the innate immune system as part of the wound healing cascade, and that THAs are often recommended in the case of inflammatory joint conditions like osteoarthritis, the biological environment can be thought to play a larger role in perpetuating implant degradation than has been considered before. Retrieval studies amply demonstrate that some of the damage seen on retrieved devices is severe, and as yet, has not been recreated under laboratory conditions. Even employing inflammatory species in the in vitro test methods at concentrations much higher than those thought to occur physiologically have not been able to faithfully replicate the corrosion damage seen

in revised devices. One of the factors, crucially, is the amount of time that devices can be implanted for, although some retrieved devices have had to be revised in a matter of months from the primary surgery. Laboratory tests can span a few days, but most do not approach the time to failure of revised devices. Another critical factor is the role of the crevice environment which has not been characterized as yet. We know the crevice corrosion aspect of implant corrosion can be enhanced by fretting corrosion and through altered solution chemistry. But the exact nature of the crevice solution chemistry and how it affects corrosion processes is as yet unknown. It is critical to also consider the biological environment forming a feedback loop with implant degradation. Clinical causes for failure include unexplained pain, aseptic loosening, often at the implant-bone interface, and infection. Device failure is also often associated with adverse local tissue reactions, including avascular necrosis, bone lysis or bone loss, and soft tissue masses known as pseudotumor, the causes for which remain largely unknown.

Through the studies forming this thesis, we have attempted to showcase the different aspects driving corrosion-related failure at acetabular taper junctions. We have presented methods that form starting points for future work to further explore the mechanisms of implant corrosion *in vivo*, not just at the acetabular junction, but in modular junctions and bearing surfaces in other devices as well. While there are materials that have been in wide usage for decades, they are not without drawbacks and disadvantages. The wrought CoCrMo alloy that formed a common thread through all the studies in this thesis was developed with its fine-grained microstructure and the dispersed hard phase carbides and Mo-Si-O particles to improve mechanical and corrosion performance. But this

improvement might also present with a cost: the risk of the hard phase particles being released due to material loss at the alloy surface. Overall, continuous improvement is the only way forward, and the hope is that through this thesis and its findings, we may be driven to design better devices and materials to improve device longevity and patient outcomes.

## **Chapter 10**

### **Conclusions**

The primary goal of this thesis was to develop and validate test methods that will investigate modular acetabular taper corrosion and characterize its mechanical and electrochemical causes and investigate immune system interactions. Through each study conducted as part of this work, we have presented findings from retrieved devices, designed in vitro test methods to investigate mechanical causes of acetabular taper corrosion, and demonstrated the deleterious effects of tribocorrosion and inflammation-driven corrosion byproducts on macrophages.

Our retrieval study primarily showed that corrosion in acetabular tapers occurs independent of mechanical stimuli. This was shown through the documentation of corrosion damage occurring outside direct mechanical contact, and the absence of clear signs of mechanical abrasion and wear processes in the vicinity of severe corrosion damage. We also presented evidence of large volumes of submicron hard phase particles released from the wrought CoCrMo alloy microstructure, which has implications for inducing adverse local tissue reactions in surrounding tissue. Finally, cellular remnants were found on the taper surfaces, with a size distribution overlapping with that of macrophages, indicating that macrophages and other immune system cells might play a larger role in taper corrosion than previously believed.

We developed a test method using near-field electrochemical impedance spectroscopy (nfEIS) and symmetry-based EIS analysis (sbEIS) to measure impedance on retrieved



liner taper surfaces on small areas, under 1 mm<sup>2</sup>. Our test method proved capable of discerning the granular nature of corrosion-driven damage types, including intergranular corrosion (IGC), oxide deposits and phase boundary corrosion (PBC), on the retrieved device surface, wherein localized corrosion damage induces unique modifications to the local impedance characteristics. Using sbEIS, we were able to scan small areas in under 30 minutes time, and in conjunction with visual assessment using electron microscopy, we found direct associations between the Bode plots and visual damage features. PBC was found to have the most intact surface, with impedance closest to a polished CoCrMo disk surface, whereas oxide deposits were found to have the least corrosion resistance and diffusion-like behavior.

In order to investigate mechanically-assisted crevice corrosion in acetabular tapers, we designed test methods to repeatably assemble shell-liner pairs and then measure fretting corrosion response to incremental cyclic compressive loading, with the construct held at a physiological angle of 55° to the normal axis. The shells used were porous-coated Ti6Al4V and the liners investigated were of three different materials: high carbon (HC) CoCrMo, low carbon (LC) CoCrMo and 316L stainless steel (SS). We found that over the course of the short-term test, with loads of up to 4000 N, the shell-liner junction did not generate currents higher than 1 µA on average. Onset loads and average currents did not differ significantly with the material change, and the contact area on the titanium shell and the liners was a small fraction of the actual taper surface area. Overall, we concluded that MACC at MoM acetabular taper junctions, in the absence of oxidizing

species and biological components, does not represent a serious driver of corrosion damage.

In order to investigate these findings further, we measured the taper stiffness of porous-coated Ti6Al4V shells and liners of the three different materials as the previous study. We conducted measurements on devices of two different sizes as well, to investigate changes in taper compliance with size increase. We found that there was no change in taper stiffness (inverse of compliance) with change in size for the shells and for HC and LC CoCrMo liners. SS liners showed a change in compliance, with the larger size liners being stiffer compared to the smaller size. We also found that within the same size grouping, shells were compliance matched to HC, LC, and SS liners. Compliance matched taper interfaces could lead to lower interfacial micromotion, thereby reducing the propensity for fretting corrosion.

Ongoing tribocorrosion was found to have a heightened lethal effect on macrophages cultured in their vicinity. Macrophage mortality was highest in the presence of ongoing potentiostatically controlled fretting corrosion, followed by uncontrolled fretting corrosion which induced a potential drop of up to -518 mV on the CoCrMo surface. An externally applied cathodic bias of -500 mV, however, had a significantly lower killing effect, which indicates that a combination of ongoing redox reactions modulated by oxide abrasion and repassivation, along with oxide debris and metal ion generation play a synergistic role in modulating macrophage mortality. Further research is recommended to investigate phenotypic changes and cell death pathways in macrophages exposed to ongoing fretting corrosion.

Finally, anodic polarization of CoCrMo can be caused due to oxidizing species such as hydrogen peroxide, hypochlorous acid and other reactive oxygen species (ROS) ubiquitous in an inflamed joint space. We investigated the effects of anodic polarization byproducts, namely Cr, Co and Mo ions and solid oxide particle debris, on macrophage viability and activation to understand how the phagocytic cells might respond to similar byproducts in vivo. Our findings show that metal ions, particularly high concentrations (>150 ppm) chromium ions, can induce almost 100% cell death at 1% by volume concentrations of fluid conditioned by anodic polarization of CoCrMo. At sublethal doses (LD50), a weak proinflammatory response was detected, marked by secretion of cytokines like TNF- $\alpha$ , interleukin (IL)-1 $\beta$  and IFN- $\gamma$ , but not to the same quantity as LPS-activated macrophages. An anti-inflammatory cytokine, IL-13, was also detected indicating that metal ions induce a complex phenotype that might be intermediate between M1 and M2 states. Solid oxide debris, rich in cobalt and oxygen, had a proximity-dependent effect on macrophage mortality, rather than concentration-dependent. These particles were stable in solution over a long period (several weeks) and were on the size scale of 100-200  $\mu\text{m}$ .

In conclusion, corrosion processes at MoM acetabular junctions are driven by more than mechanically-associated processes. Inflammatory conditions, crevice environment and immune system cells might play a larger role than we currently understand in driving corrosion related damage and material loss. Using the test methods developed in this thesis, we can further understand the interactions between corrosion, both tribocorrosion and chemically driven corrosion modes, and the local biological environment. While

some of these interactions and resulting downstream effects and implant degradation are inevitable as part of the natural wound healing process of the human body, we can develop a better understanding of how device design, mechanics and material selection might mitigate or exacerbate local corrosion processes. The goal, ultimately, is to elongate device implantations times, and to improve patient outcomes from primary surgeries. Improving designs and materials is a definitive way to achieve that goal.

## **Chapter 11**

### **Future Work**

While the studies presented in this thesis successfully advance our understanding of corrosion at the metal-on-metal acetabular junction, they also present many interesting questions that can drive further research and illuminate gaps in our knowledge of in vivo corrosion in modular metallic implants.

In terms of retrieval analysis, one of the limitations of our study was that single manufacturer, single design, single material devices were analyzed. Including devices from other manufacturers and studying corrosion and damage features in cast CoCrMo devices as well will enhance our understanding of design-specific and material-specific corrosion processes, especially since our study was restricted to MoM liners and did not include dual-mobility devices which are more widely used. MDM devices are distinct in their design from MoM devices and are also used specifically in dislocation risk revision surgeries. Patients with high risk of dislocation often present with unique anatomical challenges that alter the hip joint anatomy and gait in significant ways. Overall, expanding the sample size appropriately allows us to develop broader understanding of in vivo acetabular taper corrosion. Including acetabular shells, typically titanium alloy shells, will also provide a larger frame to understand how interfacial motion and crevice conditions might play out in different materials experiencing analogous loads and moments in the same biological environment.

The symmetry-based near-field electrochemical impedance spectroscopy (sbnfEIS) technique presented in this thesis is uniquely suited to bring an electrochemical quantitative tool into retrieval analysis. However, our study was limited in terms of the types of corrosion examined as well as in the materials studied. Expanding the sample group to include other material types, especially cast CoCrMo and Ti6Al4V which are both commonly used not only in acetabular component applications but overall, in hip implant and other joint replacement systems would be beneficial. We also presented results that show an intriguing relationship between polarization resistance,  $R_p$ , and the constant-phase element magnitude parameter,  $Q$ , which indicated that the time constants detected through the numerical analysis techniques might be an intrinsic material property, which can be examined if the sbnfEIS technique is applied to different material types. This can lead to enhancing our understanding of fundamental material structure-property relationships which are as yet unexplored. Additionally, impedance spectroscopy in general holds a lot of promise in sensor development across clinical applications, and using the sbnfEIS technique, allows us to study impedance changes across small surface areas over vast electrode regions as well. Integrating this impedance measurement technique with appropriately designed compact sensors and machine learning type algorithms might create a paradigm shift in how implanted devices can be monitored or assessed during revision surgeries or even during implantation.

We presented test methods that examines the liner-shell seating event and mechanics as well as a means to study mechanical loading and fretting corrosion correlations.

However, both test methods can be improved to resemble actual surgical practice and in

vivo physiological conditions more closely. The seating method used in our study was an incremental quasistatic ramp, which is not typical of how in situ surgical assembly of shell-liner junctions are conducted. Surgeons tend to impact the acetabular shell into an under-reamed acetabulum (in the pelvic bone) which owing to the anisotropic nature of the cancellous bone and its distribution, leads to uneven stress distribution around the hemispherical periphery of the shell [147]. In future studies, instead of employing the shell in a seating test as received in a pristine condition, the uneven stress distribution can be emulated by deforming the shell prior to seating the liner. The seating technique could also be modified to reflect surgical techniques which involve impaction into the shell rather than an incremental constant-slope load application. This would ensure that interfacial contact between the shell and liner are more physiologically relevant and might produce different contact areas and fretting corrosion outcomes compared to our current methods. Another aspect that warrants systematic investigation is the hip joint inclination angle differences and their effects on mechanical micromotion and subsequent corrosion performance of the shell-liner taper. Impingement occurs when the anteversion angle at the hip joint is higher than  $45^\circ$  and can lead to edge loading and specific wear patterns leading to implant degradation and failure.

Additionally, the solution used as electrolyte in our incremental fretting corrosion experiment was a phosphate-buffered saline (PBS), which is a good model for electrochemical evaluations. However, the biological environment and the fluids present there are far more complex. Including protein components such as fetal bovine serum, albumin, amino acids and simulating inflammatory conditions by including ROS

molecules like hydrogen peroxide would bring the test method closer to simulating biological conditions. Moreover, considering that the hip joint is highly mobile, capable of rotation, flexion-extension and abduction-adduction, simply applying cyclic compression during fretting corrosion assessments excludes important gait inputs, which can be improved by including a torsion element to the load applied. Further, to understand the links between load application during seating and subsequent cyclic loading at the shell-liner junction and the subsidence of the liner into the shell, whether it is uniform across the plane or there is canting or ratcheting of the liner into the shell, is crucial to improve our understanding of how these modular junctions perform. Including displacement sensors during seating and cyclic loading will be a valuable addition to the test methods.

Cell-material interactions studies involving tribocorrosion and inflammation-related corrosion and immune system cells can address a host of questions raised in this thesis. Pin-on-disk fretting corrosion experiments with macrophages can be used to study further downstream effects of exposure to fretting corrosion processes both on and off the disk. Analyzing the test media for signaling molecules or chemoattractant molecules expressed by cells under stress from ongoing corrosion can be useful to understand how in vivo corrosion influences immune system processes. Another aspect that warrants further investigation is the study of macrophage behavior and phenotypic/activation changes in higher temperature conditions, since local inflammation can manifest with raised temperatures. Using other cell types, potentially including co-cultures with macrophages, fibroblasts and/or osteoclasts, or using undifferentiated monocytes and tracking



differentiation into different cell types using flow cytometry and surface markers would be an excellent next step to establishing the corrosion-biology feedback loop briefly discussed in this thesis. Phenotypic changes in the cells, especially macrophages, would also be helpful to understand any proinflammatory or chemotactic cues generated from corrosion processes. Finally, the observations that cells seem to be found in tight crevice-like modular junctions across retrieval analysis studies points to a migration of cells, particularly macrophages, into these spaces, which might be prone to accelerated corrosion due to MACC or chemically-driven corrosion modes. Designing migration assays that simulate crevice conditions, and maybe fretting corrosion, is recommended.

The final research chapter in this thesis shows a link between anodic polarization byproducts and macrophage mortality. For future studies, a more systematic exploration of lower concentrations of metal ions can be explored as a means of inducing macrophage activation. Additionally, exploring the difference between wear particles and corrosion byproduct oxide particles and how each of them modulates cell death would be an interesting study to answer the questions of what kind of tribocorrosion processes can lead to maximum harm. This can help identify critical design or material changes that would mitigate that specific kind of degradation.

## REFERENCES

- [1] J. Charnley, "ARTHROPLASTY OF THE HIP. A New Operation," *Lancet*, vol. 277, no. 7187, pp. 1129–1132, May 1961.
- [2] J. Charnley, "The long-term results of low-friction arthroplasty of the hip performed as a primary intervention.," *J. Bone Joint Surg. Br.*, vol. 54, no. 1, pp. 61–76, Feb. 1972.
- [3] R. N. Stauffer, "Ten-year follow-up study of total hip replacement," *J. Bone Jt. Surg. - Ser. A*, 1982.
- [4] H. Gruen, T A, McNeice, GM, Amstuts, "'Modes of failure' of Cemented Stem-Type Femoral Components," *Clin. Orthop. Relat. Res.*, 1979.
- [5] A. Neuprez *et al.*, "Total joint replacement improves pain, functional quality of life, and health utilities in patients with late-stage knee and hip osteoarthritis for up to 5 years," *Clin. Rheumatol.*, vol. 39, no. 3, pp. 861–871, Mar. 2020.
- [6] J. Singh, V. A., S. Yu, L. Chen, and J. D. Cleveland, "Rates of Total Joint Replacement in the United States: Future Projections to 2020–2040 Using the National Inpatient Sample," *J. Rheumatol.*, vol. 46, no. 9, pp. 1134–1140, Sep. 2019.
- [7] K. Kindsfater and J. Lesko, "Survivorship of a modular acetabular cup system: medium- to long-term follow-up," *Arthroplast. Today*, Aug. 2017.
- [8] L. M. Jazrawi, F. J. Kummer, and P. E. DiCesare, "Alternative bearing surfaces for

- total joint arthroplasty [In Process Citation],” *J Am Acad Orthop Surg*, vol. 6, no. 4, pp. 198–203, 1998.
- [9] M. T. Clarke, C. Darrah, T. Stewart, E. Ingham, J. Fisher, and J. F. Nolan, “Long-Term Clinical, Radiological and Histopathological Follow-Up of a Well-Fixed McKee-Farrar Metal-on-Metal Total Hip Arthroplasty,” *J. Arthroplasty*, vol. 20, no. 4, pp. 542–546, Jun. 2005.
- [10] T. C. Gascoyne, T. R. Turgeon, and C. D. Burnell, “Retrieval Analysis of Large-Head Modular Metal-on-Metal Hip Replacements of a Single Design,” *J. Arthroplasty*, vol. 33, no. 6, pp. 1945–1952, 2018.
- [11] T. C. Gascoyne, R. M. Dyrkacz, T. R. Turgeon, C. D. Burnell, U. P. Wyss, and J. M. Brandt, “Corrosion on the Acetabular Liner Taper from Retrieved Modular Metal-on-Metal Total Hip Replacements,” *J. Arthroplasty*, vol. 29, no. 10, pp. 2049–2052, 2014.
- [12] L. J. Matsen Ko, K. E. Pollag, J. Y. Yoo, and P. F. Sharkey, “Serum Metal Ion Levels Following Total Hip Arthroplasty With Modular Dual Mobility Components,” *J. Arthroplasty*, vol. 31, no. 1, pp. 186–189, Jan. 2016.
- [13] D. R. Plummer, H. G. Botero, K. R. Berend, J. W. Pritchett, A. V. Lombardi, and C. J. Della Valle, “Salvage of Monoblock Metal-on-Metal Acetabular Components Using a Dual-Mobility Bearing,” *J. Arthroplasty*, vol. 31, no. 4, pp. 846–849, 2016.

- [14] J. N. Katz *et al.*, “Twelve-year risk of revision after primary total hip replacement in the U.S. medicare population,” *J. Bone Jt. Surg. - Ser. A*, 2012.
- [15] S. Kurtz, K. Ong, E. Lau, F. Mowat, and M. Halpern, “Projections of Primary and Revision Hip and Knee Arthroplasty in the United States from 2005 to 2030,” *J. Bone Jt. Surg.*, 2007.
- [16] K. J. Bozic, P. Katz, M. Cisternas, L. Ono, M. D. Ries, and J. Showstack, “Hospital Resource Utilization for Primary and Revision Total Hip Arthroplasty,” *J. Bone Jt. Surg.*, vol. 87, no. 3, pp. 570–576, Mar. 2005.
- [17] K. J. Bozic *et al.*, “Comparative Epidemiology of Revision Arthroplasty: Failed THA Poses Greater Clinical and Economic Burdens Than Failed TKA,” *Clin. Orthop. Relat. Res.*, 2015.
- [18] C. U. Gwam *et al.*, “Current Epidemiology of Revision Total Hip Arthroplasty in the United States: National Inpatient Sample 2009 to 2013,” *J. Arthroplasty*, vol. 32, no. 7, pp. 2088–2092, Jul. 2017.
- [19] J. J. Jauregui, T. P. Pierce, R. K. Elmallah, J. J. Cherian, R. E. Delanois, and M. A. Mont, “Dual Mobility Cups: An Effective Prosthesis in Revision Total Hip Arthroplasties for Preventing Dislocations,” *HIP Int.*, vol. 26, no. 1, pp. 57–61, Jan. 2016.
- [20] E. G. Sutter, T. R. McClellan, D. E. Attarian, M. P. Bolognesi, P. F. Lachiewicz, and S. S. Wellman, “Outcomes of Modular Dual Mobility Acetabular Components

- in Revision Total Hip Arthroplasty,” *J. Arthroplasty*, vol. 32, no. 9, pp. S220–S224, Sep. 2017.
- [21] J. J. Jacobs, “Corrosion at the Head-Neck Junction: Why Is This Happening Now?,” *J. Arthroplasty*, vol. 31, no. 7, pp. 1378–1380, Jul. 2016.
- [22] F. E. Rowan, B. Benjamin, J. R. Pietrak, and F. S. Haddad, “Prevention of Dislocation After Total Hip Arthroplasty,” *J. Arthroplasty*, vol. 33, no. 5, pp. 1316–1324, May 2018.
- [23] B. Boyer, R. Philippot, J. Geringer, and F. Farizon, “Primary total hip arthroplasty with dual mobility socket to prevent dislocation: a 22-year follow-up of 240 hips,” *Int. Orthop.*, vol. 36, no. 3, pp. 511–518, Mar. 2012.
- [24] I. De Martino, R. D’Apolito, V. G. Soranoglou, L. A. Poultsides, P. K. Sculco, and T. P. Sculco, “Dislocation following total hip arthroplasty using dual mobility acetabular components,” *Bone Joint J.*, vol. 99-B, no. 1\_Supple\_A, pp. 18–24, Jan. 2017.
- [25] S. F. Harwin, A. Khlopas, N. Sodhi, A. A. Sultan, J. Ehiorobo, and M. A. Mont, “Outcomes of dual mobility acetabular cups in total hip arthroplasty patients,” *Surg. Technol. Int.*, 2019.
- [26] K. C. Ilo, E. J. Derby, R. K. Whittaker, G. W. Blunn, J. A. Skinner, and A. J. Hart, “Fretting and Corrosion Between a Metal Shell and Metal Liner May Explain the High Rate of Failure of R3 Modular Metal-on-Metal Hips,” *J. Arthroplasty*, vol.

32, no. 5, pp. 1679–1683, 2017.

- [27] T. D. Tarity, C. N. Koch, J. C. Burket, T. M. Wright, and G. H. Westrich, “Fretting and Corrosion at the Backside of Modular Cobalt Chromium Acetabular Inserts: A Retrieval Analysis,” *J. Arthroplasty*, vol. 32, no. 3, pp. 1033–1039, 2017.
- [28] J. M. Kolz, C. C. Wyles, D. W. Van Citters, R. M. Chapman, R. T. Trousdale, and D. J. Berry, “In Vivo Corrosion of Modular Dual-Mobility Implants: A Retrieval Study,” *J. Arthroplasty*, vol. 0, no. 0, 2020.
- [29] H. S. Hothi, K. Ilo, R. K. Whittaker, A. Eskelinen, J. A. Skinner, and A. J. Hart, “Corrosion of Metal Modular Cup Liners,” *J. Arthroplasty*, vol. 30, no. 9, pp. 1652–1656, 2015.
- [30] M. T. Agne *et al.*, “Is there material loss at the backside taper in modular CoCr acetabular liners?,” *Clin. Orthop. Relat. Res.*, vol. 473, no. 1, pp. 275–85, Jan. 2015.
- [31] H. S. Hothi, A. K. Matthies, R. Berber, R. K. Whittaker, J. A. Skinner, and A. J. Hart, “The reliability of a scoring system for corrosion and fretting, and its relationship to material loss of tapered, modular junctions of retrieved hip implants,” *J. Arthroplasty*, vol. 29, no. 6, pp. 1313–1317, 2014.
- [32] J. L. Gilbert, S. Sivan, Y. Liu, S. B. Kocagöz, C. M. Arnholt, and S. M. Kurtz, “Direct in vivo inflammatory cell-induced corrosion of CoCrMo alloy orthopedic implant surfaces,” *J. Biomed. Mater. Res. Part A*, vol. 103, no. 1, pp. 211–223,

Jan. 2015.

- [33] D. C. Rodrigues, R. M. Urban, J. J. Jacobs, and J. L. Gilbert, “In vivo severe corrosion and hydrogen embrittlement of retrieved modular body titanium alloy hip-implants,” *J. Biomed. Mater. Res. - Part B Appl. Biomater.*, vol. 88, no. 1, pp. 206–219, 2009.
- [34] Y. Liao, E. Hoffman, M. Wimmer, A. Fischer, J. Jacobs, and L. Marks, “CoCrMo metal-on-metal hip replacements,” *Physical Chemistry Chemical Physics*, vol. 15, no. 3. NIH Public Access, pp. 746–756, 21-Jan-2013.
- [35] E. E. Hoffman, A. Lin, Y. Liao, and L. D. Marks, “Grain Boundary Assisted Crevice Corrosion in CoCrMo Alloys,” *CORROSION*, vol. 72, no. 11, pp. 1445–1461, Nov. 2016.
- [36] J. L. Gilbert, “Electrochemical Behavior of Metals in the Biological Milieu,” in *Comprehensive Biomaterials*, Elsevier, 2011, pp. 21–48.
- [37] J. Lin, “AN ELECTROCHEMICAL METHOD TO EVALUATE LOCALIZED CORROSION IN RETRIEVED MODULAR TAPERED ORTHOPEDIC IMPLANTS,” Syracuse University, 2016.
- [38] M. J. Wiegand, A. A. Shenoy, S. E. Littlejohn, and J. L. Gilbert, “Sensing Localized Surface Corrosion Damage of CoCrMo Alloys and Modular Tapers of Total Hip Retrievals Using Nearfield Electrochemical Impedance Spectroscopy,” *ACS Biomater. Sci. Eng.*, 2020.

- [39] R. G. Duarte, A. S. Castela, and M. G. S. Ferreira, "A new model for estimation of water uptake of an organic coating by EIS: The tortuosity pore model," *Prog. Org. Coatings*, vol. 65, no. 2, pp. 197–205, Jun. 2009.
- [40] K. Jüttner, "Electrochemical impedance spectroscopy (EIS) of corrosion processes on inhomogeneous surfaces," *Electrochim. Acta*, vol. 35, no. 10, pp. 1501–1508, Oct. 1990.
- [41] F. Bellucci and L. Nicodemo, "Water transport in organic coatings," *Corrosion*, vol. 49, no. 3, pp. 235–247, Mar. 1993.
- [42] J. R. Goldberg, J. L. Gilbert, J. J. Jacobs, T. W. Bauer, W. Paprosky, and S. Leurgans, "A multicenter retrieval study of the taper interfaces of modular hip prostheses.," *Clin. Orthop. Relat. Res.*, no. 401, pp. 149–61, Aug. 2002.
- [43] J. L. Gilbert, C. A. Buckley, and J. J. Jacobs, "In vivo corrosion of modular hip prosthesis components in mixed and similar metal combinations. The effect of crevice, stress, motion, and alloy coupling.," *J. Biomed. Mater. Res.*, vol. 27, no. 12, pp. 1533–44, Dec. 1993.
- [44] D. J. Hall, R. Pourzal, C. J. Della Valle, J. O. Galante, J. J. Jacobs, and R. M. Urban, "Corrosion of Modular Junctions in Femoral and Acetabular Components for Hip Arthroplasty and Its Local and Systemic Effects," *Modul. Tapers Total Jt. Replace. Devices ASTM STP1591*, pp. 410–427, Dec. 2015.
- [45] E. S. Ouellette, S. A. Mali, J. Kim, J. Grostefon, and J. L. Gilbert, "Design,



- Material, and Seating Load Effects on In Vitro Fretting Corrosion Performance of Modular Head-Neck Tapers,” *J. Arthroplasty*, vol. 34, no. 5, pp. 991–1002, May 2019.
- [46] G. B. Higgs, J. A. Hanzlik, D. W. Macdonald, J. L. Gilbert, C. M. Rimnac, and S. M. Kurtz, “Is Increased Modularity Associated With Increased Fretting and Corrosion Damage in Metal-On-Metal Total Hip Arthroplasty Devices ? A Retrieval Study,” *J. Arthroplasty*, vol. 28, no. 8, pp. 2–6, 2013.
- [47] S. A. Mali and J. L. Gilbert, “Correlating Fretting Corrosion and Micromotions in Modular Tapers: Test Method Development and Assessment,” *ASTM STP1591*, no. ASTM STP1591, pp. 259–282, Dec. 2015.
- [48] E. S. Ouellette, A. A. Shenoy, and J. L. Gilbert, “The seating mechanics of head-neck modular tapers in vitro: Load-displacement measurements, moisture, and rate effects,” *J. Orthop. Res.*, Feb. 2018.
- [49] A. K. Blakney, M. D. Swartzlander, and S. J. Bryant, “The effects of substrate stiffness on the in vitro activation of macrophages and in vivo host response to poly(ethylene glycol)-based hydrogels,” *J. Biomed. Mater. Res. - Part A*, vol. 100, no. 6, pp. 1375–1386, 2012.
- [50] J. A. Jones *et al.*, “Proteomic analysis and quantification of cytokines and chemokines from biomaterial surface-adherent macrophages and foreign body giant cells,” *J. Biomed. Mater. Res. Part A*, vol. 83A, no. 3, pp. 585–596, Dec. 2007.

- [51] J. M. Anderson, A. Rodriguez, and D. T. Chang, "Foreign body reaction to biomaterials.," *Semin. Immunol.*, vol. 20, no. 2, pp. 86–100, Apr. 2008.
- [52] B. Scharf *et al.*, "Molecular analysis of chromium and cobalt-related toxicity," *Sci. Rep.*, vol. 4, no. 1, p. 5729, May 2015.
- [53] H.-Y. Lin and J. D. Bumgardner, "Changes in the surface oxide composition of Co–Cr–Mo implant alloy by macrophage cells and their released reactive chemical species," *Biomaterials*, vol. 25, no. 7–8, pp. 1233–1238, Mar. 2004.
- [54] R. Tsaryk *et al.*, "Response of human endothelial cells to oxidative stress on Ti6Al4V alloy," *Biomaterials*, vol. 28, no. 5, pp. 806–813, Feb. 2007.
- [55] Q. Chen *et al.*, "TiO<sub>2</sub>nanoparticles cause mitochondrial dysfunction, activate inflammatory responses, and attenuate phagocytosis in macrophages: A proteomic and metabolomic insight," *Redox Biol.*, vol. 15, no. December 2017, pp. 266–276, 2018.
- [56] M. J. Wiegand, T. Z. Benton, and J. L. Gilbert, "A fluorescent approach for detecting and measuring reduction reaction byproducts near cathodically-biased metallic surfaces: Reactive oxygen species production and quantification," *Bioelectrochemistry*, 2019.
- [57] D. R. Bijukumar *et al.*, "In Vitro Evidence for Cell-Accelerated Corrosion Within Modular Junctions of Total Hip Replacements," *J. Orthop. Res.*, p. jor.24447, Sep. 2019.

- [58] D. R. Bijukumar *et al.*, “Wear particles induce a new macrophage phenotype with the potential to accelerate material corrosion within total hip replacement interfaces,” *Acta Biomater.*, vol. 101, pp. 586–597, Jan. 2020.
- [59] O. L. Huk, I. Catelas, F. Mwale, J. Antoniou, D. J. Zukor, and A. Petit, “Induction of apoptosis and necrosis by metal ions in vitro,” *J. Arthroplasty*, vol. 19, no. 8, pp. 84–87, Dec. 2004.
- [60] S. Landgraeber, M. Jäger, J. J. Jacobs, and N. J. Hallab, “The pathology of orthopedic implant failure is mediated by innate immune system cytokines,” *Mediators Inflamm.*, vol. 2014, 2014.
- [61] I. Catelas, A. Petit, D. J. Zukor, J. Antoniou, and O. L. Huk, “TNF- $\alpha$  secretion and macrophage mortality induced by cobalt and chromium ions in vitro - Qualitative analysis of apoptosis,” *Biomaterials*, vol. 24, no. 3, pp. 383–391, Feb. 2003.
- [62] M. A. Ferko and I. Catelas, “Effects of metal ions on caspase-1 activation and interleukin-1 $\beta$  release in murine bone marrow-derived macrophages,” *PLoS One*, vol. 13, no. 8, Aug. 2018.
- [63] Z. Salloum, E. A. Lehoux, M.-E. Harper, and I. Catelas, “Effects of cobalt and chromium ions on oxidative stress and energy metabolism in macrophages in vitro,” *J. Orthop. Res.*, vol. 36, no. 12, pp. 3178–3187, Dec. 2018.
- [64] M. S. D’Arcy, “Cell death: a review of the major forms of apoptosis, necrosis and autophagy,” *Cell Biol. Int.*, vol. 43, no. 6, pp. 582–592, Jun. 2019.

- [65] Y. Liu and J. L. Gilbert, “The effect of simulated inflammatory conditions and Fenton chemistry on the electrochemistry of CoCrMo alloy,” *J. Biomed. Mater. Res. Part B Appl. Biomater.*, vol. 106, no. 1, pp. 209–220, Jan. 2018.
- [66] G. W. Kubacki and J. L. Gilbert, “The effect of the inflammatory species hypochlorous acid on the corrosion and surface damage of Ti-6Al-4V and CoCrMo alloys,” *J. Biomed. Mater. Res. Part A*, vol. 106, no. 12, pp. 3185–3194, Dec. 2018.
- [67] J. L. Gilbert, “Corrosion in the Human Body: Metallic Implants in the Complex Body Environment,” *CORROSION*, vol. 73, no. 12, pp. 1478–1495, Dec. 2017.
- [68] C. Valero and A. Igual, “Electrochemical Aspects in Biomedical Alloy Characterization: Electrochemical Impedance Spectroscopy,” in *Biomedical Engineering, Trends in Materials Science*, InTech, 2011.
- [69] J. L. Gilbert, S. A. Mali, and Y. Liu, “Area-dependent impedance-based voltage shifts during tribocorrosion of Ti-6Al-4V biomaterials: theory and experiment,” *Surf. Topogr. Metrol. Prop.*, vol. 4, no. 3, p. 034002, Jun. 2016.
- [70] M. P. Abdel, “Dual-Mobility Constructs in Revision Total Hip Arthroplasties,” *J. Arthroplasty*, vol. 33, no. 5, pp. 1328–1330, 2018.
- [71] J. L. Gilbert, S. A. Mali, and S. Sivan, “Corrosion of Modular Tapers in Total Joint Replacements: A Critical Assessment of Design, Materials, Surface Structure, Mechanics, Electrochemistry, and Biology,” *ASTM STP1591*, no. ASTM

STP1591, pp. 192–223, Dec. 2015.

- [72] I. De Martino, J. B. Assini, M. E. Elpers, T. M. Wright, and G. H. Westrich, “Corrosion and Fretting of a Modular Hip System: A Retrieval Analysis of 60 Rejuvenate Stems,” *J. Arthroplasty*, vol. 30, no. 8, pp. 1470–1475, Aug. 2015.
- [73] A. A. Shenoy and J. L. Gilbert, “In vitro test methods for seating and fretting corrosion behavior of modular metal-on-metal acetabular tapers,” *J. Orthop. Res.*, p. jor.24554, Dec. 2019.
- [74] S. N. Shah, R. J. Kaye, N. H. Kelly, E. P. Su, D. E. Padgett, and T. M. Wright, “Retrieval Analysis of Failed Constrained Acetabular Liners,” *J. Arthroplasty*, vol. 24, no. 6, pp. 54–57, Sep. 2009.
- [75] M. T. Agne *et al.*, “Is There Material Loss at the Backside Taper in Modular CoCr Acetabular Liners?,” *Clin. Orthop. Relat. Res.*, vol. 473, no. 1, pp. 275–285, 2015.
- [76] Y. Liao, R. Pourzal, M. A. Wimmer, J. J. Jacobs, A. Fischer, and L. D. Marks, “Graphitic Tribological Layers in Metal-on-Metal Hip Replacements,” *Science* (80-. ), vol. 334, no. 6063, pp. 1687–1690, Dec. 2011.
- [77] H. S. Hothi *et al.*, “Damage Patterns at the Head-Stem Taper Junction Helps Understand the Mechanisms of Material Loss,” *J. Arthroplasty*, vol. 32, no. 1, pp. 291–295, Jan. 2017.
- [78] J. Jacobs, J. Gilbert, and R. Urban, “Current Concepts Review-Corrosion of Metal Orthopaedic Implants,” *J Bone Jt. Surg*, vol. 80, pp. 268–82, 1998.

- [79] J. P. Bearinger, C. a Orme, and J. L. Gilbert, "Effect of hydrogen peroxide on titanium surfaces: in situ imaging and step-polarization impedance spectroscopy of commercially pure titanium and titanium, 6-aluminum, 4-vanadium.," *J. Biomed. Mater. Res. A*, vol. 67, no. January 2016, pp. 702–712, 2003.
- [80] M. T. Ehrensberger and J. L. Gilbert, "The effect of static applied potential on the 24-hour impedance behavior of commercially pure titanium in simulated biological conditions," *J. Biomed. Mater. Res. - Part B Appl. Biomater.*, vol. 93, no. 1, pp. 106–112, 2010.
- [81] E. Akbarinezhad, M. Bahremandi, H. R. Faridi, and F. Rezaei, "Another approach for ranking and evaluating organic paint coatings via electrochemical impedance spectroscopy," *Corros. Sci.*, vol. 51, no. 2, pp. 356–363, Feb. 2009.
- [82] D. Loveday, P. Peterson, and B. Rodgers, "Evaluation of Organic Coatings with Electrochemical Impedance Spectroscopy," *JCT Coatings Tech*, vol. 8, pp. 46–52, 2004.
- [83] J. L. Gilbert and P. Khullar, "Analysis of Electrochemical Impedance Spectra Using Phase Angle Symmetry Across Log Frequency," *J. Electrochem. Soc.*, vol. 167, no. 2, p. 021505, Jan. 2020.
- [84] M. J. Wiegand, A. A. Shenoy, S. E. Littlejohn, and J. L. Gilbert, "Sensing Localized Surface Corrosion Damage of CoCrMo Alloys and Modular Tapers of Total Hip Retrievals Using Nearfield Electrochemical Impedance Spectroscopy," *ACS Biomater. Sci. Eng.*, vol. 6, no. 3, pp. 1344–1354, Mar. 2020.

- [85] D. J. Hall, R. Pourzal, H. J. Lundberg, M. T. Mathew, J. J. Jacobs, and R. M. Urban, “Mechanical, chemical and biological damage modes within head-neck tapers of CoCrMo and Ti6Al4V contemporary hip replacements,” *J. Biomed. Mater. Res. Part B Appl. Biomater.*, vol. 1, Aug. 2017.
- [86] M. . Wimmer, J. Loos, R. Nassutt, M. Heitkemper, and A. Fischer, “The acting wear mechanisms on metal-on-metal hip joint bearings: in vitro results,” *Wear*, vol. 250, no. 1–12, pp. 129–139, Oct. 2001.
- [87] A. Shenoy, S. Kurtz, and J. Gilbert, “Biological, Chemical and Mechanical Damage Modes in Corrosion of CoCrMo Acetabular Liners,” in *ISTA 2018, London*, 2018, pp. 785–787.
- [88] J. R. Macdonald *et al.*, *Impedance Spectroscopy: Emphasizing Solid Materials and Systems*. John Wiley and Sons Inc., 1987.
- [89] S. Kerwell *et al.*, “Electrochemically Induced Film Formation on CoCrMo Alloy for Hip Implant Application,” *J. Bio- Tribo-Corrosion*, vol. 3, no. 1, p. 4, Mar. 2017.
- [90] M. Lyvers *et al.*, “Electrochemically induced tribolayer with molybdenum for hip implants: Tribocorrosion and biocompatibility study,” *Thin Solid Films*, vol. 644, pp. 82–91, Dec. 2017.
- [91] G. B. Higgs, “In Vivo Performance of the Femoral Head-Neck Taper Connection and Development of an Electrochemical Framework for Quantitative Corrosion

Investigations,” Drexel University, 2020.

- [92] P. Kinov *et al.*, “Role of free radicals in aseptic loosening of hip arthroplasty.,” *J. Orthop. Res.*, vol. 24, no. 1, pp. 55–62, 2006.
- [93] L. M. Jazrawi, F. J. Kummer, and P. E. DiCesare, “Alternative bearing surfaces for total joint arthroplasty.,” *J. Am. Acad. Orthop. Surg.*, vol. 6, no. 4, pp. 198–203, 1998.
- [94] H. G. Willert *et al.*, “Wear Behavior and Histopathology of Classic Cemented Metal on Metal Hip Endoprotheses.,” *Clin. Orthop. Relat. Res.*, vol. 329, 1996.
- [95] D. R. Plummer, J. M. Christy, S. M. Sporer, W. G. Paprosky, and C. J. Della Valle, “Dual-Mobility Articulations for Patients at High Risk for Dislocation,” *J. Arthroplasty*, vol. 31, no. 9, pp. 131–135, Sep. 2016.
- [96] J. A. Ortega-Saenz, M. A. L. Hernandez-Rodriguez, V. Ventura-Sobrevilla, R. Michalczewski, J. Smolik, and M. Szczerek, “Tribological and corrosion testing of surface engineered surgical grade CoCrMo alloy,” *Wear*, vol. 271, no. 9–10, pp. 2125–2131, Jul. 2011.
- [97] M. D. Mathew, K. Laha, and V. Ganesan, “Improving creep strength of 316L stainless steel by alloying with nitrogen,” *Mater. Sci. Eng. A*, vol. 535, pp. 76–83, Feb. 2012.
- [98] V. Swaminathan and J. L. Gilbert, “Fretting corrosion of CoCrMo and Ti6Al4V interfaces,” *Biomaterials*, vol. 33, no. 22, pp. 5487–5503, 2012.



- [99] J. Chen and F. Y. Yan, "Tribocorrosion behaviors of Ti-6Al-4V and Monel K500 alloys sliding against 316 stainless steel in artificial seawater," *Trans. Nonferrous Met. Soc. China (English Ed.)*, vol. 22, no. 6, pp. 1356–1365, Jun. 2012.
- [100] J. L. Gilbert and S. A. Mali, "Medical Implant Corrosion: Electrochemistry at Metallic Biomaterial Surfaces," in *Degradation of Implant Materials*, N. Eliaz, Ed. New York, NY: Springer New York, 2012, pp. 1–516.
- [101] S. M. Smith and J. L. Gilbert, "Compliant interfaces and fretting corrosion of modular taper junctions in total hip implants: The micromechanics of contact," *Tribol. Int.*, vol. 151, p. 106437, Nov. 2020.
- [102] O. Vingsbo and S. Söderberg, "On fretting maps," *Wear*, vol. 126, no. 2, pp. 131–147, Sep. 1988.
- [103] S. R. Small, M. E. Berend, L. A. Howard, D. Tun??, C. A. Buckley, and M. A. Ritter, "Acetabular Cup Stiffness and Implant Orientation Change Acetabular Loading Patterns," *J. Arthroplasty*, vol. 28, no. 2, pp. 359–367, 2013.
- [104] L. P. Milne, A. M. Kop, and M. S. Kuster, "Polyaxial locking and compression screws improve construct stiffness of acetabular cup fixation: A biomechanical study," *J. Arthroplasty*, vol. 29, no. 5, pp. 1043–1051, 2014.
- [105] F. Contu, B. Elsener, and H. Böhni, "Corrosion behaviour of CoCrMo implant alloy during fretting in bovine serum," *Corros. Sci.*, 2005.
- [106] V. Swaminathan and J. L. Gilbert, "Potential and frequency effects on fretting

corrosion of Ti6Al4V and CoCrMo surfaces,” *J. Biomed. Mater. Res. Part A*, vol. 101A, no. 9, pp. 2602–2612, Sep. 2013.

[107] M. S. Caicedo, R. Desai, K. McAllister, A. Reddy, J. J. Jacobs, and N. J. Hallab, “Soluble and particulate Co-Cr-Mo alloy implant metals activate the inflammasome danger signaling pathway in human macrophages: A novel mechanism for implant debris reactivity,” *J. Orthop. Res.*, vol. 27, no. 7, pp. 847–854, Jul. 2009.

[108] I. Papageorgiou *et al.*, “The effect of nano- and micron-sized particles of cobalt–chromium alloy on human fibroblasts in vitro,” *Biomaterials*, vol. 28, no. 19, pp. 2946–2958, Jul. 2007.

[109] M. J. Pearson *et al.*, “The effects of cobalt-chromium-molybdenum wear debris in vitro on serum cytokine profiles and T cell repertoire,” *Biomaterials*, vol. 67, pp. 232–239, 2015.

[110] Y. Niki *et al.*, “Metal ions induce bone-resorbing cytokine production through the redox pathway in synoviocytes and bone marrow macrophages,” *Biomaterials*, vol. 24, no. 8, pp. 1447–1457, Apr. 2003.

[111] Y. D. Levy and K. A. Ezzet, “Poor short term outcome with a metal-on-metal total hip arthroplasty.,” *J. Arthroplasty*, vol. 28, no. 7, pp. 1212–1217, 2013.

[112] J. J. Jacobs, H. J. Cooper, R. M. Urban, R. L. Wixson, and C. J. Della Valle, “What Do We Know About Taper Corrosion in Total Hip Arthroplasty?,” *J.*

*Arthroplasty*, vol. 29, no. 4, pp. 668–669, Apr. 2014.

- [113] T. Hui, G. W. Kubacki, and J. L. Gilbert, “Voltage and wear debris from Ti-6Al-4V interact to affect cell viability during in-vitro fretting corrosion,” *J. Biomed. Mater. Res. Part A*, vol. 106, no. 1, pp. 160–167, Jan. 2018.
- [114] M. Haeri, T. Wöllert, G. M. Langford, and J. L. Gilbert, “Electrochemical control of cell death by reduction-induced intrinsic apoptosis and oxidation-induced necrosis on CoCrMo alloy in vitro,” *Biomaterials*, vol. 33, no. 27, pp. 6295–6304, 2012.
- [115] S. Sivan, S. Kaul, and J. L. Gilbert, “The effect of cathodic electrochemical potential of Ti-6Al-4V on cell viability: voltage threshold and time dependence,” *J. Biomed. Mater. Res. Part B Appl. Biomater.*, vol. 101, no. 8, pp. 1489–1497, Nov. 2013.
- [116] M. J. Wiegand, G. W. Kubacki, and J. L. Gilbert, “Electrochemical potential zone of viability on CoCrMo surfaces is affected by cell type: Macrophages under cathodic bias are more resistant to killing,” *J. Biomed. Mater. Res. - Part A*, 2019.
- [117] B. Taciak *et al.*, “Evaluation of phenotypic and functional stability of RAW 264.7 cell line through serial passages,” *PLoS One*, vol. 13, no. 6, p. e0198943, 2018.
- [118] Y. Liu, D. Zhu, D. Pierre, and J. L. Gilbert, “Fretting initiated crevice corrosion of 316LVM stainless steel in physiological phosphate buffered saline: Potential and cycles to initiation,” *Acta Biomater.*, vol. 97, pp. 565–577, Oct. 2019.

- [119] D. Zhu, Y. Liu, and J. L. Gilbert, "In vitro fretting crevice corrosion damage of CoCrMo alloys in phosphate buffered saline: Debris generation, chemistry and distribution," *Acta Biomater.*, 2020.
- [120] M. S. Caicedo, L. Samelko, K. McAllister, J. J. Jacobs, and N. J. Hallab, "Increasing both CoCrMo-alloy particle size and surface irregularity induces increased macrophage inflammasome activation in vitro potentially through lysosomal destabilization mechanisms," *J. Orthop. Res.*, vol. 31, no. 10, pp. 1633–1642, Oct. 2013.
- [121] J. L. Gilbert, L. Zarka, E. Chang, and C. H. Thomas, "The reduction half cell in biomaterials corrosion: Oxygen diffusion profiles near and cell response to polarized titanium surfaces," *J. Biomed. Mater. Res.*, vol. 42, no. 2, pp. 321–330, 1998.
- [122] P. F. Doorn, J. M. Mirra, P. A. Campbell, and H. C. Amstutz, "Tissue Reaction to Metal on Metal Total Hip Prostheses," *Clin. Orthop. Relat. Res.*, vol. 329, pp. S187–S205, Aug. 1996.
- [123] C. Case *et al.*, "Widespread dissemination of metal debris from implants," *J. Bone Joint Surg. Br.*, vol. 76-B, no. 5, pp. 701–712, Sep. 1994.
- [124] E. Hollville, "Measuring apoptosis by microscopy and flow cytometry," *Methods*, vol. 61, no. 2, pp. 90–97, Jun. 2013.
- [125] I. Vermes, C. Haanen, H. Steffens-Nakken, and C. Reutellingsperger, "A novel

- assay for apoptosis Flow cytometric detection of phosphatidylserine expression on early apoptotic cells using fluorescein labelled Annexin V,” *J. Immunol. Methods*, vol. 184, no. 1, pp. 39–51, Jul. 1995.
- [126] Invitrogen Molecular Probes, “LIVE/DEAD Viability/Cytotoxicity Kit for mammalian cells,” *Prod. Information, Cat. number MP 03224*, pp. 1–7, 2005.
- [127] M. Kalbacova *et al.*, “The effect of electrochemically simulated titanium cathodic corrosion products on ROS production and metabolic activity of osteoblasts and monocytes/macrophages,” *Biomaterials*, vol. 28, no. 22, pp. 3263–3272, 2007.
- [128] S. Dupré-Crochet, M. Erard, and O. Nüße, “ROS production in phagocytes: why, when, and where?,” *J. Leukoc. Biol.*, vol. 94, no. 4, pp. 657–670, Oct. 2013.
- [129] N. J. Hallab and J. J. Jacobs, “Chemokines associated with pathologic responses to orthopedic implant debris,” *Front. Endocrinol. (Lausanne)*, vol. 8, no. JAN, pp. 1–10, 2017.
- [130] P. Panigrahi *et al.*, “Intergranular pitting corrosion of CoCrMo biomedical implant alloy,” *J. Biomed. Mater. Res. - Part B Appl. Biomater.*, 2014.
- [131] L. J. Matsen Ko, K. E. Pollag, J. Y. Yoo, and P. F. Sharkey, “Serum Metal Ion Levels Following Total Hip Arthroplasty With Modular Dual Mobility Components,” *J. Arthroplasty*, vol. 31, no. 1, pp. 186–189, Jan. 2016.
- [132] H. J. Cooper, “The local effects of metal corrosion in total hip arthroplasty,” *Orthop. Clin. North Am.*, vol. 45, no. 1, pp. 9–18, 2014.

- [133] T. L. DesMarias and M. Costa, "Mechanisms of chromium-induced toxicity," *Current Opinion in Toxicology*, vol. 14. Elsevier B.V., pp. 1–7, 01-Apr-2019.
- [134] D. Bagchi, M. Bagchi, and S. J. Stohs, "Chromium (VI)-induced oxidative stress, apoptotic cell death and modulation of p53 tumor suppressor gene," *Mol. Cell. Biochem.*, vol. 222, no. 1–2, pp. 149–158, 2001.
- [135] K. Schroder, P. J. Hertzog, T. Ravasi, and D. A. Hume, "Interferon- $\gamma$ : an overview of signals, mechanisms and functions," *J. Leukoc. Biol.*, vol. 75, no. 2, pp. 163–189, Feb. 2004.
- [136] T. Veremeyko, S. Siddiqui, I. Sotnikov, A. Yung, and E. D. Ponomarev, "IL-4/IL-13-dependent and independent expression of miR-124 and its contribution to M2 phenotype of monocytic cells in normal conditions and during allergic inflammation," *PLoS One*, vol. 8, no. 12, Dec. 2013.
- [137] M. Bosmann *et al.*, "Interruption of Macrophage-Derived IL-27(p28) Production by IL-10 during Sepsis Requires STAT3 but Not SOCS3," *J. Immunol.*, vol. 193, no. 11, pp. 5668–5677, Dec. 2014.
- [138] Y. Cao, P. D. Doodes, T. T. Glant, and A. Finnegan, "IL-27 Induces a Th1 Immune Response and Susceptibility to Experimental Arthritis," *J. Immunol.*, vol. 180, no. 2, pp. 922–930, Jan. 2008.
- [139] D. D. Taub, K. Conlon, A. R. Lloyd, J. J. Oppenheim, and D. J. Kelvin, "Preferential migration of activated CD4<sup>+</sup> and CD8<sup>+</sup> T cells in response to MIP-

- 1 $\alpha$  and MIP-1 $\beta$ ,” *Science* (80-. ), vol. 260, no. 5106, pp. 355–358, Apr. 1993.
- [140] S. Gronthos and A. C. W. Zannettino, “The role of the chemokine CXCL12 in osteoclastogenesis,” *Trends in Endocrinology and Metabolism*, vol. 18, no. 3. Elsevier Current Trends, pp. 108–113, 01-Apr-2007.
- [141] T. Luo *et al.*, “Adipocytes enhance expression of osteoclast adhesion-related molecules through the CXCL12/CXCR4 signalling pathway,” *Cell Prolif.*, vol. 50, no. 3, Jun. 2017.
- [142] E. Gibon *et al.*, “The biological response to orthopaedic implants for joint replacement: Part I: Metals,” *J. Biomed. Mater. Res. Part B Appl. Biomater.*, vol. 105, no. 7, pp. 2162–2173, Oct. 2017.
- [143] G. W. Kubacki and J. L. Gilbert, “The effect of the inflammatory species hypochlorous acid on the corrosion and surface damage of Ti-6Al-4V and CoCrMo alloys,” *J. Biomed. Mater. Res. Part A*, vol. 106, no. 12, pp. 3185–3194, Dec. 2018.
- [144] E. Brooks, M. Tobias, K. Krautsak, and M. Ehrensberger, “The influence of cathodic polarization and simulated inflammation on titanium electrochemistry,” *J. Biomed. Mater. Res. - Part B Appl. Biomater.*, vol. 102, no. 7, pp. 1445–1453, 2014.
- [145] B. Brüne *et al.*, “Redox control of inflammation in macrophages,” *Antioxidants and Redox Signaling*, vol. 19, no. 6. Mary Ann Liebert, Inc., pp. 595–637, 20-Aug-

2013.

- [146] D. Bagchi, E. A. Hassoun, M. Bagchi, and S. J. Stohs, "Chromium-induced excretion of urinary lipid metabolites, DNA damage, nitric oxide production, and generation of reactive oxygen species in Sprague-Dawley rats," *Comp. Biochem. Physiol. Part C Comp.*, 1995.
- [147] D. F. M. PAKVIS, D. JANSSEN, B. W. SCHREURS, and N. VERDONSCHOT, "ACETABULAR LOAD-TRANSFER AND MECHANICAL STABILITY: A FINITE ELEMENT ANALYSIS COMPARING DIFFERENT CEMENTLESS SOCKETS," *J. Mech. Med. Biol.*, vol. 14, no. 05, p. 1450063, Oct. 2014.



## APPENDICES

### **A1. Retrieved device section and surface preparation for microstructural analysis**

1. Identify device with intergranular corrosion (IGC) or similar penetrating forms of corrosion such as pitting.
2. Keep in mind that the high-speed abrasive cut-off wheel will cause localized heating and can introduce shear forces, so associated material loss along the section must be accounted for.
3. Select the abrasive cut-off wheel appropriate for the material of the device: choice will depend on material hardness.
4. Install the cut-off wheel in the high-speed abrasive cutting equipment and ensure the coolant tank has sufficient coolant and is attached to the nozzle within the cutting chamber. Ensure the nozzle is positioned to allow coolant flow onto the wheel and the surface about to be sectioned.
5. Secure the device using grips supplied with the machine. Ensure there is minimal movement of the device along all axes, and that the surface to be cut is positioned in a way as to allow the wheel to contact a flat surface perpendicular to the wheel edge.
6. Close the chamber hood and start the coolant flow. Position the cut-off wheel at its highest point away from the device.

7. Start the cutting action on the machine and move the wheel slowly at a steady pace towards the section. Continue at a steady pace in the downward direction until the device is sectioned through. DO NOT reverse the direction of the lever controlling the wheel while cutting.
8. Remove the sectioned device and rinse thoroughly in a mild detergent solution.
9. Dry the sectioned surface, and wet polish the surface using emery paper of progressively finer grit. Starting with 240 grit, pass the sectioned surface over the length of the paper in a single direction, back and forth about 10 times. Turn 180 degrees and repeat until the surface is uniform. Repeat with 320, 400 and 600 grit papers.
10. Using a 1  $\mu\text{m}$  alumina suspension, wet polish the surface to a mirror finish until no visible scratches remain. Repeat with 0.3  $\mu\text{m}$  alumina suspension.
11. Sonicate the device in a 50% ethanol solution for 5 minutes.
12. Dry thoroughly. The surface is now ready for scanning electron microscopy (SEM) image analysis.

## **A2. Preparation of microelectrode for near-field EIS measurements**

1. Cut off about 2-3 mm from the tip of a 1000  $\mu\text{L}$  pipette tip, creating a larger opening.
2. Prepare a 2% agar solution in 1X phosphate-buffered saline (PBS). Using a syringe, fill the pipette tip with the solution up to 1 cm height. Ensure no bubbles or air space between the opening and the agar gel. Allow to dry.
3. The agar solution can be stored at room temperature and reused by reheating in short bursts of 10 seconds until liquification.
4. Fill the pipette with about 750  $\mu\text{L}$  PBS.
5. Cover the other end of the pipette tip with Parafilm. Insert a platinum wire and a chloride Ag wire taking care to prevent contact between the two.

### **A3. Preparation of tribocorrosion chamber for fretting corrosion experiment with macrophages**

1. Prepare a 35 mm petri dish by drilling a 0.5 cm diameter opening in the base using a drill press, taking care to use a steady pace and slowly bringing the drill bit in contact with the petri dish to prevent crack formation.
2. Thoroughly clean the petri dish using a Kim wipe and 70% ethanol solution.
3. Prepare a CoCrMo disk by mirror polishing.
4. Apply a thin layer of peelable silicon sealant onto the petri dish, ensuring evenness and coverage up to the edge of the opening.
5. Gently place the petri dish with the sealant onto the disk, and press down lightly to form a strong, water-tight seal. Take care to not displace the petri dish, to avoid the sealant from leaking into the opening.
6. Allow to air dry for at least 24 hours and sterilize using UV light before use.

**A4. Preparation of cells in tribocorrosion chamber (petri dish + metal disk) sample for SEM analysis**

1. Remove any media or solutions remaining in the petri dish adhered atop the metal disk.
2. Rinse with 1X PBS.
3. Pipette in, gently, 2 mL of cold 4% paraformaldehyde (PFA) solution. Cover, and place in  $-4^{\circ}\text{C}$  for 2 hours.
4. Prepare 50%, 75%, 90%, 100% ethanol (EtOH) solutions in PBS.
5. At the end of 2 hours, replace the 4% PFA with 1 mL of 50% EtOH. Incubate at room temperature for 15 minutes. Repeat with 75%, 90%, 100% EtOH solutions, for 15 minutes each.
6. Place the sample, covered, into  $-20^{\circ}\text{C}$  freezer overnight to freeze dry.
7. After overnight freezing, sputter coat the sample with a gold coat. Sample is now ready for SEM and EDS analysis.

## CURRICULUM VITAE

### Aarti A. Shenoy

Charleston, SC 29407

email: aarti.shenoy17@gmail.com

Phone: 315-806-8100

#### **Education:**

University of Mumbai	Biomedical Engineering	B.E.	2012
Syracuse University	Biomedical Engineering	M.S.	2014
Clemson University	Bioengineering	Ph.D.	2020

#### **Appointments:**

Spring 2013-Spring 2017	Research Assistant	Dept. of Biomedical Engineering, Syracuse University
Fall 2017-Fall 2020	Research Assistant	Dept. of Bioengineering, Clemson University
Fall 2014	Teaching Assistant	ECS 326: Engineering Materials, Processes & Properties
Spring 2015	Teaching Assistant	BEN 433/633: Drug Delivery
Fall 2015	Teaching Assistant	ECS 326: Engineering Materials, Processes & Properties
Spring 2016	Teaching Assistant	BEN/CEN 212: Experimental Methods in Chemical Engineering
Spring 2017	Teaching Assistant	BEN 468/668: Biomaterials & Medical Devices

#### **Journal Publications:**

1. E.S. Ouellette, **A.A. Shenoy**, J.L. Gilbert, “The seating mechanics of head-neck modular tapers in vitro: Load-displacement measurements, moisture, and rate effects”, *Journal of Orthopedic Research*, Sept 2018 (DOI: 10.1002/jor.23725)
2. **A.A. Shenoy**, J.L. Gilbert, “In vitro test methods for seating and fretting corrosion behavior of modular metal-on-metal acetabular tapers”, *Journal of Orthopedic Research*, Dec 2019 (DOI: 10.1002/jor.24554)
3. M. Wiegand, **A.A. Shenoy**, S. Littlejohn, J.L. Gilbert, “Sensing Localized Surface Corrosion Damage of CoCrMo Alloys and Modular Tapers of Total Hip Retrievals

Using Nearfield Electrochemical Impedance Spectroscopy”, *ACS Biomaterials Science and Engineering*, Jan 2020 (DOI: 10.1021/acsbomaterials.9b00945)

4. **A.A. Shenoy**, J.L. Gilbert, “Non-Tribological Corrosion Modes Dominate Wrought CoCrMo Acetabular Taper Corrosion: A Retrieval Study”, under review (2020)
5. **A.A. Shenoy**, J.L. Gilbert, “Near-field Electrochemical Impedance Spectroscopy of Retrieved Hip Implants”, (in preparation) 2020
6. **A.A. Shenoy**, J.L. Gilbert, “Tribocorrosion Debris and Cathodic Voltage Shifts in CoCrMo Affect Murine Macrophage Viability Outcomes in In Vitro Fretting Corrosion”, (in preparation) 2020

#### **Conference Abstracts:**

1. A. Ferrel, T. Alzubaydi, **A.A. Shenoy**, J.L. Gilbert, “Fretting Corrosion Analysis of 316L Stainless Steel (316LSS) under 240 Grit, 320 Grit and 600 Grit Surface Roughness”, Society for Biomaterials Annual Meeting & Exposition 2014, Denver, CO, USA (Talk)
2. S.A. Mali, **A.A. Shenoy**, V. Singh, J.L. Gilbert, “Fretting Corrosion Response of Spinal Fixation Devices with CoCrMo Rods of Different Surface Roughness”, Orthopedic Research Society Annual Meeting 2015, Las Vegas, NV, USA (Poster)
3. E.S. Ouellette, **A.A. Shenoy**, J.L. Gilbert, “Influence of Seating Load, Loading Rate, and Initial Moisture on Connection Strength of Modular Head-Neck Junctions on Total Hip Replacements”, World Biomaterials Conference 2016, Montreal, Canada (Poster)
4. J.L. Gilbert, **A.A. Shenoy**, “Bio-metallurgical interactions during in vivo corrosion: Beyond fretting corrosion, a study of the forms of corrosion in retrieved modular implants, their causes and consequences”, ASTM Symposium 2017, Toronto, Canada
5. **A.A. Shenoy**, J.L. Gilbert, “A Modular Acetabular Test Method to Assess Shell-Liner Taper Seating and Fretting Corrosion Behavior”, Orthopedic Research Society Annual Meeting 2018, New Orleans, LA (Poster)
6. **A.A. Shenoy**, S.M. Kurtz, J.L. Gilbert, “Biological, Chemical and Mechanical Damage Modes in Corrosion of CoCrMo Acetabular Liners”, International Society for Technology in Arthroplasty Annual Meeting 2018, London, UK (Young Investigators Session, Talk)
7. **A.A. Shenoy**, J.L. Gilbert, “Near-Field Electrochemical Impedance Spectroscopy Methods for Retrieval Surface Analysis”, International Society for Technology in Arthroplasty Annual Meeting 2019, Toronto, Canada (Talk)

#### **Awards:**

1. Young Investigators Award, International Society for Technologies in Arthroplasty (ISTA) 2019

2. Clemson University Graduate Travel Grant (\$1000), Fall 2019
3. Merit-based 50% scholarship for MS Biomedical Engineering, Syracuse University
4. Nunan Travel Grant at Syracuse University in Fall 2015

**Professional Service:**

1. Bioengineering Department Representative at College of Engineering & Computer Science – Graduate Student Organization (2015 - 2016)
2. Conference Volunteer, World Biomaterials Congress (May 2016)
3. Orthopedic Research Society (ORS) Insider (Jan 2018 - Jan 2019)

**Mentees:**

Brianna Gamble, high school senior from Charleston Charter School for Math & Science, Summer 2019 Research Experience